INVESTIGATION OF THE PLASMA BEHAVIOUR IN THE DENSE PLASMA FOCUS USING LASER LIGHT SCATTERING TECHNIQUES

by

RICHARD ERNEST KIRK

Department of Physics
Royal Holloway College
University of London

This thesis is submitted for the
Degree of Doctor of Philosophy
in the University of London

July 1984

ABSTRACT

The frequency spectrum of density fluctations in a Plasma Focus device has been investigated by Thomson scattering of laser light. A ruby laser scattering diagnostic has been developed to enable the co-operatively scattered ion feature, $S_i(\underline{k},\omega)$ to be measured simultaneously along different density fluctuation $\underline{k}$ vectors. Data derived from this apparatus is interpreted in terms of the time and space variations of local plasma parameters such as electron and ion temperatures, drift velocity, bulk velocity and level of turbulence. The total scattered intensity, $S_i(k)$ is shown to depend on the direction in which the fluctuations are sampled by the scattering geometry, with scattered intensities along a $\underline{k}$ vector parallel to the current flow enhanced considerably above thermal levels.

The data is found to be most satisfactorily interpreted in terms of a double radial shell model of the plasma, each shell with its own characteristic particle temperatures, density, drift and bulk velocity. At peak compression of the pinch onto the z-axis of symmetry for example, the core plasma has typically electron and ion temperatures T_e=200 eV, T_i=250 eV respectively, while the outer sheath region exhibits a shot to shot variation in the temperature structure, with T_e=2.3 keV, T_i=850 eV and T_e=1.65 keV, T_i=1.4 keV respectively. An examination of the relative enhancement and broadening of $S_i(k,\omega)$ along the various k-vectors has been interpreted in terms of current driven turbulence. The various mechanisms for inducing turbulence have been considered and lower-hybrid drift, electron-cyclotron drift and ion acoustic instabilities are thought to play a role in the various phases of the plasma discharge.

The development of the multiple $\underline{k}$ scattering diagnostic has overcome the ambiguity in interpreting scattering results from an irreproduceable inhomogeneous plasma. This problem has restricted the interpretation of the results in previous scattering experiments on the Plasma Focus using single $\underline{k}$ vector scattering arrangements.

Table of Contents

LIST OF FIGURES

LIST OF TABLES

ACKNOWLEDGEMENTS

I wish to express my thanks to Dr N J Peacock, my supervisor at Culham Laboratory, for all his support and advice, and my College supervisor, Dr E R Wooding for his encouragement throughout this work. I am indebted to M J Forrest for having taught me the 'art' of scattering laser light exclusively off electrons, and for his and Dr D G Muir's support and good humour during the course of the experiments. I would also like to thank D L Trotman for his advice and assistance with the detector electronics, and Christine Shepherd for typing the mathematics in this thesis.

I acknowledge the assistance given to me by Dr D G Muir in obtaining and analysing the holographic interferometry data.

Finally, I gratefully acknowledge the research grants provided to me by the SERC and the UKAEA Culham Laboratory.

To my parents and friends
for their support and
encouragement.

CHAPTER 1 INTRODUCTION

The advent of lasers during the early 1960's provided a suitable source of coherent and intense visble light for a whole new range of plasma diagnostic measurements in this region of the electromagnetic spectrum. These active diagnostics which include laser scattering, interferometry and Faraday rotation, all have the common advantage of being non-perturbing. That is, they do not change the plasma parameters during the course of the measurements, in contrast to plasma probes, for example. Of the three, laser scattering has been the most widely exploited diagnostic on a variety of plasmas, for the determination of a range of parameters. It is now a standard technique for determining electron temperatures and densities on magnetically confined toroidal devices [1,2] and has been used for the measurement of magnetic fields [3,4] and laterly for studying laser-plasma interactions [5,6]. The application of laser scattering on the Plasma Focus device in a detailed investigation of the plasma behaviour, will form the principle subject of this thesis.

The Plasma Focus was developed independently during the early 1960's by Mather [7,8,9] in the United States and Filippov [10] in the Soviet Union. Figure 1.1 shows a sectional view of the cylindrical electrode arrangements of the two types of devices. The essential difference between the two arrangements is that the Mather type device has a long coaxial electrode arrangement which is not present in the Filippov device. All the work described in this thesis relates to the Mather type device.

The operation of the Plasma Focus can be divided into several

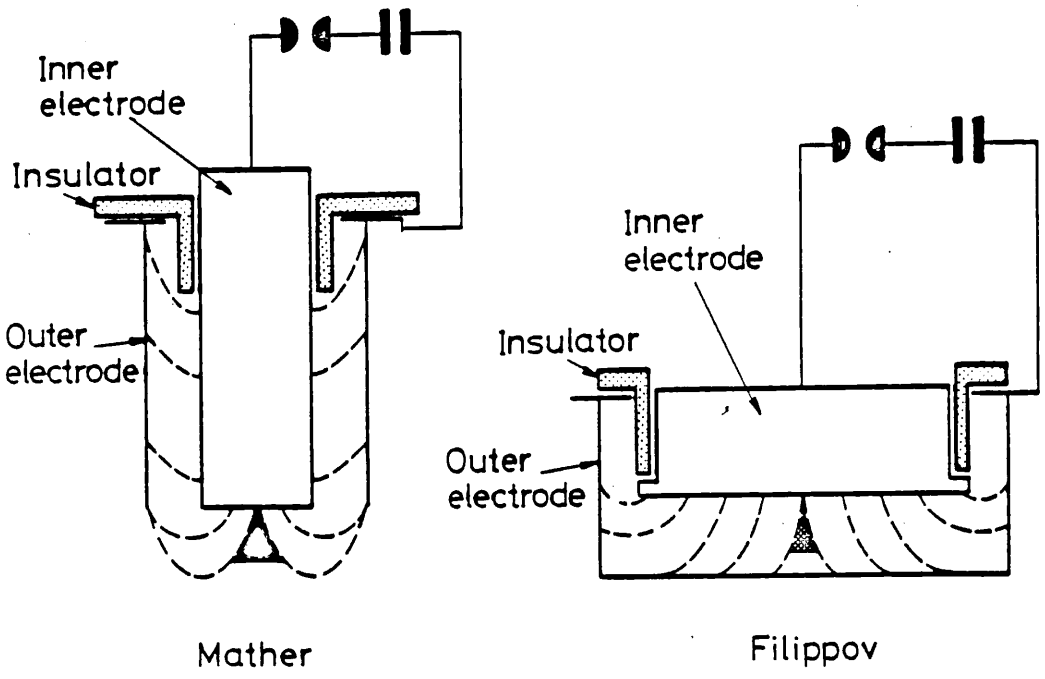

Figure 1.1
Mather and Filippov type Plasma Foci.

discrete regions:

(1) Run-down phase On switching the capacitor bank, a plasma sheath is formed across the insulator in the background gas (normally a few torr of deuterium). The current through the plasma produces a magnetic field within the volume between the electrodes and the insulator side of the sheath. The magnetic pressure, or volume $\underline{J} \times \underline{B}$ force, drives the sheath away from the insulator, along the length of the gun, 'snow-ploughing' the low pressure gas ahead. This latter phase, commonly known as the run-down phase, is absent in the Filippov device. The duration of the run-down phase is of the order of 2.5 μs in the Culham Plasma Focus.

(2) Collapse phase On reaching the open end of the electrodes, the annular sheath collapses radially due to the $\underline{J} \times \underline{B}$ radial force component, resulting in an asymmetric, quasi-cylindrical pinch on axis.

This phase of the discharge is called the collapse phase and has a duration of the order of 100 ns. The gas filling pressure and capacitor bank voltage are normally adjusted to maximise the plasma current at this time. Typical parameters of the plasma at peak compression (minimum radius) are a diameter of the order few millimetres and a peak electron density of greater than 10^{25} m^{-3}.

(3) Dense-pinch phase Peak compression is followed by the dense-pinch phase, during which the plasma relaxes. The duration of this phase varies from device to device in the range 10 - 100 ns, during which the plasma emits a copious burst of neutrons and soft X-rays.

(4) Break-up phase The dense-pinch phase is terminated with the onset of m=0 and m=1 MHD instabilities and is known as the break-up phase. The plasma then forms a broad diffuse plasma column or diffuse-pinch and emits a second burst of neutrons and soft X-rays.

Detailed comparative reviews of the performance of Plasma Foci have been given by several authors [11,12,13,14]. These include details of diagnostics which have been implemented to study the Plasma Focus and the various phenomena which are associated with the device.

The motion of electrons in a highly ionised plasma can be studied effectively using laser light scattering. Depending on the ratio of the plasma electron density, n_e and temperature, T_e, and on the choice of laser wavelength, λ_o and scattering angle, θ, a range of plasma parameters can be measured. The above parameters are generally formulated in terms of the scattering parameter, α which on evaluation of constants is given by,

$$\alpha \simeq 1.07 \times 10^{-5} \frac{\lambda_o}{\sin(\theta/2)} \left[\frac{n_e}{T_e}\right]^{\frac{1}{2}} \qquad (1.1)$$

where n_e has units of m^{-3} and T_e is in eV. Depending on its value, two

distinct scattering regimes can be investigated. For a thermalised plasma, that is one having electron and ion velocity distributions which are Maxwellian, the $\alpha \ll 1$ regime results in the Doppler shifted scattered spectrum reflecting the random thermal motions of the electrons. The width of this type of spectrum yields a value for the plasma electron temperature. For $\alpha \geq 1$ the scattered spectrum reflects the cooperative motion of the electrons. This may be due to the electron shielding cloud round each ion, in which case the scattered spectrum has a width dependent on the random thermal motions of the ions and can be used to measure the plasma ion temperature. Additionally in this regime, scattering can be used to study plasma waves. A detailed review of the theoretical aspects of laser light scattering is given in chapter 2.

When the investigation of the Plasma Focus using laser light scattering was commenced, previous measurements using ruby laser (λ_o=694.3 nm) scattering with a range of scattering angles had been reported by several authors [15,16,17,18,19,20]. All these experiments were based on measurements of the cooperatively scattered ion spectrum. We shall see in chapter 3, that the plasma temperature values determined from these experiments varied greatly. On detailed analysis of the plasma parameters, it was found that the disparity in the results could be explained in terms of the steep radial electron density profile and an assumed inversed radial temperature profile. From eq 1.1 it can be seen that this will result in the scattering parameter, α, varying with radius. The total ion spectrum scattered energy contribution of a particular radius of the plasma is proportional to $(\alpha^2/1+\alpha^2)^2$, therefore depending on the chosen scattering angle, θ, different radii of the plasma will dominate the scattered light profile. Additionally, with the exception of one

previous work [20], the broadening of the scattered spectrum due to the radial velocity component during the collapse and dense-pinch phases of the plasma for scattering geometries having a component of the differential scattering vector, $\underline{k}$ in the radial direction, had not been taken into consideration. Here the differential scattering vector will be defined as $\underline{k}=\underline{k}_s-\underline{k}_o$, where $\underline{k}_o$ and $\underline{k}_s$ are the incident and scattered wavevectors respectively.

Of particular interest in this earlier work, was the observation of varying levels of enhancement and asymmetry of the scattered ion spectra, when the differential scattering vector, $\underline{k}$ had a component aligned with the plasma current direction (plasma $\underline{z}$-axis). This was attributed by Baconnet et al [17] and Bernard et al [19] as being due to current driven turbulence. The consequences of this may be of significance to the neutron production mechanisms operating in the Plasma Focus reviewed by Morgan [11] and the observations of intense ion beams [21,22] and electron beams [22,23,24].

In conclusion, the previous work presented a certain disparity in the results, but investigation of these gave some clear indications of the approach to a new series of scattering experiments on the Plasma Focus. The objectives of this work, were to undertake a more comprehensive investigation of the collapse, dense-pinch and break-up phases of the plasma. The dynamics of the collapse phase are of particular importance, because the conditions of this phase may have a strong bearing on the neutron and ion/electron beam production mechanisms of the later phases. To overcome the ambiguities of the results of an inhomogeneous plasma, it was decided to employ ruby laser scattering to measure the scattered spectrum originating from several scattering geometries, so that comparative analysis would be possible.

The choice of a ruby laser and the range of n_e and expected T_e of the Plasma Focus, limited the scattering to the cooperatively scattered regime ($\alpha \geq 1$) and the available laser power further restricted the measurements to the scattered ion feature. The Plasma Focus presents a major problem to the objectives of comparative analysis, in that it suffers from irreproducibility from shot to shot. This problem is highlighted by previous work [17,19] where varying degrees of enhancement and asymmetry were observed for $\underline{k}$ vectors having components aligned with the z-axis. To overcome this problem, it was considered desirable to develop an experimental technique which would permit the simultaneous measurement of the scattered ion spectrum from more than one scattering geometry during a single plasma shot. Such a multiple-$\underline{k}$ scattering arrangement would then enable comparative analysis between the measured spectra of various $\underline{k}$'s to be undertaken.

In chapter 4 the experimental arrangement of the Culham Plasma Focus device, the diagnostic ruby laser and the various control systems and operating arrangements are given. Additionally, the secondary diagnostics are discussed. The principle one of these was holographic interferometry which provided data on the radial electron density profiles and radial velocity as a function of time. This data was later utilised in the analysis of the scattered spectra.

In order to record several dispersed scattered spectra simultaneously, a large number of detection channels are required. Additionally, previous single-$\underline{k}$ experiments were limited by the small number of detection channels available, which prevented detailed analysis of the spectral profile to be undertaken. In chapter 5, the possible dispersion instrument/detection system arrangements which were considered are discussed. The arrangement used, consisting of a 1 m

Czerney-Turner grating spectrometer and a gated Vidicon Optical Multichannel Analyser (OMA) and its implementation with the Plasma Focus scattering system are detailed. The system provided 500 detection channels with an inverse linear dispersion of $\sim$ 0.02 nm/channel.

The multiple-$\underline{k}$ ruby laser scattering technique is described in detail in chapter 6. Three scattering collection optics were used. Two with scattering angles of 10 and 45 degrees had their differential scattering vector, $\underline{k}$ orthogonal to the $\underline{z}$-axis. The third with a scattering angle of 10 degrees was arranged so that the $\underline{k}$ vector was aligned with the $\underline{z}$-axis (plasma current direction). The three collection optics imaged an essentially identical scattering volume, located on the plasma axis 10 mm from the centre electrode, onto three fibre optics. The output ends of the three fibre optics were imaged onto three parallel 100 μm input slits mounted on the grating spectrometer. The three dispersed images of the slits were then recorded in the output focal plane by the OMA. Two distinct but comparable aspects of the Plasma Focus behaviour were investigated using this technique. Firstly, the radial ion and electron temperature profiles as a function of plasma time were determined using the two scattering geometries having differential scattering vectors, $\underline{k}$ orthogonal to the $\underline{z}$-axis. Secondly, the effects of current driven turbulence parallel to the $\underline{z}$-axis were determined using the third geometry with a scattering angle of 10 degrees having its $\underline{k}$ vector aligned with the $\underline{z}$-axis. This arrangement permitted direct comparison between this geometry and the 10 degree $\underline{k}$ orthogonal spectrum.

The analysis of the scattered data, described in chapter 7, was based on a double radial shell model of the plasma. During the

collapse phase of the plasma, the radial profile was approximated as consisting of a core region surrounded by a collapsing sheath region. A profile function consisting of the composite scattered profiles for each region was fitted to the experimental data. The profile function for each region incorporated the effects of the radial velocity component which was determined from the holographic interferometry. From the Faraday rotation polarimetry measurements of Muir [25] on the same Plasma Focus, it was known that during the collapse phase of the plasma, the plasma current is restricted to the plasma skin with a penetration depth of $\sim$ 0.7-0.8 mm. These measurements permitted the double radial shell model to be applied to the scattered data obtained from the 10 degree $\underline{k}$ aligned with $\underline{z}$-axis arrangement to determine a value of the electron drift velocity as a function of time during the collapse phase, in addition to the plasma bulk velocity in the direction of the $\underline{z}$-axis. Following peak compression of the pinch, comparison of the varying levels of enhancement observed between the three geometries was made. This permitted a lower limit to be determined for the scale length of turbulence observed during this phase. The interpretation of the measured parameters obtained from the analysis and their significance to the complex dynamics of the Plasma Focus are then discussed.

A summary and discussion of the results of the investigation is presented in the first section of chapter 8, followed by an appraisal of possible future research using laser light scattering techniques on the Plasma Focus device.

CHAPTER 2 THEORY OF LASER LIGHT SCATTERING BY A PLASMA

2.1 INTRODUCTION

The theory of light scattering is very complex and has been treated in detail by several authors [26,27,28]. Excellent reviews of the subject and its application to laboratory plasmas can be found in references [29,30]. As this is mainly an experimental thesis, only those parts of the theory relevant to the development of a description of the theoretical aspects of the experiments will be considered. The scattering cross section, the effects of the incident radiation on the plasma, the scale length for scattering and the frequency spectrum of the scattered light will each be discussed. Additionally, the effects of a plasma current and magnetic field on the scattered light will be considered.

2.2 THOMSON CROSS SECTION

A free charged particle in the presence of an electromagnetic wave behaves as an oscillating electric dipole which radiates electromagnetic waves that in its own frame of reference are in phase with the incident radiation. Thus a fraction of the illuminating radiation is 'scattered'. In the classical explanation of Thomson scattering we neglect any momentum transfer to the scattering electrons. Such a neglect of the Compton effect is implicit in this

classical treatment of the interaction of radiation and matter and is justified in the limit $h\nu << mc^2$, where ν is the frequency of the incident radiation in the particle frame and m is the rest mass of the particle. The validity of the classical treatment for the scattering experiments discussed here will be established as we progress.

For plane polarised light the value of the differential Thomson cross-section is,

$$d\sigma = \left(\frac{1}{4\pi\varepsilon_o}\right)^2 \left(\frac{Z^2 e^2}{mc^2}\right)^2 \sin^2\gamma d\Omega \qquad (2.1)$$

where m is the particle mass, Ze is the particle charge, γ is the angle between the electric vector and the scattering direction and $d\Omega$ is the collection solid angle.

Since $d\sigma$ is proportional to $\frac{Z^4}{m^2}$, the scattering by ions can be safely ignored in comparison with the scattering by electrons.

Introducing the classical radius of an electron:

$$r_e = \left(\frac{1}{4\pi\varepsilon_o}\right) \frac{e^2}{m_e c^2} \simeq 2.8 \times 10^{-15} \text{ (m)} \qquad (2.2)$$

where m_e is the mass of an electron.

Equation 2.1 can be written as,

$$\frac{d\sigma}{d\Omega} = r_e^2 \sin^2\gamma \qquad (2.3)$$

Integrating eq 2.3 over the solid angle $d\Omega = 2\pi \sin\gamma \, d\gamma$ we obtain an expression for the total Thomson cross-section,

$$\sigma_T = \frac{8\pi}{3} r_e^2 = 6.65 \times 10^{-29} \text{ m}^2 \simeq 2/3 \text{ barn} \qquad (2.4)$$

Rearranging eq 2.3 we get,

$$\frac{d\sigma}{d\Omega} = \frac{3}{8\pi}\ \sigma_T \sin^2\gamma \qquad (2.5)$$

Ideally for laser scattering experiments γ is set equal to 90 degrees to obtain maximum scattered light. It should be noted that under these conditions the fraction of the total scattered light detected is $\frac{3d\Omega}{8\pi}$, not $\frac{d\Omega}{4\pi}$ as is frequently assumed. This latter value is applicable only when the incident radiation is unpolarised, which results in an isotropic scattered light distribution.

In the introduction to the section, it was stated that the classical treatment is not valid for higher frequencies, when the Compton effect is important. Here scattering must be treated quantum mechanically taking into account the conservation of energy as well as momentum. The asymptotic forms of the total cross-section are given by the Klein-Nishina formulas (Sheffield [30]) as,

$$\sigma_{KN} = r_e^2 \begin{cases} \frac{8\pi}{3}\left(1 - \frac{2h\nu}{m_e c^2} + \ldots\ldots\right) & h\nu << m_e c^2 \\ \pi \frac{m_e c^2}{h\nu}\left[\ell n\left(\frac{2h\nu}{m_e c^2}\right) - \tfrac{1}{2}\right] & h\nu >> m_e c^2 \end{cases} \qquad (2.6)$$

For our situation with $h\nu << m_e c^2$ and an electron of velocity 6×10^7 m.s^{-1} (energy of 10 KeV) towards the illuminating source, the resultant correction to the cross section for a wavelength of 700 nm is less than 10^{-4} and can be safely ignored.

2.3 EFFECTS OF THE INCIDENT RADIATION ON THE PLASMA

In the introduction to this thesis, it was stated that laser light scattering has the advantage of being a non-perturbing diagnostic. For this statement to be valid, several requirements are placed on the parameters of the incident radiation. It is required that the plasma be virtually transparent to the incident electromagnetic wave. This condition is satisfied provided the frequency of the incident wave, ω_o, is much greater than the plasma frequency, ω_{pe} given by,

$$\omega_{pe} = \left(\frac{n_e e^2}{m_e \varepsilon_o}\right)^{\frac{1}{2}} \tag{2.7}$$

where n_e is the electron density. For $\omega_o < \omega_{pe}$, the incident wave will be reflected. However, even for the condition of $\omega_o > \omega_{pe}$, absorption of the incident wave can occur. For ω_o near to ω_{pe} collective effects must be considered, but for our situation with $\omega_o >> \omega_{pe}$, the main absorption process is that of inverse bremsstrahlung, where a photon is absorbed by an electron in the proximity of an ion, the ion serving to conserve momentum. The average power dissipated per unit volume by the incident wave is given by [30],

$$P_D = \frac{n_e e^2 \nu_{ei}}{m_e c \varepsilon_o \omega_o^2} \quad \frac{P_o}{A_o} \tag{2.8}$$

where P_o is the power of the incident wave, A_o is the cross sectional area of the incident beam in the plasma and ν_{ei} is the electron-ion collision frequency.

Kunze [31] has compared the energy deposited per unit volume by the incident wave, with the electron thermal energy density, $3/2\ \kappa T_e n_e$, where κ is Boltzmann's constant. The fractional increase in electron

temperature is given by,

$$\frac{\Delta T_e}{T_e} = \frac{\int_0^{\tau} \bar{P}_D \, dt}{3/2 \kappa T_e \, n_e} \qquad (2.9)$$

where τ is the duration of the incident wave.

The electron-ion collision frequency for singly charged ions is given by,

$$\nu_{ei} = 2.92 \times 10^{-12} \, n_i \, [T_e(eV)]^{-3/2} \, \ell n \Lambda \; (s^{-1}) \qquad (2.10)$$

where n_i is the ion density and $\Lambda = 12 \, n_e \lambda_D^3$. λ_D is defined as the Debye length given by,

$$\lambda_D = \left(\frac{\varepsilon_o \kappa T_e}{e^2 \, n_e} \right)^{\frac{1}{2}} \qquad (2.11)$$

On substituting eq 2.10 and 2.8 into 2.9, we get for the fractional increase in electron temperature,

$$\frac{\Delta T_e}{T_e} = 3.63 \times 10^{-17} \, \frac{\lambda_o^2 \, n_i \, \ell n \Lambda}{A_o T_e^{5/2}} \int_o^{\tau} P_o \, dt \qquad (2.12)$$

where λ_o is the wavelength of the incident wave and T_e now has units of eV.

With $n_i = n_e \sim 1 \times 10^{25} \; m^{-3}$ and an average electron temperature, $T_e \sim 300$ eV (to be established later), $\ell n \Lambda = 9.0$. With a ruby laser ($\lambda_o = 694.3$ nm) pulse energy of 6 J, $\Delta T_e / T_e \sim 6 \times 10^{-5}$. ($A_o \approx 10^{-4} m^2$)

The focussing of a laser beam to a small spot can produce very high local electric fields, such that the illuminated free electron may achieve relativistic velocities where the Lorentzian force term is no

longer negligible. Kunze [31] gives for the maximum relativistic β for such electrons,

$$\beta = \frac{v_{max}}{c} = \frac{e E_o}{m_e \omega_o c} \tag{2.13}$$

where E_o is the laser beam peak electric field in $V.m^{-1}$ of frequency ω_o. The irradiance of the laser is given in terms of the peak electric field by,

$$I_o = \frac{1}{2} c \varepsilon_o E_o^2 \tag{2.14}$$

where I_o has units of $W.m^{-2}$. Rearranging eq 2.14 and substituting into eq 2.13 gives,

$$\beta = 8.53 \times 10^{-6} \lambda_o \sqrt{I_o} \tag{2.15}$$

Thus if high intensity effects are to be neglected ($\beta \ll 1$), it is required that,

$$I_o \ll 2.8 \times 10^{22} W.m^{-2} \text{ for } \lambda_o = 700 \text{ nm}$$

This condition is readily satisfied by the focussed laser beams used in the majority of scattering experiments.

2.4 SCALE LENGTH FOR SCATTERING

The detection system of a scattering experiment in the visible wavelength region measures the intensity of the scattered light. To determine the value of the intensity it is necessary to sum the electric amplitudes of the scattered photons from each contributing electron, taking the phase differences at the detector into consideration. Figure 2.1 shows the geometry of a scattering experiment with a scattering angle θ. The position of one electron in the plasma is given by R_e, and that of the detector by R_d. R is the

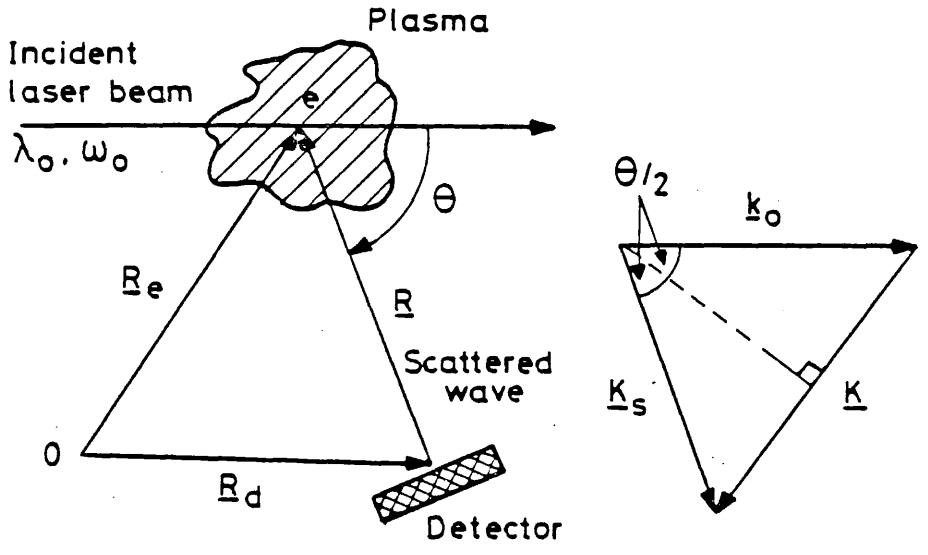

Figure 2.1
Scattering Wave Vector Diagram

vector from the detector to the electron. For an incident wave of frequency, ω_o, and wavelength, λ_o, the electric field at the electron at a retarded time $t'=t-|\underline{R}|/c$ is given by,

$$\underline{E}_o(\underline{R}_e,t') = \underline{E}_{oo} \cos(\underline{k}_o.\underline{R}_e-\omega_o t') \qquad (2.16)$$

where $\underline{k}_o$ is the wavevector of the incident wave.
Neglecting the magnetic field because we are assuming $v_e/c<<1$, the scattered electric field at the detector at a time $t=t'+|\underline{R}|/c$ is given by Sheffield [30] as,

$$\underline{E}_s(\underline{R}_d, t) = \frac{r_e}{|\underline{R}|^3} [\underline{R}x(\underline{R}x\underline{E}_{oo})]\cos(\underline{k}_s.\underline{R}_d-\omega_s t-(\underline{k}_s-\underline{k}_o).\underline{R}_e) \qquad (2.17)$$

where ω_s and $\underline{k}_s$ are the frequency and wavevector of the Doppler-sfifted electromagnetic wave radiated by the electron. The frequency shift, ω and differential scattering vector, $\underline{k}$ are given by conservation of

energy and momentum as,

$$\omega = \omega_s - \omega_o$$
$$\underline{k} = \underline{k}_s - \underline{k}_o \qquad (2.18)$$

where the momentum transfer to the scattering electron has been neglected (Compton effect). The correction to the wavelength shift if the Compton effect is included is given by,

$$\Delta\lambda = \left(\frac{2h}{m_e c}\right) \sin^2(\theta/2) = 4.8 \times 10^{-3} \sin^2(\theta/2) \quad (nm) \qquad (2.19)$$

This factor is independent of frequency and can be neglected for the scattering experiments under consideration.

The direction of the differential scattering vector, $\underline{k}$, as shown in figure 2.1 is normal to the bisector of the scattering angle, θ, between the direction of the incident and scattered waves and has a magnitude,

$$|\underline{k}| = 2|\underline{k}_o| \sin(\theta/2) = \frac{4\pi}{\lambda_o} \sin(\theta/2) \qquad (2.20)$$

If we replace the phase factor, $(\underline{k}_s - \underline{k}_o).\underline{R}_e$ of eq 2.17 by $\underline{k}.\underline{R}_e$ (eq 2.18), we see that the phase of the scattered wave depends on both $\underline{k}$ and the electron position $\underline{R}_e$. Electrons with positions such that $\underline{k}.\underline{R}_e$ is constant, lie in a plane orthogonal to $\underline{k}$. Other parallel planes separated from this one by integer multiples of $2\pi k^{-1}$ will have phase shifts different to the first by integer multiples of 2π. Electrons lying in all these planes will scatter in phase. The quantity $2\pi k^{-1}$ is known as the scale length for scattering. The configuration of electrons in a plasma relative to these planes determines the scattered signal at the detector. For example, for N electrons confined to these planes, which would scatter in phase, the

intensity at the detector would be $(NE_s)^2$ and proportional to N^2. A uniform distibution of electrons would lead however to exact cancellation by interference of the electric field at the detector. In reality, random statistical density fluctuations ensure that the difference in population of two equal volume elements in the plasma is proportional to $N^{\frac{1}{2}}$, which results in the scattered light intensity at the detector being proportional to N. In choosing a $\underline{k}$ therefore, we are effectively selecting to observe one spatial Fourier component of the electron density distribution for which the wave number is $\underline{k}$.

The Debye length given by eq 2.11, is a measure of the radius of the electron shielding cloud surrounding each ion in the plasma. Therefore for a scale length, $k^{-1} << \lambda_D$, the motions within the cloud are viewed and the scattered spectrum reflects the individual motions of the electrons. For $k^{-1} >> \lambda_D$, the resolution is small and the scattered spectrum reflects the the motions of the electron shielding clouds. We shall define these two different scattering domains in terms of the scattering parameter α, defined as,

$$\alpha = \frac{1}{k\lambda_D} \qquad (2.21)$$

For $\alpha << 1$ the individual motion of the electrons are observed.
For $\alpha \geq 1$ the cooperative behaviour of the electrons through the electron shielding clouds are observed.

2.5 FREQUENCY SPECTRUM OF SCATTERED LIGHT FROM A PLASMA

The frequency spectrum of scattered light from a plasma can be divided into two regimes; one where the electron motions in the plasma are independent, and the other where the correlations between the motions have a marked effect on the frequency spectrum. These correlations can be due to several effects such as the presence of other electrons and ions, of plasma waves, collisions, magnetic fields and currents in the plasma.

The usual specification of the scattering process is in terms of a differential cross-section $\sigma(\underline{k},\omega)$ defined by Evans & Katzenstein [29] as,

$$P(\underline{k},\omega)\,d\omega d\Omega = N\,I_o\;\sigma(\underline{k},\omega)\,d\omega d\Omega. \qquad (2.22)$$

where $P(\underline{k},\omega)$, is the scattered power frequency spectrum in Watts/frequency/steradian, N is the number of scattering centres, and I_o is the incident laser intensity in $W.m^{-2}$.

As we have already demonstrated in the previous section, the light scattered by a plasma is as a result of density fluctuations and $\sigma(\underline{k},\omega)$ is defined by,

$$\sigma(\underline{k},\omega) = \frac{3}{8\pi}\;\sigma_T\;S(\underline{k},\omega) \qquad (2.23)$$

where $S(\underline{k},\omega)$ is known as the dynamic form factor, which is the Fourier transform in time of the autocorrelation function of the spatial Fourier component of the electron density fluctuations. The dynamic form factor reflects the frequency shifts resulting from the electron motions as well as the effects of correlations between electrons. The calculation of the electron density fluctuation for a fully ionised

plasma has been calculated by several methods which are reviewed in [29,30].

The dynamic form factor can be expressed [29,30] for a plasma in terms of G_e and G_i, the dielectric susceptibilities of the electrons and ions. Writing the plasma dielectric coefficient, $\varepsilon = 1-G_e-G_i$ the form factor can be shown to be,

$$S(\underline{k},\omega) = \frac{|1-G_i(\omega/k)|^2 F_e(\omega/k) + Z|G_e(\omega/k)|^2 F_i(\omega/k)}{|\varepsilon|^2} \tag{2.24}$$

where F_e and F_i are the velocity distributions of the electrons and ions respectively.

We shall assume zero-order Maxwellian velocity distributions for the electrons and ions, which corresponds to a plasma in thermal equilibrium, or certain limited deviations from thermal equilibrium. By the latter, we allow for the possibility of different electron and ion temperatures and the possibility of a displacement of the electron and ion distribution functions in velocity. The zero-order velocity distributions F_{oe} and F_{oi} are given by the expressions,

$$\begin{aligned} F_{oe}(v) &= \left(\frac{n_e}{v_e \pi^{\frac{1}{2}}}\right) \exp\left\{ - \left(\frac{v}{v_e}\right)^2 \right\} \\ F_{oi}(v) &= \frac{n_e}{Z}\left(\frac{1}{v_i \pi^{\frac{1}{2}}}\right) \exp\left\{ - \left(\frac{v}{v_i}\right)^2 \right\} \end{aligned} \tag{2.25}$$

where $v=\omega/k$ is the magnitude of the velocity vector of the particle, and v_e and v_i are the electron and ion mean thermal speeds defined in terms of the electron and ion temperatures as,

$$v_e = \left(\frac{2\kappa T_e}{m_e}\right)^{\frac{1}{2}} \quad : \quad v_i = \left(\frac{2\kappa T_i}{m_i}\right)^{\frac{1}{2}} \tag{2.26}$$

where m_i is the mass of an ion and the temperatures are in units of degrees Kelvin. We can replace $\kappa T_{e,i}$ by $eT_{e,i}$ so that the temperatures can be stated in units of eV. Introducing the dimensionless frequency variables, x_e and x_i,

$$x_e = \frac{\omega}{kv_e} \quad : \quad x_i = \frac{\omega}{kv_i} \tag{2.27}$$

the dielectric susceptibilities can be written [29] as

$$G_e = -\alpha^2 W(x_e)$$

$$G_i = -Z \frac{T_e}{T_i} \alpha^2 W(x_i) \tag{2.28}$$

where α is the scattering parameter which has already been defined in eq 2.21, and

$$W(x) = 1-2xe^{-x^2}\int_0^x e^{p^2} dp - i\pi^{\frac{1}{2}} xe^{-x^2} \tag{2.29}$$

is the plasma dispersion function given by Fried & Conte [32]. The imaginary part of this is the Landau damping term. It should be noted that the real part of W(x) can be approximated by the following series for large and small values of the argument,

$$\begin{aligned} Re\, W(x) &\simeq 1 - 2x^2 (1-2/3x^2 + 4/15x^4 + ...) \quad x<<1 \\ Re\, W(x) &\simeq -\frac{1}{2x^2}\left(1 + \frac{3}{2x^2} + \frac{15}{4x^4} + ...\right) \quad x>>1 \end{aligned} \tag{2.30}$$

Substituting the expressions 2.25 and 2.28 into 2.24 we obtain for the dynamic form factor,

$$S(\underline{k},\omega)\,d\omega = \left| \frac{1 + Z\alpha^2 (T_e/T_i) W(x_i)}{1 + \alpha^2 W(x_e) + \alpha^2 Z (T_e/T_i) W(x_i)} \right|^2 \exp(-x_e^2) \frac{dx_e}{\pi^{\frac{1}{2}}}$$

$$+ Z \left| \frac{- \alpha^2 W(x_e)}{1 + \alpha^2 W(x_e) + \alpha^2 Z (T_e/T_i) W(x_i)} \right|^2 \exp(-x_i^2) \frac{dx_i}{\pi^{\frac{1}{2}}} \qquad (2.31)$$

This full form factor for a plasma with a Maxwellian velocity distribution can be simplified into useful analytic results which can be applied to experiments provided the approximations made are valid. These analytic results are detailed in the subsequent sections.

2.5.1 SALPETER APPROXIMATION - Te/Ti $\lesssim$ 1

Salpeter [26] showed that under a certain approximation based on the large disparity of scale of the variables x_e and x_i for a given frequency shift ω and for values of the electron-ion temperature ratio which are not too large, the dynamic form factor can be written as the sum of two terms: an electron spectrum term whose frequency scale is kv_e, the characteristic Doppler shift at the electron thermal speed, and an ion spectrum whose frequency scale is kv_i, the characteristic Doppler shift at the ion thermal speed. Equation 2.31 can now be written in terms of the same function of x, given by,

$$\Gamma_\alpha(x) = \frac{\exp(-x^2)}{|1 + \alpha^2 W(x)|^2} \qquad (2.32)$$

The equation for the form factor now becomes,

$$S(\underline{k},\omega)\,d\omega = \Gamma_\alpha(x_e) \frac{dx_e}{\pi^{\frac{1}{2}}} + Z \left(\frac{\alpha^2}{1+\alpha^2}\right)^2 \Gamma_\beta(x_i) \frac{dx_i}{\pi^{\frac{1}{2}}} \qquad (2.33)$$

where β^2 is defined as,

$$\beta^2 = z\left(\frac{\alpha^2}{1+\alpha^2}\right)\frac{T_e}{T_i} \tag{2.34}$$

and $\Gamma_\beta(x_i)$ has the same functional form as $\Gamma_\alpha(x_e)$ and is plotted in Figure 2.2

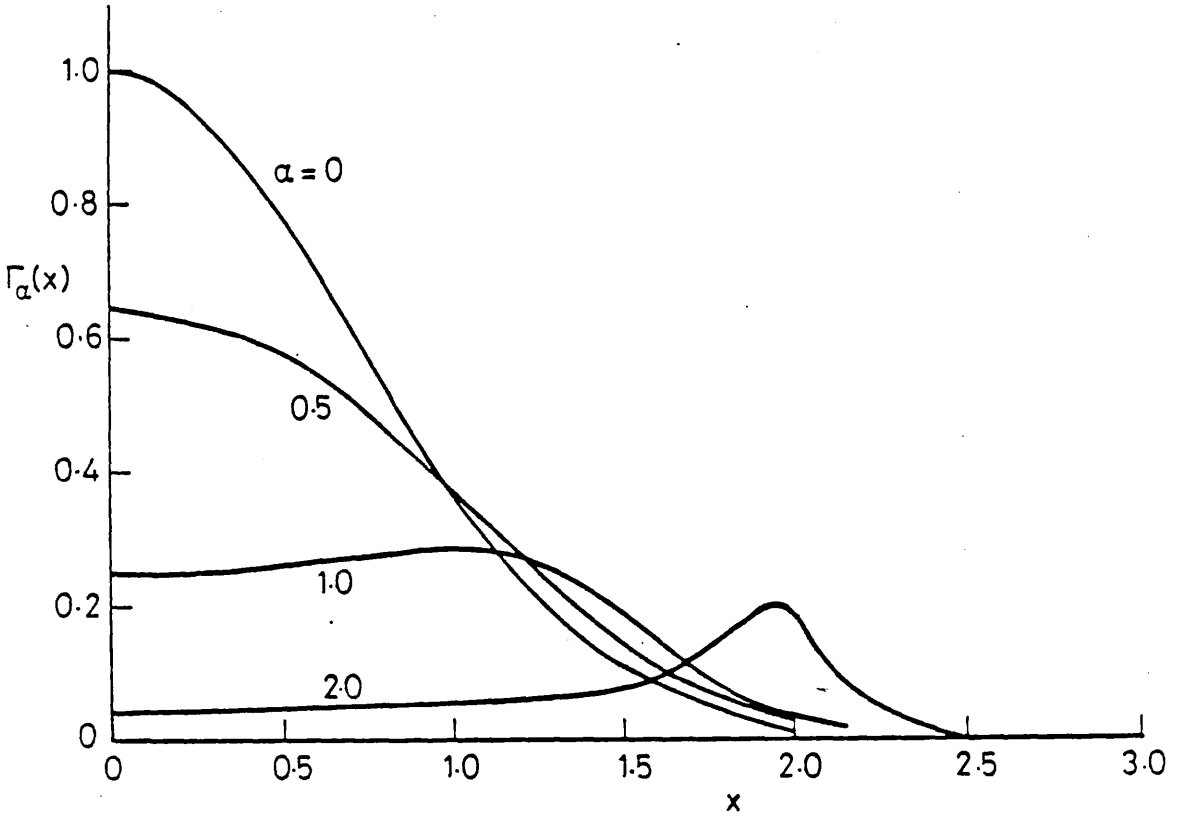

Figure 2.2
The function Γ_α (x) plotted for various values of the parameter α.

The Electron term

The first term of eq 2.33 is denoted the electron term. It includes the contributions to the spectrum from free electrons for $\alpha \ll 1$, and from electrons plus their Debye shields for $\alpha \gg 1$. It should be noted that at high frequencies (i.e. $x_e \simeq 1$) $x_i \gg 1$. When

$\alpha \ll 1$, the spectrum is dominated by this term, which is approximately a Gaussian whose half-width is the characteristic Doppler shift at the electron thermal speed. It can therefore be used to measure the electron temperature if k is known. The Gaussian shape is distorted as α increases and the maximum , x_p, shifts away from zero as α becomes greater than unity. For $1 \leq \alpha \leq 2$ it can be seen from figure 2.2 that the peak, x_p, almost coincides numerically with the value of α :

$$x_p \simeq \alpha$$

or

$$\frac{\omega_p}{kv_e} = \frac{\sqrt{2}}{kv_e}\ \omega_{pe} \tag{2.35}$$

where ω_{pe} is the electron plasma frequency defined by eq 2.7. Sustituting for ω_{pe} we get,

$$\omega_p = 79.6\ n_e^{\frac{1}{2}} \tag{2.36}$$

We can see therefore that for the range $1 \leq \alpha \leq 2$ the position of the peak alone is a useful diagnostic for determining the electron density n_e.

When $\alpha > 2$ it can be shown that [29]

$$\begin{aligned} x_p^2 &= \frac{1}{2}(\alpha^2 + 3) \\ \omega_p^2 &= \omega_{pe}^2 + 3/2k^2v_e^2 \end{aligned} \tag{2.37}$$

Equation 2.37 is the Bohm and Gross dispersion relation [33] for electron waves in the limit of wavelengths large compared with the Debye length. For $\alpha > 2$ then, the high frequency components of the spectrum show well developed electron satellites at $\pm x_p$. The profile of these satellites in the vicinity of the resonance has the form of a Lorentzian line of height and half intensity half-width given by,

$$S_e(\underline{k},\phi) = \left(\frac{2}{\pi^{3/2}}\right) \frac{\exp(\alpha^2)}{\alpha^6}$$

$$(\Delta\omega)_{\frac{1}{2}} = \frac{\pi^{\frac{1}{2}}\,\alpha^4}{2} \exp\left(-\frac{\alpha^2}{2}\right) \qquad (2.38)$$

As α increases the width decreases, corresponding to a reduction of Landau damping of the plasma waves. Although the peak height increases with α , the total scattered energy of both satellites decreases as α^{-2} as will be seen in eq 2.41 below for the integrated cross sections. It should be noted that the preceding result assumes that the only contribution to damping of the electron oscillations (and hence the width of the satellites) is Landau damping which vanishes in the limit of wavelengths long compared to the Debye length. The effects of collision damping must then be included.

It is only at the lower frequencies, $x_i \gtrsim 1$ and $x_e << 1$ that the ions play a role. However, for $T_e \gtrsim T_i$ the ion-acoustic resonance is weak due to heavy ion Landau damping. The case of $T_e > T_i$ will be discussed below in section 2.5.2.

The Ion term

The second term of eq 2.33 gives the contribution to the scattering from the electron shielding cloud of each ion. It should be noted that the contribution of this term vanishes as α^4 for $\alpha < 1$, and is therefore only of significance for $\alpha \geq 1$. Because of the factor of $\exp(-x_i^2)$ the term is only important in the regime $0 < x_i \leq 2$. There is no high frequency component of the order $x_e \gtrsim 1$. For large α values the parameter β^2 approaches T_e/T_i and it is this parameter which determines the shape of the spectrum. As $\beta \to 0$ the shape of the spectrum approaches a Gaussian whose half-width is the characteristic Doppler

shift at the ion thermal speed. When $\beta > 1$ the spectrum shape is the product of the above Gaussian and a function with a maxima at $x_i \simeq 1.5$. As in the electron case, the peak alone is a diagnostic indication when $1 \leq \beta \leq 2$. Now it is a measure of T_e however, provided α is known. The frequency shift of the peak is given by,

$$\omega_p = kv_e \left(\frac{\alpha^2}{1+\alpha^2}\right)^{\frac{1}{2}} \left(\frac{m_e}{m_i}\right)^{\frac{1}{2}} \tag{2.39}$$

Within the assumptions of the Salpeter approximation T_e/T_i is restricted to small values, so the ion term cannot have a resonance, because the real part of the denominator of the second term of eq 2.31 has no real root for $\beta^2 < 3.45$.

Total Cross-section

In concluding this section on the Salpeter approximation we will state the total cross-section for all frequency shifts for both electron and ion spectra.

Firstly, let us write eq 2.33 as

$$S(\underline{k},\omega) = S_e(\underline{k},\omega) + S_i(\underline{k},\omega) \tag{2.40}$$

Integrating over all frequencies it can be shown that [29]

$$\begin{aligned} S_e(\underline{k}) &= \frac{1}{1+\alpha^2} \\ S_i(\underline{k}) &= \frac{Z\alpha^4}{(1+\alpha^2)^2}\left(\frac{1}{1+\beta^2}\right) \\ S(\underline{k}) &= \frac{1 + \alpha^2[1 + ZT_e/T_i] + Z\alpha^4}{(1+\alpha^2)[1+\alpha^2(1+ZT_e/T_i)]} \end{aligned} \tag{2.41}$$

For a plasma with Z=1 (hydrogen plasma) and equal electron and ion temperatures, the ratio of the light intensities of the electron spectrum and the ion spectrum is,

$$\frac{S_e(\underline{k})}{S_i(\underline{k})} = \frac{1 + 2\alpha^2}{\alpha^4} \qquad (2.42)$$

Thus the dependance of the origin of the scattered light on α can be seen. For $\alpha < 1$ the electron feature dominates the scattering, and for $\alpha > 1$ the influence of the ions on the scattered spectrum predominates.

2.5.2 Te/Ti > 1 - THE ION-ACOUSTIC RESONANCE

In discussing the electron term we saw that for large α ($\alpha^2 > 2.0$) an electron wave resonance occurs at $\omega = \pm\omega_{pe}$, the electron plasma frequency. If we now consider the case of an electron temperature greater than the ion temperature (contrary to the conditions of the Salpeter approximation) a second resonance occurs at the ion-acoustic frequency, $\omega_{ac} = k\left(\frac{ZkT_e}{m_i}\right)^{\frac{1}{2}}$. It can be shown that [29] the contribution of the ion term to this resonance is negligible for sufficiently large temperature ratios, T_e/T_i. So even for large α, the principle contribution to the cross section comes from the electron term, and the dynamic form factor in this case can be written as,

$$S_e(\underline{k},\omega) = \frac{1}{\pi^{\frac{1}{2}}} \frac{(\omega_{ac}/\omega)^4 (Zm_e/2m_i)^{\frac{1}{2}} (d\omega/\omega_{ac})}{\{1 - (\omega_{ac}/\omega)^2\}^2 + \pi(Zm_e/m_i)} \qquad (2.43)$$

This is just a Lorentzian line centred at $\omega = \pm\omega_{ac}$ with a total cross

section over all frequencies, $S_e(\underline{k})=1/2$ for each resonance. This ion-acoustic resonance is lightly damped for large T_e/T_i ratios.

2.5.3 ELECTRON-ION RELATIVE DRIFT

In this section we will consider the effect of a relative drift between electrons and ions which constitutes an electric current in a plasma. In this situation we are saying that the velocity distribution function of the electrons is displaced in velocity space with respect to that of the ions. This can result in a marked change of shape of the spectrum, and produce an enhancement of the total scattering cross section above its thermal level. We begin by redefining the zero-order electron velocity distribution function of eq 2.25 as,

$$F_{oe}(v) = \left(\frac{n_e}{v_e \pi^{\frac{1}{2}}}\right) \exp\left(-\frac{(v-\hat{\underline{k}}.\underline{D})^2}{v_e^2}\right) \tag{2.44}$$

where $\hat{\underline{k}}$ is a unit vector parallel to the differential scattering vector $\underline{k}$ and $\underline{D}$ is the electron-ion drift velocity. The ion velocity distribution function and its screening integral G_i remain unchanged to eq 2.25 and 2.28 respectively. The electron screening integral becomes,

$$G_e(x_e) = -\alpha^2 W(x_e - d_r) \tag{2.45}$$

where d_r is the ratio of the drift velocity component parallel to $\underline{k}$ and the electron mean thermal velocity,

$$d_r = \frac{\hat{\underline{k}}.\underline{D}}{v_e} \tag{2.46}$$

Sustituting eqs 2.44 and 2.45 into 2.24 we obtain an expression for the full dynamic form factor,

$$S(\underline{k},\omega)\,d\omega = \left| \frac{1 + Z\alpha^2 (T_e/T_i) W(x_i)}{1+\alpha^2 W(x_e-d_r)+\alpha^2 Z (T_e/T_i) W(x_i)} \right|^2 \exp(-(x_e-d_r)^2) \frac{dx_e}{\pi^{1/2}}$$

(2.47)

$$+ Z \left| \frac{-\alpha^2 W(x_e-d_r)}{1+\alpha^2 W(x_e-d_r)+\alpha^2 Z (T_e/T_i) W(x_i)} \right|^2 \exp(-x_i^2) \frac{dx_i}{\pi^{1/2}}$$

We may again make use of the Salpeter approximation to separate the dynamic form factor into an electron and an ion term,

$$S(\underline{k},\omega)\,d\omega = \left| \frac{1}{1 + \alpha^2 W(x_e-d_r)} \right|^2 \exp(-(x_e-d_r)^2) \frac{dx_e}{\pi^{1/2}}$$

$$+ Z \frac{\alpha^4 |W(-d_r)|^2}{|1 + \alpha^2 W(-d_r) + \alpha^2 Z (T_e/T_i) W(x_i)|^2} \exp(-x_i^2) \frac{dx_i}{\pi^{1/2}} \qquad (2.48)$$

The electron term remains unchanged except for the replacement of the variable x_e by x_e-d_r resulting in a Doppler shift of the entire spectrum corresponding to the electron drift velocity.

The ion term however is drastically changed by the electron drift velocity. There exists a resonance on the short-wavelength wing which is enhanced for $\underline{D}$ parallel to $\underline{k}$, and a resonance on the long-wavelength wing which is enhanced for $\underline{D}$ antiparallel to $\underline{k}$. For each of these two conditions the resonance on the opposite wing is more heavily damped than for a thermal equilibrium spectrum. An alternative way of expressing this, is that the electron drift contributes a negative Landau damping to the ion-acoustic wave whose phase velocity is in the same direction as the drift velocity and an additional positive Landau damping to the ion-acoustic wave whose phase velocity is in the opposite direction to the drift velocity. Figure 2.3 shows a plot of

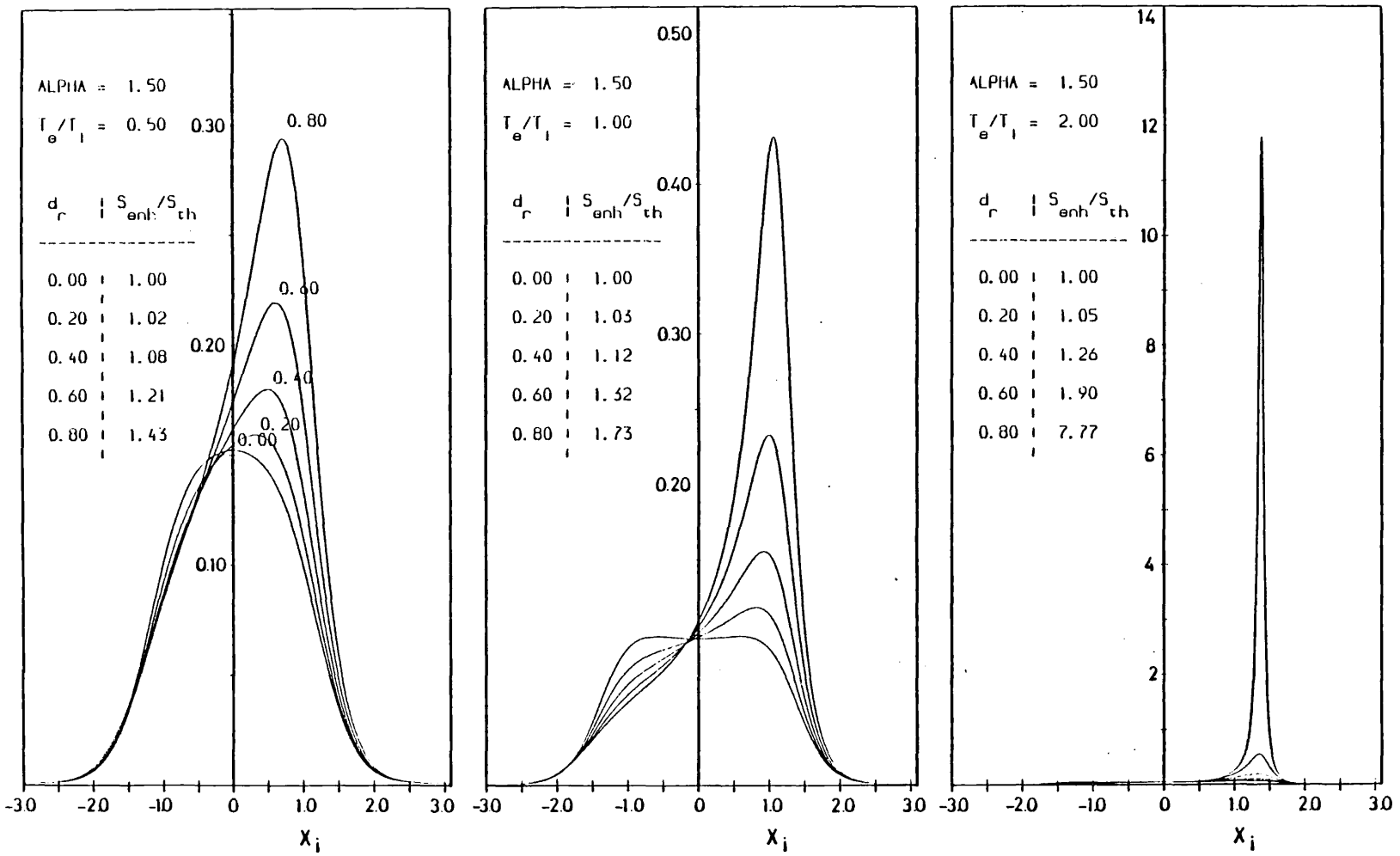

Figure 2.3

Plot of scattered ion spectrum resulting from an electron-ion drift velocity for a range of Te/Ti and electron drift ratios, d_r.

the ion spectrum obtained using the dynamic form factor given by eq 2.47, for a range of T_e/T_i ratios and drift velocity ratios. The fractional increase in total cross section of each spectra relative to $d_r=0$, calculated numerically, is also tabulated.

The theory so far discussed is based on the zero-order, F_0, velocity distribution functions for electrons and ions. This approximation is based on the fact that the first order velocity distribution functions, $F_1 << F_0$. It should be noted however, that for sufficiently large drift ratios, d_r, the scattering cross section based on eqs 2.47 and 2.48 approaches infinity, implying that the electron density fluctuation approaches the mean density. For this situation the whole theory needs reworking to handle these conditions, but due to its complexity will not be discussed further here.

In the case of the ion-acoustic resonance for large T_e/T_i ratios, when the spectrum consists of two Lorentzian lines at $\pm\omega_{ac}$, the effect of an electron drift velocity parallel or antiparallel to $\underline{k}$ is to enhance one line and suppress the other. The short-wavelength line being enhanced for $\underline{D}$ parallel to $\underline{k}$, and vice-versa.

2.5.4 EFFECT OF A MAGNETIC FIELD

The effect of a uniform stationary magnetic field, $\underline{B}$ on the electron spectrum is detailed by Evans & Katzenstein [29], Sheffield [30] and Carolan [34]. As we shall see in chapter 3, scattering on the Plasma Focus is limited to $\alpha \geq 1$ so we will only consider the effect of such a magnetic field on the cooperative spectrum. In the case of a collisionless plasma, the dynamic form factor including the effects of a relative electron-ion drift velocity

has been derived by Boyd et al [35] as,

$$S(\underline{k},\omega) = \frac{1}{\pi} \left\{ \frac{\frac{Im(-F_e)}{\omega-\underline{k}.\underline{D}} \left| 1 + \alpha^2 \frac{T_e}{T_i} W(x_i) \right|^2 + \alpha^4 \frac{Im[-W(x_i)]}{\omega} \left| F_e \right|^2}{\left| 1 + \alpha^2 F_e + \alpha^2 \frac{T_e}{T_i} W(x_i) \right|^2} \right\} \tag{2.49}$$

where x_i and $W(x)$ have been previously defined by eqs 2.27 and 2.29 and the other parameters are given by,

$$F_e = 1 - \frac{2X}{\cos\phi} e^{-\left(\frac{\sin^2\phi}{2X_e^2}\right)} \sum_{n=-\infty}^{\infty} I_n \left(\frac{\sin^2\phi}{2X_e^2}\right) e^{-\left(\frac{X-nX_e}{\cos\phi}\right)^2}$$

$$x \left[\int_0^{\frac{X-nX_e}{\cos\phi}} e^{t^2} dt + \frac{i\sqrt{\pi}}{2} \right]$$

where ϕ is the angle between $\underline{k}$ and $\underline{B}$, I_n is a Modified Besel function and

$$X = \frac{\omega - \underline{k}.\underline{D}}{kv_e} \quad : \quad X_e = \frac{\omega_{ce}}{kv_e}$$

The electron cyclotron frequency, ω_{ce} is given by,

$$\omega_{ce} = \frac{eB}{m_e} \tag{2.50}$$

Equation 2.49 requires that the ions are considered unmagnetised. This condition is reasonable where the detection system resolution is too low to detect the fine structure in the scattered spectrum due to the

ion cyclotron motion.

The effect of including the magnetic field, is that the total cross section of the ion spectrum, $S_i(k)$ can be substantially increased even for small drift ratios, d_r when the value of ϕ is close to 90 degrees. Additionally the spectrum can exhibit resonances at values of the parameters for which Gary & Sanderson [36] predict growth of the electron-ion drift instability.

CHAPTER 3 APPLICATION OF SCATTERING THEORY

TO THE PLASMA FOCUS

3.1 INTRODUCTION

In this chapter the application of the scattering theory discussed in the previous chapter to the Plasma Focus will be discussed. A review of scattering experiments performed on the Plasma Focus by previous workers, will provide a valuable insight into the considerations given to the designing of the experiments presented in this thesis. The choice of laser wavelength, scattering angle, $\underline{k}$ orientation, scattering volume dimensions and the detection systems requirements will each be considered. The chapter will be concluded with calculations of the signal to noise ratios that may be obtained with the selected scattering geometries and an outline of the proposed scattering experiments will be given.

Before starting a detailed discussion of the application of scattering theory to the Plasma Focus, it will prove useful to give some definitions which will be adhered to for the rest of this thesis.

Coordinate system and k orientation

The (r,z) coordinate system will be used to define a position within the plasma where the $\underline{z}$-axis is defined as the plasma axis of symmetry having a direction pointing away from the centre electrode. The differential scattering vector orientation, $\underline{k}$ will be defined relative to this axis of symmetry.

As an example, a scattering volume at z=10 mm, r=5 mm with $\underline{k}$ orthogonal to $\underline{z}$, illustrated in figure 3.1, will be situated 10 mm away from the centre electrode, 5 mm from the plasma axis of symmetry with $\underline{k}$ only having a radial component. For this off-axis position $\underline{k}$ may be pointing towards or away from the $\underline{z}$-axis.

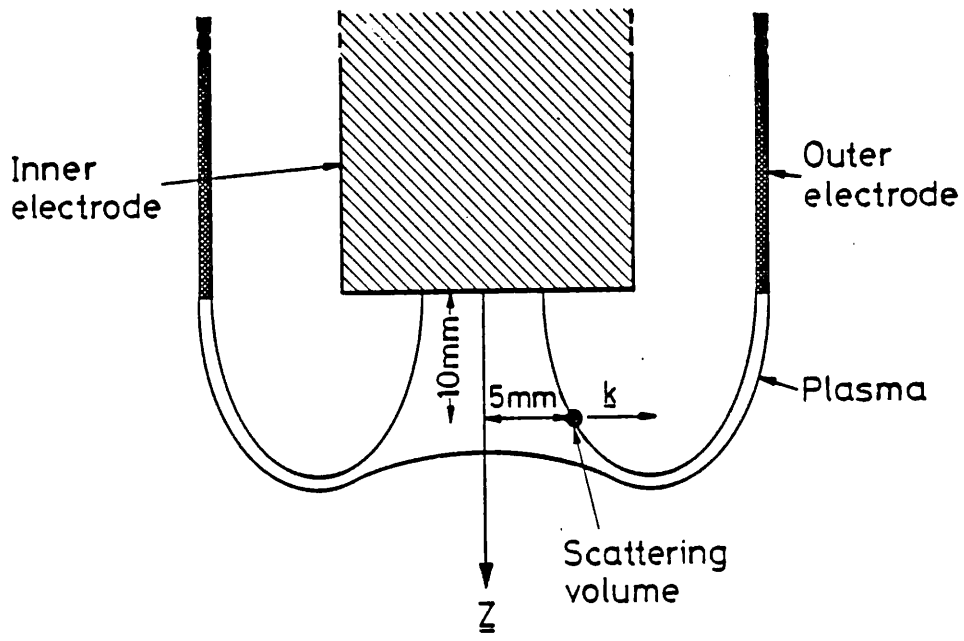

Figure 3.1
Plasma Focus coordinate system and $\underline{k}$ orientation.

Plasma timing

Temporal evolution of the spectra will be defined relative to the first peak of the dI/dt trace (section 4.5.1). This has previously been defined as corresponding to the first contraction of the plasma on the axis. It is important to note however that this defintion depends on z position, since as the z value increases the first minima of plasma radius occurs at increasingly later times as will be demonstrated in section 4.5.3.5. In this section we will see that in the Culham Plasma Focus the peak of the dI/dt trace (t=0 ns) corresponds to the first plasma radius minima for z in the range 5-10 mm. Times before this

during the collapse phase will be defined as negative, those following the first minima as positive.

3.2 PREVIOUS PLASMA FOCUS SCATTERING EXPERIMENTS

3.2.1 REVIEW

All the previous experiments prior to this thesis work [15,16,17,-18,19,20,37,38] have several common features: (1) In each case the investigation was performed on a Mather type Plasma Focus (2) A ruby laser (λ_o=694.3 nm) was used as the diagnostic laser, with scattering angles between 7 and 90 degrees and range of $\underline{k}$ orientations. (3) The cooperative scattering regime ($\alpha \geq 1$) was investigated.
One experiment using a CO_2 laser (λ_o=10.6 micron) and a scattering angle of 90 degrees has been reported recently [39].

The dominance of the cooperative scattering regime in this work, will become apparent if we look at the dependence of α on the incident wavelength, λ_o and the plasma electron density, n_e and temperature, T_e. Substituting eqs 2.20 and 2.11 for k and the Debye length, λ_D into eq 2.21 for α we get,

$$\alpha = \frac{\lambda_o}{4\pi \sin(\theta/2).7400}\sqrt{\frac{n_e}{T_e}} \simeq 1.075 \times 10^{-5}\frac{\lambda_o}{\sin(\theta/2)}\sqrt{\frac{n_e}{T_e}} \qquad (3.1)$$

where T_e is in units of eV. The peak density of a Plasma Focus $\sim 10^{25}$ m^{-3} is 5 to 7 orders of magnitude larger than that of toroidal plasma devices. Therefore with similar electron temperature ranges of 10 - 10^3 eV, scattering in the region $\alpha \geq 1$ is easily attainable using

visible wavelength lasers and realizable scattering angles. In fact the non-cooperative region ($\alpha \ll 1$) is not generally accessible. This can be easily seen if we insert some values for the parameters into eq 3.1. The smallest practical value of λ_o that is obtainable which satisfies the requirements of a high power laser, is to use a frequency doubled Neodymium laser at 530 nm. For α to be a minimum, requires $\sin(\theta/2)$ to be a maximum, i.e. θ =180 degrees (backscattering). Using the average scattering volume electron density value assumed by Bernard et al [19] at peak compression of 5×10^{24} m^{-3}, we can insert these values into eq 3.1 to obtain,

$$\alpha = (162/T_e)^{\frac{1}{2}} \qquad (3.2)$$

Therefore for $\alpha < 1$ requires $T_e > 162$ eV and even for T_e=1 keV $\alpha \sim 0.4$. Obviously for lower density regimes the α value will be less, but the above calculation demonstrates the predominantly cooperative nature of visible scattered light from the Plasma Focus.

The Salpeter approximation (section 2.5.1) permits the dynamic form factor, $S(\underline{k}, \omega)$ to be separated into two terms: an electron term and an ion term. If we assume for the present that the conditions of the Plasma Focus satisfy the Salpeter limits (i.e. $T_e \leq T_i$), then we can use eq 2.42 for the ratio of the two integrated cross sections, $S_e(\underline{k})/S_i(\underline{k})$ for a hydrogen or deuterium plasma with $T_e = T_i$, to compare the scattered light levels of the two terms.

(i) For α in the range $1 \leq \alpha \leq 2$, the ratio is in the range 3 - 0.56. However because of the large disparity in scale of the dimensionless variables x_e and x_i of eq 2.27, with $T_e = T_i$ the electron spectrum is $\sim (m_i/m_e)^{\frac{1}{2}}$ wider than the ion spectrum. For a deuterium plasma this factor is ~ 60. The disparities in scale must be born in mind when comparing the spectrally resolved scattered signal recieved by a

detection channel. In the signal to noise calculations in section 3.5.5 we shall see that measuring the electron spectrum is prohibited with the laser powers available for $\alpha \lesssim 2$.

(ii) For $\alpha > 2$ we saw in section 2.5.1 that the electron spectrum consists of two satellites produced by a well defined electron plasma wave oscillation (Langmuir wave) of frequency ω_p given by eq 2.37 and width, $\Delta\omega_p$ given by eq 2.38. As ω_p is dependent on ω_{pe}, for the case of the Plasma Focus with a rapidly changing density profile, the calculation of the $S_e(\underline{k})/S_i(\underline{k})$ ratio for this α region is more complex. The signal to background emission ratio for the electron satellites will be given in section 3.5.5.3. The calculated value, for the laser power available, is a lot less than unity, which means that the satellites are unobservable.

From the preceding considerations, it can now be seen why all the previous work with the exception of that of Forrest, Peacock et al [37] and Tanimoto et al [38] has concentrated on measurements of the ion spectrum. The work of Forrest, Peacock et al and Tanimoto et al was related to the study of non-linear laser plasma interactions between an incident CO_2 laser and the Plasma Focus. This can result in enhanced Langmuir wave turbulence which in turn leads to an enhancement of the electron satellite scattering cross section. As this work was not directly related to the understanding of the dynamics of the Plasma Focus, it will not be discussed further. A description of the previous scattering experiments now follows which for convenience have been divided into sections of the experimental groups that performed the work.

3.2.2 REPORTED LITERATURE

(1) Culham Group

In the scattering experiment carried out on the Culham Plasma Focus by Forrest & Peacock [28], a ruby laser pulse of 6 J and 20 ns FWHM (full width half maximum) was focussed to a 3 mm diameter spot on the $\underline{z}$-axis at z=12.5 mm. The scattering geometry is detailed in figure 3.2 and had a scattering angle, $\theta = 45$, with the differential scattering vector, $\underline{k}$ orthogonal to the plasma $\underline{z}$-axis.

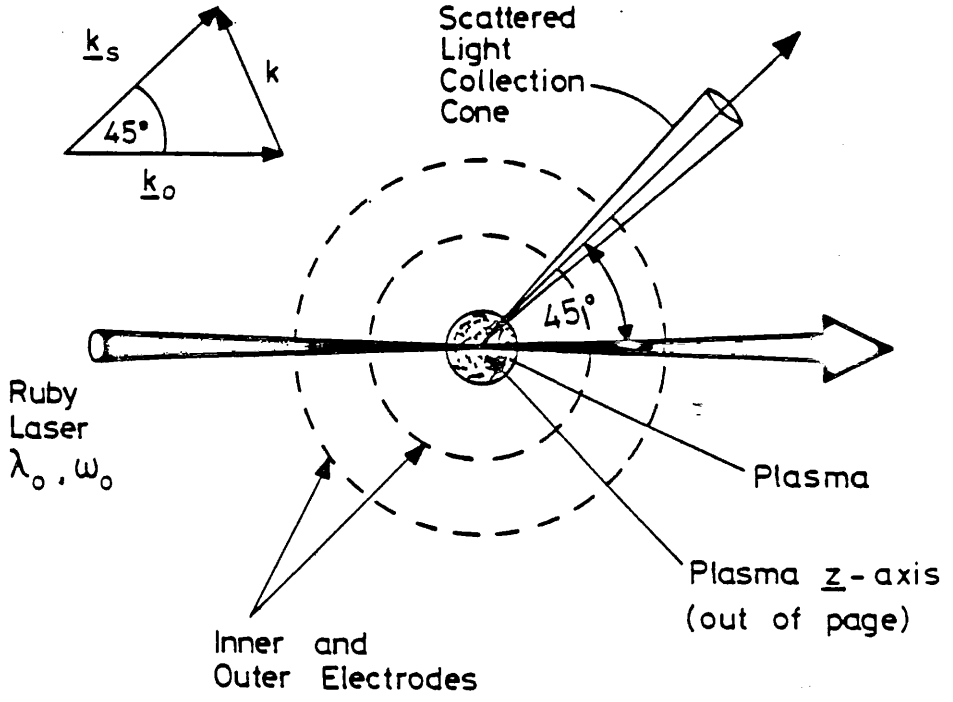

Figure 3.2
Culham Plasma Focus 45 degree ruby laser scattering arrangement with $\underline{k}$ orthogonal to the $\underline{z}$-axis.

An f/10 echelle grating spectrometer with a fibre optic output array coupled to a bank of 6 photomultipliers was used to resolve the scattered spectrum. Each channel had a wavelength bandwidth of

0.18 nm. The experiment had two aims: (a) to measure the ion temperature and β^2 factor (eq 2.34) for a deuterium plasma, and (b) to investigate the effects of the addition of small quantities of impurity gases such as neon on the scattered spectrum profile.

With a pure deuterium plasma it was not possible to obtain a comprehensive time sequence of measured profiles due to the irreproducibility of the discharge, but profile fitting to the experimental points indicated at t=0 ns, T_i=3 keV, T_e=2 keV, and at t=+30 ns, T_i=2 keV, T_e=1.5 keV. When 4% neon by volume was added to the discharge, profile fitting based on the dynamic form factor for a multi-ion species plasma of Evans [40] indicated T_i=0.7 keV, T_e=2.25 keV and a neon ion temperature, T_{ne}=9 keV.

(2) Limeil Group

The experiments performed by this group were undertaken on a Plasma Focus with similar electrode dimensions to the Culham device, but with a hollow centre electrode. For the first set of experiments by Baconnet et al [16,17] the device was operated at a bank energy of 15 kJ with a filling of 3 torr of deuterium. The scattering geometry of these experiments is shown in figure 3.3. A scattering volume located axially at z=10 mm was illuminated by a 12 J, 15 ns FWHM ruby laser pulse incident through a hole in the centre electrode. The scattered light was collected at an angle of 90 degrees orthogonal to the z-axis from a volume of 1 mm diameter and 6 mm axial length. The $\underline{k}$ orientation thus had equal axial and radial components. Measurement of the scattered light profiles was accomplished by a spectrometer with an output fibre optic array of 8 channels coupled to photomultipliers. Scattered light signals were observable only between t=-50 ns and t=0

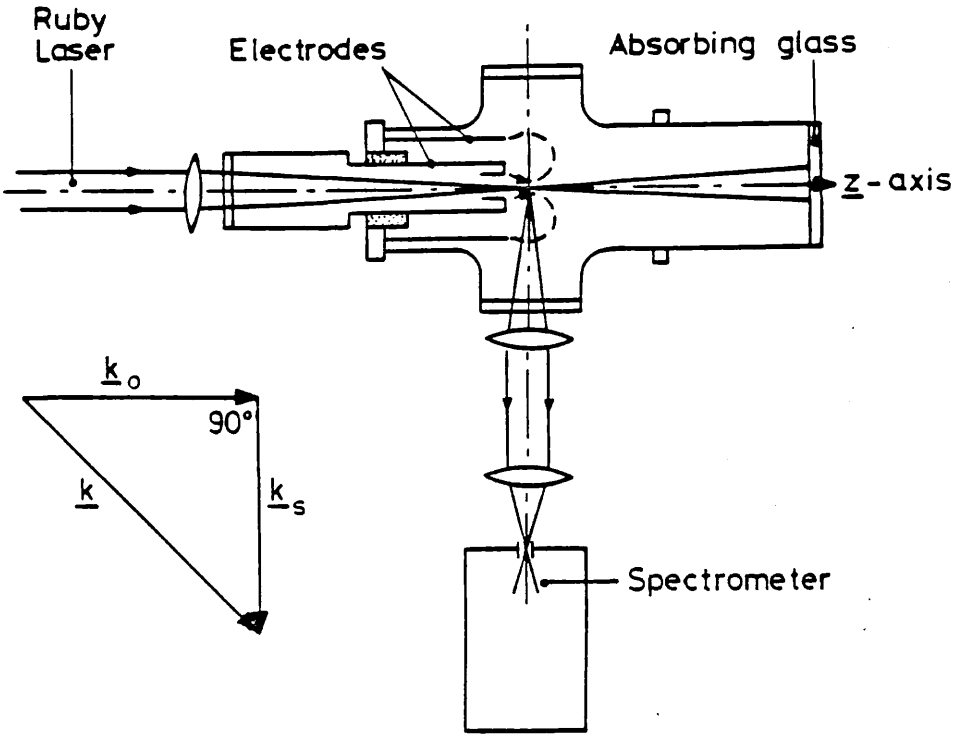

Figure 3.3
Limeil 90 degree ruby laser scattering arrangement with $\underline{k}$ orientation having equal components parallel and orthogonal to the $\underline{z}$-axis.

relative to the peak of the plasma dI/dt trace. Two types of spectrum were observed:

(a) A symmetric spectrum, red-shifted by $\sim$ 0.35 nm with respect to the ruby wavelength. Fitting the Salpeter ion term form factor to the data indicated a T_i in the range 390 eV < T_i < 470 eV. Using Rayleigh scattering to calibrate the detection system, the authors calculated an average scattering volume electron density, $n_e > 4 \times 10^{24}$ m^{-3} and hence were able to calculate a T_e range of 40 eV < T_e < 120 eV. The red-shift was explained as being due to a bulk motion of the plasma with a velocity of 1.7×10^5 $m.s^{-1}$ in the $\underline{z}$-axis direction.

(b) The second type of scattered spectrum observed was again red-shifted but by $\sim$ 0.7 nm. This type of spectrum showed a marked asymmetry and had an intensity of about twice that of the first type.

The explanation offered for this was a relative electron-ion drift velocity anti-parallel to the z-axis, plus possibly a total shift of the spectrum due to the bulk plasma motion as observed in (a).
The authors gave no indication of the temporal occurrence of these two types of spectrum, but concluded that the observation of scattering only before peak compression was due to an increase in electron temperature following this time. An increase in electron temperature as we shall see later in section 3.4, can result in an $\alpha < 1$ when the electron spectrum will dominate the scattering and be unobservable due to the signal to noise ratio being less than unity. The explanation of the plasma bulk motion being responsible for the spectral red-shift in the first type of spectrum does not seem reasonable however. Detailed examination of the scattering vector diagram shown in figure 3.3 indicates that a bulk velcity in the z-axis direction will result in a blue-shifted spectrum. The observed red-shifts for both types of spectrum are more likely to be as a result of the electron-ion drift velocity antiparallel to z during the changing conditions of the collapse phase.

These initial experiments were followed by further work by Bernard et al [18,19] on a similar Plasma Focus operating at a bank energy of 27 kJ (maximum current 600 kA) with a deuterium filling pressure of 3 torr. The incident laser orientation was now orthogonal to the z-axis with scattering in the forward direction at an an angle of 7 degrees from a scattering volume of 2 - 3 mm^3. The k orientation could be rotated from being orthogonal to the z-axis to a position aligned with the z-axis by means of a mask as illustrated in figure 3.4. A Fabry-Perot etalon coupled to a Fafnir multimirror system [41] with 12 channels monitored by photomultipliers was used to spectrally analyse the scattered light. Each channel had a wavelength

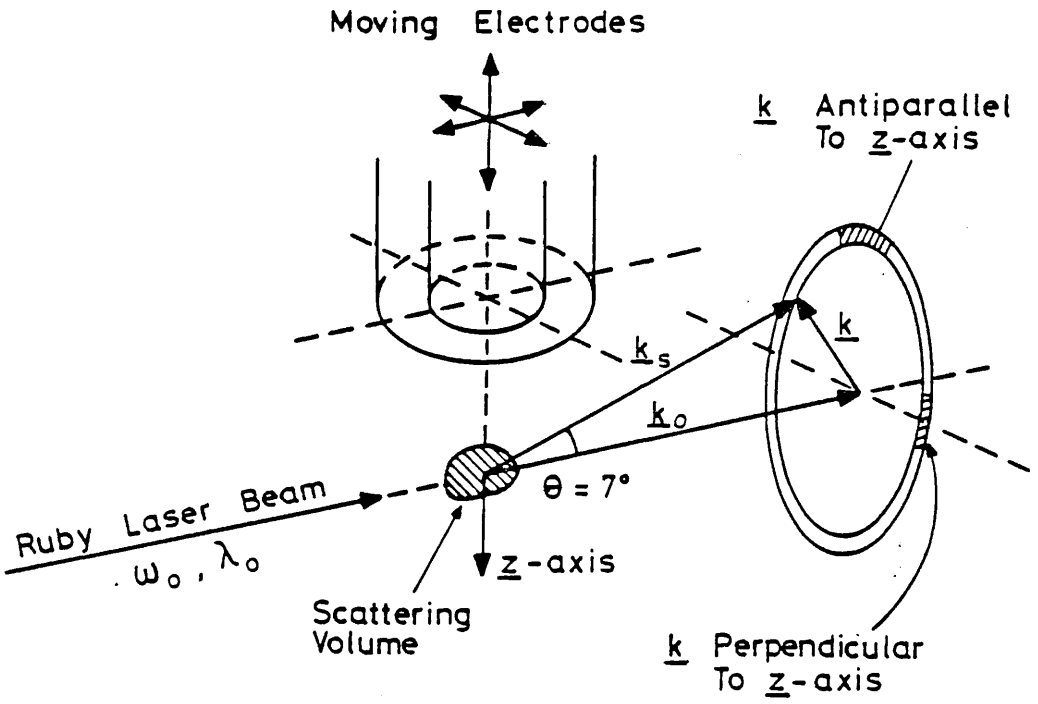

Figure 3.4
Limeil 7 degree ruby laser scattering arrangement with variable $\underline{k}$ orientation.

bandwidth of 0.04 nm. Measurements were made with the scattering volume located at three plasma positions:

(i) z=10 mm, r=7 mm, k orthogonal to z The spectra obtained at this off-axis position were shifted either to the red or the blue of the laser wavelength, the direction depending on the $\underline{k}$ orientation with respect to the radial collapse velocity $\underline{V}_r$. In both cases the shift was 0.05±0.02 nm which corresponds to a radial velocity $|\underline{V}_r| = 1.8 \pm 0.7 \times 10^5$ m.s^{-1}, whereas streak camera photographs indicated a value of 3×10^5 m.s^{-1}. Profile fitting of the data gave for a β =0.5, T_i=300 eV and T_e=75 eV and for β =0, T_i=500 eV with $T_e \ll T_i$.

(ii) z=10 mm, r=0 mm, k aligned with z The results in this position were not reproducible, the scattered power varying by a factor of greater than 30. Some shots produced spectra which were symmetrical

with respect to the laser wavelength, others had two maxima with a complete lack of symmetry. For symmetrical spectra, profile fitting indicated $T_e < T_i \leq 1$ keV with an average T_i=700 eV and an n_e in the range 10^{25} to 10^{26} m^{-3}. In other shots the enhancement in intensity would have required an average scattering volume density of $2x10^{27}$ m^{-3} assuming a thermal plasma. Spectral analysis gave profile widths varying with discharge between 0.04 nm and 0.2 nm. Compared with peak electron density measurements by interferometry of $n_e=5x10^{25}$ m^{-3} the authors concluded that turbulence is responsible for the anomalous level of scattering of up to $S_i(\underline{k}) \geq 100$.

(iii) <u>z=30 mm, r=0 mm, k aligned with z</u> Scattering here was observed between t=+50 ns and t=+100 ns and was fairly reproducible. The wavelengthe shifts of the spectra were again interpreted as being due to a bulk plasma velocity in the <u>z</u> direction of 10^5 $m.s^{-1}$ compared with a shock front velocity of $3-4x10^5$ $m.s^{-1}$ measured with a streak camera. Profile fitting to a theoretical Maxwellian velocity distribution indicated a T_i<800 eV and a density of 10^{24} m^{-3}. No large scale enhancements were mentioned by the authors at this axial position.

(3) <u>University of Houston group</u>

The work of Downing and Eisner [20] was undertaken on a device with electrode diameters of 50 mm and 96 mm and a gun length of 145 mm operated at 15 kV (15 kJ stored energy) with a filling pressure of 9-10 torr of hydrogen. Time resolved 90 degree scattering was observed using a ruby laser. The differential <u>k</u> orientation was orthogonal to the <u>z</u>-axis and results were obtained for two axial scattering volumes at z=6 and 13 mm. The scattering volume had an axial cross section of 25 microns x 1.5 mm. Analysis of the scattered light was accomplished using a spectrometer with light pipes coupling the output to 5

photomultipliers. One of these channels at 689.6 nm was used for subtraction of the bremsstrahlung background light, the other 4 with wavelength shifts from the ruby wavelength of 0.1 nm, 0.5 nm, -0.225 nm and -0.6 nm for spectrum shape determination. The authors developed a radial velocity dominated model to explain the experimental data they obtained. The basis of this model is illustrated in figure 3.5a. For a rectangular cross sectional scattering volume centred axially, the radially collapsing plasma sheath will consist essentially of two similar scattering volumes.

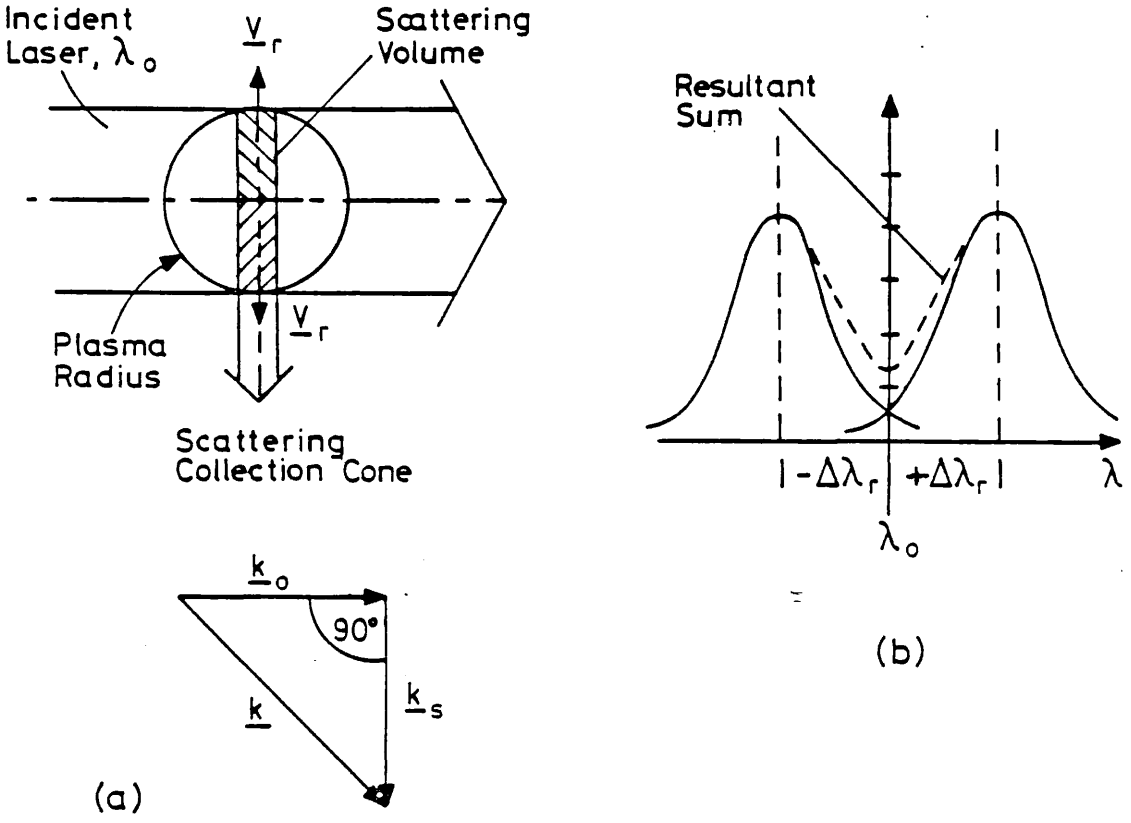

Figure 3.5
(a) 90 degree scattering arrangement of radial velocity dominated model with the scattering volume centred axially and scattering vector diagram. (b) Two shifted profiles and their superposition profile.

If we assume in the rest frame of each volume a Maxwellian particle velocity distribution, then each volume will contribute a scattered signal shifted from the laser wavelength by $\Delta\lambda_r$, given by,

$$\Delta\lambda_r = \pm \frac{\lambda_o^2}{2\pi c} \underline{k}.\underline{V}_r = \frac{\lambda_o^2}{2\pi c} |\underline{k}||\underline{V}_r|\cos\Phi \qquad (3.3)$$

where the radial velocity $\underline{V}_r$ is defined as having a direction away from the $\underline{z}$-axis (and will therefore be negative for the collapsing sheath) and Φ is the angle between $\underline{V}_r$ and $\underline{k}$. The signal from the upper volume (with $\Phi = 135^o$) will be blue-shifted with respect to the laser wavelength, λ_o and that of the lower volume (with $\Phi = 45^o$) red-shifted as illustrated in figure 3.5b. The combined profile shape will depend on $\Delta\lambda_r$ and the individual profile shapes.

For a similar scattering volume displaced from the plasma $\underline{z}$-axis as illustrated in figure 3.6a, the value of Φ will change constantly with position from top to bottom of the scattering volume. The scattered profile will now consist of an infinite number of scattered signal profiles each shifted from λ_o by a different $\Delta\lambda_r$. Downing and Eisner considered the problem by dividing the scattering volume into 5 equal sections to compute the superposition of the shifted profile from each illustrated in figure 3.6b. They assumed a homogeneous plasma but noted that the density and temperature profiles could also be taken into account. They concluded that for off-axis scattering volumes the scattered signal profile will be asymmetric for radial velocities of the order of the ion thermal velocities. Only when the ion thermal velocities >> $\underline{V}_r$ will the asymmetry be negligible, though the shift will still be present.

Using eq 2.26 we can calculate an equivalent ion temperature of a thermal plasma whose ion mean speed is the same as $|\underline{V}_r|$, given by,

$$T_i \equiv \frac{|\underline{V}_r|^2 m_i}{2e} \qquad (3.4)$$

Taking $|\underline{V}_r| = 3\times10^5$ m.s^{-1}, which is a typical plasma radius velocity

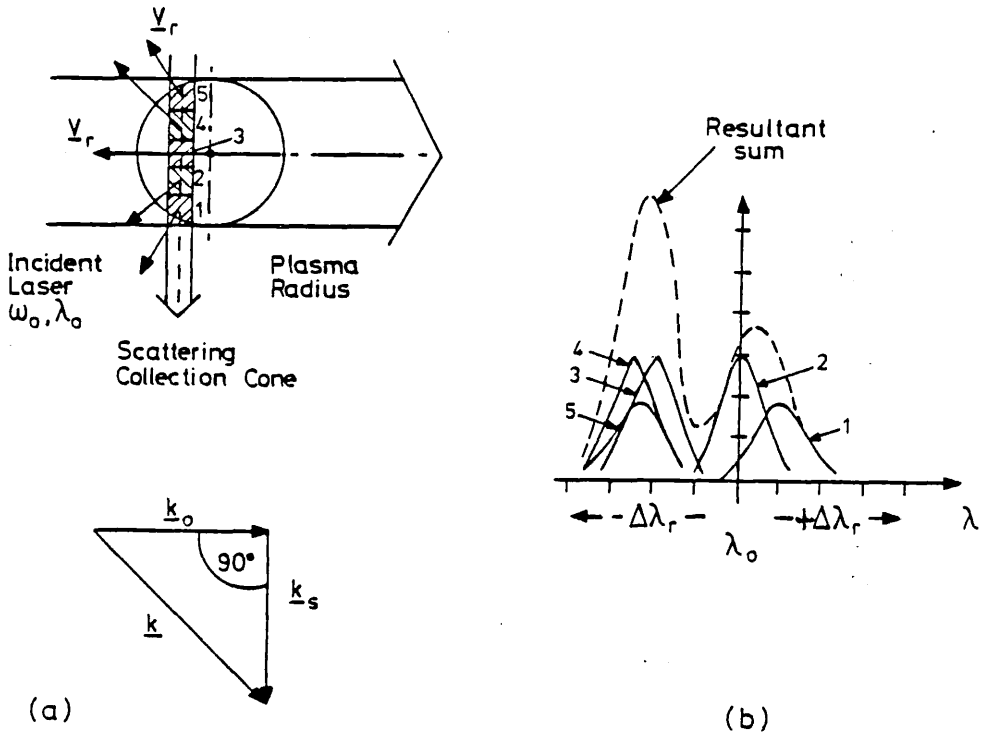

Figure 3.6
(a) 90 degree scattering arrangement of radial velocity dominated model with a non-axial scattering volume and scattering vector diagram.
(b) Five shifted profiles and their superposition profile.

during the collapse phase, the equivalent ion temperature is 470 eV for a hydrogen plasma and 939 eV for a deuterium plasma. Therefore if the plasma ion temperature is of the same order and the scattering geometry is such that the $\cos(\phi)$ factor is significant then the scattered profile shape and width will be effected by the radial velocity contribution. We will consider how the $\cos(\phi)$ factor affects other scattering geometries in section 3.4.2.

Downing and Eisner observed scattered signals from approximately t=-15 ns to t=+80 ns. The scattered signal at z=6 mm was approximately twice that at z=13 mm. The observed scattered profiles were not symmetric about the laser wavelength and asymmetries to both sides of

this wavelength were observed for different discharges. The signals for each of the 4 channels had different temporal shapes and did not peak simultaneously. A Gaussian profile superposition technique based on the radial velocity dominated model indicated a local ion temperature of T_i=70 eV and $|\underline{V}_r|$=3-4x10^5 m.s^{-1} for times up to t=+10 ns. The quality of the data did not permit quantitative analysis after this time. The authors concluded that as the signals in the four channels did not vary together, the local ion temperature could not have been significantly larger than this value. However, they did acknowledge the possibility of a plasma core region after peak compression which might have a greater ion temperature and for which $\alpha < 1$ or/and the scattering number density of this region was less than that of the plasma sheath.

(4) University of Wisconsin group

A scattering experiment has been reported recently by Neil & Post [39], in which a CO_2 laser (λ_o=10.6 micron) was used as a diagnostic laser. The use of such a long wavelength laser has several consequences. The laser beam will only penetrate the plasma provided $\omega_{CO_2} > \omega_{pe}$, which requires using eq 2.7 that $n_e < 10^{25}$ m^{-3}. Secondly, it is necessary that the laser intensity does not exceed the threshold for non-linear laser-plasma interactions which can result in absorption of the incident wave for $\omega_{CO_2} \sim \omega_{pe}$. The experiment was of particular interest because the authors concluded that it suggested the existence of localised turbulence in the post-pinch phases of the plasma, which is highly relevant to the work in this thesis.

The experiments were performed on a 250 mm long Mather device with a 50 mm diameter hollow centre electrode and a 100 mm diameter outer

electrode. This was operated at 16 - 18.4 kV (17.28 - 22.85 kJ) with a filling pressure of 0.7 - 2.2 torr of deuterium with approximately 4% Argon added to aid reproducibility. Current at peak compression was in the range 320 - 450 kA. A linearly polarised 20 MW, 100 ns FWHM CO_2 laser pulse was focussed to a 3 mm diameter spot on the z-axis. The incident intensity was below the threshold for non-linear interactions. Two scattering geometries were used:

(i) CO_2 laser incident parallel to the z-axis through a hole in the centre electrode with the scattered light collected at 90 degrees orthogonal to the z-axis (similar to the Limeil group 90 degree arrangement). With this arrangement $\underline{k}$ has equal z-axis and radial components.

(ii) Radial scattering with the CO_2 laser incident orthogonal to the z-axis with the scattered light collected at 90 degrees orthogonal to the z-axis. The $\underline{k}$ vector now only had a radial component.

With the first arrangement the laser polarisation was such that the angle γ of eq 2.5 was 90 degrees and in the second it could be changed from $\gamma = 90$ (favourable polarisation) to $\gamma = 0$ when scattering from electrons would not be expected to be observed. The advantage of being able to change the polarisation orientation was that it enabled scattering from overdense regions, $n_e > 10^{25}$ m^{-3} to be distinguished from cooperative scattering. In the case of overdense scattering, the scattered power collected by a solid angle, $d\Omega$, may then be estimated [39] by the size of the local overdense spot as,

$$dP_s = \frac{P_o}{A_o} \pi a^2 \frac{d\Omega}{4\pi} \qquad (3.5)$$

where P_o is the incident laser power, a is the radius of the overdense spot (assuming $a >> \lambda_o$) and A_o is the area of the incident CO_2 laser spot. Any frequency shift of the scattered light in this case would be as a

result of the doppler effect due to the motion of the overdense region. The scattered light was analysed by a grating monochromator with a resolution of 0.02 micron in conjunction with a cryogenic Cu:Ge detector. The resolution of the instrument enabled a doppler shift corresponding to a bulk plasma velocity of 1.5×10^5 m.s^{-1} to be detected and the detector sensitivity was such that a thermal level signal from an average plasma scattering volume density of 5×10^{24} m^{-3} should be measurable.

With the radial scattering geometry approximately equal signals were observed for both favourable (γ=90 degrees) and unfavourable (γ=0) incident laser polarisation. Operating at lower currents and filling pressures (300 kA and 0.7 torr D_2) the initial overdense signal from the plasma at peak compression was smaller and enabled a later signal to be observed in about 50% of the shots. These late signals at t=+25 - +125 ns consisted of short duration ($\leq$20 ns FWHM) pulses of approximately equal levels for both incident polarisations. A triple pinhole soft X-ray camera was employed simultaneously with the scattering system to observe intense X-ray emission spots. Such localised X-ray emission have been previously reported by other authors [42,43]. Whenever soft X-ray emission spots were observed in the scattering volume, high level scattered signals were always observed in the post-pinch phase. The converse was also true. The scattered power in either geometry indicated using eq 3.5 that the overdense region was 40 microns in diameter which was in agreement with the spot size observable in the X-ray pinhole pictures. No doppler shift of the scattered light was observable within the limits of instrumental resolution.

3.3 TEMPERATURE MEASUREMENTS BASED ON X-RAY OBSERVATIONS

The electron temperature has been determined on the Culham Plasma Focus operating in deuterium with a small percentage of Argon added by Peacock [44] from measurements of the free bound (Ar^{+18}, Ar^{+17}) continuum emission in the X-ray region and from the intensities of the lines of Li-like ions, which are a satellite to the He-like ion resonance lines in ionised Argon. The value of T_e determined by these methods was 2.0 ± 0.5 keV. Line profile analysis of Ar XVII indicated an argon impurity temperature of 10 keV. The measurements were made on a 1 mm diameter axial volume, with an integration time of 400 ns determined from temporal measurements.

Bertalot et al [45] have determined the radial electron temperature profile by analysing the bremsstrahlung continuum radiation using the two filter method, assuming a Maxwellian electron velocity distribution. Two double pinhole cameras equipped with 10 μm and 25 μm Be filters, channel plates and phosphor screens were used. Exposure times of 1 ns were obtained by pulsing the channel plates. Analysis of the photographic emission pictures, which included an Abel inversion in conjunction with the radial electron density profiles, obtained by holographic interferometry, gave the radial electron temperature profile as a function of time. The electron temperature was found to rise in the order of 10 ns to greater than 2 keV at peak compression (t=0) for certain radial positions, before decreasing in the expansion phase to 250-350 eV within 10 ns.

3.4 COMMENTS AND CONCLUSIONS

Before commenting on the scattering experiments it will prove useful to appraise the variation of scattering parameter, α for the range of scattering angles and the two wavelengths used. Reproducing equation 3.1, for the scattering parameter α ,

$$\alpha \simeq 1.075 \times 10^{-5} \frac{\lambda_o}{\sin(\theta/2)} \sqrt{\frac{n_e}{T_e}}$$

we see that for a fixed λ_o and θ , α depends only on the square root of the ratio n_e/T_e. Figure 3.7 shows a plot on logarithmic axes of α against n_e/T_e for the four scattering arrangements, where the curves represent the following:

(1A) λ_o =694.3 nm, θ =7 degrees, (3A) λ_o =694.3 nm, θ =45 degrees,

(4A) λ_o =694.3 nm, θ =90 degrees, (5A) λ_o =10.6 micron, θ =90 degrees.

In addition curve 2A represents λ_o =694.3 nm and θ =10 degrees which will be used later. Using eq 2.41 for the integrated ion term cross section of the Salpeter approximation and assuming Z=1 and $T_e = T_i$, $S_i(\underline{k})$ reduces to the form,

$$S_i(\underline{k}) = \frac{\alpha^4}{1 + \alpha^2(3 + 2\alpha^2)} \qquad (3.6)$$

This function is also plotted linearly in figure 3.7 against n_e/T_e for each of the above scattering arrangements as dotted curves 1S - 5S respectively. It should be noted that a different T_e/T_i ratio results in a different maximum $S_i(\underline{k})$ but the general shape of the curves is similar. The two vertical dotted lines represent the extremes of the ratio n_e/T_e that are expected on the Plasma Focus:

(A) At peak compression the maximum average density over a finite

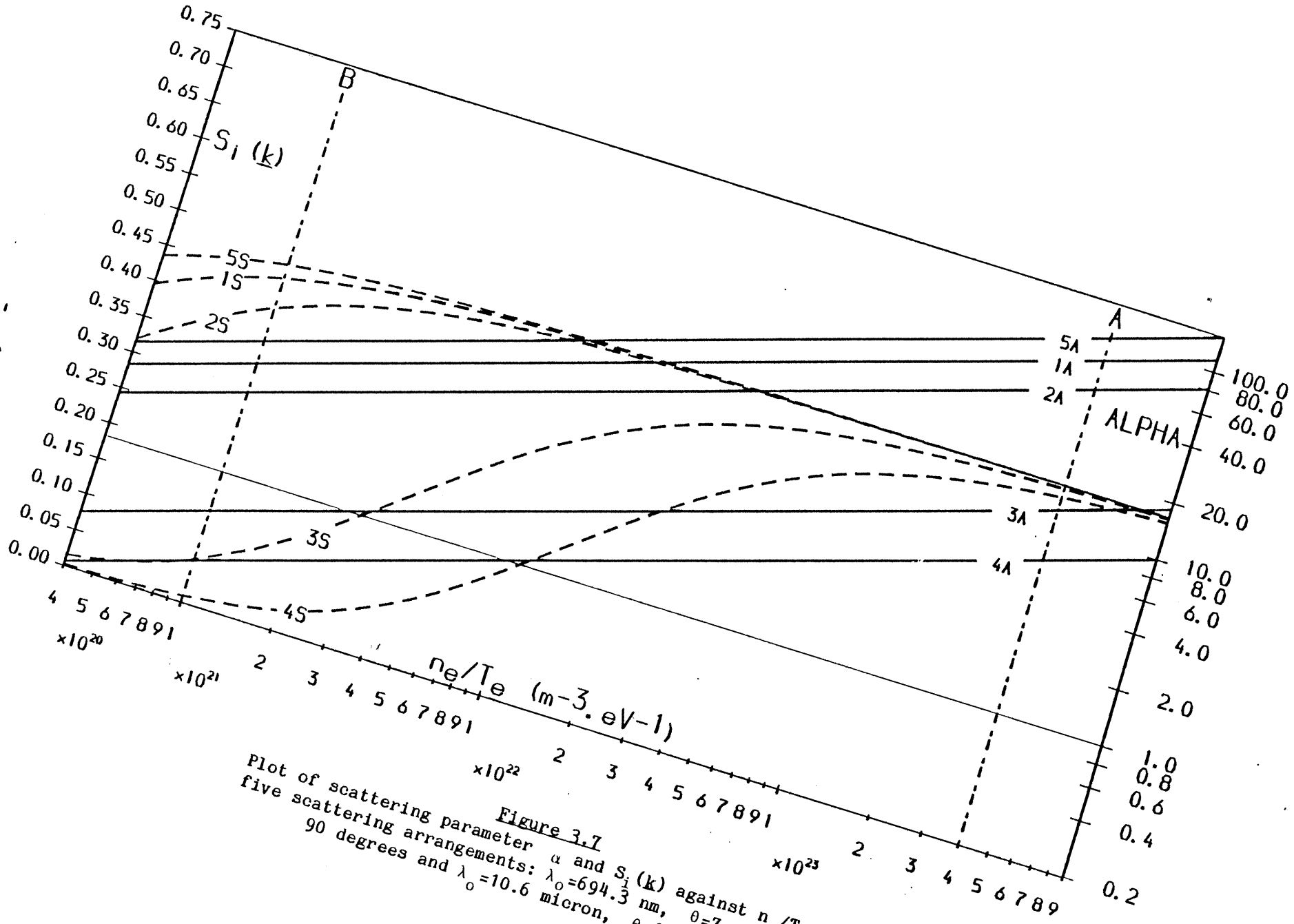

Figure 3.7

Plot of scattering parameter α and $S_i(k)$ against n_e/T_e for five scattering arrangements: λ_o=694.3 nm, θ=7, 10, 45 and 90 degrees and λ_o=10.6 micron, θ=90 degrees.

scattering volume, $n_e=2x10^{25}$ m^{-3} with a minimum $T_e=50$ eV gives an upper ratio limit of $4x10^{23}$ $m^{-3}.eV^{-1}$.

(B) At earlier times during the compression phase at t=-30 ns the peak density $n_e=2x10^{24}$ m^{-3} (section 4.5.3.4) and the maximum probable $T_e=2$ keV gives a ratio of $1x10^{21}$. This will also correspond to a possible high electron temperature, $T_e=2$ keV low density edge, $n_e=2x10^{24}$ m^{-3} at peak compression or during the dense pinch phase. Therefore the region of significance on the Plasma Focus is bounded by lines A and B. The curves will prove useful for the comparison of the previous results discussed below.

3.4.1 TEMPERATURE COMPARISONS

The experiments previously performed fall into two groups in determining the temperatures of the Plasma Focus. The forward ruby scattering experiments of Bernard et al at 7 degrees and those of Forrest & Peacock at 45 degrees concluded that the temperatures at peak compression were in the range 0.7 keV $< T_i <$ 3 keV with $T_e<T_i$. The higher results of the 45 degree experiment may be due to the significant radial velocity contribution at this angle, discussed in the next section, which would not have effected the 7 degree $\underline{k}$ aligned with $\underline{z}$ spectra of Bernard et al. If we study figure 3.7, it will be seen that $\alpha>>1$ for the 7 degree scattering within the bounds of the expected n_e/T_e ratios. For the 45 degree scattering, $\alpha \geq 1$ for the majority of the range, although the $S_i(\underline{k})$ curve falls off at lower n_e/T_e ratios which will result in a far smaller contribution from these regions. Of course the total scattering electron number for each region must be taken into account when calculating such an effect.

The 90 degree ruby scattering experiments of Baconnet et al and Downing & Eisner both indicated far lower ion and electron

temperatures. The results of Baconnet et al are difficult to interpret due to the $\underline{k}$ vector orientation having equal radial and $\underline{z}$-axis components. The radial component can lead to spectral modification due to a radial velocity contribution and the $\underline{z}$-axis component will be effected by a plasma bulk motion and/or an electron-ion relative drift velocity (section 2.5.3) in the $\underline{z}$-axis direction. Downing & Eisner concluded that taking the radial velocity contribution into consideration the local ion temperature, $T_i \sim 70$ eV. If we again study the α and $S_i(\underline{k})$ curves of figure 3.7 for this geometry we see that this may well be true for a high density low T_e regime. However, a low n_e/T_e (and possibly high T_i) regime will contribute little to the total scattered profile. Unfortunately Downing & Eisner were only able to utilise four channels to determine the profile widths of their scattered data, which would limit the observation of any overall broadening of the base of a scattered profile due to a high T_i low α value contribution. This explanation of the disparity between the two observed plasma temperature regimes is amplified by the fact that the results of Bernard et al at 7 degrees and those of Baconnet et al at 90 degrees were carried out by the same group on a similar Plasma Focus.

3.4.2 EFFECTS OF A RADIAL VELOCITY COMPONENT

It is worth considering at this point the effects of a radial velocity component outlined by Downing & Eisner [20] on the three scattering angles. For simplicity we will consider only the case of $\underline{k}$ orthogonal to the $\underline{z}$-axis (i.e. not the multicomponent experiment of Baconnet et al) and for a homogeneous plasma with $T_i >> T_e$. In the absence of a radial velocity component the scattered spectrum would be near Gaussian in shape with a profile given by the Salpeter ion term

expression of eq 2.33 which will have a 1/e frequency half width, $\Delta\omega = kv_i$. Substituting for k and v_i from eqs 2.20 and 2.26 respectively and converting to wavelength we obtain a profile 1/e half width given by,

$$\Delta\lambda_w = \frac{2\lambda_o}{c} \sin(\theta/2) \left(\frac{2eT_i}{m_i}\right)^{\frac{1}{2}} \qquad (3.7)$$

where T_i is in units of eV.

Consider a scattering volume cross section and scattering vector diagram illustrated in figure 3.8.

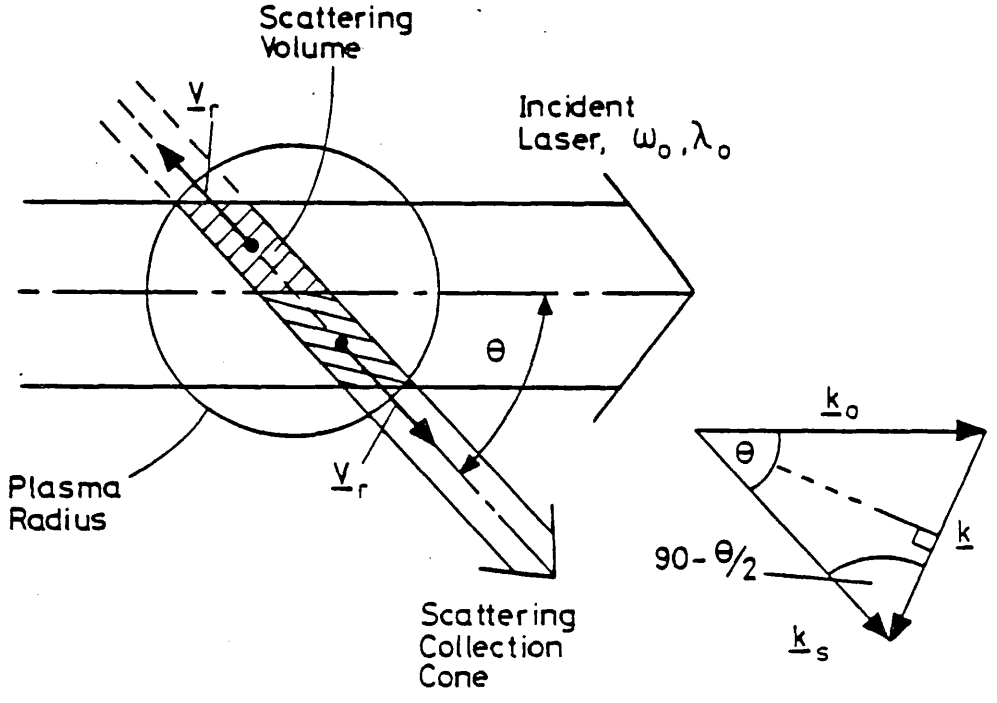

Figure 3.8
Scattering volume cross section and scattering vector diagram for an arbitrary scattering angle θ . The radial velocity, $\underline{V}_r$ is defined as pointing away from the z-axis.

If we consider the situation where the beam waist diameter is small compared with the plasma dimensions, the radial velocity components which are defined as pointing away from the plasma z-axis will produce

a scattered profile which is the superposition of two Gaussians which are shifted from the laser wavelength by the shift given in eq 3.3. Substituting for $\underline{k}$ and by geometry $\cos(\Phi)=\sin(\theta/2)$ we get,

$$\Delta\lambda_r = \pm \frac{2\lambda_o}{c} |\underline{v}_r| \sin^2(\theta/2) \tag{3.8}$$

Using this expression and eq 3.7 we can derive a simple expression for the fractional increase in width of the thermal profile due to a radial velocity component,

$$\left|\frac{\Delta\lambda_r}{\Delta\lambda_w}\right| = \left(\frac{m_i}{2e}\right)^{\frac{1}{2}} \frac{|\underline{v}_r|}{T_i^{\frac{1}{2}}} \sin(\theta/2) \tag{3.9}$$

The effect of a radial velocity component on the width of a spectrum can now be assessed by implementing a condition such that,

$$\left|\frac{\Delta\lambda_r}{\Delta\lambda_w}\right| < f \tag{3.10}$$

where f is a limit to the acceptable increase in profile width due to a radial velocity component such that it may be ignored. Substituting this in eq 3.9 we get,

$$T_i > \left(\frac{m_i}{2e}\right) \frac{|\underline{v}_r|^2}{f^2} \sin^2(\theta/2) \tag{3.11}$$

must be satisfied for the validity of the above condition. The strong dependence of the effect on the scattering angle is now apparent. Table 3.1 below lists the values of the T_i minimum condition for the three scattering angles θ, with either a hydrogen or a deuterium plasma. Each is tabulated for two f values of 0.1 and 0.25. We can see immediately that for the 90 degree experiments of Downing & Eisner that although their ion temperature measurement may have been very localised, their inclusion of the radial velocity contribution to the

θ (degrees)	Ti minimum (eV) f=0.10 Hydrogen	Deuterium	Ti minimum (eV) f=0.25 Hydrogen	Deuterium
7	175	349	28	56
45	6883	13713	1103	2197
90	23500	46820	3765	7500

Table 3.1
T_i minimum values for neglect of radial velocity component for a range of scattering angles.

profile width determination was reasonable. Their suggestion in the paper [20] that their radial velocity dominated model may contribute to the explanation of the early work of Baconnet et al at 90 degrees also seems plausible and its non inclusion may account for the slightly higher temperatures that were determined by this experiment. For the 45 degree experiments of Forrest & Peacock [15] where a T_i=3 keV was determined for a deuterium plasma at t=0 ns, we can see from the table that the radial velocity may well have contributed to the overall width of the spectrum. More importantly it will lead to a substantial change of shape and may account for the hollow profiles observed. Obviously at peak compression, t=0 ns the velocity of the plasma radius will be zero, but with a laser pulse of 20 ns FWHM a substantial contribution will result from the collapse and expansion phases about t=0 ns. Although the 7 degree axial measurements of Bernard et al were undertaken with $\underline{k}$ aligned with $\underline{z}$, it is worth noting that at this angle, neglect of the radial velocity contribution may be reasonable for $\underline{k}$ orthogonal to $\underline{z}$ spectra. For small angles, the effect is far more likely to modify the shape of the spectrum than contribute significantly to the overall width. The difference in ion temperature measured by Bernard et al [19] (T_i=700 eV) and Forrest & Peacock [15] (T_i=3 keV) is therefore possibly due to the significant radial velocity effect on the latter.

It should be noted that our discussion here has assumed a collection beam waist diameter which is small compared with the plasma radial dimensions, which may not be true as the plasma approaches peak compression. If this condition is not satisfied and the plasma is also inhomegeneous, the effect becomes more difficult to formulate. This situation will be discussed fully in chapter 7 on the analysis and interpretation of the results.

3.4.3 NON THERMAL SCATTERING OBSERVATIONS

Bernard et al [19] observed scattered profiles at a scattering angle of 7 degrees with $\underline{k}$ aligned with the $\underline{z}$-axis which varied in intensity by a factor ~ 30 with a maximum cross section ~ 100 above thermal during the time period t=-50 ns to t=+50 ns. Some of these profiles were symmetric, others showed a strong asymmetry. Similar enhancements, but by only a factor of 2 were observed by Baconnet - et al [17] at 90 degrees. The enhanced spectra being asymmetric. It should be noted that the experiemnts of Baconnet et al were conducted with the $\underline{k}$ orientation at 45 degrees to the $\underline{z}$-axis, which must be included when comparing with the enhancements of Bernard et al. In addition, the two scattering angles will each probe a different part of the k-spectrum of any turbulence. If we again study figure 3.7, we can see that for a particular n_e/T_e region of the plasma the α value at 90 degrees will be less than that at 7 degrees. With the 90 degree experiment the α value is typically in the range 0.4 - 5 which will result in far stronger Landau damping of ion-acoustic turbulence for example. The possible connection between these observations and those of Neil & Post [39] of scattering from overdense regions during the dense pinch phase which were well correlated with the observation of X-ray hot spots in the scattering volume cannot be discounted. This

will be discussed further in chapter 7.

3.4.4 OVERALL CONCLUSIONS

The results of Bernard et al, derived from the symmetric scattered profiles on axis, probably represent the best indicator of the average ion temperature in the Plasma Focus, even though they were measured with $\underline{k}$ aligned with $\underline{z}$. However, both the 90 degree experiments of Baconnet et al and Downing & Eisner indicate that there is probably a substantial region of the plasma with a far lower ion temperature $\sim$ 100 eV. If the X-ray measurements of $T_e \geq 2$ keV correspond to localised regions of the plasma, the result will be a very small contribution to the scattered ion spectrum from these regions compared with lower T_e regions. Clearly this temperature inhomogeneity must be born in mind when considering the design of a new experiment and in particular a far more sophisticated model is required for analysis of the experimental data.

The large scale enhancements observed with a $\underline{k}$ orientation aligned with the $\underline{z}$-axis and the observation of overdense CO_2 laser scattering particularly during the post compression phase may be an indicator of the neutron production mechanism in the Plasma Focus.

3.5 CONSIDERATIONS FOR SUITABLE SCATTERING EXPERIMENTS

The objectives of a new series of scattering experiments on the Plasma Focus may be summarised as follows:

(a) A more detailed investigation of $\underline{k}$ orthogonal to $\underline{z}$ scattered

spectra to obtain a better measurement of the radial temperature variation. In addition the time region surveyed should be extended to include the post compression phase of the plasma.

(b) A thorough investigation of $\underline{k}$ aligned with $\underline{z}$ scattered spectra to establish the possible mechanisms producing asymmetry and enhancement of the spectra.

We will now consider the possible scattering geometries which are applicable to a new set of experiments bearing in mind the advantages and limitations of those experiments already discussed.

3.5.1 CHOICE OF LASER WAVELENGTH

The selection of a laser for a plasma scattering system is determined by several requirements. Firstly, a high power small divergence ($\sim$few milliradian) output is required and in the case of the Plasma Focus with a short lived plasma, a short pulse duration is necessary for temporal resolution. Secondly, it is required that the laser frequency, ω_o should be far greater than the peak ω_{pe} value, if laser absorption is to be avoided (see section 2.3). It was for this reason that the work of Neil & Post [39] was limited to a low power CO_2 laser which consequently prevented them from measuring the scattered profile of the underdense plasma. Therefore the choice was limited to a 'Q switched' ruby laser operating at 694.3 nm or a Neodymium laser operating at 1.06 μm. The possibility of frequency doubling a Neodymium laser output to produce a wavelength of 530 nm was considered, but offers little advantage over a ruby system and results in a more complex laser arrangement. A third consideration is the detector quantum efficiency. Although photomultipliers with quantum efficiencies $\sim$ 7% at 1.06 μm [46] are now available, for experimental

reasons detailed in chapter 5, the choice of detector selected was a gated Vidicon Optical Multichannel Analyser (OMA) which has a very low efficiency at 1.06 μm. Therefore a 'Q switched' ruby laser providing a 300 MW, 20 ns FWHM pulse was selected. This will be described in detail in section 4.3. The use of the pulse clipping technique descibed in section 4.5.3.1 utilized in the holographic interferometry was not practical for greater temporal resolution in the scattering experiments because of the limit set by the signal to noise ratio which will be discussed in section 3.5.5.4.

3.5.2 SELECTION OF SCATTERING ANGLE AND k ORIENTATION

Having selected a laser for the scattering experiments, only the scattering angle, θ can then be varied to determine the scattering regime. The choice of scattering angle is further complicated in the Plasma Focus by the small size and inhomegenity of the plasma which rapidly changes with time resulting in a range of n_e/T_e ratios as has already been seen in section 3.4. The physical arrangement of the diagnostic ports on the Culham Plasma Focus vacuum chamber and the provision of a laser beam dump limited the choice of scattering geometries. Only the following geometries were possible:

(1) θ=8 - 10 degrees with $\underline{k}$ between the perpendicular and anti-parallel orientation to $\underline{z}$.

(2) θ=45 degrees with $\underline{k}$ perpendicular to $\underline{z}$.

(3) θ=90 degrees with $\underline{k}$ perpendicular to $\underline{z}$.

(4) θ=135 degrees with $\underline{k}$ perpendicular to $\underline{z}$.

(5) θ=170 - 180 degrees with $\underline{k}$ perpendicular to $\underline{z}$.

In section 3.4.1 we concluded that the previous work with a scattering angle of 90 degrees was difficult to interpret because it was possible that low n_e/T_e plasma regions would contribute significantly less to

the scattered profile than high n_e/T_e regions. The situation for angles > 90 degrees only aggravates this problem still further. In addition in section 3.4.2 we noted that it is preferable to work at smaller scattering angles as the radial velocity contribution for a given ion temperature is less significant as the angle decreases. We are therefore limited to scattering in the forward direction between 8 and 10 degrees with either $\underline{k}$ orientation, and at 45 degrees with $\underline{k}$ perpendicular to $\underline{z}$. Scattering in the forward direction with a $\underline{k}$ orientated between the perpendicular and antiparallel directions was posssible but was not considered as it further complicates analysis of the spectrum as was illustrated in the summary of the work by Baconnet et al.

3.5.3 SCATTERING VOLUME DIMENSIONS AND LOCATION

The scattering volume is defined by the intersection volume of the focussed laser and collection optics beam waists as illustrated in figure 3.9, where d is the focussed laser spot diameter and w is the diameter of the collection beam waist. The experimental limits placed on the laser input optics (section 6.2.1) resulted in a minimum obtainable value of d=5.5 mm. A value of w much less than d does not improve the radial resolution, although it does have the advantage of simplifying the radial velocity component calculation. However, as a result of the irreproducibility of the plasma and the objective to investigate turbulence in the post compression phases, a value of w=4.0 mm was selected. Because of the rapidly changing density profile and asymmetric profiles produced by the radial velocity component for off-axis positions, it was decided to locate the plasma volume on the $\underline{z}$-axis. Locating the scattering volume too close to the centre electrode, results in the laser beam 'f' cone clipping the outer

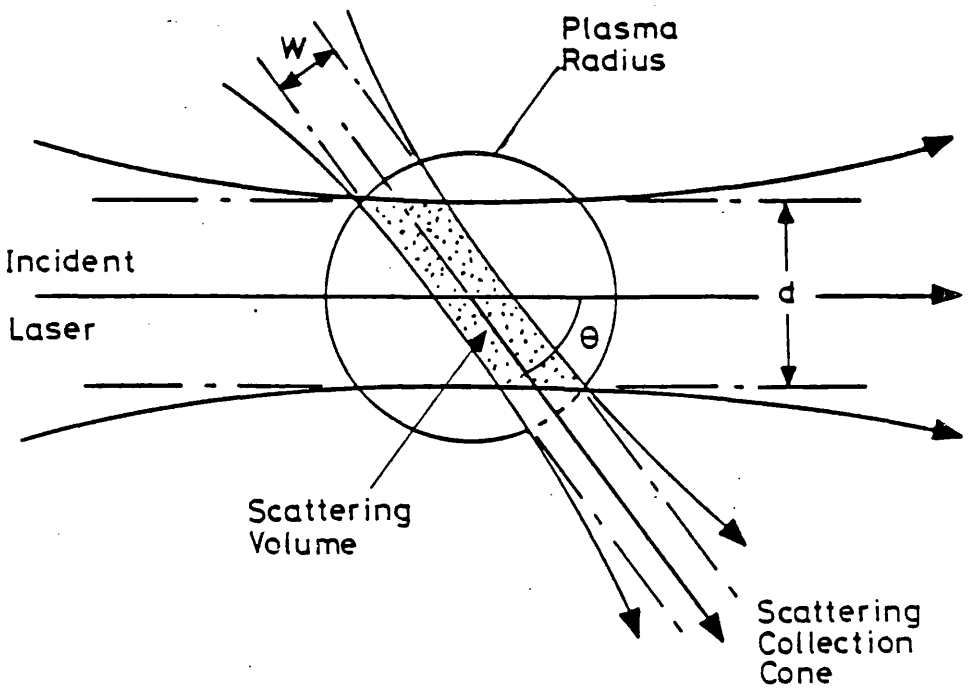

Figure 3.9
Scattering Volume consisting of the intersection volume of the focussed laser beam diameter, d and the collection optics beam waist, diameter, w.

electrode which would be catastrophic to stray light suppression. A position of z=10 mm was therefore selected as being the optimum.

3.5.4 SPECTRAL ANALYSIS OF THE SCATTERED LIGHT

We have seen in the sections discussing the previous work that scattered profiles obtained from the Plasma Focus are far from simple in origin and consequently in interpretation. The small density scale lengths of the plasma, $(1/n_e . \partial n_e/\partial r)^{-1}$ which has a value $\sim 6 \times 10^{-4}$ m at t=0 ns means that even for a homogeneous temperature plasma the n_e/T_e ratio will change rapidly with radius. During the collapse phase, the plasma current has been measured by Muir [25] as being confined to the

plasma skin with a penetration depth of 0.7 - 0.8 mm. Electron heating in this region is therefore a possibility which will further extend the range of n_e/T_e ratios present within a scattering volume. In addition we have seen that a radial velocity contribution can significantly effect the profile shape and width for all but small angle scattering. It was therefore important that a new scattering experiment should be provided with a far greater number of wavelength detection channels than had been previously used, so as to measure the profile shape with good resolution over the whole significant wavelength range of the scattered spectra. Using eq 3.7 for the 1/e wavelength half width, we can calculate a range of ion spectrum widths for the two scattering angles under consideration. Table 3.2 below lists these widths for a ruby laser scattered spectrum from a deuterium plasma for the two scattering angles of 10 and 45 degrees.

Ti (eV)	$\Delta\lambda_w$ (nm) θ =10	$\Delta\lambda_w$ (nm) θ =45
100	0.0395	0.1734
500	0.0883	0.3878
1000	0.1249	0.5484

Table 3.2
Ruby scattered ion spectrum 1/e wavelength half widths
for scattering angles of 10 and 45 degrees
and a range of ion temperatures.

If we take for example a wavelength interval width of 0.02 nm for each detection channel and assume that the channels are adjacent in wavelength, then the smallest 1/e full width for the 10 degree scattering will be $\sim$ 4 channels and the largest for the 45 degree scattering will be $\sim$55 channels. Covering the spectrum on both sides of the laser wavelength will enable any asymmetry to be determined. We

see that to cover the whole significant part of a 1 keV, 45 degree spectrum, will therefore require greater than 60 channels. The provision of a large number of wavelength detection channels will have the additional advantage of permitting the observation of any broadening of the wings of the scattered light profile due to a low α (low n_e/T_e) region with a high T_i. This provision is of particular importance with a scattering angle of 45 degrees as has already been illustrated.

3.5.5 SIGNAL TO NOISE CALCULATIONS

For the scattering experiments under consideration we need to assess both the scattered signal to background plasma light emission ratio and also the scattered signal to statistical noise ratio. Having derived relationships for the ratios, the values relating to the proposed scattering geometries will be calculated. These will be based on the use of a Vidicon OMA detection system which will be described in detail in chapter 5.

3.5.5.1 SIGNAL TO BACKGROUND RATIO

The signal to backgound ratio is important because with a detector having a limited linear dynamic range (section 5.4.4), too small a ratio will result in the backgound using up useful range. In a hot, dense, fully ionised plasma the principle source of plasma light emission is electron-ion bremsstrahlung. However, with a short duration plasma like the Plasma Focus, one cannot be sure that the classical bremsstrahlung law is applicable or that recombination emission isn't dominant. Nevertheless, we will base our calculations on bremsstrahlung emission and compare the calculated value with

experimental observations later. We shall calculate the ratio of detected scattered photons, N_{SC}, to bremsstrahlung photons, N_{BC}, given by,

$$\frac{N_{SC}}{N_{BC}} = \frac{E_S(\underline{k},\lambda)\,d\lambda d\Omega.\lambda/hc.f.Q}{E_B(\lambda)\;d\lambda d\Omega.\lambda/hc.f.Q} \qquad (3.12)$$

where $E_S(\underline{k},\lambda)$ is the scattered energy spectrum as function of wavelength shift, $E_B(\lambda)$ is the bremsstrahlung emission spectrum, f is the transmission factor of the collection system and dispersion instrument, and Q is the quantum efficiency of the detector which in the case of the OMA is $\sim 7\%$ at 694.3 nm (ISIT detector head, section 5.2.1)

The classical expression for the bremsstralung emission by a volume of plasma, V_p, into a solid angle $d\Omega$, and in the wavelength interval $\lambda - \lambda + d\lambda$ is given by Sheffield [30] and the references therein as,

$$P_B(\lambda)\,d\lambda d\Omega = 2.09 \times 10^{-44} g\, Z^2 \left(\frac{n_e n_i}{\lambda^2 T_e^{\frac{1}{2}}}\right) \times \exp\left(\frac{-1.24\times10^{-6}}{\lambda T_e}\right) V_p\, d\lambda \frac{d\Omega}{4\pi} \quad (W) \qquad (3.13)$$

where Z is the charge on the ion, g the Gaunt factor which is near unity for $\lambda \leq 10^{-7}$ m, and T_e is in eV. Confining ourselves to the ruby laser, $\lambda_o = 694.3$ nm and to $T_e > 10$ eV we can neglect the exponential term which is near unity. For a fully ionised deuterium plasma, $n_e = n_i$ and Z=1 and with a detector temporal gating width t_g, the bremsstrahlung energy spectrum emitted will be given by,

$$E_B(\lambda)\,d\lambda d\Omega = 2.09 \times 10^{-44} \left(\frac{n_e^2}{\lambda^2 T_e^{\frac{1}{2}}}\right) t_g V_p\, d\lambda \frac{d\Omega}{4\pi} \quad (J) \qquad (3.14)$$

Utilising eq 2.22 for the scattered power spectrum in terms of

frequency,

$$P_S(\underline{k},\omega)\,d\omega d\Omega = NI_o\sigma(\underline{k},\omega)\,d\omega d\Omega$$

and integrating over the length of the laser pulse, we can derive an expression for the scattered energy spectrum as,

$$E_S(\underline{k},\omega)\,d\omega d\Omega = \frac{NE_o}{\pi d^2/4} \cdot r_e^2 \sin^2\gamma . S(\underline{k},\omega)\,d\omega d\Omega \qquad (3.15)$$

where E_o is the laser pulse energy and d is the focussed laser beam waist diameter. Converting from units of frequency to wavelength we get,

$$E_S(\underline{k},\lambda)\,d\lambda d\Omega = \frac{4NE_o}{\pi d^2} .r_e^2 \sin^2\gamma . S(\underline{k},\lambda)\,d\lambda d\Omega \qquad (3.16)$$

where $S(\underline{k},\lambda)$ is given by the same definition as $S(\underline{k},\omega)$ in eq 2.33 with x_e and x_i redefined as,

$$x_e = -\frac{2\pi c}{\lambda_o^2}\,\frac{\lambda}{kv_e} \quad : \quad x_i = -\frac{2\pi c}{\lambda_o^2}\,\frac{\lambda}{kv_i} \qquad (3.17)$$

The value of $S(\underline{k},\lambda)$ at the centre of the spectrum, $S(\underline{k},0)$, is given by Evans & Katzenstein [29] where $T_e=T_i$ and Z=1 is assumed as,

$$S(\underline{k},0)_{\alpha<<1} = \frac{c}{2\pi^{\frac{1}{2}}}\left(\frac{1}{\lambda_o \sin(\theta/2)\,v_e}\right)$$

$$S(\underline{k},0)_{\alpha>>1} = \frac{1}{2}\left(\frac{m_i}{m_e}\right)^{\frac{1}{2}} S(\underline{k},0)_{\alpha<<1} \qquad (3.18)$$

where v_e is given by eq 2.26. It should be noted that for a given scattering geometry, the difference in $S(\underline{k},0)$ between the two scattering regimes is $1/2(m_i/m_e)^{\frac{1}{2}}$, which for a deuterium plasma is $\sim$30. As we are primarily interested in the $\alpha \geq 1$ regime we shall use

the $\alpha >>1$ expression. Substituting this in equation 3.16 to evaluate the scattered energy at the centre of the spectrum we get,

$$E_S(\underline{k},0)\,d\lambda d\Omega \underset{\alpha>>1}{=} \frac{n_e V_s E_o r_e^2 \sin^2\gamma\, c}{\pi^{3/2} d^2 \lambda_o \sin(\theta/2)} \left(\frac{m_i}{2eT_e}\right)^{\frac{1}{2}} d\lambda d\Omega \qquad (3.19)$$

where N has been replaced by the scattering volume size, V_S, and electron density, n_e. The plasma light emission can be reduced by a factor of 2 by including a polariser in the scattering collection optics orientated to transmit the scattered light polarisation. If we include the effect of a polariser in the collection system, we get substituting eq 3.14 and 3.19 into 3.12 the signal to background (S/B) ratio, where it has been assumed that the plasma emits continuum radiation like a classical optically thin source,

$$\frac{N_{SC}}{N_{BC}}\underset{\alpha>>1}{} = 2.7 \times 10^{44} \frac{E_o r_e^2 \sin^2\gamma\, c\, \lambda_o}{\pi^{\frac{1}{2}} d^2 \sin(\theta/2) n_e t_g} \left(\frac{m_i}{e}\right)^{\frac{1}{2}} \cdot \frac{V_S}{V_p} \qquad (3.20)$$

This reduces for a deuterium plasma on evaluating the constants to,

$$\frac{N_{SC}}{N_{BC}}\underset{\alpha>>1}{} = 5.2 \times 10^{19} \frac{E_o \sin^2\gamma\, \lambda_o}{n_e d^2 t_g \sin(\theta/2)} \cdot \frac{V_S}{V_p} \qquad (3.21)$$

3.5.5.2 SIGNAL TO NOISE RATIO

Two sources contribute to the statistical noise. Firstly there is the quantum statistical noise of counting both the scattered and the background photons, and secondly there is the detector noise. If N_{SP} and N_{BP} are the number of scattered and background photons reaching an OMA detector channel element respectively, then the number counted for each source and the total number of counts, N_{TC} is given by,

$$N_{SC} = N_{SP} \cdot Q$$
$$N_{BC} = N_{BP} \cdot Q \qquad (3.22)$$
$$N_{TC} = (N_{SP} + N_{BP}) \cdot Q$$

For this situation, where the detection probability is small, statistical theory tells us the probability of obtaining (N_{TC}) counts is the Poisson distribution given by Sheffield [30] and the references therein as,

$$P(N_{TC}) = e^{-m} m^{-N_{TC}} / N_{TC}! \qquad (3.23)$$

where $m = (N_{SP}+N_{BP}).Q$ is the most probable number of counts. The standard deviation is $\sigma = m^{\frac{1}{2}}$.

The signal for a given channel is therefore,

$$N_{TC} = (N_{SP}+N_{BP}) . Q \pm [(N_{SP}+N_{BP}) .Q]^{\frac{1}{2}} \qquad (3.24)$$

From this the scattered signal to noise ratio, $N_{SC}/(N_{TC})^{\frac{1}{2}}$, is given by,

$$\frac{S}{N} = \frac{N_{SP} \cdot Q}{[(N_{SP}+N_{BP}) .Q]^{\frac{1}{2}}} \qquad (3.25)$$

In addition we need to evaluate the consequence of detector noise. If the standard deviation of the baseline count for each channel is, σ_D, we will consider this as adding σ_D^2 /Q photons to the genuine signal in order to calculate the S/N ratio. Eq 3.25 now becomes,

$$\frac{S}{N} = \frac{N_{SP} \cdot Q}{[(N_{SP}+N_{BP}) .Q+\sigma_D^2]^{\frac{1}{2}}} \qquad (3.26)$$

$$= \frac{N_{SC}^{\frac{1}{2}}}{[1 + N_{BC}/N_{SC} + \sigma_D^2/N_{SC}]^{\frac{1}{2}}}$$

σ_D was measured (section 5.4.4) as ≤ 2.5, therefore compared with the

expected signal calculated below, $\sigma_D^2 / N_{SC} << N_{BC}/N_{SC}$ and may therefore be ignored. Equation 3.26 is reduced to the final form,

$$\frac{S}{N} = \frac{N_{SC}^{\frac{1}{2}}}{[1 + N_{BC}/N_{SC}]^{\frac{1}{2}}} \tag{3.27}$$

If we estimate the N_{SC}/N_{BC} ratio using eq 3.21, we need only to evaluate the corresponding detected signals at the centre of the spectrum to calculate the expected signal to noise ratio.

Using eq 3.19 for the scattered energy at the centre of the spectrum for $\alpha >> 1$ and converting to OMA detector counts, N_{SC}, we get the expression,

$$N_{SC}\underset{\alpha>>1}{} = \frac{n_e V_S E_o r_e^2 \sin^2\gamma d\lambda d\Omega}{h \pi^{3/2} d^2 \sin(\theta/2)} \left(\frac{m_i}{2eT_e}\right)^{\frac{1}{2}} f.Q \tag{3.28}$$

where f and Q are as previously defined. On evaluation of the constants for a deuterium plasma we get,

$$N_{SC_{\alpha>>1}} = 0.22 \times \frac{n_e V_S E_o \sin^2\gamma d\lambda d\Omega \; f \; Q}{d^2 \sin(\theta/2) T_e^{\frac{1}{2}}} \tag{3.29}$$

3.5.5.3 EXPERIMENTAL VALUES FOR RATIOS

The signal to background and signal to noise ratios for the two scattering angles of 45 and 10 degrees can now be estimated. Because of the inhomogeneity of the Plasma Focus, the calculations will be limited to specified spatial regions which may not necessarily represent the total scattering volume. The values used in each case, for the average density and scattering volume size, were based on a scattering volume model which will be described in chapter 7.

Ion spectrum

(1a) The worst case will be for θ =45 degrees. It should be noted that the condition α >>1 may not be satisfactorily met at this angle for all regions of the plasma, although at peak compression (t=0) the central core of the plasma with $\bar{n}_e=8x10^{24}$ will satisfy the condition provided T_e is not too large. Taking E_o=6 J, d=5.5 mm, γ =45 degrees, t_g=100 ns and assuming $V_S=V_P$, then N_{SC}/N_{BC}=12. The γ and t_g values will be explained in chapters 4 and 5.

(1b) At earlier times during the compression phase at say t=-30 ns, the peak electron density of the sheath is $2x10^{24}$ (section 4.5.3.4). Taking a plasma volume density, $\bar{n}_e=1.8x10^{24}$, N_{SC}/N_{BC}=52. It should be noted recalling figure 3.7, that the condition α >>1 for this region and scattering angle may not be satisfied. The effect of this will be a reduced ion term cross section and consequently reduced N_{SC}/N_{BC} ratio.

(2) For the smaller 10 degree scattering angle with $\underline{k}$ orthogonal to $\underline{z}$ (γ=80 degrees), the ratios for the above two conditions will be increased to 100 and 443 respectively. Studying figure 3.7 we can see that $\alpha \geq 3$ at this angle for all expected n_e/T_e ratios.

The value of Q for the OMA detector has already been stated as $\sim$ 7% at 694.3 nm. However, the product f.Q was measured for the various collection systems described in chapter 6 as having a value of $2x10^{-5}$. We shall additionally use the solid angle values of the multiple-$\underline{k}$ experiment described in the chapter. These were $4x10^{-3}$ str for the 45 degree collection optics and $2.5x10^{-3}$ str for the 10 degree systems. Using a value of T_e=350 eV, we can calculate N_{SC} values using eq 3.29 for the regimes considered in the signal to background calculations above. It will be assumed that α >>1 for these regions so as to assess

the respective values.

(1a) For the core region at t=0 ns, with $V_s = 3 \times 10^{-8}$ m and $\bar{n}_e = 8 \times 10^{24}$, $N_{SC} = 195$ at the centre of the 45 degree spectrum.

(1b) For the peak region of the collapsing sheath at t=-30 ns, with $V_s = 1 \times 10^{-8}$ m and $\bar{n}_e = 1.8 \times 10^{24}$, $N_{SC} = 15$ at the centre of the 45 degree spectrum.

(2) The equivalent values for the 10 degree spectra are 1038 and 78 respectively.

Substituting these values into eq 3.27 and utilising the corresponding N_{SC}/N_{BC} values from the signal to background calculations, the S/N ratios for the centre of the spectra are:

$$\frac{S}{N} = \begin{cases} 13.4 & \text{- 45 degree scattering from the core region, t=0 ns.} \\ 3.8 & \text{- 45 degree scattering from the collapsing sheath, t=-30 ns.} \\ 32.0 & \text{- 10 degree scattering from the core region, t=0 ns.} \\ 8.8 & \text{- 10 degree scattering from the collapsing sheath, t=-30 ns.} \end{cases}$$

From these calculations it can be seen that the signal to noise ratios for the ion spectrum are adequate except for possibly the 45 degree scattering from the sheath region at earlier times in the compression phase.

Electron spectrum

In section 3.2.1 it was demonstrated that the large disparity in scale of the dimensionless variables x_e and x_i, results in an electron spectrum which will be $\sim$ 60 times wider than the ion spectrum for a deuterium plasma with $T_e = T_i$. The peak height of the electron spectrum for $\alpha \ll 1$ (eq 3.18), will be $\sim$ 1/30 of that of the ion spectrum with $\alpha \gg 1$. From the calculations above for the ion spectrum signal to noise ratios, it can now be seen why the electron spectrum will be unobservable for $\alpha \leq 2$.

For $\alpha > 2$ the electron spectrum consists of two electron satellites of frequency, ω_p given by the Bohm and Gross dispersion relation (eq 2.37). For the case of an inhomogeneous plasma with a radial electron density profile, $n_e(r)$, eq 2.37 will have the form,

$$\omega_p(r) = [\omega^2_{pe}(r) + 3/2\ v^2_e(r).k^2_L]^{\frac{1}{2}} \tag{3.30}$$

where k_L is the Langmuir wave number probed by a scattering geometry having a differential scattering vector, $k=k_L$. The frequency shift of the scattered electron satellites, $\omega = \pm\omega_p$. Therefore for the blue--shifted satellite we have,

$$\omega(r) = [\omega^2_{pe}(r) + 3/2\ v^2_e(r).k^2_L]^{\frac{1}{2}} \tag{3.31}$$

Now $\omega^2_{pe} >> k^2_L\ v^2_e$, and assuming T_e varies more slowly with radius than n_e,

$$\frac{\partial \omega_{pe}}{\partial r} >> \frac{\partial v_e}{\partial r} \tag{3.32}$$

and therfore,

$$\frac{\partial \omega}{\partial r} = \frac{\partial \omega_{pe}}{\partial r} \tag{3.33}$$

or the incremental frequency spread relating to a radial plasma incremental, Δr, is given by,

$$\Delta\omega = \Delta r \frac{\partial \omega_{pe}}{\partial r} \tag{3.34}$$

For the case of plasma having a radial electron density profile, eq 2.7 for the electron plasma frequency becomes,

$$\omega_{pe}(r) = \left(\frac{n_e(r).e^2}{m_e \varepsilon_o}\right)^{\frac{1}{2}} \tag{3.35}$$

To calculate the incremental frequency spread we therefore need to know $n_e(r)$. The density scale length, L_n is given by,

$$L_n = \left(\frac{1}{n_e} \cdot \frac{\partial n_e}{\partial r}\right)^{-1} \tag{3.36}$$

From the holographic interferometry results described in section 4.5.3.4, the value of L_n at peak compression (t=0) was calculated to have an average value of 6.25×10^{-4} m. At this time, the radial electron density profile can be approximated as an exponential of the form,

$$n_e(r) = n_p \exp\left[-r/L_n\right] \tag{3.37}$$

where n_p is the peak density of 4×10^{25} m^{-3}.

Substituting eq 3.37 into eq 3.35 we get,

$$\omega_{pe}(r) = \left(\frac{n_p e^2}{m_e \varepsilon_o}\right)^{\frac{1}{2}} \exp[-r/2L_n] \tag{3.38}$$

and

$$\frac{\partial \omega_{pe}}{\partial r} = \frac{1}{2L_n} \left(\frac{n_p e^2}{m_e \varepsilon_o}\right)^{\frac{1}{2}} \tag{3.39}$$

Rearranging eq 3.34 and substituting for $\partial\omega_{pe}/\partial r$,

$$\Delta r = 2L_n \left(\frac{m_e \varepsilon_o}{n_p e^2}\right)^{\frac{1}{2}} \Delta\omega = \frac{4\pi c L_n}{\lambda_o^2} \left(\frac{m_e \varepsilon_o}{n_p e^2}\right)^{\frac{1}{2}} \Delta\lambda \tag{3.40}$$

For a detection channel wavelength bandwidth, $\Delta\lambda$ =0.02 nm, $\Delta r = 2.74 \times 10^{-7}$ m at peak compression.

Using eq 3.16 and 2.41, the scattered energy from one of the two electron satellites in a wavelength interval $\Delta\lambda$ is given by,

$$E_S(\underline{k})\, d\lambda d\Omega = \frac{4E_o}{\pi d^2} \cdot \bar{n}_e \left[2\pi\, r_{\bar{n}_e} \cdot \Delta r . d\right] r_e^2 \sin^2\gamma \frac{1}{2(1+\alpha^2)}\, d\Omega \tag{3.41}$$

where the term between brackets, [], is the volume of a radial shell of

incremental thickness, Δr and height d (the laser spot diameter), having a density $\bar{n}_e$. Sustituting for Δr from eq 3.40 and using the values of L_n and n_p for peak compression, with d=5.5 mm, we get,

$$E_S(\underline{k})\,d\lambda d\Omega = 3.8 \times 10^{-35} \frac{\bar{n}_e . r_{\bar{n}_e}}{\lambda_o^2} . \sin^2\gamma \frac{1}{(1+\alpha^2)}\, d\lambda d\Omega \qquad (3.42)$$

The signal to background ratio, S/B can be calculated using eq 3.14 as,

$$\frac{S}{B} = 2.29 \times 10^{10} \frac{E_o\, r_{\bar{n}_e} . \sin^2\gamma . T_e^{\frac{1}{2}}}{(1+\alpha^2) . \bar{n}_e\, t_g\, V_p} \qquad (3.43$$

where it has been assumed that $\lambda=\lambda_o$.

From figure 3.7 it can be seen that for $\alpha \geq 2$ and if Landau damping is to be avoided $\alpha > 5$, only the 10 degree scattering will satisfy the requirements across the range of n_e/T_e.

For the core region of the plasma at peak compression with $\bar{n}_e = 8\times10^{24}$, T_e=350 eV and θ =10 degrees, $\alpha \sim 13$. Using a value of $V_p = 3\times10^{-8}$ m^{-3} for the background emission volume, $r_{\bar{n}_e}$ =1.0 mm at peak compression for $\bar{n}_e = 8\times10^{24}$, and the previously used values for E_o, t_g and γ for 10 degree scattering, we get a S/B value of 6×10^{-4}. The ratio is so small that it would not be possible to make experimental measurements on the thermal level electron satellite spectrum.

3.5.5.4 CLIPPED LASER PULSE RATIOS

It was previously mentioned in section 3.5.1 that the use of a shorter laser pulse to provide better temporal resolution was precluded by too small a signal to noise ratio. Using the clipped pulse technique described in section 4.5.3.1 and a second ruby amplifier, provided a laser pulse of 120 mJ and 1.5 ns FWHM. The minimum gating time on the CMA was 40 ns which reduces the S/B ratios calculated for

the ion spectrum in section 3.5.5.3 by a factor of 20 and the detected signals levels by a factor of 50 because of the reduced energy. These reduced S/B and the resultant S/N ratios of less than unity for the 45 degree scattering and of the order of unity for the 10 degree scattering, precluded the use of such a short laser pulse.

3.6 OUTLINE OF THE PROPOSED SCATTERING EXPERIMENTS

The case for the implementation of a large number of detection channels for measurements of the scattered ion spectrum has already been established. The experimental difficulties of utilising a dispersive instrument and a conventional multichannel photomultiplier system, which had been exclusively used for all the previous ruby laser experiments, was not a serious possibility. A comparitive assessment of the alternative detection arrangements is given in the introduction to chapter 5 and the solution using a gated Vidicon Optical Multichannel Analyser is then fully discussed.

In section 3.4.3 we compared the observations of enhanced levels of scattering observed by the various authors when the $\underline{k}$ orientation was aligned with the $\underline{z}$-axis. The shot to shot variation of these type of spectra observed by Baconnet et al [17] and Bernard et al [19], make comparisons with $\underline{k}$ orthogonal spectra obtained on different shots difficult to interpret. Therefore the possibility of measuring more than one $\underline{k}$ orientation and/or scattering angle simultaneously from one plasma shot was considered highly desirable. A multiple-$\underline{k}$ scattering experiment based on a single grating spectrometer and the OMA was developed. The experimental arrangement of this system will be

described in chapter 6. The technique permitted the dispersed ion spectra of three scattering arrangements to be measured on one shot, from an essentially identical scattering volume. The scattering arrangements were as follows:

(1) θ=45 degrees with $\underline{k}$ orthogonal to $\underline{z}$.

(2) θ=10 degrees with $\underline{k}$ orthogonal to $\underline{z}$.

(3) θ=10 degrees with $\underline{k}$ antiparallel with $\underline{z}$.

The implementation of this technique provided experimental data which was not subject to the shot to shot variance, when comparison of the various $\underline{k}$ geometries was important. This was singularly the most important aspect of the work described here and enabled analysis and interpretation of scattering data from the Plasma Focus to be undertaken which had not been previously possible. The further advantages of this experimental technique will become apparent later in the analysis and conclusions chapters.

CHAPTER 4 THE EXPERIMENTAL APPARATUS AND DIAGNOSTICS

4.1 INTRODUCTION

In this chapter a description of the experimental apparatus will be given, excluding the scattering detection and optical arrangements which will be discussed in the two subsequent chapters. Details of the Culham Plasma Focus device and its operation will be given first, followed by an account of the ruby laser system employed in the optical diagnostics. The timing system developed to synchronise the laser pulse with the plasma will then be outlined. The chapter will be concluded with a description of the additional diagnostics to the scattering system, employed to monitor and diagnose the plasma, which provided essential information for the analysis of the laser scattering data.

4.2 THE PLASMA FOCUS

The Mather type Plasma Focus [47] consisted of a coaxial electrode gun of length 230 mm with electrode diameters of 50 mm and 92 mm connected by 216 coaxial cables to a capacitor bank of approximately 94 microfarad with a normal working voltage of 20-30 kV. Eight spark-gap switches which are triggered in parallel using Blumlein cables were used to initiate the discharge. The end of the gun projected into an octagonal vacuum vessel equipped with eight ports for diagnostics.

4.2.1 DETAILED MECHANICAL CONSTRUCTION

The detailed layout of the gun, vacuum vessel and electrical connections are illustrated in figure 4.1. The central electrode (1), which was the anode, consisted of a solid copper cylinder of diameter 50 mm. The lower open end of the electrode was capped with a heavy metal section (95% W + 5% Cu) of length 30 mm to reduce erosion due to electron bombardment. The high current connection at the top of the electrode to the brass high voltage plate (2) was made by the liquid nitrogen shrink fit technique.

The outer electrode (3) was a copper tube of internal diameter 92 mm and length 230 mm. It was perforated by a regular array of 228 9.5 mm diameter circular holes to improve the focussing mechanism [48]. The electrode was bolted firmly to the brass earth plate (4) to produce a low resistance connection. Alternating polythene and melinex sheets insulated the earth plate from the brass high voltage plate. Isolation of the two electrodes from each other is accomplished by an open ended 'top hat' pyrex insulator (5). The tubular sleeve of this has an OD of 63.5 mm and extends the first 46 mm of the gun. The gun projects into an octagonal sided stainless steel vacuum chamber (6), five of the sides having 50 mm ports and three having 75 mm ports one of which was used for vacuum pumping. Directly below the gun was a 100 mm port to which was attached a 600 mm long pyrex tube to trap eroded material from the electrodes and to dissipate the plasma kinetic energy. This prevented accumulated debris from being disturbed during a discharge and damaging high quality windows used for diagnostics.

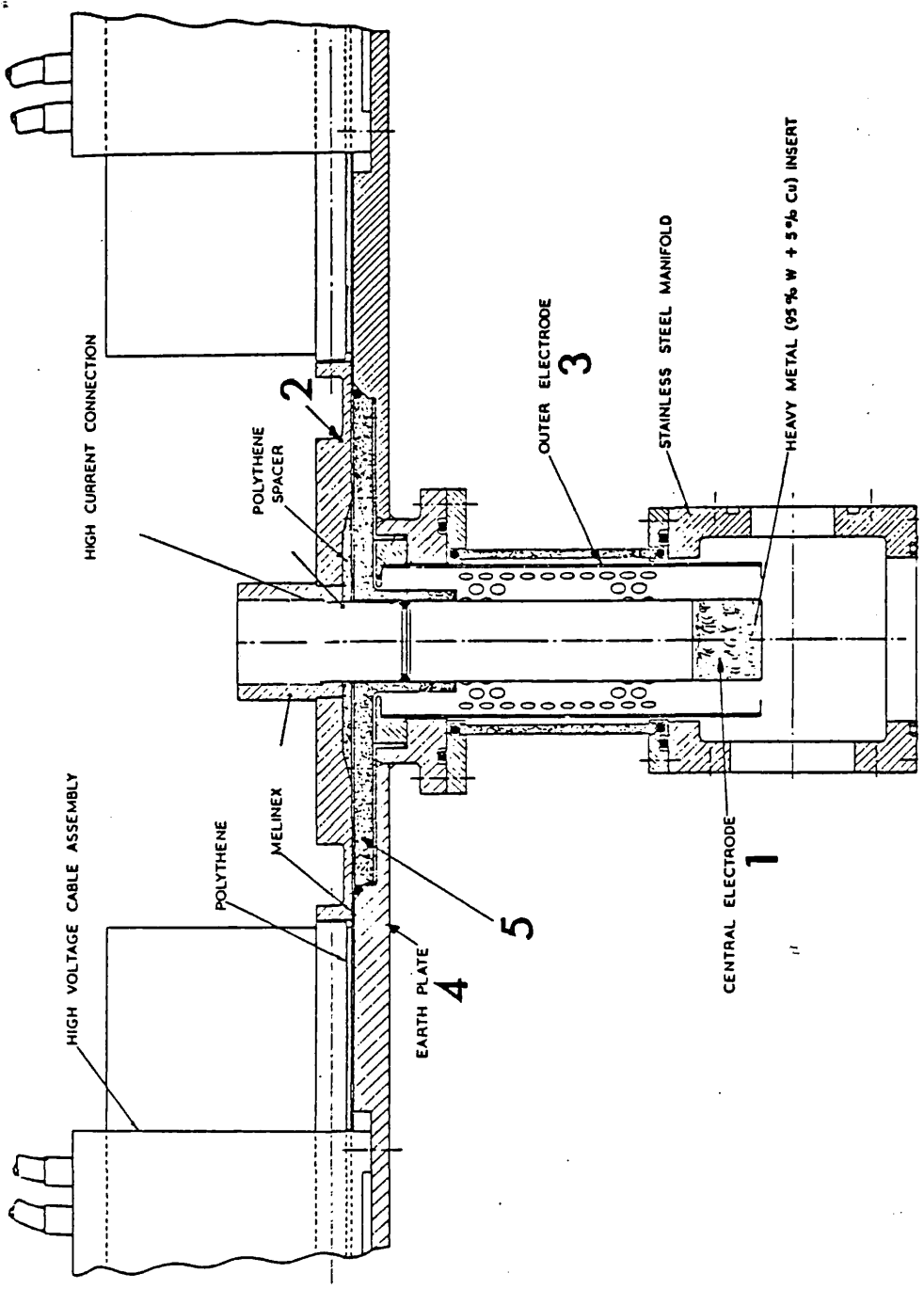

Figure 4.1
Plasma Focus assembly.

4.2.2 THE VACUUM AND GAS FILLING SYSTEMS

The vacuum chamber and gun assembly were evacuated through one of the 75 mm ports via a 'T' piece, so as not to lose the use of that port. A single-stage rotary oil pump with a capacity of $\sim$450 litres/minute at 100 torr, served as backing to a 150 mm diameter, oil diffusion pump. The latter pump incorporated a water-cooled baffle to reduce oil vapour pressure in the vacuum chamber. The pressure was further reduced by a refrigerated baffle fitted between the diffusion pump and chamber. A remote controlled motor valve was situated adjacent to this baffle and was used to isolate the vacuum chamber.

A background pressure of 5×10^{-6} torr was usually achieved. The pressure in the system was measured using one of three gauges. A Pirani gauge was used in the range 100 torr to 10^{-3} torr, and an ionisation gauge at lower pressures. For accurate pressure filling of the system with deuterium, a mercury manometer was used. With the diffusion pump at working temperature, the pressure in the system could be reduced from 1.8 torr (typical operating pressure) to $<10^{-5}$ torr in about 3 minutes.

Gas was introduced into the system by means of a hot-wire leak valve. This was used in conjunction with the mercury manometer to fill the system to the required working pressure.

4.2.3 THE CAPACITOR BANK AND DISCHARGE CIRCUIT

The capacitor bank consisted of 32 capacitors, each of nominal capacity of 3 microfarad, with a total measured capacitance of 93.85 microfarad. The maximum working voltage of the bank was 40 kV, but it was operated at 24.1 kV with a stored energy of 27.25 kJ. The capacitors were charged by a power supply consisting of a step-up transformer and half-wave rectifier, in conjunction with a voltage--doubling circuit. A maximum current of 200 mA at 50 kV could be delivered by the supply.

The capacitor bank was divided into four modules, each of which was further divided into two circuits. Each circuit was switched into the gun by a 3-electrode swinging-cascade spark-gap switch. The capacitor bank fed the high voltage and earth plates of the gun, through the spark gaps, via 216 coaxial cables of 50 ohm impedance. Using many parallel cables enables a low source inductance to be achieved, so that the capacitor bank energy can be rapidly delivered to the gun. Likewise, using eight parallel spark gaps results in a switching inductance which is 1/8 of that of a single spark gap. The measured source inductance and resistance of the system (section 4.5.1) was 33.7 nH and 2.25 mΩ respectively. The cables were connected to the gun in four symmetric groups, the cable braids being at earth potential.
A Blumlein cable charged to 35 kV triggered the eight spark gaps in parallel. The cable itself was switched by a master spark gap, which was triggered by a 15 kV pulse from a thyratron valve unit. The typical breakdown time for a spark gap, from when the trigger pulse was applied to the trigger electrode, to the time when the main gap started to conduct, was 25 nsec. Typical shot to shot jitter was 5 nsec. Thus, on the time scale of the discharge circuit, of quarter period

$\sim$ 2.8 microsecond, the eight spark gaps were well synchronisd.

4.2.4 OPERATION OF THE DEVICE

The operational procedure of the Plasma Focus was as follows:

(a) The vacuum chamber was pumped for 2-3 minutes until the background pressure was $\leq 5 \times 10^{-6}$ torr.

(b) The chamber and gun were isolated from the vacuum pumps by closing the motorised baffle valve.

(c) Using the hot-wire leak valve, the chamber and gun were filled with deuterium to the required pressure - usually 1.8 torr.

(d) The Blumlein tigger cable was charged to 35 kV.

(e) The capacitor bank was charged to the required voltage, following which the discharge was initiated. This was repeated 10-15 times for a single filling of gas before the proceedure was repeated.

When the vacuum chamber and gun had been allowed up to atmospheric pressure for alignment of diagnostics etc, 50 to 100 shots were fired to 'discharge clean' the device before retaking data. This was to ensure reproducibility of conditions.

For the operation of the Plasma Focus, either at a fixed bank voltage or filling pressure, it was important to maximise the energy transfer from the capacitors to the dense pinch. Optimum energy transfer occurred when the collapse phase commenced at the time of the first current maximum in the discharge circuit (section 4.5.1), when the energy is inductively stored and the capacitor bank voltage is approximately zero. Monitoring the current waveform shot by shot,

either the bank voltage or filling pressure was varied, as appropriate, until the characteristic dip in the waveform occurred at peak current. The optimised values used for the experiments reported here were 24.1 kV with a filling pressure of 1.8 torr deuterium.

4.3 THE RUBY LASER SYSTEM

4.3.1 INTRODUCTION

The ruby laser system was employed for both the scattering experiments and for the determination of the radial electron density profile using holographic interferometry. The laser ouput requirements for each of these were different. The modifications made to the laser optical layout for the holographic interferometry diagnostic will be described in section 4.5.3. Here, the basic laser system employed in the scattering diagnostics will be described.

4.3.2 THE LASER OPTICAL LAYOUT

The choice of laser system for providing a scattering diagnostic on the Plasma Focus was discussed in the previous chapter. Here, the requirements will be summarised as a high power, low divergence output at 694.3 nm. In addition shot to shot reproducibility is highly desirable.

The optical layout of the laser system is illustrated in figure 4.2. The laser oscillator consisted of a modified Korad K1 laser system with a 9.5 mm diameter, 100 mm long ruby rod, pumped by a

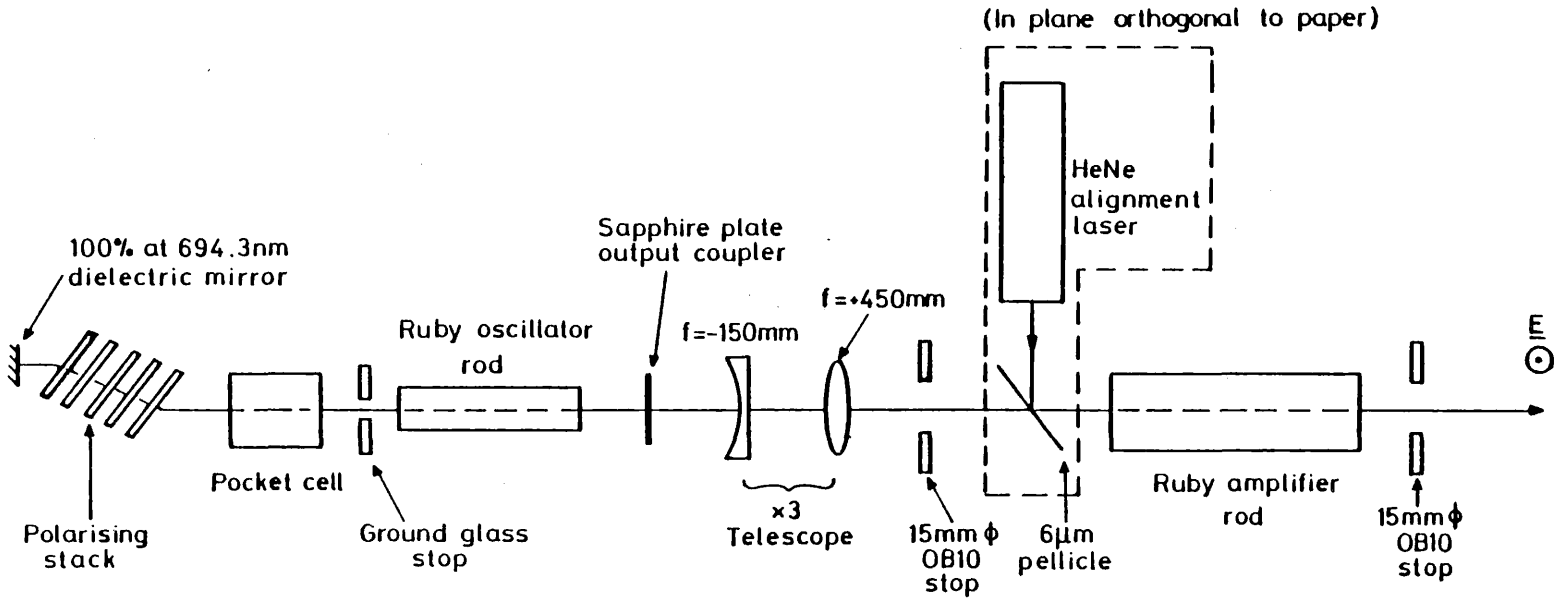

Figure 4.2
Ruby laser layout.

helical flash tube which was powered by a capacitor bank of 400 microfarad operated at 3.5-4.0 kV. The laser cavity was formed between a 100% reflecting (at 694.3 nm) dielectric mirror and an output coupler which was a sapphire plate (26% reflecting at 694.3 nm). The polarising stack transmits light only when it's polarised in the plane of the paper. Since the c-axis of the ruby rod also lies in this plane, lasing is impossible when the Pockel cell is unstressed. The cavity is 'Q-switched' by stressing the Pockel cell to a $\lambda/2$ plate by means of a 40 kV pulse from a voltage-doubling Blumlein cable, switched by a thyratron at maximum poulation inversion in the rod. This occurs approximately 1 ms after triggering the helical oscillator flash tube discharge circuit and depends on the oscillator capacitor bank charge voltage. The pulse energy was measured using a TRG Control Data Corp. 107 Thermopile and a microvolt-ammeter and was typically 0.6 J. The pulse shape, which had a FWHM of 20 ns, was monitored using a vacuum photodiode (ITL 125 ohm S-20) with a rise time of 0.2 ns, connected to a 500 MHz bandwidth Tektronix 7000 series oscilloscope.

The oscillator output was expanded with a x3 Galilean telescope following which the spatial quality of the beam was improved with an annular OB10 blue glass stop (highly absorbing at 694.3 nm) with a clearance diameter of 15 mm. The beam was then passed through an amplifier with a 19 mm diameter, 225 mm long ruby rod, followed by another 15 mm diameter annular OB10 stop. The c-axis alignment of the amplifier rod was identical to that of the oscillator. The amplifier rod was pumped with a helical flash tube powered by a capacitor bank of 400 microfarad operated at a voltage of 8-9.5 kV, the flash tube being in series with a pulse shaping inductance of 385 μH. The capacitor bank was switched using an ignitron. Reliable pre-ionisation of the flash tube was achieved using a series trigger. This consisted of a

transformer placed adjacent to the amplifier head which produced a 22 kV pre-ionisation pulse at the flash tube at the same time as the ignitron was switched. A total ouput energy of 6 J was delivered by the system, corresponding to a average power of 300 MW. The ruby rods in the system along with the oscillator cavity mirror mounts were thermally stabilised by the flow of deionised cooling water maintained at a temperature of $15 \pm 1^{o}C$.

The output polarisation of the laser system was in the horizontal plane. This resulted in a γ angle value (eq 2.5) for the 45 degree scattering arrangement of 45 degrees. A vertically polarised laser output would have increased this angle to 90 degrees, doubling the collected scattered light signal. Modification of the laser Pockel cell arrangement to produce a verticallly polarised output was possible, but this necessitated a more complex HeNe laser alignment system. Experimentation with a $\lambda/2$ plate prior to the amplifier stage, to rotate the polaristaion from the horizontal to the vertical, was unsuccessfull due to rapid laser damage of the $\lambda/2$ plate. However, adequate signal levels were achieved for the 45 degree scattering with the horizontal polarisation, and the reliability of the laser system in this mode of operation was very good.

4.4 THE TIMING CONTROL SYSTEM

A major experimental problem encountered when using a pulsed laser in conjunction with a gated detector to diagnose a short duration pulsed plasma, is to devise a timing and monitor system to temporally synchronise the three pieces of apparatus with minimal shot to shot

jitter. The timing layout developed for the work described in this thesis is illustrated in figure 4.3, and consisted of Culham trigger and delay units (type- 95/8287-1/6 and 95/8288-1/6) and a Space Technology Laboratories Inc. (STL) nanosecond delay generator. The system was situated in a diagnostic screened room to facilitate flexibility of the relative timing of the trigger circuits of the Plasma Focus, ruby laser system and high voltage pulse generator used for gating the Vidicon Optical Multichannel Analyser (OMA) detector head (section 5.2.3).

The time taken for the 'Q-switched' ruby laser pulse to build up once the oscillator cavity was switched with the Pockel cell was approximately 120 ns. However, the total time taken from the Pockel cell thyratron trigger pulse leaving the screened room to the output of the laser pulse was approximately 700 ns. This was made up of the 120 ns pulse build up time, plus cable delays in both the trigger cables and the propagation time of the high-voltage Pockel cell gating pulse. This time interval and that of the Plasma Focus time cycle from triggering the master spark gap to the pinch compressing on axis of 2.75 μs are negligible in comparison with the ruby flash tube pumping time of $\sim$ 1 ms.

The trigger timing sequence was therefore as follows: The master trigger, derived from the OMA external electronics (section 5.4.3), triggered first the ruby amplifier and then the oscillator flash tubes, followed by the triggering of the Plasma Focus spark gaps $\sim$ 1 ms later. Jitter in the Plasma Focus trigger circuits and the long run-down time interval of the plasma in comparison with the peak compression phase lasting only tens of nanoseconds prevented the use of a further delay unit to trigger the 'Q-switch' circuit directly, because a jitter of >40 ns resulted in the synchronisation between the ruby laser pulse and

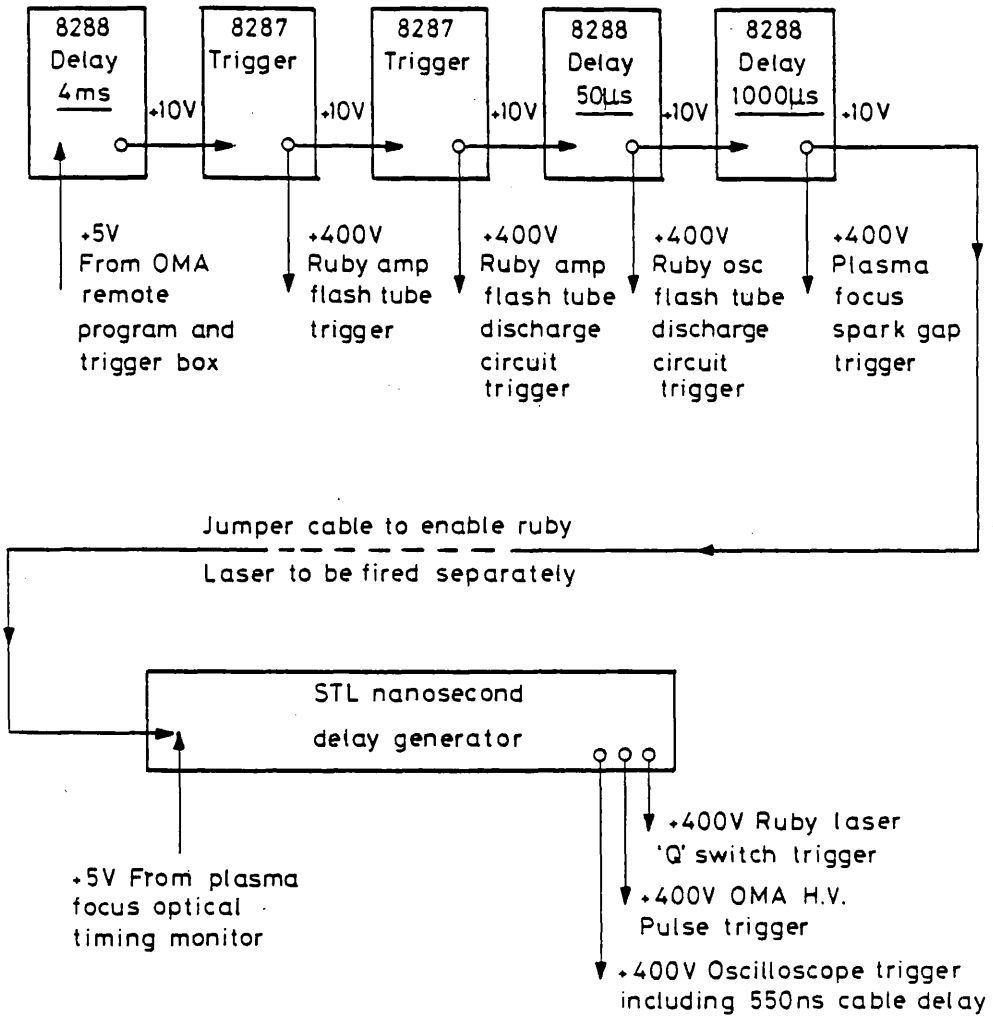

Figure 4.3
Schematic of the Timing Control System.

the Plasma Focus. In order to achieve a synchronisation jitter of <10 ns a timing pulse was derived from the Plasma Focus by optically monitoring the accelerating plasma sheath in the final stages of the run-down phase. The optical monitoring system consisted of a collimating copper tube (300 mm long with an ID of 3 mm) located with one end perpendicular to the lower end of the glass tube surrounding the electrodes. It was located opposite one of the holes in the outer electrode so that light from the passing plasma sheath could be collected. To the other end was attached a 400 μm diameter fibre optic cable connected to an optical trigger isolator reciever (Culham type 95/8283-1/6) in the screened room. This produced a trigger pulse of +5 V, the leading edge of which was used to trigger the STL nanosecond delay unit which provided a fine adjustment for the Plasma Focus - ruby laser pulse and detector gating pulse synchronisation. The ruby laser pulse was synchronised to the detector high-voltage gating pulse by adjustment of the trigger delay provided on the high voltage pulse generator.

The output pulse from the STL delay unit was also utilised, using cable delays, to provide oscilloscope trigger pulses for use with either a 100 or 50 ns/div timebase. Two Tektronix 7844 dual beam oscilloscopes were used to monitor the synchronisation of (1) the Plasma Focus dI/dt (section 4.5.1) and the ruby laser photodiode signals, (2) the ruby laser photodiode and OMA high voltage pulser monitor signals.

4.5 ADDITIONAL PLASMA DIAGNOSTICS

In addition to the laser scattering diagnostics several other diagnostics were operational on the Plasma Focus. A current and voltage monitoring system provided electrical information at the gun, and was used as a timing marker for the other diagnostics. A total neutron yield monitor was used as an indication of the quality of the plasma compression from shot to shot. In chapter 2 it was shown that the intensity of the scattered light signal is proportional to the electron density, n_e, within the scattering volume. In addition the shape of the spectrum is dependent on the scattering parameter, α which is proportional to $n_e^{\frac{1}{2}}$. In the analysis of the scattering data it is therefore desirable to know the radial electron density, $n_e(r)$, as a function of time. A holographic interferometer was therefore developed to provide this information. In addition, a Faraday rotation polarimeter was employed to obtain the radial magnetic field profile of the plasma as a function of time. This work is described in detail by Muir [25] and the results provided valuable data on the plasma current distribution for comparison with results obtained from laser scattering with a differential scattering vector, $\underline{k}$ parallel to the electron-ion drift velocity direction. Each of these diagnostics is described in the subsequent sections.

4.5.1 CURRENT AND VOLTAGE MONITORING OF THE DISCHARGE

The electrical equivalent circuit of the Plasma Focus is illustrated in figure 4.4. The capacitor bank and discharge circuit components were discussed in section 4.2.3. In addition there are the components enclosed within the dotted area associated with the load assembly and plasma. R_s=2.25 mΩ and L_s=33.7 nH represent the source resistance and inductance respectively. R_ℓ is the leakage resistance across the pyrex glass insulator between the electrodes and L_g the inductance of the coaxial gun. R_p and L_p are the plasma resistance and inductance respectively.

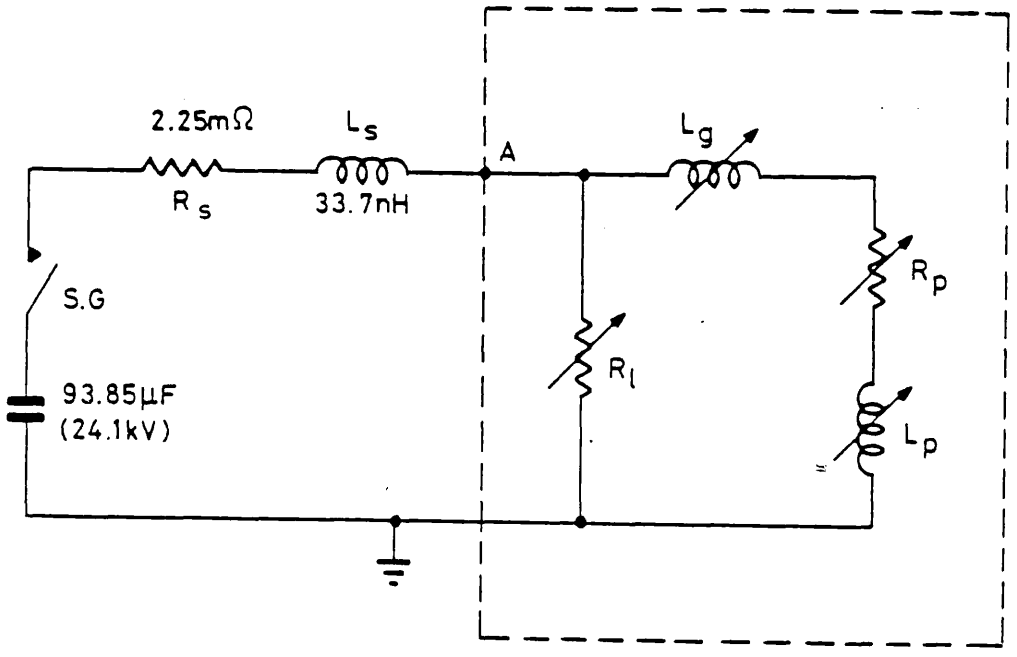

Figure 4.4
Electrical equivalent circuit of Plasma Focus.

Direct measurement of the plasma current is not possible due to the coaxial electrode arrangement. However, indirect measurements were

obtained from the Faraday rotation diagnostic [25]. The total current flowing between the electrodes which includes the current across the insulator was monitored at point A on figure 4.4 using a Rogowski coil. The coil was looped round the gun between the high voltage and earth plates, so that the current flow threaded the coil. A voltage, α dI/dt, was induced in the coil, and by means of a potential divider a fraction of this voltage could be monitored. This signal was utilised in the timing synchronisation of the ruby laser with the plasma, providing a timing position of the laser pulse relative to the peak of the dI/dt signal, corresponding to the first compression of the plasma on axis. Alternatively the dI/dt signal could be fed to the integrating circuit via a matched coaxial cable illustrated in figure 4.5. The time constant of the circuit, RC $\sim$ 80 microsecond, was much longer than the quarter period of the discharge circuit, $\sim$ 2.8 microsecond, so that the integrated signal displayed on the oscilloscope was proportional to I.

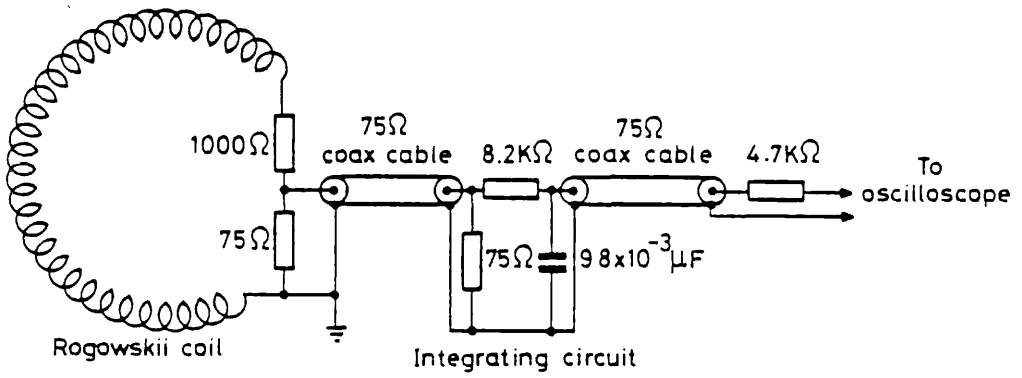

Figure 4.5
Schematic diagram of the current measuring circuit.

The current monitor had been previously calibrated [11], by observing the oscillatory current waveform when the feed plates to the gun were short-circuited. From measuring the amplitude of successive peaks, the damping rate was determined. This yielded a value for the peak current and hence the current monitor calibration factor. Additionally, the time period of the waveform enabled the circuit inductance to be determined, which had a value of 33.7 nH.

The voltage between the gun electrodes was monitored between point A and ground (figure 4.4), by using a high-impedance voltage divider to obtain a small fraction of the total signal, and displaying the attenuated signal on an oscilloscope.

A typical dI/dt and current signal, obtained at V=24.1 kV and filling pressure, p=1.8 torr, are shown in figure 4.6. For these initial conditions, the total peak current determined at point A on figure 4.4 was 490 kA. The plasma current determined from the Faraday rotation measurements was 340 kA [25] which is approximately 70% of the total circuit current. The difference in the two values can be probably accounted for by current leakage across the insulator (R_ℓ) which is known to occur [49]. During the collapse phase, the plasma inductance, L_p increases sharply, causing the circuit current to decrease correspondingly. A high voltage is induced between the electrodes, α d/dt(LI), up to five times the magnitude of the initial bank voltage. Neutrons are always produced during a discharge having such waveforms. Usually the waveforms alternated from shot to shot between the above and a current waveform which exibited no breakaway with a voltage waveform having no high voltage spikes. No significant neutron production was observed during such discharges.

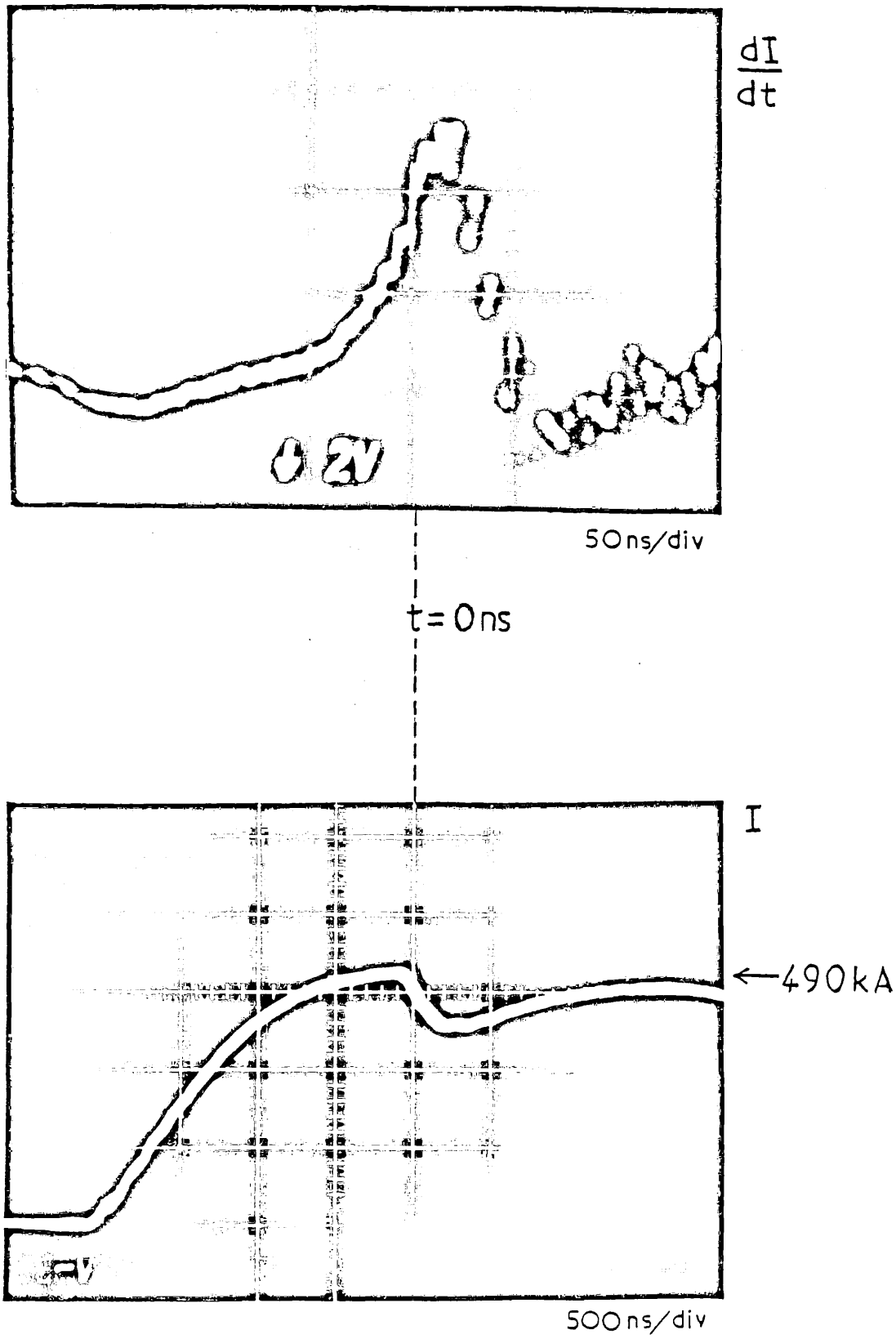

Figure 4.6
dI/dt and current profiles for V=24.1 kV, p=1.8 torr.

4.5.2 NEUTRON OUTPUT MONITORING

The neutron yield per discharge was monitored using a silver activation technique. A Geiger-Muller counter with a thin silver window was embedded in a block of Polythene, which moderated the neutrons of energy $\sim$2.45 MeV produced by D-D reactions in the plasma. The thermalised neutrons activated the silver which decayed by β emission with a half-life of $\sim$2.4 minutes. An amplifier-scalar system (Nuclear Enterprises, Scalar-Timer ST6) recorded the number of pulses produced by the counter, due to the β particles, during the 100 sec interval following each discharge. The total count produced was proportional to the total neutron production of the plasma.

This diagnostic was used in an uncalibrated form. However, it provided a useful indicator of the quality of the focus discharge, for shot to shot comparison. A good discharge in the Culham Plasma Focus produces $>10^9$ neutrons [11] and a 'no focus' shot $\leq 10^6$ neutrons. By a 'no focus' shot we mean those shots which do not exhibit the characteristic dip in the current waveform discussed in the previous section.

4.5.3 HOLOGRAPHIC INTERFEROMETRY

Double exposure holographic interferometry, detailed by Johoda & Siemon [50], is now commonly employed to determine the electron density of a plasma when the line integral $\int_o^\ell n_e \, dl$ is in the range 10^{21} - 10^{23} electrons.m^{-2}. In ordinary interferometry one measures the difference in optical path length between two waves going through

different paths simultaneosly. With holography the two waves go through the same path at different times and are recorded on the same photographic plate. One is recorded with the plasma, the other without. After development, white light reconstruction permits both wavefronts to be observed and the phase shift between them is revealed by the Moire fringe pattern.

A non-diffuse, imaged holographic technique was used as opposed to normal diffuse methods. This has the advantage of reducing noise due to speckle pattern which in turn increases the Moire fringe resolution [50]. The disadvantage of the imaged holographic technique is that it is sensitive to the spatial coherence of the laser. This problem was overcome by only using a small area of the output beam from the laser, and ensuring near-identical source overlapping of both the scene and reference beams on the holographic plate. Temporal coherence of the scene and reference beams was achieved by ensuring their difference in path length was significantly smaller than the coherence length of the laser, given by Faw & Dulforce [51] as $\lambda_o^2/4\Delta\lambda_o$, where $\Delta\lambda_o$ is the laser line width. For the ruby laser used, $\Delta\lambda_o$=0.01 nm, giving a coherence length of <10 mm.

The Plasma Focus presents one major problem to performing holographic interferometric measurements in that the density profile varies rapidly with time. Typical radial velocities of the sheath during the collapse phase are $>2\times10^5$ $m.s^{-1}$ (200 $\mu m.ns^{-1}$). Therefore to 'freeze' the plasma motion, the exposing laser pulse needs to be as short as possible while containing sufficient energy to expose the photographic plate. A pulse clipping technique was employed to shorten the ruby laser oscillator pulse to 1.5 ns with an energy of 20 mJ. This arrangement and the holographic interferometer are detailed below.

4.5.3.1 LASER PULSE CLIPPING ARRANGEMENT

The pulse clipping optical arrangement is illustrated in figure 4.7. The oscillator output (0.6 J, 20 ns FWHM, horizontally polarised) was expanded in beam diameter by a x2 Galilean telescope and then stopped down using a 8 mm diameter OB10 stop to improve the spatial coherence. The polarisation of the beam was then rotated through 90 degrees using a $\lambda/2$ plate to enable the clipping bench layout to be in the more convenient horizontal plane. The 'Q-switched' oscillator pulse was 'clipped' to a 1.5 nsec pulse using the half-wave switching technique. The vertically polarised beam passes through a Pockel cell (Electro Optics Developments Ltd type PC125) which is initially unstressed, and is then reflected from a Glan-Thomson polariser onto a nitrogen pressurised laser triggered spark gap. The spark gap consists of an annular anode through which the laser beam is focussed onto the cathode by a lens. The electrode spacing was adjustable and was set at 300 μm. The pressure of high purity nitrogen required for a given applied spark gap voltage was determined simply by increasing it until the gap was observed to be no longer 'self switching'. This was typically 50-80 psi. Figure 4.8 illustrates the electrical layout for half-wave switching. The Pockel cell has a 50 ohm high voltage BNC input and output socket for each electrode with impedance matching maintained between the two, and a manufacturers quoted risetime of <0.3 ns.

The coaxial cables are charged up to the required switching voltage through an 8 MΩ resistance from a variable high voltage Brandenburg power supply. When the spark gap is broken down by the initial part of the leading edge of the 'Q-switched' laser pulse a negative going pulse of risetime, L/Z and falling edge with a time constant, CR propagates from the spark gap towards the Pockel cell. Here L is the inductance

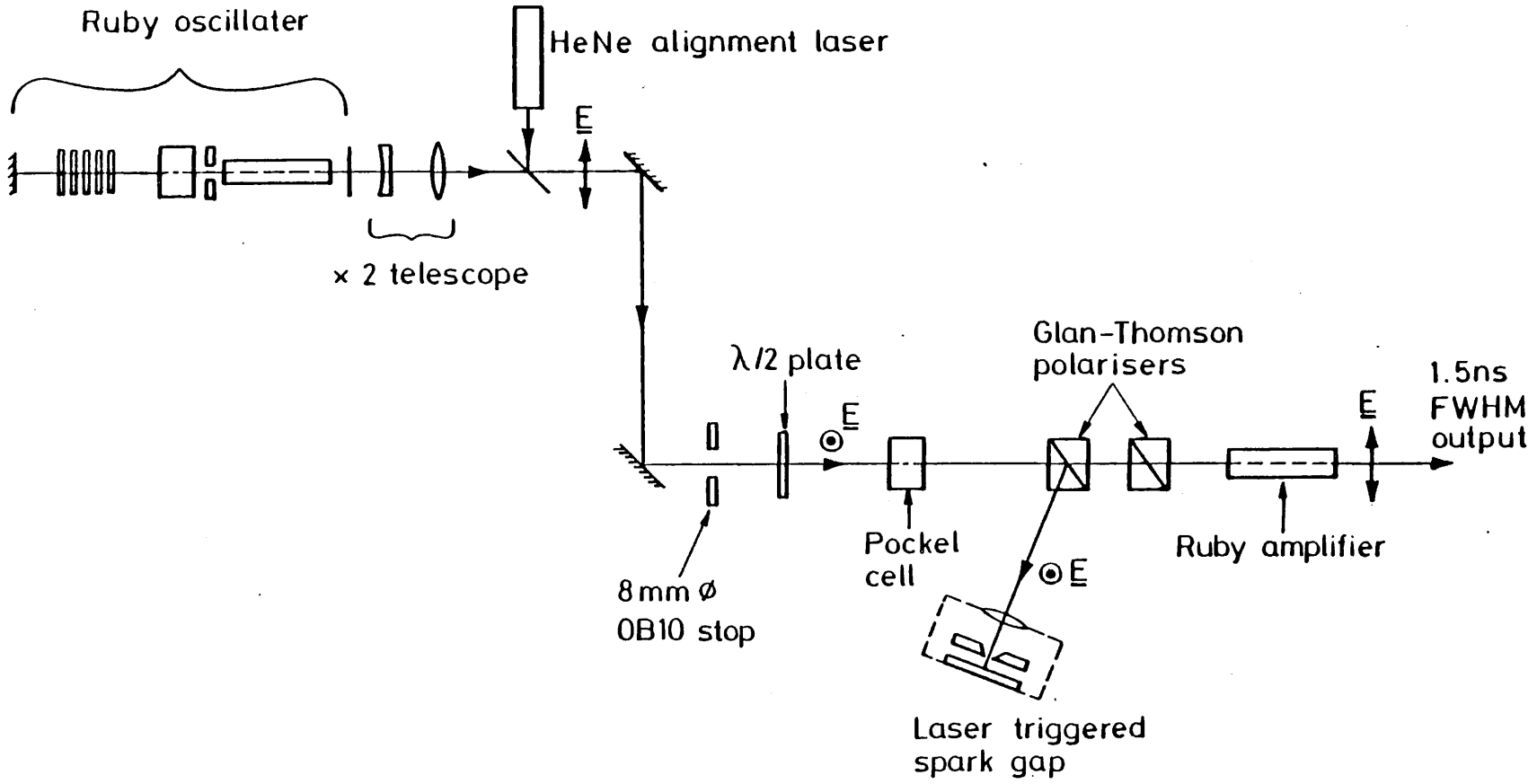

Figure 4.7
Ruby laser layout for holographic interferometry.

of the spark gap, Z the impedance of the cable, and R is the charging resistance). The pulse reaches the Pockel cell in a time l/v (where v is the speed of propagation in the cable). At this point there is then a voltage difference between the electrodes of the Pockel cell, stressing it, and rotating the beam polarisation through 90 degrees. The voltage difference remains between the electrodes until the electrical pulse reaches the second electrode after a further time s/v. The pulse then continues on along a dump cable until it reaches a capacitive dump which prevents reflection.

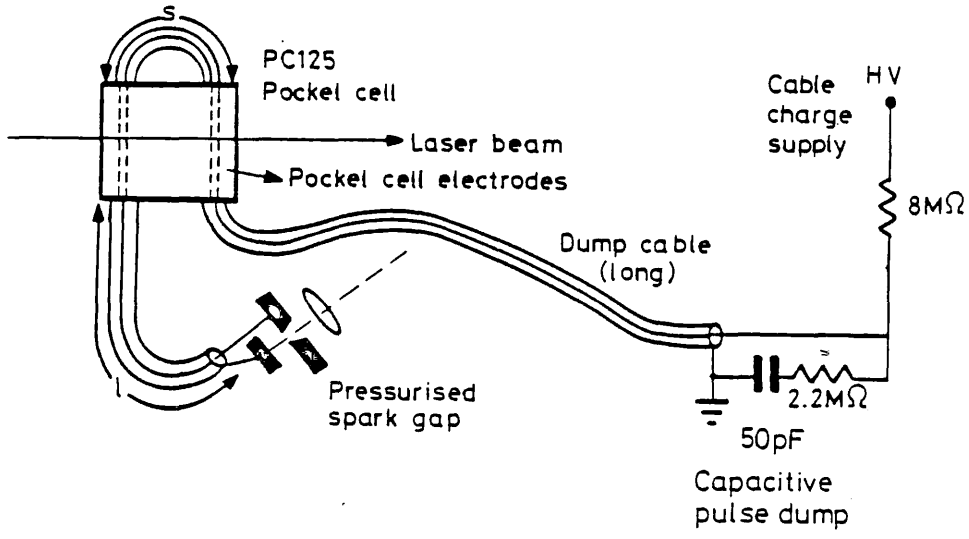

Figure 4.8
Electrical layout of half-wave switching arrangement.

During the time period s/v when the Pockel cell is stressed, the 'Q-switched' laser pulse can be transmitted through the Glan-Thomson polariser because of its polarisation rotation to the horizontal. Control of the 'clipping' interval at the peak of the 'Q-switched' pulse can be obtained either by changing the time of breakdown of the

spark gap relative to the 'Q-switched' pulse by use of neutral density filters infront of the spark gap focussing lens, or by changing the cable length, l.

The second Glan-Thomson provides a higher rejection ratio against the vertical polarisation. The transmitted 'clipped' laser pulse was then amplified using a 14.3 mm diameter, 100 mm long laser rod with a helical flash tube and discharge circuit that were similar to that of the oscillator. Both the reflected laser pulse and the amplified transmitted pulse where monitored with vacuum photodiodes (ITL 125 ohm S-20) connected to a Tektronix 7934 storage oscilloscope. Neutral density filters were used infront of the photodiodes to provide suitable attenuation of the signals.

4.5.3.2 THE HOLOGRAHIC INTERFEROMETER

The optical layout of the interferometer is shown in figure 4.9. The output beam from the pulse clipping bench is split into two beams by a 50% reflecting (at 694.3 nm) dielectric beam splitter, BS1, providing a scene beam and reference beam.

The scene beam was then expanded by a x10 Galilean telescope (lenses L1 and L2) to provide a suitable field of view of the plasma. The 20 mm diameter OB10 stop half way between the telescope elements defines that the centre 4 mm of the 8 mm output from the clipping bench is expanded to a 40 mm diameter beam. The beam then passes through the vacuum chamber and plasma. Lens L3 of focal length 650 mm and 75 mm diameter images the plasma axis onto the holographic plate with a magnification of 2.2. The overall magnification of the scene beam was therefore 22. The arrangement of using only 2 mm of the output from the oscillator (4 mm from the clipping bench) was found to provide adequate spatial coherence and the energy density was sufficient for exposure of the

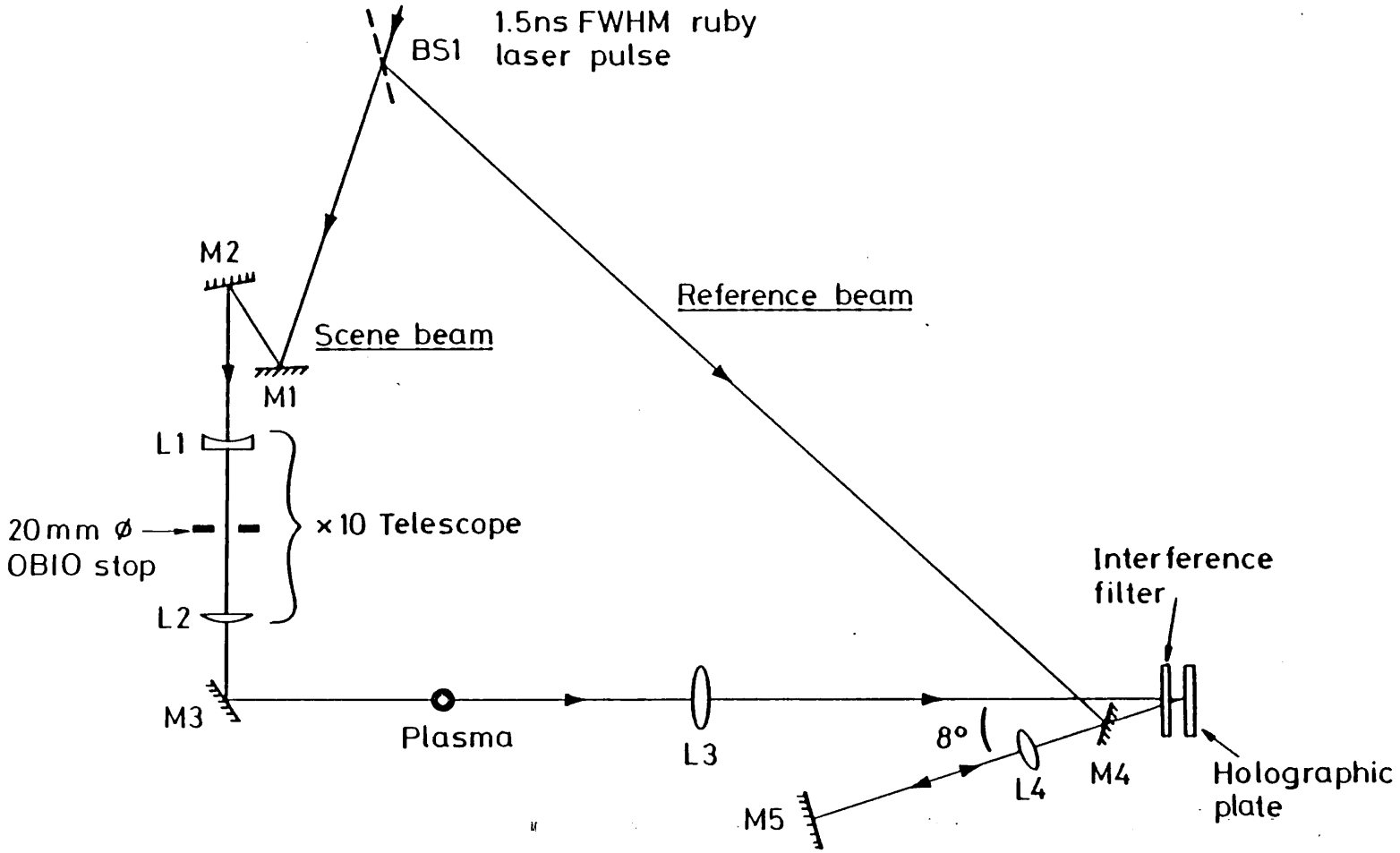

Figure 4.9
Holographic interferometer optical layout.

holographic plate.

The reference beam was relayed via two 100% dielectric mirrors, M4 and M5 onto the holographic plate. The +10 mm focal length lens, L4 between the two mirrors was positioned to produce a x22 expansion of the reference beam at the plate (identical to the scene beam).

4.5.3.3 EXPERIMENTAL MEASUREMENTS

Holographic interferograms were recorded during the collapse, dense-pinch and break-up phases of the plasma, from t=-100 ns to t=+50 ns. Agfa-Gevaert 10E75 holographic plates with a resolution of 2800 lines per mm were used for the measurements. These require an exposure of approximately 5×10^{-2} $J.m^{-2}$ for an optical density of unity. They were protected from the room light and plasma emission by an intereference filter centred at 694.3 nm which is indicated in figure 4.9. Two exposures were made on each plate. The first with the plasma, following which mirror M5 (figure 4.9) was tilted slightly to displace the reference beam vertically, after which a second exposure was made without the plasma. Tilting mirror M5 between exposures produces reference fringes parallel to the end of the centre electrode, making the phase shift readily measurable. The plates were developed in Neofin-Blue and were converted from amplitude to phase holograms with ferricyanide bleach, which has the advantage of giving bright reconstructed holograms with sharp fringes. The various processing techniques are reviewed by Faw & Dullforce [51].

To extract the interferometric data, the holograms had firstly to be reconstructed. White light reconstruction was accomplished using the optical arrangement of Jahoda & Siemon [50], which is shown

schematically in figure 4.10. Light from a lamp S is collected by a condenser lens L1 behind the holographic plate and focussed to a point F, which additionally produces similar converging first order diffracted light cones on either side. The reconstructed interferogram is photographed by positioning the camera's objective lens L2 at the focus of one of the diffracted light cones. The images were recorded on Polaroid type 55 positive/negative film.

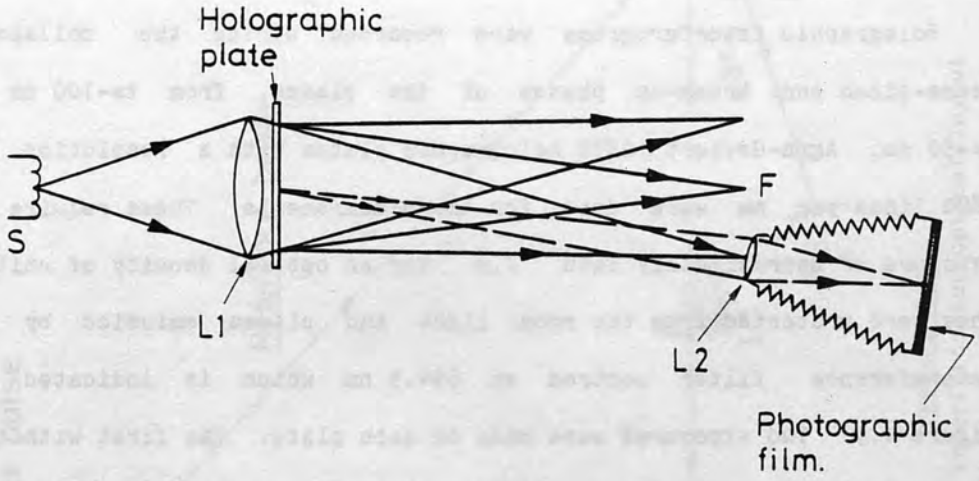

Figure 4.10
Optical arrangement for White light reconstruction of holographic interferograms.

Comments on the results

A sequence of six reconstructed holograms is shown in figures 4.11 and 4.12 illustrating the evolution of the discharge.

At time t=-30 ns, the radially collapsing sheath is clearly visible against the background reference fringes. Small amplitude instabilities are visible. At time t=-10 ns, the plasma column is more developed and larger amplitude instabilities are now apparent, although

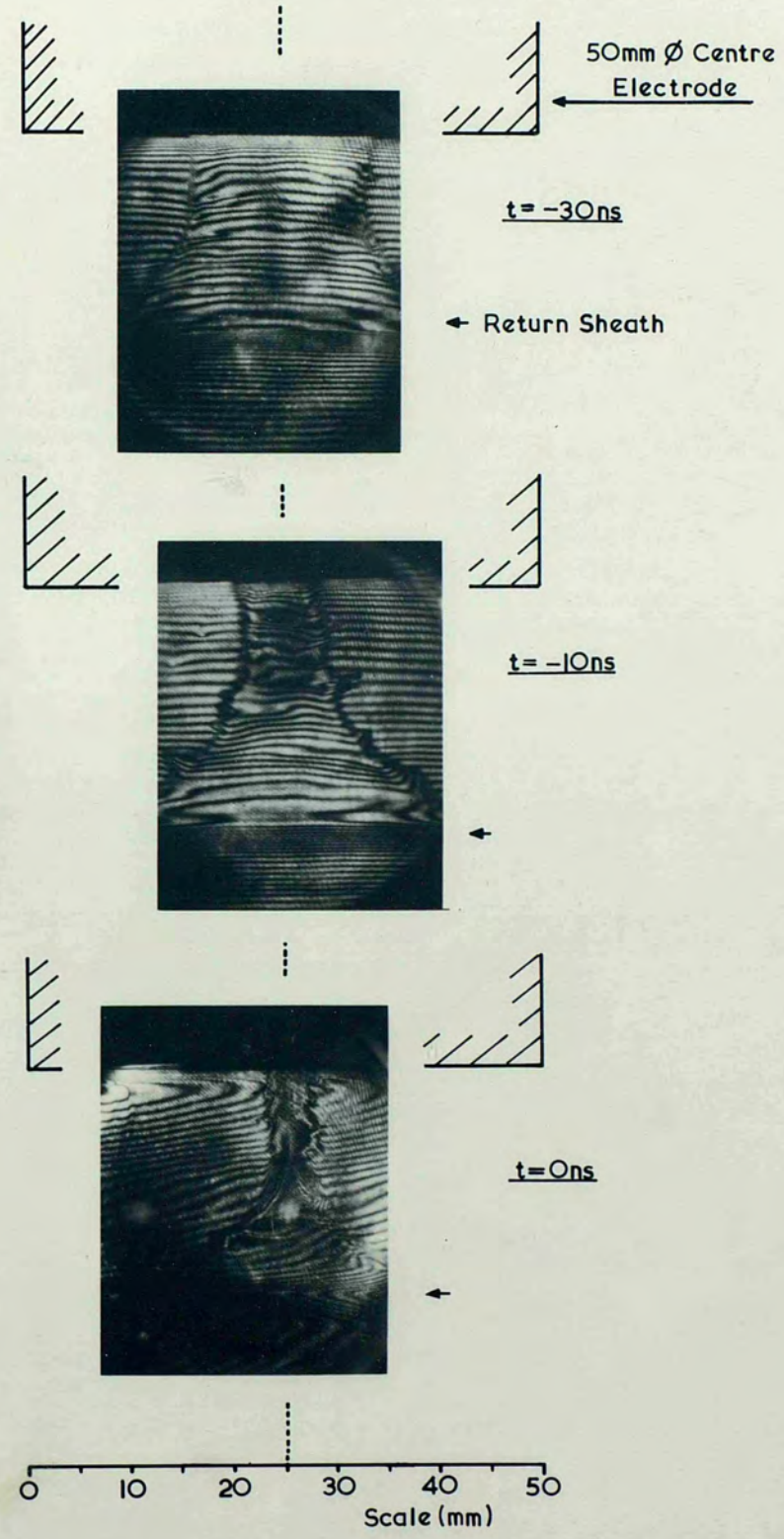

Figure 4.11
Reconstructed holographic interferograms for times t=-30 ns, t=-10 ns and t=0 ns.

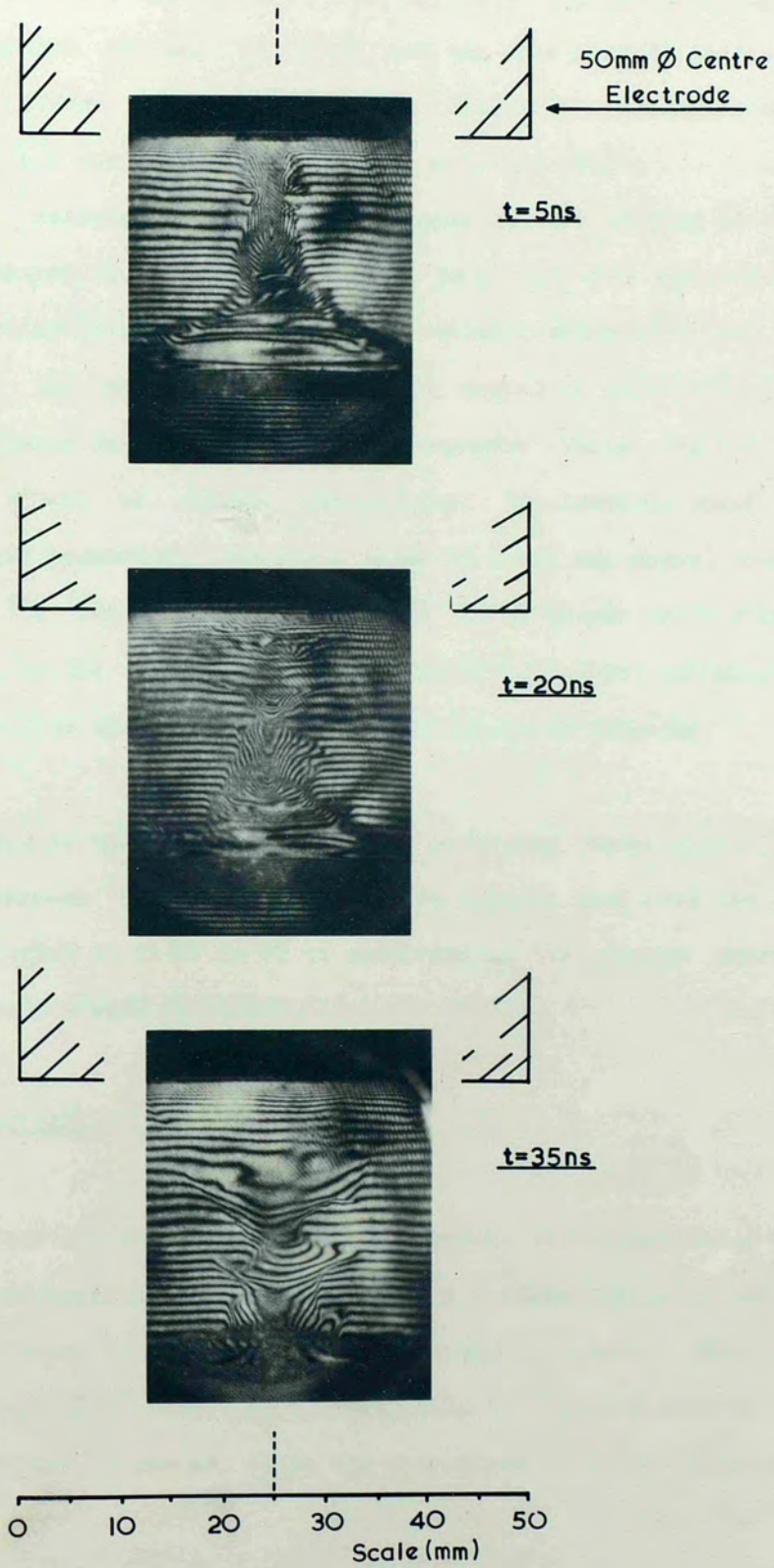

Figure 4.12
Reconstructed holographic interferograms for times t=+5 ns, t=+20 ns and t=+35 ns.

the plasma is still symmetric. At t=0 ns, peak compression occurs over an axial length of z=0 to 10 mm and the fringe shift distribution across the plasma image indicates a relatively uniform density gradient. This completes the end of the collapse phase.
At t=+5 ns (dense-pinch phase), the plasma appears similar to that at peak compression and the instabilities have not yet destroyed the pinch. By time t=+20 ns, the plasma has clearly expanded in the region adjacent to the centre electrode. It should be noted that in this shot, the plasma has divided into two separate dense regions as a result of a m=0 or sausage instability. The break-up phase of the pinch has now commenced. The final frame at t=+35 ns, shows that the plasma in the centre electrode region is no longer observable. An upper limit to the electron density of $3x10^{-22}m^{-3}$ was estimated for this region from the known sensitivity of the interferometer.

It should be noted that during these post peak compression frames that the densest pinch region has moved axially away from the centre electrode, until at t=+35 ns it is occurring in the region where the return current sheath is formed.

4.5.3.4 ANALYSIS OF THE INTERFEROGRAMS

During the collapse and dense-pinch phases, the Plasma Focus is to a good approximation, azimuthally symmetric. This therefore enables a cylindrical model to be employed to analyse the data. The fringe shift, F resulting from light propagating through a plasma of radius R_{pv} at an impact parameter, h, in the r-θ plane is given by Veron [52] as,

$$F(h) = \frac{1}{\lambda_o n_c} \int_h^{R_{pv}} n_e(r)\, r (r^2 - h^2)^{-\frac{1}{2}} dr \qquad (4.1)$$

where λ_o is the probe beam wavelength and n_c is the critical electron density for that wavelength. Using eq 2.7, the critical density for a ruby laser (λ_o=694.3 nm) is 2.3×10^{27} m^{-3}. Equation 4.1 is a form of Abel's integral equation. The solution for the electron density profile is given by,

$$n_e(r) = -\frac{2\lambda_o n_c}{\pi} \int_h^{R_{pv}} \left\{\frac{dF(h)}{dh}\right\} (h^2 - r^2)^{-\frac{1}{2}} dh \qquad (4.2)$$

We see that the integral depends on the gradient of the fringe shift profile with impact parameter. As the observed fringe shift profiles did not in general correspond to known analytic solutions, it was necessary to determine the Abel inverse integral numerically. This is conveniently achieved using the method of Bockasten [53] which assumes cylindrical symmetry.

The type 55 negatives were examined by projecting them with an enlarger to gain a magnification of approximately 12 over the real plasma dimensions. The radial fringe shift profile was detemined as follows:

(1) A line was drawn between the vacuum fringes on either side of the plasma image at the z postion of interest.

(2) The distances between the z-axis and the intersections of the fringes with this line were measured, yielding the radial postions of integer fringe shift.

(3) The axial finge shift was estimated using linear interpolation.

(4) A continuous curve was then fitted numerically through the raw data using a N-1 cubic spline fit computer library subroutine, where N was

the number of data points. Typically 10-15 data points were used. This permitted a sequence of fringe shift values F_k, for equidistant impact parameters, $h = kR_{pv}/n$ $(k=0,1,2,....,n-1)$ to be be calculated, were n is an integer. The F_k values were then used to calculate n values of the radial electron density profile, $n_e(r_j)$ at the radial positions $r = jR_{pv}/n$ $(j=0,1,2,....,n-1)$ using the Abel inversion equation of Bockasten [53],

$$n_e(r_j) = \frac{2\lambda_o n_c}{R_{pv}} \sum_k \alpha_{jk} F_k \qquad (4.3)$$

where the coefficients α_{jk} are tabulated by Bockasten for n values of 10, 20 and 40. The coefficients for n=20 were used to analyse the data presented here and provided reasonable accuracy over the range of radial profile distributions.

Three typical fringe shift profiles for times t=-25 ns, 0 ns and +10 ns are shown in figure 4.13 and a sequence of Abel inverted electron density distributions during the collapse phase from times t=-44 ns to t=-7.5 ns are shown in figure 4.14. These are representative for axial positions in the range z=5 to 10 mm. During the earlier times the pinching sheath is well defined. At t=-44 ns, the axial density of 8×10^{22} m^{-3} is 60% of the density for a completely ionised deuterium gas at the 1.8 torr filling pressure used. The axial density increases to 1.3×10^{23}, corresponding to the filling density approximately 6 ns later. From $t \gtrsim -10$ ns the distribution maximises on axis and grows rapidly until peak compression is reached. Figure 4.15 shows a similar sequence of Abel inverted density profiles from peak compression, t=0 ns until t=+20 ns, again for the z range 5 to 10 mm. At peak compression the plasma radius is 2.35 mm with an axial density of 4.2×10^{25}, equivalent to 300 times the filling density.

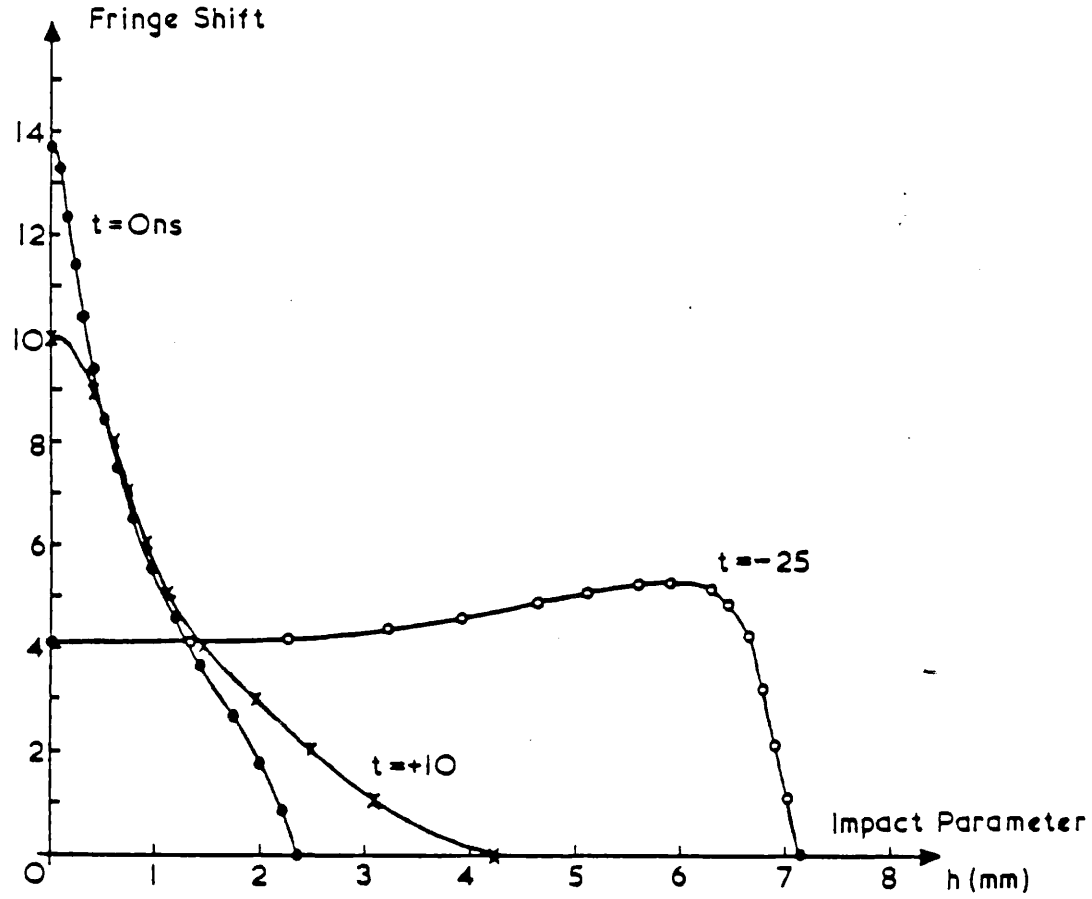

Figure 4.13
Radial fringe shift distribution for times t=-25 ns, t=0 ns and t=+10 ns.

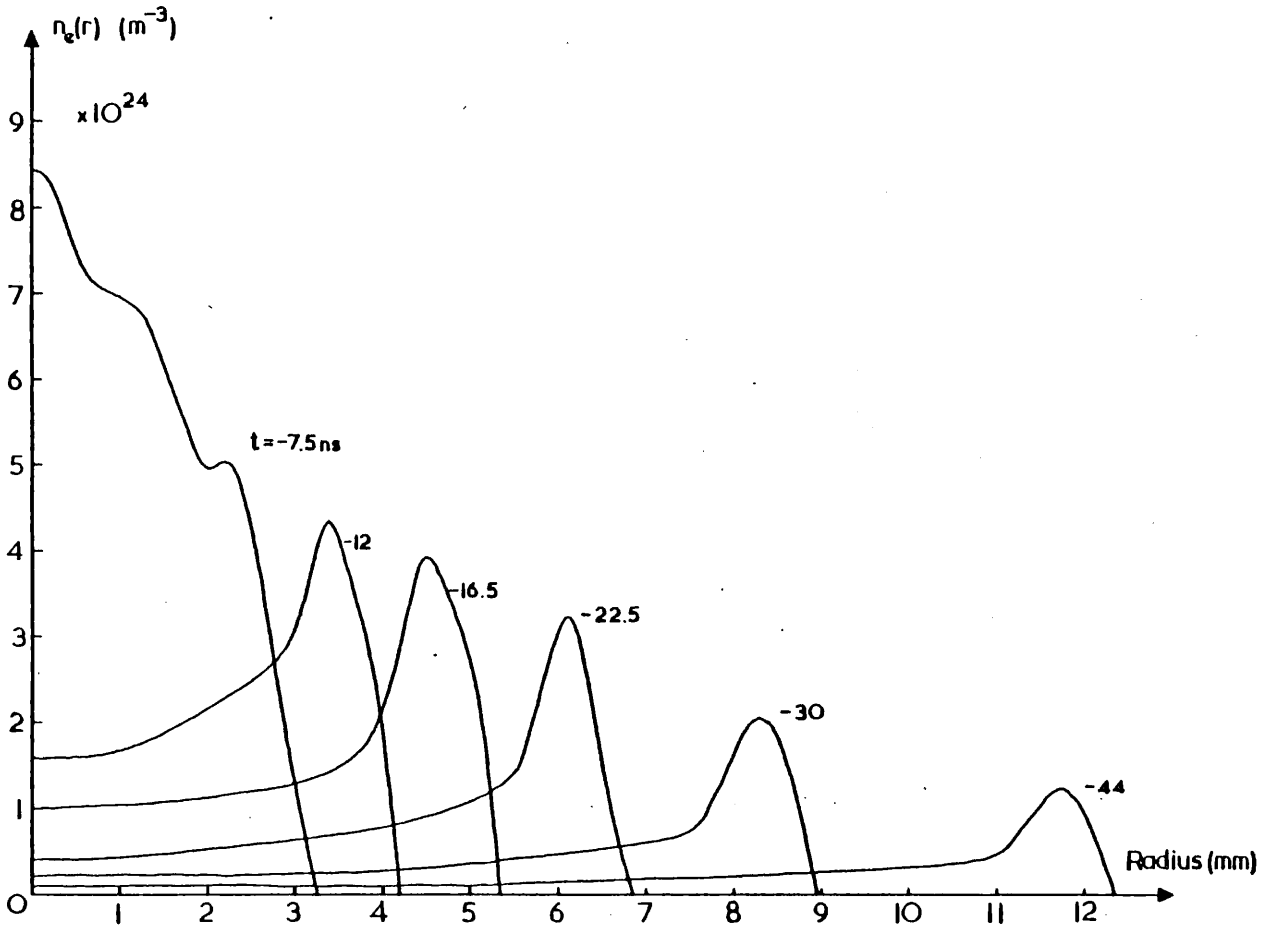

Figure 4.14
Abel inverted electron density distributions for times t=-44 ns to t=-7.5 ns.

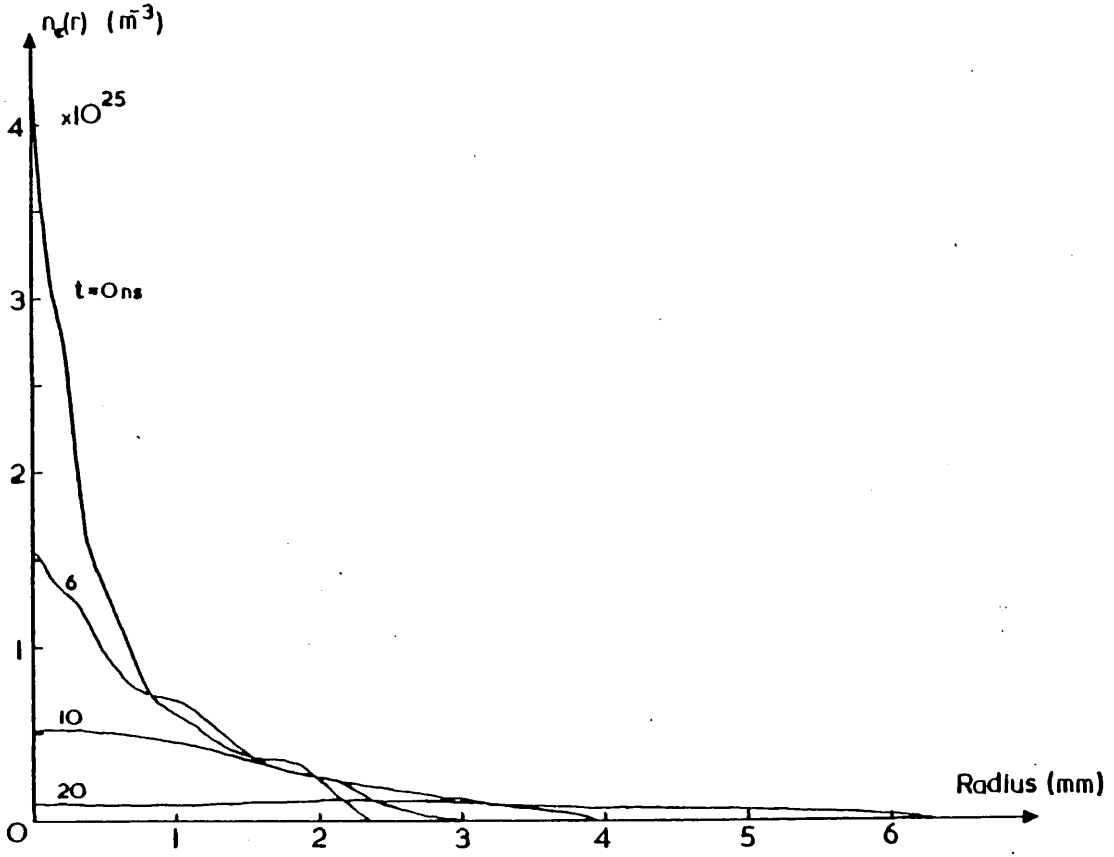

Figure 4.15
Abel inverted electron density distributions for times t=0 ns to t=+20 ns.

By t=+10 ns, the axial density has decreased to 5.2×10^{24}.

During the time period investigated, the plasma column was perturbed by Raleigh-Taylor instabilities, which resulted in not every holgram being analysed at the desired z position. Therefore several profiles from adjacent z postions were utilised. This proved a valid analysis approximation as no significant axial dependence was observable for $z \leq 10$ mm.

The data from figures 4.14 and 4.15 was amalgamated to generate an isometric plot of the temporal behaviour of the radial electron density distribution which is shown in figure 4.16 for t=-44 ns to + 26 ns. Linear interpolation was used to generate data for times between the known density profiles. The data base used to generate the plot was used in the analysis of the scattering data which will be described in chapter 7.

Assessment of Errors

A detailed evaluation of the errors incurred in performing interferometry on the Plasma Focus is given by Morgan [11] who used a Mach-Zehnder interferometer. Only good quality holograms were used for the analysis that has been discussed. Those exhibiting poor fringe structure and fringe splitting due to poor laser spatial coherence were not utilised. The errors in measurements and their assessment can be summarised as follows:

(1) Using the real space magnification of 12 for the analysis of the holograms, the error in determining the fringe shift position was $\sim$ 1 mm, or 0.1 mm for the plasma dimensions. A background fringe

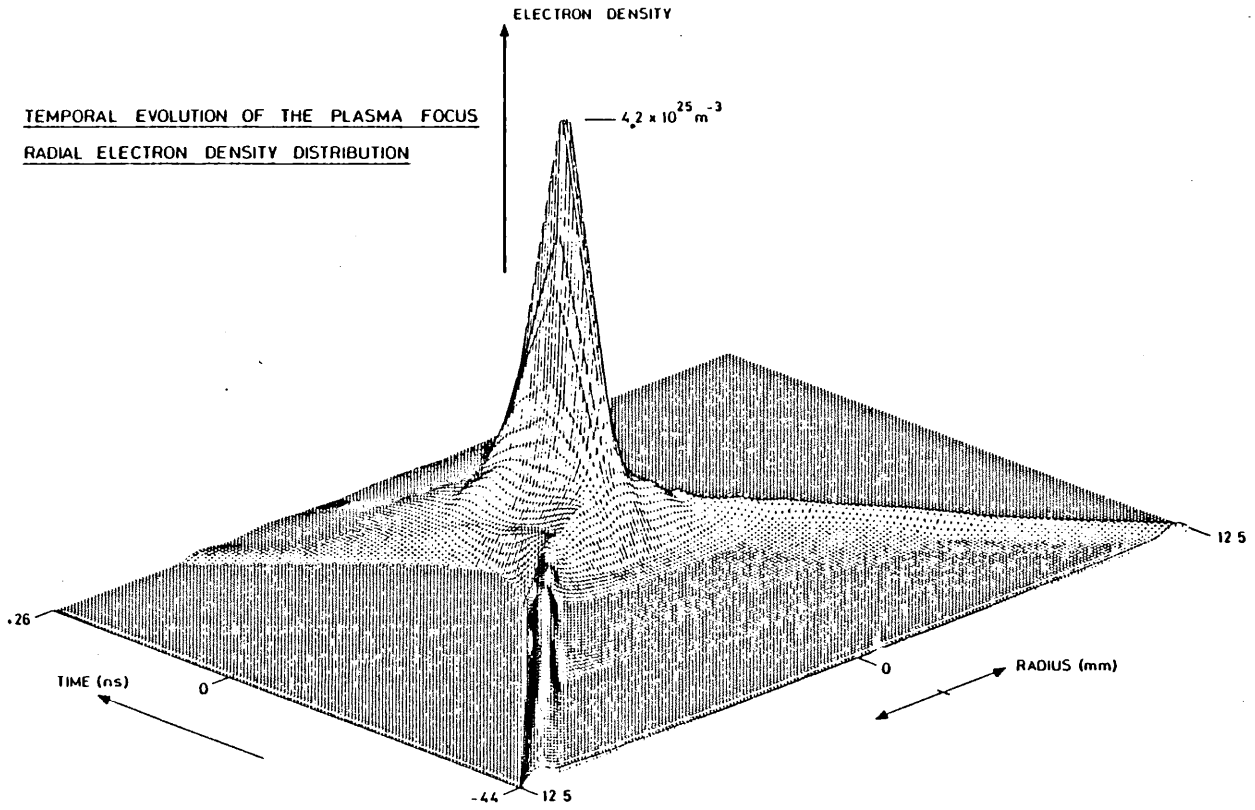

Figure 4.16
Isometric plot of temporal behaviour of electron density distribution for time region t=-44 ns to t=+26 ns.

spacing of 1-1.5 mm was employed, so the fringe shift error, δF was 0.1.

(2) An error arises in the measurement of the plasma-vacuum boundary radius, R_{pv} due to the difficulty in determining the exact position of fringe shift commencement. This error, δR_{pv}, was typically 0.25 mm, or a 10% relative error in the measurement of the plasma radius at peak compression. The error will be reduced for earlier and later plasma times.

(3) During the time period investigated, the plasma column diameter was a lot less than the return current sheath diameter of $\sim$ 90 mm. Therefore, any fringe shift due to the return current sheath will be approximately constant over the range of plasma impact parameters and vacuum region surrounding the plasma. The effect of the return sheath will therefore be unobservable, resulting in negligible errors.

(4) The large diameter lens, L3 (figure 4.9) was used to correct for plasma refraction of the scene beam. However, an error occurs in the phase shift due to the actual path through the plasma rather than the apparent. This is estimated by Morgan [11] as,

$$\delta F = \frac{R_{pv}^{3} \lambda_o^{3}}{6} \left(\frac{e^2}{8\pi^2 \varepsilon_o c^2 m_e} \frac{\partial n_e}{\partial r} \right) \qquad (4.4)$$

With an axial density at peak compression of 4.2×10^{25} m^{-3} and a plasma radius of 2.35 mm, $\partial n_e / \partial r \simeq 1.79 \times 10^{28}$ m^{-2}, giving a fringe shift error, $\delta F \sim 0.05$.

(5) The reference fringes should be parallel, but due to the generally

poor spatial coherence of ruby lasers, deviations of the fringes occur across the field of view. The fringe shift error due to this was estimated by drawing parallel lines across several typical holograms, from which the vacuum reference fringe deviation was measured as approximately 0.1 mm, giving a fringe shift error, $\delta F \sim 0.1$.

(6) The accuracy of the Bockasten Abel inversion technique [53] has been estimated by Muir [25] by using analytic expressions for the fringe shift profile which had known analytic solutions of Abel's integral equation (eq 4.2). The error was estimated as $\sim$ 1% on or near the axis, rising to 5% at the plasma edge.

Compounding the fringe shift errors from (1), (4) and (5) we obtain a value for $\delta F = 0.15$.

Using the compounded fringe shift error and the relative error in the radius, the relative error in the electron density at any radius can be estimated. From eq 4.3, the relative error in the Abel inverted electron density at a radius, r_j is given by,

$$\delta n_e(r_j) = \left\{ \left[\frac{\partial n_e}{\partial R_{pv}} \delta R_{pv} \right]^2 + \sum_k \left[\frac{\partial n_e}{\partial F_k} \delta F_k \right]^2 \right\}^{\frac{1}{2}} \qquad (4.5)$$

where δF_k is the error in the fringe shift at an impact parameter h_k. The relative error in the density at a radius r_j is therefore given by,

$$\frac{\delta n_e}{n_{e_{r=r_j}}} = \left\{ \left[\frac{\delta R_{pv}}{R_{pv}} \right]^2 + \frac{\sum_k (\alpha_{jk} \delta F_k)^2}{(\sum_k \alpha_{jk} F_k)^2} \right\}^{\frac{1}{2}} \qquad (4.6)$$

As the fringe shift error has been estimated as constant over impact parameter, then eq 4.6 reduces to the form,

$$\frac{\delta n_e}{n_{e_{r=r_j}}} = \left\{ \left[\frac{\delta R_{pv}}{R_{pv}} \right]^2 + \frac{4\lambda_o^2 n_c^2 \delta F^2}{R_{pv}^2 n_e^2(r_j)} \sum_k \alpha_{jk}^2 \right\}^{\frac{1}{2}} \qquad (4.7)$$

The relative error in n_e is therefore a combination of the relative plasma radius error and the relative error due to fringe shift uncertainty. The value of the sum $\sum_k \alpha_{jk}^2$ varies from 370 to 2 for j in the range 0 to 19. Substituting for values of R_{pv}, δR_{pv}, n_e and n_c at peak compression with $\delta F=0.15$, the relative electron density error is 14% on axis and 35% at the plasma edge. For other plasma times, the error follows this general pattern, with a 10-15% central error rising to 30-40% at the plasma edge.

4.5.3.5 THE PLASMA RADIAL AND AXIAL VELOCITY

In chapter 3 it was demonstrated that significant modification to the scattered light profile could result from a radial velocity component aligned with the differential scattering vector, $\underline{k}$. Therefore, the temporal evolution of the plasma-vacuum boundary radius, R_{pv} was additionally determined from the holographic interferograms, for use in the scattering data analysis. The utilisation of this data will be described in chapter 7.

Figure 4.17 shows a plot of plasma radius as a function of time at z=10 mm, at which the scattering volumes were located. It can be seen that the radius decreases linearly with a velocity of 2.68×10^5 m.s^{-1}, until at approximately t=-15 ns the radius deaccelerates until the velocity is zero at peak compression, t=0 ns, when the plasma has a radius of 2.35 mm. The error in measuring the plasma radius from a single hologram has already been discussed in the previous section. It is at a maximum at peak compresion when the relative error is $\sim$10%.

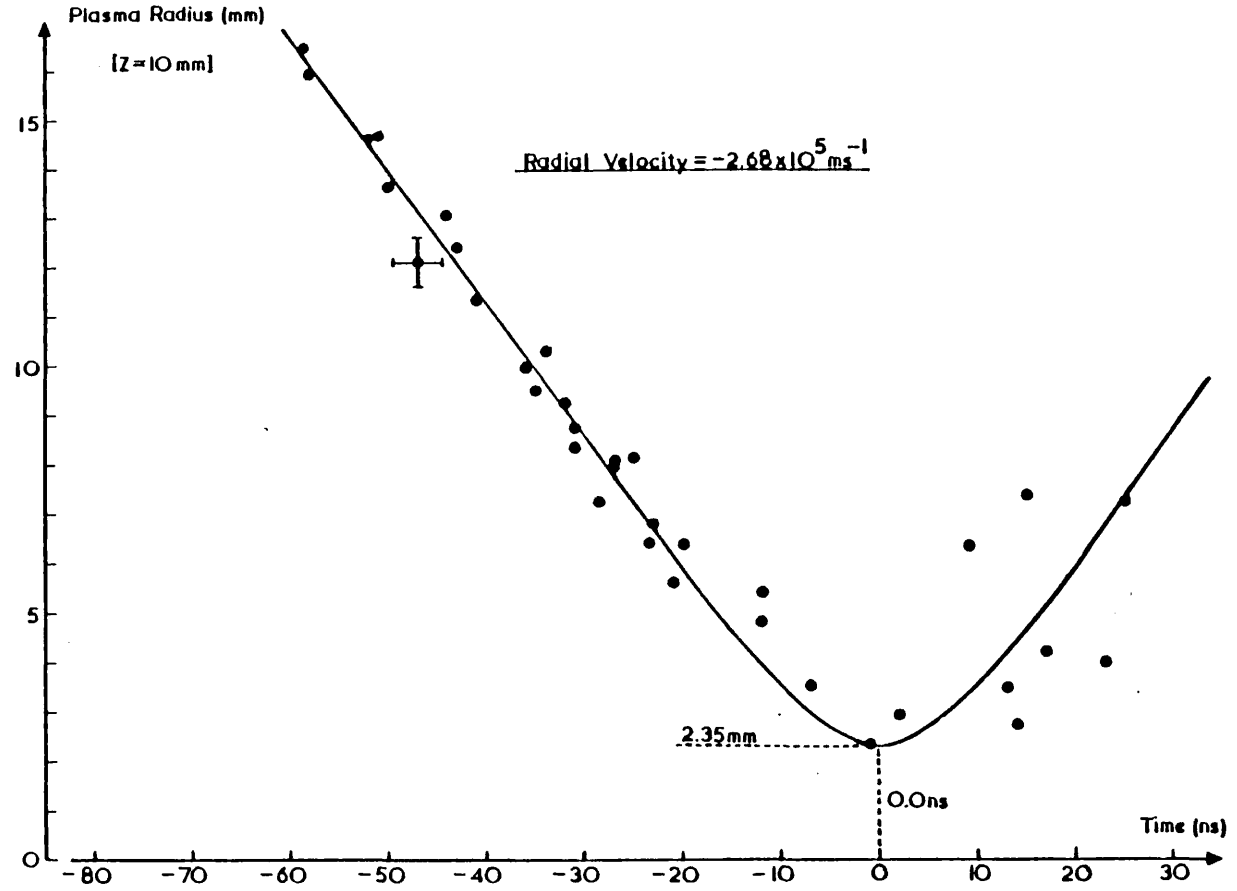

Figure 4.17
Plasma-vacuum boundary radius as a function of time at z=10 mm.

The curve fitting the data points of figure 4.17 is hyperbolic and has the form,

$$R_{pv}(t) = r_1'\left[1 + \frac{1}{r_2'^2}(t-t_o)^2\right]^{\frac{1}{2}} + r_3' \qquad (4.8)$$

where $r_1'+r_3'$ is the minimum plasma radius at time t_o (for z=10mm, t =0 ns). The ratio r_1'/r_2' is the gradient of the hyperbola's asymptote and is also the velocity of the plasma-vacuum boundary. The value of r_3' is given by the radius at which the asymptote intersects the line $t=t_o$. The gradient was determined by a least-squares fit of a linear curve to the data for $r \geq 6$ mm. For times $t > 0$ ns, following peak compression, the fit is poorer, due to the development of instabilities.

Figure 4.18 shows the z=10 mm plasma radius as a function of time curve with those determined additionally for z=5, 7.5, 12.5 and 15 mm. It should be noted that for z>10 mm the minimum radius is reached at times after t=0 ns, the time and minimum radius increasing with z. Correspondingly the level of compression decreases as z increases. This may well be due to axial flow of the plasma from z positions closer to the centre electrode, as observed in the scattering experiments of Bernard et al [19]. These measurements discussed previously in chapter 3, indicated an axial flow velocity $\sim 10^5$ m.s^{-1}.

The axial velocity of the plasma column, which should not be confused with the axial flow velocity, was determined from measurement of the distance between the centre electrode shadow in the holographic interferograms and the z position where the vacuum fringe shift pattern

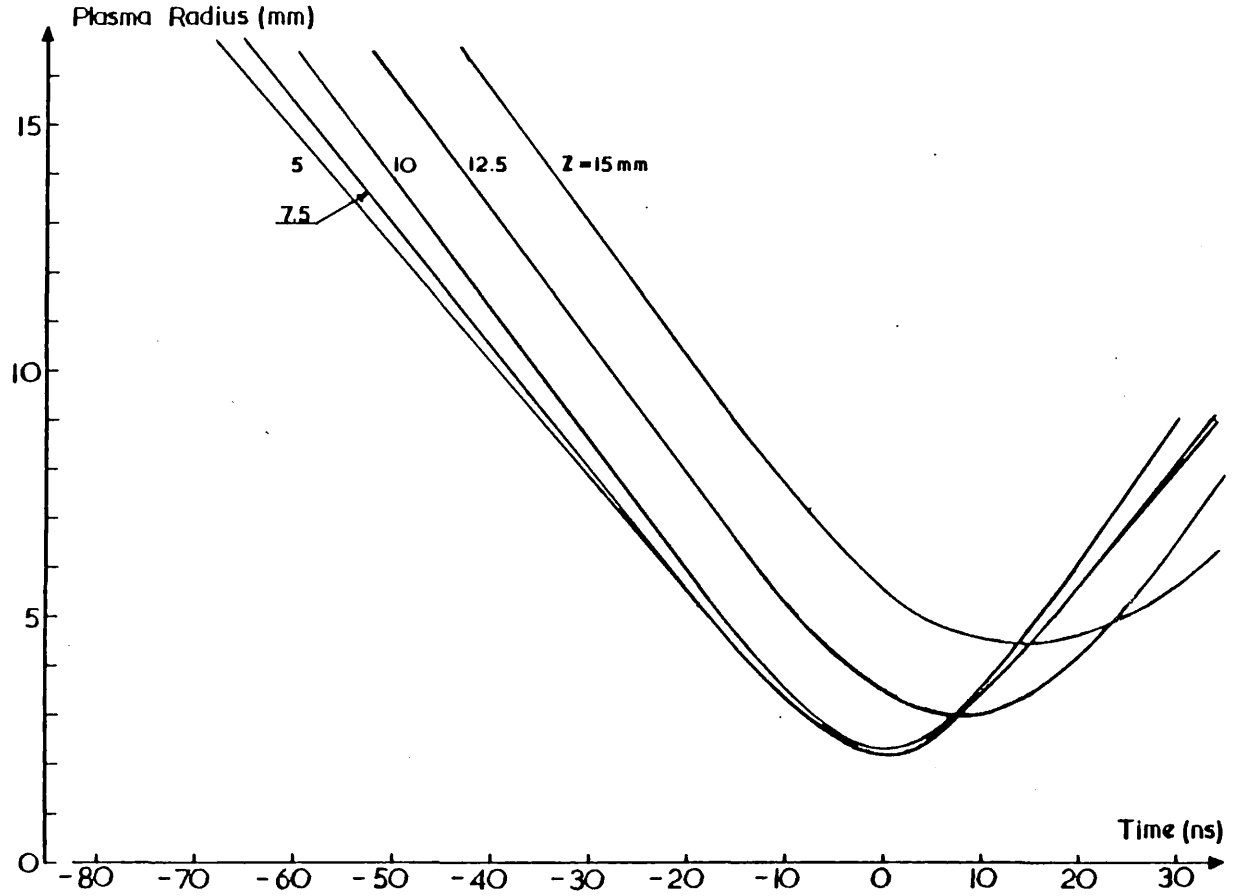

Figure 4.18
Plasma-vacuum boundary radius as a function of time
at z=5, 7.5, 10, 12.5 and 15 mm.

first appeared perturbed. At t=0 ns, the plasma has an axial length of ~22.5 mm. The temporal evolution of this dimension yielded values for the axial velocity. For times during the collapse phase before t=-25 ns, the velocity was constant at 1.57×10^5 m.s^{-1} in the z-axis direction. Following this time it decreased to 7.5×10^4 m.s^{-1} by t=+10 ns and then remained constant. The error in measuring the axial length of the plasma column was 0.75 mm. This corresponds to a relative error of 3% for z=22.5 mm.

4.5.4 FARADAY ROTATION POLARIMETER

The technique employed to measure the magnetic field structure of the Plasma Focus is detailed fully by Muir [25]. The optical system employed a polarimeter to measure the Faraday rotation of a plane polarised ruby laser probe by the Plasma Focus. The polarimeter was based on the differential half-shade method [54], and operated with a 2 degree half-shade angle giving a senstivity of 0.4 mrad. At the laser wavelength, 694.3 nm, the rotation by the plasma was typically 7 mrad. Measurements along a single viewing chord of diameter 250 μm, were taken during the 40 ns FWHM laser pulse with a time resolution of 2.5 ns. The full spatial and temporal details of the Faraday rotation were built up on a shot to shot basis at several viewing chord positions. Abel inversion of the rotation data, together with the electron density profiles obtained by the holographic interferometry, gave the temporal evolution of the azimuthal magnetic field profiles. The radial current density profiles were then obtained by applying Amperes' law.

CHAPTER 5 SCATTERING DETECTION SYSTEM

5.1 INTRODUCTION

In this chapter the experimental arrangement of the dispersive instrument and detection system used to analyse the scattered light will be described. In order to appreciate the advantages of the system used to perform the experiments described here, an outline will be given first of previously used scattering detection system arrangements. Following this, a description of the Optical Multi-channel Analyser (OMA) will be given, and its integration with the Plasma Focus scattering experiment will be discussed. A description of the techniques employed to calibrate the various parameters of the complete scattering optical and detection system will be given in chapter 6.

Previous scattering systems, using lasers with visible wavelength outputs, have primarily used photomultipliers as the basis of a detection system. Depending on the wavelength resolution required, they have been used in conjunction with Fabry-Perot etalons or grating spectrometers. A scattered spectrum has been measured using a single photomultiplier and Fabry-Perot etalon, by scanning in wavelength over several plasma discharges [3,34,55]. Several techniques have been employed to obtain a single shot scattered spectrum. The main one, particularly to obtain electron temperature and density measurements on toroidal plasma systems, has been to use a grating spectrometer with the output coupled by a fibre optic array to a bank of photo-

multipliers [1,56]. For higher resolution work a Fabry-Perot can be utilised as a multichannel device by coupling it to a Fafnir multimirror system [41] with a bank of photomultipliers to analyse the selected wavelength intervals [19,57].

Two problems make the acquisition of a scattered spectrum from a fast pinch plasma such as the Plasma Focus over a number of shots undesirable. The shot to shot jitter, in relative timing of the plasma and laser, would result in a change of parameters during the measurement of the spectrum. Secondly, any plasma turbulence or non reproducible feature would be smoothed over by averaging, making the spectral shape difficult to interpret. It was therefore felt essential that a multichannel single shot detection system was employed. These considerations as will be seen later from the results described in chapter 7 proved justified. A grating spectrometer or a Fabry--Perot / Fafnir multimirror combination coupled to a bank of photomultipliers, is one solution which has been used extensively, as detailed above. This arrangement however has the requirements of having to monitor and calibrate each channel separately, although a data acquisition system employing analogue to digital converters (ADCs) increases the operational ease of such a system. The experimental limitations of the above multichannel techniques, have resulted in the number of wavelength channel intervals sampled, being restricted to $\sim$ 6 - 10. In the review of previous Plasma Focus scattering experiments in chapter 3, it was concluded that a far greater number of channels was required than this.

Recently much research and development work into multichannel detection devices has been undertaken. These devices can be divided into three main groups; diode arrays, charge coupled diode arrays and

electron beam scanned silicon (Vidicon) optical multichannel devices. An excellent review of commercially available devices has been undertaken [46]. At the time of commencement of the scattering experimental work, intensified Vidicon devices were the only systems providing sufficiently good detector signal to noise ratios for the detection of low light level intensities. Recent developments in intensified diode arrays would now enable these to be used as an alternative detector system, though the basic dispersive instrument--detector system would be similar to that used with an intensified Vidicon device. Several papers [5,58,59], have reported the successful use of Vidicon OMAs for scattering detection systems, but for different experiments to those described here.

The detection system employed was based on the Princeton Applied Research Corporation 1200 series Vidicon OMA system. This provides a 1-D array of 500 channels, each 25 microns wide and 2.5 mm high. If employed in conjunction with a f/10 grating spectrometer of 1 metre focal length and a 1200 lines/mm grating, the spectrometer first order inverse linear dispersion of approximately 0.8 nm/mm, results in an inverse linear dispersion for the combined system of 0.02 nm/channel and a 'wavelength window' of 10 nm.

5.2 THE OMA SYSTEM

The 1200 series OMA consists of three main components which are illustrated in figure 5.1 coupled to a grating spectrometer: (1)Detector Head, (2)1205A Control Console, (3)1211 High Voltage Pulse Generator used to gate the intensified detector head. In addition,

interfaces are provided for various output peripherals.

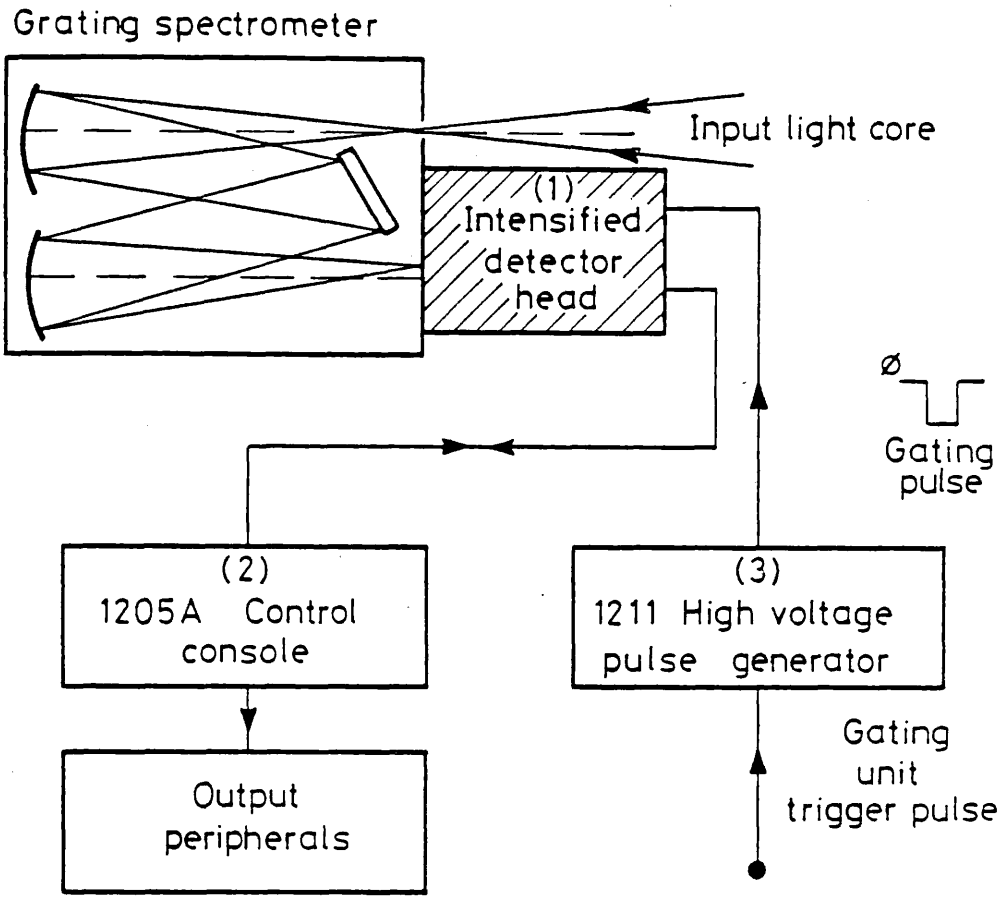

Figure 5.1
Optical Multichannel Analyser (OMA) System Layout
coupled to a Grating Spectrometer.

5.2.1 DETECTOR HEAD

The 1200 series detectors used with the OMA have several common features. They all have 500 detection channels which are active simultaneously, and are read one at a time by a scanning electron beam. All the detectors are storage devices and light falling on them is integrated until read by the electron beam. Lastly, the detectors have a linear light intensity response over their dynamic range.

A model 1205I detector head, which is illustrated in figure 5.2, was used for the experiments presented in this thesis. This detector head can be gated, which has the advantage of permitting the suppression of integrated background light from the plasma (bremsstrahlung emission). The detector head consists of an intensified silicon intensified target (ISIT) camera tube, deflection components, high-voltage power supply and preamplifier.

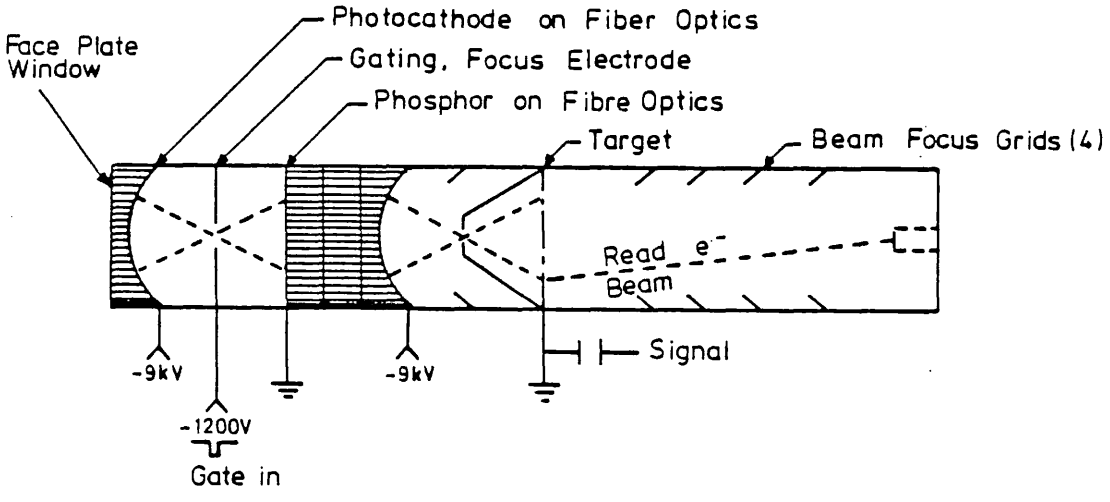

Figure 5.2
Diagramatic of Model 1205I Intensified Detector Head (ISIT).

Photons falling on the faceplate window of the detector are projected through a fibre optic coupling array to the photocathode (S-20) and converted into photoelectrons. An electrostatic lens (which is gateable) accelerates these photoelectrons and focusses them onto a second fibre optic array. This has a phosphor coating on the input side to convert the photoelectrons back to photons, followed by a further photocathode on the output side. A second electrostatic lens then accelerates and focusses the photoelectrons onto a silicon target. This consists of a thin silicon wafer upon which a tightly spaced matrix of p-n junction diodes is formed. The target area has dimensions of 12.5 mm x 5.0 mm. Each diode is 8 microns in diameter

and is separated by 25 microns (centre to centre) from its neighbours. The accelerated photoelectrons produce multiple dissociations of electron-hole pairs in the diodes on which they fall. The holes are collected on the p-side of the discharged diodes, which are recharged to the electron gun cathode potential by a scanning electron beam. The necessary current for this is measured, amplified and forms the video signal which is analysed by the 1205A Control Console. The use of a two-stage intensifier section ahead of the target section permits an improvement in sensitivity without increasing dark current or preamplifier noise compared with an unintensified head. The intensifier sections of the 1205I also provide a convenient gain control capability through changes in photocathode (accelerating) voltage. A range of 2 - 9 kV provides electron gains ranging from 1 to 1500 for each intensifier [60]. The maximum available gain was utilised for the scattering experiments.

The front intensifier can be gated by controlling the voltage between the photocathode and the intensifier focus electrode. It is gated off by switching the photocathode to a more positive voltage on the high--voltage potential-divider chain, and can be gated on by means of a negative going high-voltage pulse of 12% of the full accelerating voltage.

The faceplate image format of the 1205I detector head is illustrated in figure 5.3. This is divided into two identical sections. The top section being the 'signal' half and the lower the 'dark' half which is subtracted from the 'signal' half to eliminate dark current and preamplifier noise.

Figure 5.4 shows the manufacturer's spectral response curve for the 1205I detector head. It can be seen that at a wavelength of 700 nm, where the detector was employed, the quantum efficiency, Q $\sim$ 7%.

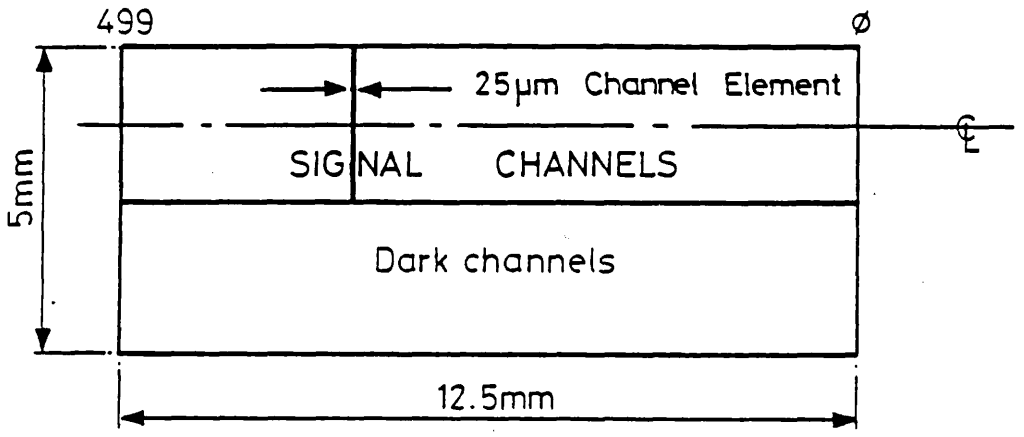

Figure 5.3
Faceplate image format of 1205I detector head.

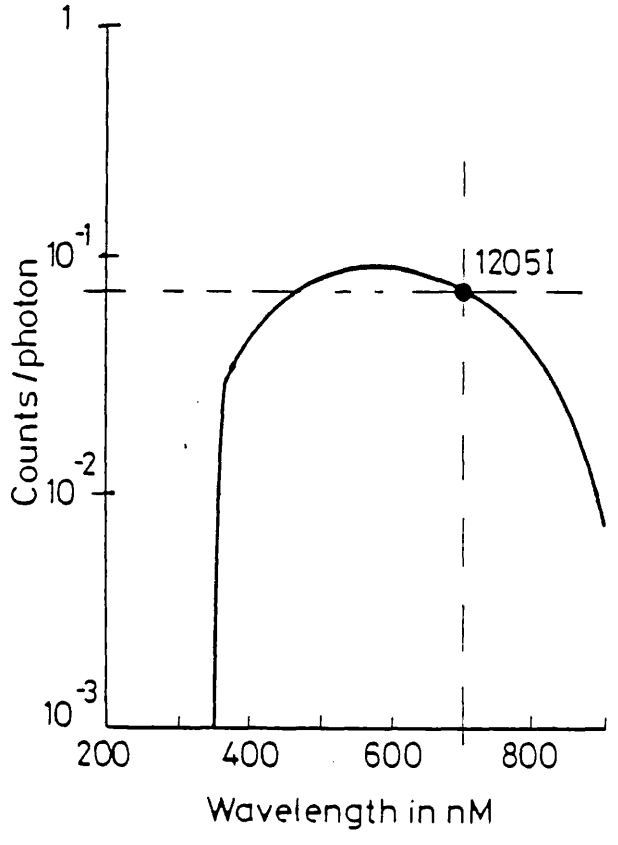

Figure 5.4
Manufacturer's spectral response curve for 1205I detector head.

5.2.2 THE 1205A CONTROL CONSOLE

The Control Console has several functions. It provides the control voltages for the detector head scanning electronics, synchronised with an internal clock. Secondly, it contains the circuitry to digitize the video signal from the detector by means of an analogue to digital converter (ADC). Once in digital form the data may be directed to either of two 512 word, 21-bit memories. These memories may be used to accumulate either a single or a number of 32.8 ms frames from the detector.

Once the data is stored, each channel may be read digitally on the front panel or may be directed to an output peripheral (printer or high speed paper tape punch). A high speed analogue output is used to drive a 7904 Tektronix scope to provide a continuous X-Y display.

5.2.3 THE 1211 HIGH VOLTAGE PULSE GENERATOR

The intensified detector head was gated by a 1211 High Voltage Pulse Generator which produces a negative going high-voltage pulse. The amplitude of the output pulse is variable in the range -500 V to -1500 V to facilitate focussing of the detector head according to the applied photocathode accelerating voltage. The pulse width is adjustable between 40 ns and 999 us with rise and fall times of less than 40 ns (10%/90%) [61] and pulse jitter is typically less than 5 ns. The unit also provides a monitor output pulse of 1 V/kV into 50 ohms which enables the gating unit to be synchronised with the scattering laser pulse.

5.3 OPERATIONAL ASPECTS OF THE OMA SYSTEM

The 1205A Control Console incorporates a timing system to which all the OMA system is synchronised, with the exception of the High Voltage Pulse Generator. The 1205A timing system consists of an internal crystal oscillator providing a 16 MHz clock rate followed by a binary scaler providing additional 8, 4, 2 and 1 MHz clock pulses. Further scalers provide other clock pulse rates as required by the internal electronics.

The machine cycle is divided into two major times; an active time when the Vidicon scanning beam is normally raster sweeping the 500 channels and a blanking time during which the beam is blanked and retraced. The machine cycle may be broken into 512 line times each of 64 μs. The active time takes 500 line times; the blanking time takes 12. The line time is broken into smaller time segments to control various parts of the 1205A. Therefore a machine cycle is the time between successive readouts of the same channel element on the Vidicon (equal to 512 x 64 μs=32.768 ms).
An accumulation cycle consists of an integral number of machine cycles, and may include delay cycles in which the Vidicon beam is blanked for the full 512 line times and accumulation to memory is inhibited.

The Vidicon line scan is driven by an analogue circuit. It accepts a digital timing signal from the timing circuitry and generates a square wave illustrated in figure 5.5a to drive the line-scan coil of the detector head. This square wave voltage output produces a triangular current waveform in the inductive line-scan coil. Similarly the Vidicon frame scan is driven by another circuit which generates a

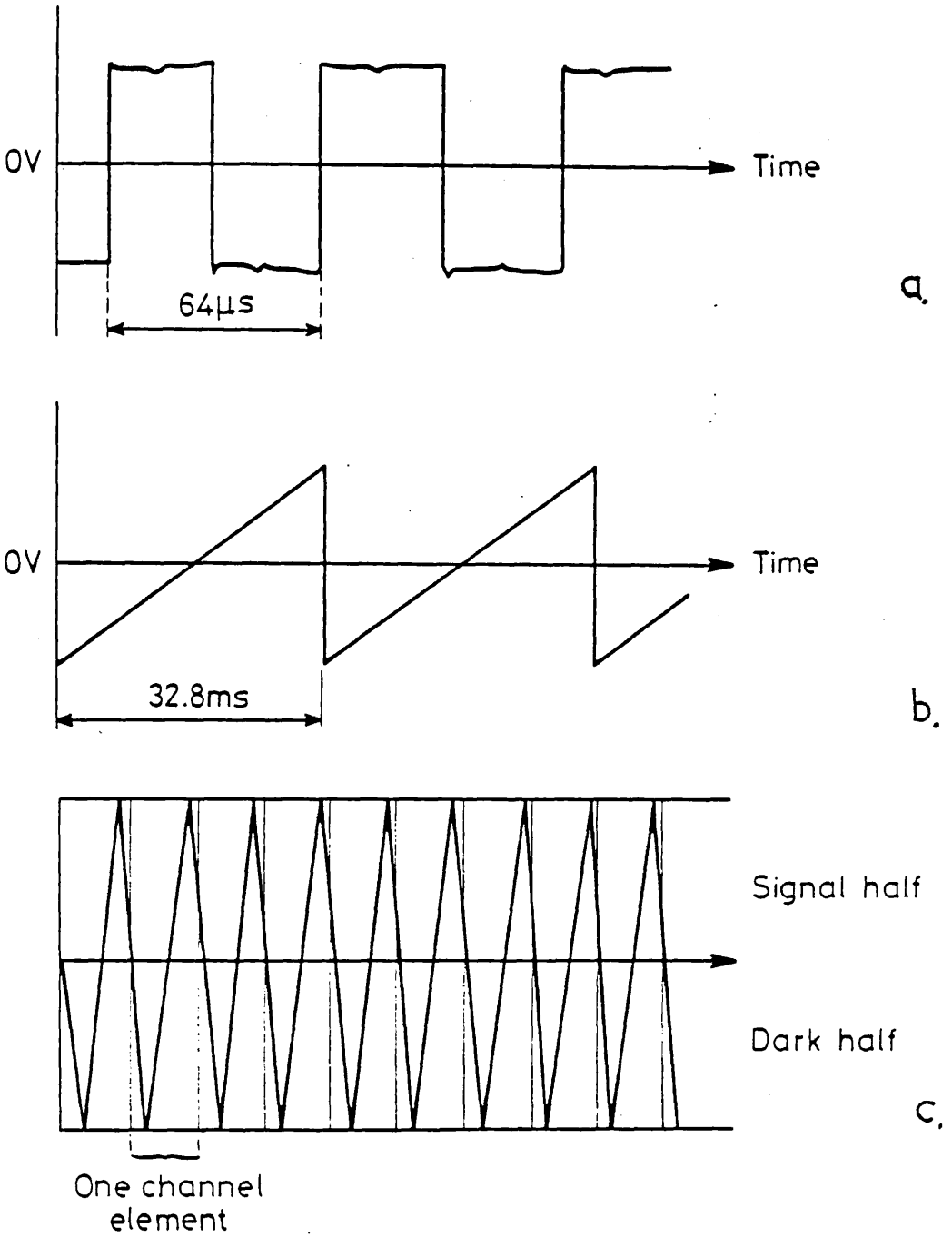

Figure 5.5
(a) Vidicon line scan waveform (b) Frame scan waveform
(c) Raster scan pattern of silicon target.

sawtooth wave for the frame-scan coil. This sawtooth waveform is generated by allowing a capacitor to linearly charge. A digital signal from the timing circuitry results in the clamping of this capacitor to zero to produce a sawtooth waveform of period 32.8 ms as shown in figure 5.5b. The combination of these two electron beam steering circuits produces a raster scan of the silicon target as illustrated in figure 5.5c.

The input operation of the video signal from the detector head may be divided into two major functions; analogue subtraction and analogue to digital (A-D) conversion. During each 64 μs interval, the output from one channel element is undergoing A-D conversion while the signal from the next channel is being scanned at the Vidicon target and processed by the scan-beam chopping circuitry. The analogue subtraction circuitry is controlled by a digital line from the clock timing circuitry. The 'dark' half of each detector channel element (scan line) is scanned during the first 32 μs of the cycle. During this period the digital line is 'low', and a positive signal from the detector preamplifier causes the output of the integrator of the A-D converter to go negative. During the next 32 μs period when the 'signal' half of the target is scanned, the digital line is 'high', and a positive signal from the preamplifier causes the integrator output to go positive. D.C. signals such as dark current and preamplifier offset approximately cancel over the full 64 μs cycle, so the integrator output at the end of the 64 μs cycle represents the net light read off the 'signal' half of the detector element.

At the end of the line cycle the analogue subtraction output appears as a stable voltage on a sample hold capacitor. During the next 64 μs line-scan period, this previous line-scan output is A-D converted and

stored in one of the 21 one-bit by 512 MOS dynamic shift registers.

The overall operation of the OMA can be divided into two distinct modes; Real Time Mode and Accumulation Mode.
In Real Time Mode the memory is effectively updated after every complete scan of the Vidicon and at any time contains the level of the signal present at each channel during the last scan.
In Accumulation Mode the Vidicon is constantly scanned (and effectively erased) without the signal being stored in memory until the accumulation is initialised. Then the signal from the scanned Vidicon is additively stored in memory for a preset number of cycles (including delay cycles if required). Figure 5.6 diagramatically illustrates this with the preset number of cycles equal to three.

In normal operation the maximum input signal is limited by the A-D conversion range. The usable signal maximum is also effected by the fact that the arithmetic cycle (during which the data is transfered from either memory to the output registers) occupies part of the 64 μs conversion time. Depending on the mode of operation, the internal electronic arrangement [60] limits the maximum input signal to 783 counts per channel per scan in Real Time Mode and 859 counts per channel per scan in Accumulation Mode. The effect of this on the dynamic range of the device when measuring short duration events will be considered in section 5.4.4.

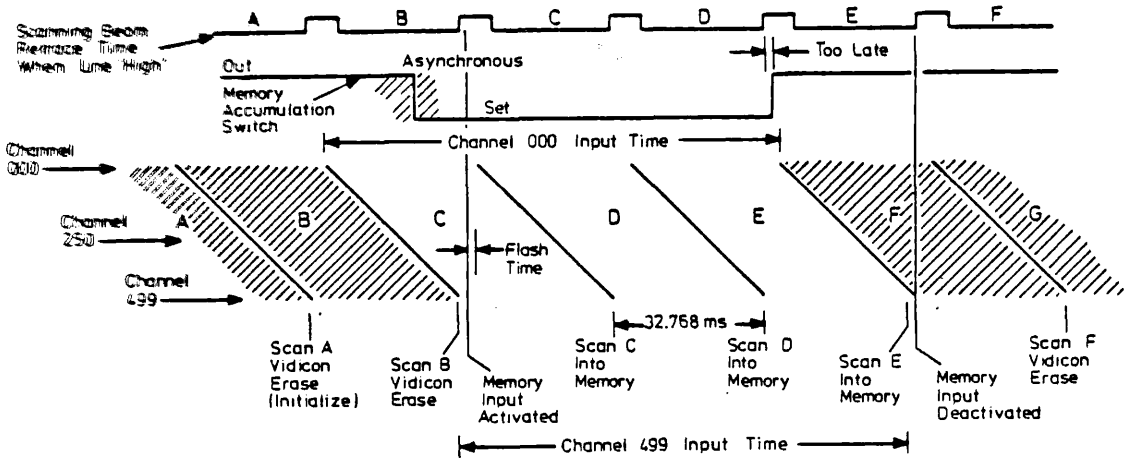

Figure 5.6
Timing diagram of the OMA System in Accumulation mode for three preset scan cycles accumulated into memory.

5.4 INTEGRATION OF THE OMA WITH THE PLASMA FOCUS SCATTERING EXPERIMENT

Having described the basic working of the OMA, the integration of the device with the Plasma Focus scattering experiment will now be considered. For clarity, the system will be described for the case of a single spectrometer input slit, although the the same description applies to the case of the triple input slit assembly used for the multiple-$\underline{k}$ experiment which is described in chapter 6. The layout of the detection system was illustrated in figure 5.1. The output slit of

a Monospek 1000 monochromator was replaced by the OMA intensified detector head mounted on an adjustable adaptor plate which will be decribed in detail later. The dispersed image of the 2.5 mm high input slit was now formed on the signal half of the detector faceplate window, so that each detector channel viewed a different wavelength interval. Using a Q-switched ruby laser pulse with a FWHM of 20 ns as a diagnostic laser will produce a dispersed scattered signal on the OMA faceplate of the same temporal length. On the time scale of an OMA cycle this is short and can be considered as a 'flash' event. Several problems result from using the OMA in this configuration and these will be discussed in the next two sections.

5.4.1 TARGET LAG AND CHANNEL SKEW

Target lag is associated with the ability of the scanning beam to read out the light signal integrated on a target element in a single scan. Although the OMA can detect picosecond light pulses, several scans may be required to completely read the signal from a low intensity 'flash' event. The peak channel of the scattered spectrum will be in the range of 100-800 counts, but low intensity signals need to be considered for the spectrum wing channels. A minimum of approximately 70% of the charge on a channel element is read out per scan for low intensity signals [60]. So after say 5 scans in accumulation mode, >99.5% of the signal on a target element will have been read into memory.

Each channel element integrates light for the entire interval from one scan of that element to the next, and each target element is active for the same amount of time. However, since the channels are scanned sequentially the time interval seen by each channel differs from that of adjacent channels by 64 μs. Thus the measurement interval seen by

channel 0 starts and stops exactly 32 ms before channel 499. This effect is called channel skew and is most apparent if the light signal is turned on and off during the input cycle, resulting in the channels scanned prior to the signal not 'seeing it' during the scan.
A second order effect called skew lag effect is caused by a combination of channel skew and target lag. If for example a 'flash' event of 20 ns duration occurs at the beginning of the 64 μs scan of channel 250, then channels 0-249 will be scanned 1 scan less than channels 250-499 for any preset number of scans.
These problems are minimal for large signals on the Vidicon but can present a problem for the lower intensity wings of a spectrum.

5.4.2 LASER SYNCHRONISATION AND GATING NOISE

The ruby laser was synchronised with the Plasma Focus as described in the timing system section (section 4.4). As the OMA has its own internal clock timing cycle, a technique had to be developed to synchronise the rest of the experimental apparatus with this. Temporally synchronising the ruby laser pulse and high-voltage pulse used to gate the intensified detector heads was not a major problem. The trigger pulse from the same source as the laser 'Q-switching' trigger pulse was used to trigger the 1211 High Voltage Pulse Generator and provided acceptable synchronisation jitter. However, to avoid gate pulse interference in the detector preamplifier and 1205A video processor it is desirable to gate while the Vidicon is not scanning (reading beam blanked). For 'flash' events with a complete time cycle of less than 600 μs the gating can be performed within the Vidicon retrace interval of 768 μs (see figure 5.6). The limit of 600 μs in the 768 μs interval is due to the fact that there is no OMA internal signal conveniently available to mark the exact beginning of

the desired interval.

In the application of the OMA to ruby laser scattering this method is not possible as it takes approximately 1 ms from the triggering of the ruby oscillator flash tube before the cavity can be 'Q-switched' at maximum poulation inversion in the ruby rod.

The solution to the above problems was achieved by modifications to the 1205A Console and additional external electronics.

5.4.3 MODIFICATIONS TO THE OMA SYSTEM

In the previous two sections the problems of target lag, channel skew and the synchronisation of the experimental apparatus with the OMA have been outlined. To overcome these, what is ideally required is a delay cycle as the first input cycle of the memory accumulation, followed by several accumulation scans for optimum readout. With the extra delay cycle one now has 32.768 ms + 600 μs in which to fire the experiment including gating the intensified section of the detector head. This also has the advantage of the Vidicon being unscanned during the complete experimental time cycle ($\sim$ 1 ms) and therefore prevents any electromagnetic interference due to the experiment corrupting the scanned signal.

To facilitate the above timing sequence, modifications were made to the OMA control console and external electronics were constructed in the form of a Remote Program and Trigger Generator (RPTG). This permitted between 1 and 15 delay cycles to be programmed at the beginning of memory accumulation and in addition provided a trigger signal at the beginning of the first delay cycle for the external experimental timing circuitry. Figure 5.7 diagramatically illustrates the timing sequence of the OMA under control of the RPTG and shows the

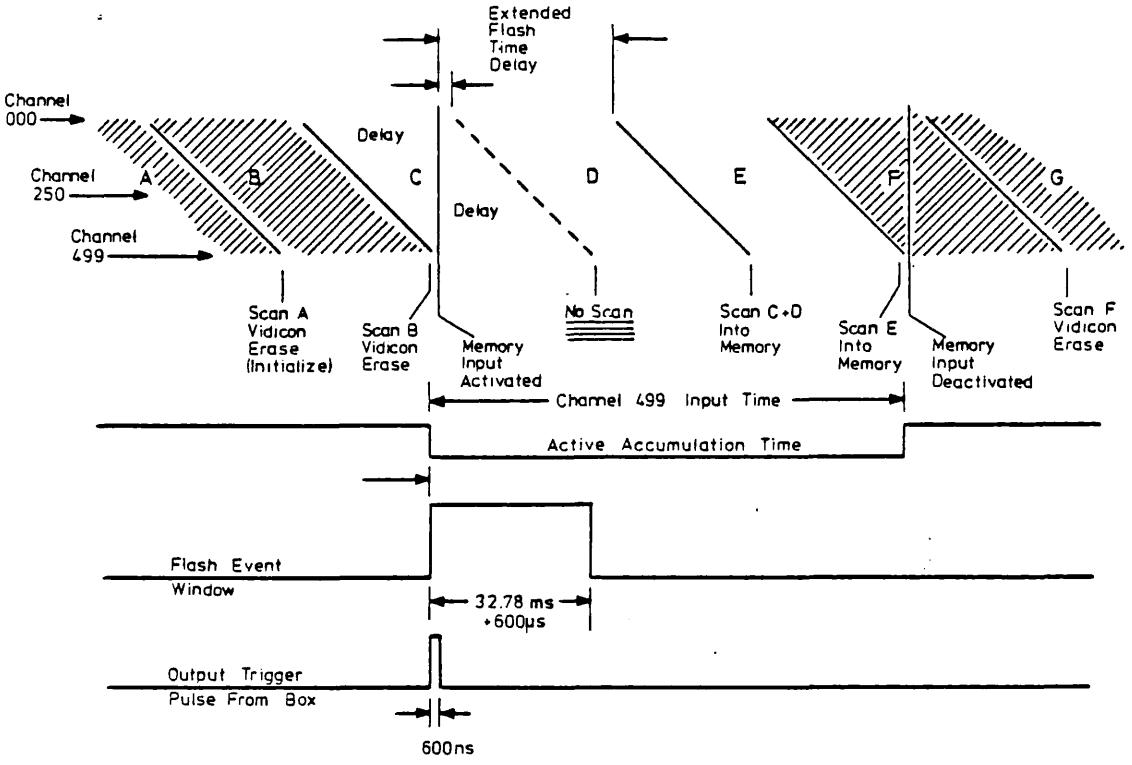

Figure 5.7
Timing diagram of the OMA under control of the Remote Program and Trigger Generator with one delay cycle and two scan cycles.

timing position of the output trigger pulse from this relative to the OMA timing cycle. For all the experiments undertaken 1 delay cycle followed by 5 scan cycles was used to accumulate the spectra.

In addition to the electronic modifications to permit the OMA's use with the scattering experiment, a great deal of care was taken to provide adequate screening of the detector head and high voltage pulse generator against electromagnetic radiation produced by the Plama Focus discharge circuit. It was possible to place the 1205A Control Console in a screened room outside the high-voltage area and run a 36 metre control cable to the detector head inside copper pipe. However, in order to prevent deterioration of the shape of the high-voltage gating

pulse, the cable length between the high voltage pulse generator and detector head is limited to 1 metre. Both the detector head and pulse generator were therefore enclosed in copper boxes to screen against electromagnetic radiation. The trigger and monitor cables for the pulse generator were also enclosed in the copper pipe leading to the screened room. Minor modifications were made to the trigger circuitry of the high voltage pulse generator to remove earth loop problems intrinsic in the circuit design. The above measures proved satisfactory in preventing problems due to electromagnetic interference.

5.4.4 OMA DYNAMIC RANGE

The linear dynamic range of the OMA when used for measuring 'flash' events is governed by the input signal limit of the A-D converter (section 5.3). In Accumulation mode the limit is 859 counts per channel per scan. The preamplifier noise is quoted [60] as ± 1.5 counts per channel per scan for the ISIT head. Experimentally the baseline count was found to have a peak to peak fluctuation of ≤ 5 counts for a programmed Accumulation of 1 delay scan followed by 5 scans into memory. This yields a figure for the dynamic range of $\sim$ 170. For this reason, great care was taken to prevent saturation of the peak of a spectrum by use of attenuating neutral density (ND) filters in the collection optics. With the multiple-$\underline{k}$ experiment where the spectra peak levels vary greatly with $\underline{k}$, a range of ND filter values was used to ensure as large a recorded signal as possible for each of the three spectra without running into the saturation regime.

5.5 EXPERIMENTAL SETUP OF THE OMA SYSTEM

5.5.1 ALIGNMENT OF THE DETECTOR HEAD

The OMA was used in conjunction with a 1 metre f/10 Czerney-Turner grating spectrometer (Monospek 1000) fitted with a 1200 lines/mm ruled grating (Bausch & Lomb). Spectral analysis of the scattered light was undertaken operating the instrument in the first order. The Monospek output slit assembly was replaced by an adjustable adaptor plate which permitted the detector head to be bolted to the spectrometer. The adaptor was designed to permit rotational and vertical translational adjustment of the detector head so that correct positioning could be achieved.

Translational adjustment is necessary to permit an offset of the detector faceplate by 1.25 mm relative to the spectrometer optical axis so that the dispersed spectrum image of the input slit falls only on the 'signal' half of the detector.

Rotational adjustment of the intensified heads is necessary whenever the accelerating photocathode voltage is changed, and is a result of image rotation in the intensifier section of the head. The rotational alignment of the channel elements is much more critical than the alignment of the dispersed spectrum image with the frame scan direction. If the detector head is rotated approximately 1/2 a degree from the optimum position, a single channel input (width 25 microns) will be rotated over two detector channels, halving the per-channel signal and also increasing the instrumental profile width. Figure 5.8 illustrates this problem. In order to achieve accurate rotational adjustment of the detector head for a given photocathode accelerating voltage, advantage was taken of the 2-D option card fitted to the 1205A

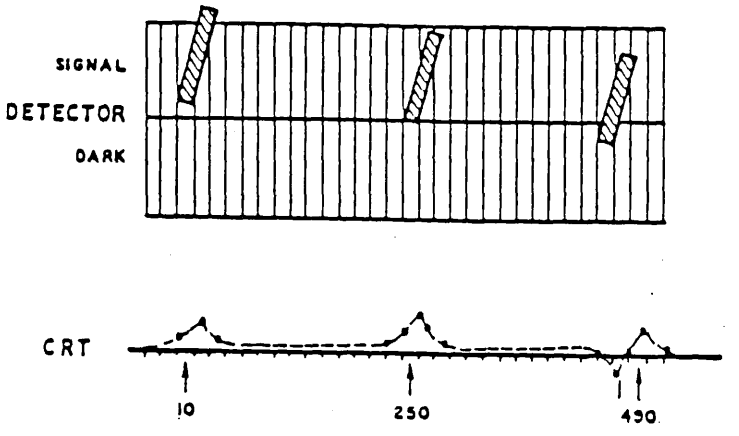

Figure 5.8
Detector assembly rotational misalignment

console.

The 2-D option card allows intensity information in two dimensions (X-Y) to be read from the detector head. Data is read by scanning sequential tracks, each of which corresponds to a normal frame scan except with a reduced line scan amplitude. The line scan amplitude is reduced in proportion to the total number of tracks to be scanned (1-256). After each track scan the d.c. current in the line-scan coil is changed to advance to the position of successive tracks. Data may be accumulated into the 1205A memories from any selected track.

The number of tracks to be scanned can be selected by means of two internal hexadecimal switches although advantage was taken of a 25 pin remote control connector to enable the number of tracks to be selected externally. This connector also permitted the track to be accumulated into memory to be selected.

It should be noted that when the 2-D option is selected the background subtraction circuitry is switched off and the whole of the faceplate

area illustrated in figure 5.3 is used for signal acquisition. The use of the whole faceplate area without the background subtraction circuitry switched in, results in baseline curvature. However, this was not a major problem as the 2-D option was only used for rotational adjustment.

The technique employed to achieve correct rotational adjustment was to illuminate a straight input slit of width 25 microns and height 10 mm with a low pressure neon spectral calibration source (Ealing Beck type 26-4861) The source was imaged onto the input slit with a lens to provide an adequate input 'f' cone into the spectrometer. With the grating adjusted to a setting of 652.0 nm it was possible to observe two neon lines at 650.65 nm and 653.29 nm simultaneously with the OMA (detector head ungated). Attenuation of the source with neutral density filters prevented saturation of the detector electronics.
Using the 2-D option with the head divided into typically 40 tracks, it is possible to see the peak channel position of each of the two lines corresponding to different positions along the height of the input slit. By rotating the head it was possible to achieve a position where the peak channel number of each spectral line was constant over all the tracks. This process was done in two stages; firstly by using the Real Time Mode to achieve a course adjustment and secondly using the Accumulation Mode from selected tracks to achieve fine adjustment. Figure 5.9 illustrates this adjustment technique with the detector divided into 12 sequential tracks for simplicity. With the head incorrectly aligned with the image of the input slit as in situation A, a series of scans into memory from track 1 indicates the peak of the spectral line at channel 261. Similarly a series of scans into memory from track 12 indicates the peak at channel 259. Rotation of the head by the angle θ in the direction indicated by the arrow yields a

situation where the peak channel number is identical for every track.

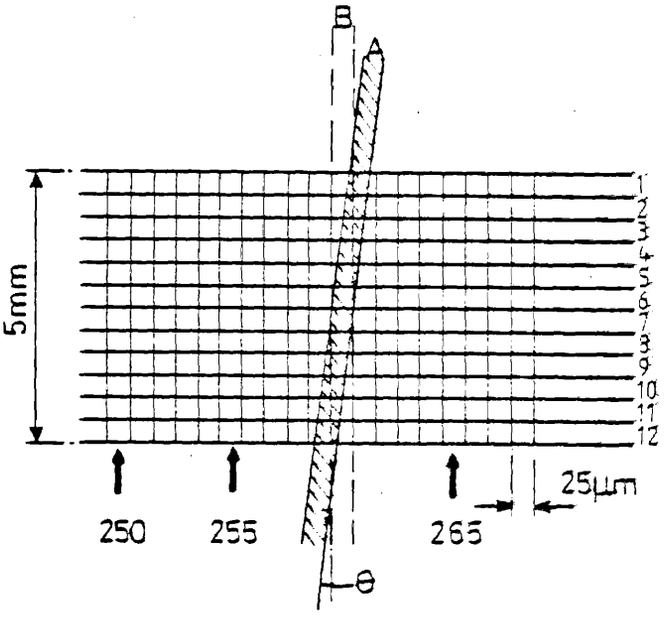

Figure 5.9
Rotational adjustment of the OMA Detector Head

5.5.2 ADJUSTMENT OF THE HIGH VOLTAGE GATING PULSE

To ensure that the front intensifier section of the detector head remain in focus in the gated mode, stable, flat-topped gating pulses with sharp rise and fall times and correct voltage amplitude are required. These were provided as described already by a Model 1211 high voltage pulse generator.

In order to obtain correct pulse amplitude and hence focussing of the intensifier section with short gating pulse widths of the order of 100 ns FWHM (130 ns pulse width setting) an expanded HeNe laser beam was focussed on the input slit (25 microns wide and 2.5 mm high) with a

lens to provide an adequate input 'f' cone. With the grating set at 632.9 nm the High voltage pulser was triggered at a 10 kHz repetition rate which provided an acceptable signal for the OMA in Real Time Mode. By adjusting the pulse amplitude it was possible to achieve a 'best focus' situation by maximising the peak count of the central channel of the HeNe laser line.

CHAPTER 6 THE MULTIPLE-k LASER SCATTERING EXPERIMENT

6.1 INTRODUCTION

Following the review in chapter 3 of previous Plasma Focus scattering experiments, it was concluded that it was highly desirable to measure the scattered spectrum of more than one $\underline{k}$ magnitude and orientation simultaneously on a single plasma shot. The development of a multiple-$\underline{k}$ experimental scattering arrangement to facilitate these objectives was based on the following considerations.

Initially it might be assumed that it would be necessary to have a dispersive instrument and detection array for each $\underline{k}$ to be measured. The experimental complexity and expense of such a system for the measurement of more than two $\underline{k}$'s simultaneously would be undesirable. The technique devised to overcome this problem was based on the fact that the OMA system provides 500 detection channels. It was therefore considered possible to place more than one dispersed scattered spectrum on the OMA detector array simultaneously. This can be done by using several parallel vertical input slits (one for each $\underline{k}$) with an inter-slit separation which will produce a suitable spacing of the spectra on the detector array. The 1/e half widths of the ion spectrum for scattering angles of 10 and 45 degrees and a range of ion temperatures were tabulated in table 3.2 (p.78). For a plasma having a 1 keV ion temperature, the 1/e full width of the spectrum (neglecting any radial velocity component broadening) will be $\sim$ 55 channels with an dispersion-detection system inverse dispersion of 0.02 nm/channel. The

equivalent 10 degree spectrum will be $\sim$ 12 channels. The experimentally measured energy spectrum will result from a composite source function of the form,

$$E(\lambda) = E_B(\lambda) + E_S(\underline{k},\lambda) \qquad (6.1)$$

where $E_B(\lambda)$ is the background (bremsstrahlung) plasma emision term as a function of wavelength and $E_S(\underline{k},\lambda)$ is the scattered profile function. In order to achieve accurate profile fitting to the experimental data, it is necessary to have a reasonable number of baseline data points on either side of the scattered profile function where $E_S(\underline{k},\lambda) \rightarrow 0$. In section 3.5.2, the possible scattering arrangements on the Culham Plasma Focus were detailed, and it was concluded that the following three arrangements were the most appropriate for an investigation of the plasma parameters:

(1) $\theta = 10$ degrees with $\underline{k}$ orthogonal to $\underline{z}$.

(2) $\theta = 10$ degrees with $\underline{k}$ antiparallel to $\underline{z}$

(3) $\theta = 45$ degrees with $\underline{k}$ orthogonal to $\underline{z}$.

Therfore, if a triple input slit assembly is used with a $\frac{1}{4}$ mm inter--slit spacing, the three scattered spectra can be accommodated on the OMA detector array as illustrated in figure 6.1, where the 45 degree spectrum has been positioned centrally. This layout results in $\geq$63 additional side channels for each wing of the spectra, although this number can be increased by overlapping the baseline data point region used in the analysis of each spectrum. This large number of additional channels for each spectrum will adequately handle any broadening or shift of the spectra due to radial or bulk velocity effects.

The use of a triple input slit arrangement results in several experimental problems:

(i) Only one of the three slits will be at the focus of the

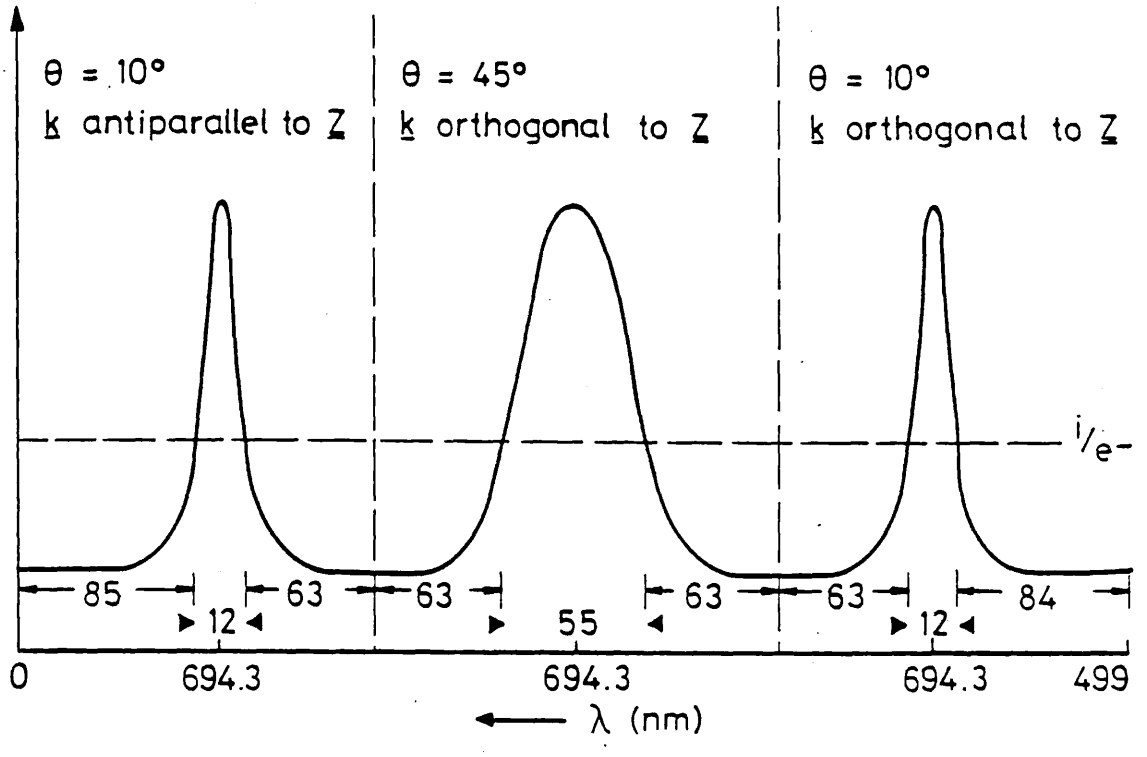

Figure 6.1
Illustration of three spectra layout using triple input slit assembly.

spectrometer collimating mirror. However, for small slit separations ∿ few mms and a relatively large slit width of 100 μm on a 1 m f/10 spectrometer, there will be only a small increase in the width of the instrument profile for the two imperfectly focussed slits. This fact was established by the measurement of each slit's instrument profile (section 6.6.3). The increase in instrument profile 1/e full width of the two side slits being <9%.

(ii) From figure 6.1 it can be seen that the dispersed wavelength region resulting from each slit, overlaps that of the others. This results in the background plasma emission contribution, which forms the baseline of each spectra, being the composite contribution from all three scattering collection systems. This was not a problem for the 10 degree scattering because of the large expected signal to background ratio for this angle (section 3.5.5.3). However, it could have presented a problem for the 45 degree scattering. The problem was

overcome because attenuation of the 10 degree scattered light signals by neutral density (ND) filters was necessary to prevent saturation of the OMA (section 6.5). In addition the collection solid angle of the 45 degree scattering arrangement was nearly twice that used for the 10 degree systems. The combined effect of these two measures resulted in only a small decrease in the 45 degree signal to background ratio. (iii) By definition, multiple $\underline{k}$ measurements will result in the collection optics for each defined $\underline{k}$ having an axis with a radial direction out from the plasma scattering volume which would necessitate a rather complex arrangement of mirrors and lenses to relay the scattered light from each collection optics onto the triple input assembly. This problem was overcome by using fibre optics as an intermediate relay system. The use of fibre optics has the added advantage of mechanically decoupling the collection system optics from the dispersion-detector system optics, alleviating problems of misalignment when the plasma vacuum chamber is pumped down.

6.2 INPUT OPTICS AND STRAY LIGHT SUPPRESSION

A primary consideration to the design of all experiments involved with laser scattering from plasmas is the suppression of stray light due to the scattering of the incident laser beam by optical components and from secondary reflections. The technique used to minimise the stray light is illustrated in figure 6.2. The incident laser beam was focussed onto the plasma $\underline{z}$-axis by a plano-convex lens external to the the vacuum chamber through an input window mounted on a 700 mm long baffled input tube. The baffling consisted of annular OB10 glass stops mounted along the length of the input tube at regular intervals. The

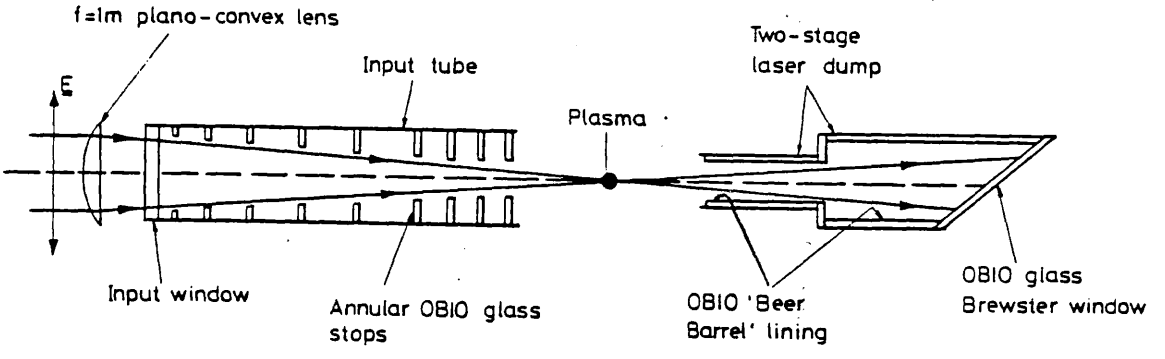

Figure 6.2
Layout of laser input optics and dump.

aperture diameter of each stop was slightly greater than the laser beam waist diameter at that position, so as to prevent scattering of the laser beam from the stop edges. In addition the individual position of the stops was such as to prevent secondary reflections from the input tube wall which had a black matt finish as an additional precaution. An additional benefit of using a long input tube assembly is that it allows the input window to plasma distance to be increased. This is a necessity with a Plasma Focus device having a solid centre electrode, as rapid surface damage of optical components occurs if they are too close to the discharge assembly. However, the main drawback of this arrangement is the requirement to then use a focussing lens of long focal length resulting in a larger diameter focussed laser spot size for a given laser beam divergence.

On the opposite side of the vacuum chamber to the input tube was a two--stage laser beam dump. This consisted of two tube sections of internal diameters 25 mm and 40 mm, each with an OB10 glass 'beer barrel' lining, followed by an OB10 glass Brewster window. Any transmission of light by this window was prevented by covering the external surface with black masking tape. With accurate alignment of the laser beam through the input and beam dump tubes, and with a high quality dust free focussing lens and input window, stray light was reduced to a level that was unobservable with the OMA detection system.

6.3 OPTICAL LAYOUT OF THE SCATTERING SYSTEM

The optical arrangement of the multiple-$\underline{k}$ scattering experiment is shown in figure 6.3 with a colour illustration opposite in figure 6.4. An illustration of the scattering vector diagram for the experiment is shown in figure 6.5. The $|\underline{k}|$ values for the two scattering angles using eq 2.20 are, $|\underline{k}|_{10}=1.58\times10^{6}\ m^{-1}$ and $|\underline{k}|_{45}=6.93\times10^{6}\ m^{-1}$. It should be noted that in the case of the 10 degree $\underline{k}$ antiparallel to $\underline{z}$ arrangement, the $\underline{k}$ vector is inclined at an angle of 5 degrees to the to the negative $\underline{z}$-axis direction. Each of the optical sections is described in detail below with reference to figure 6.3 and their alignment will be detailed in the subsequent section.

Laser Input Arrangement

The 'Q-switched' ruby laser output (1) of 6 J in a 20 ns FWHM pulse was focussed with a f=1 m plano-convex lens, L1 through the baffled input tube described in the previous section, onto the plasma $\underline{z}$-axis

10 mm below the centre electrode. The input beam polarisation was in the horizontal plane for the reasons discussed in section 4.3.2. The spot size diameter of the focussed laser beam, d was 5.5 mm. The determination of this diameter is described in section 6.4.

Collection Imaging System

Three sets of collection optics (2,3,4) view an essentially identical axial scattering volume centred at z=10 mm. Each collection optical arrangement consisted of a f=50 mm plano-convex lens, L2-4, which imaged the plasma scattering volume onto the end of a 400 μm fibre optic (5,6,7). The object to image distances were in the ratio 10:1, so that the overall magnification of the collection systems was 0.1. Thus the beam waist of the scattered light collection cone had a diameter, w of 4.0 mm. Alternative focal length lenses and postions could have been used to provide a different beam waist diameter. The selected diameter was based on the considerations discussed in section 3.5.3. The optical tables on which the collection optics were mounted were firmly located onto the plasma vacuum chamber preventing any optical misalignment during the vacuum pump-down. The engineering design incorporated long collection tubes on which the collection windows were mounted, to prevent rapid damage and contamination of the windows by the plasma. By increasing the plasma to window distance, negligible window damage was apparent after 500 plasma shots. In addition, the collection tubes were baffled with annular OB10 glass stops as a further precaution against stray light problems. Mounted after each collection window was a HN22 sheet polariser, P1-3, accurately aligned so that only light with the same polarisation as the incident laser would be transmitted. Following this was a calibrated ND filter on the 10 degree scattering systems to prevent saturation of

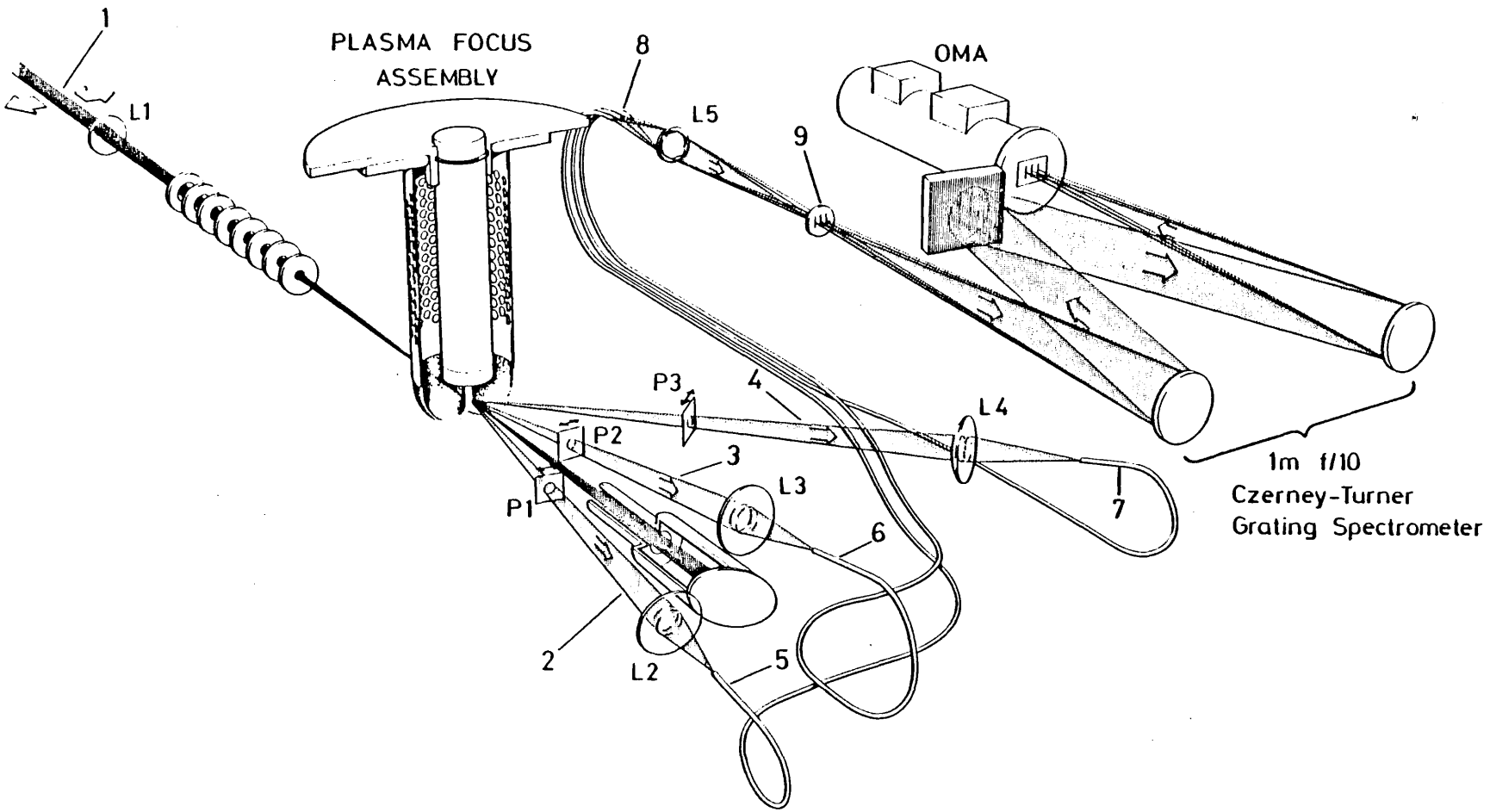

Figure 6.3
Schematic of the optical layout of the Multiple-$\underline{k}$ Laser Scattering experiment for the measurement of three differential scattering vectors simultaneously.

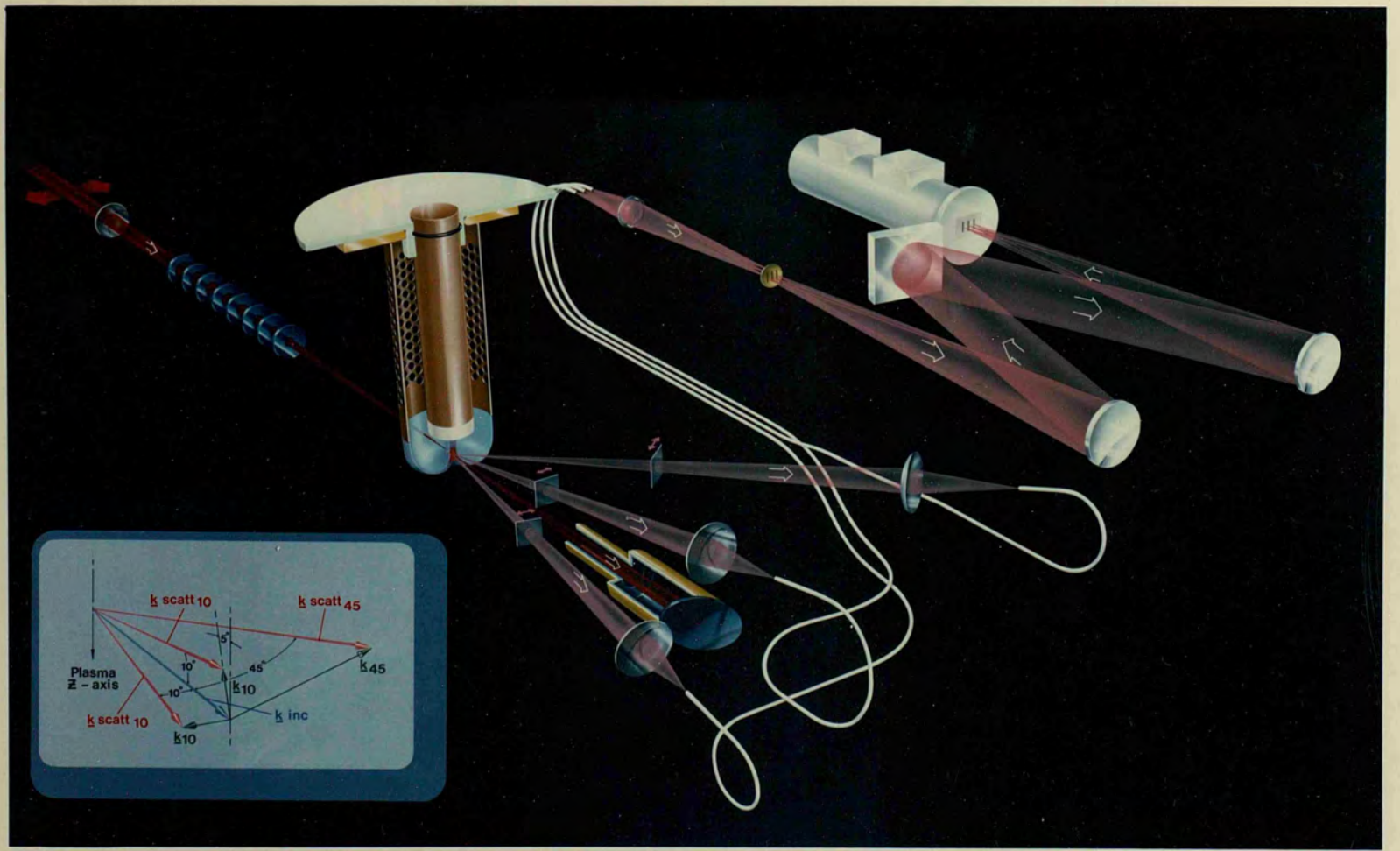

Figure 6.4
Illustration of the optical layout of the Multiple-k Laser Scattering experiment.

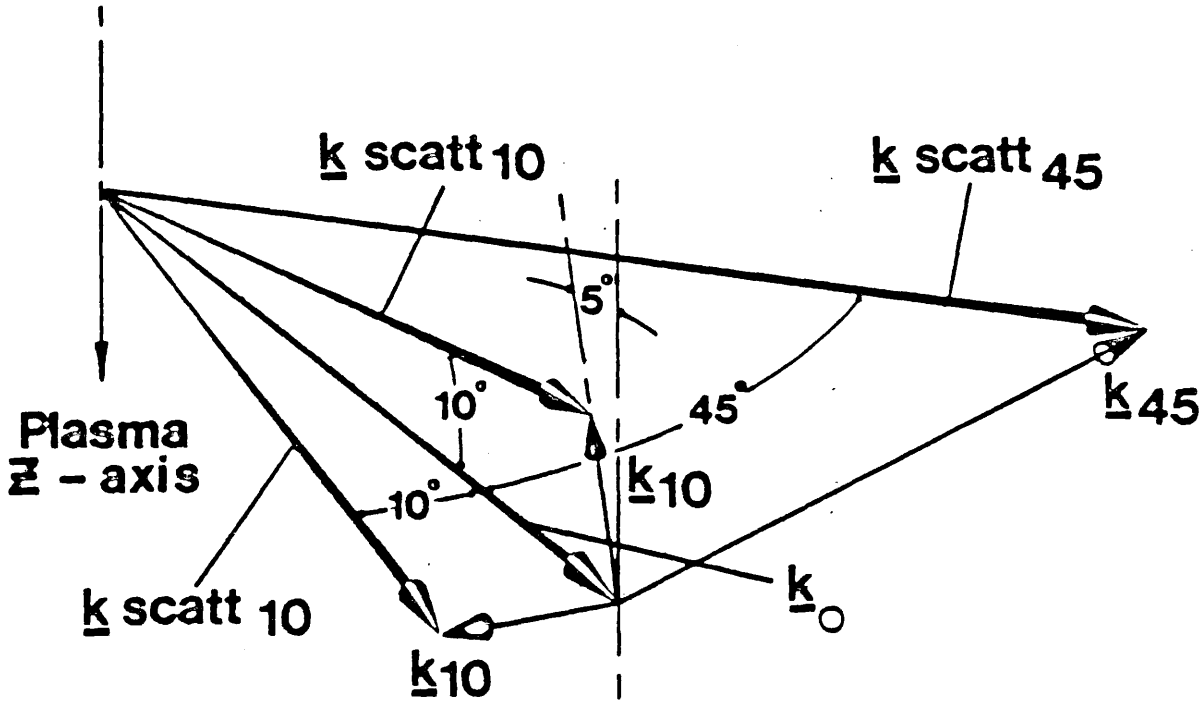

Figure 6.5
Scattering vector diagram for Multiple-k Scattering experiment with: (1) θ=10 degree k orthogonal to z (2) θ=10 degree k anti-parallel to z (3) θ=45 degree k orthogonal to z.

the OMA, which was discussed in section 6.5. The solid angle of the 45 degree scattering collection optics, $d\Omega_{45}=4.15\times10^{-3}$ str and for the two 10 degree scattering collection optics, $d\Omega_{10}=2.50\times10^{-3}$ str.

Intermediate Imaging System

The output ends of the three collection fibre optics were terminated in a horizontal line by mounting the ends on an intermediate object plate (8) with an an accurate centre to centre spacing between each of 1.6 mm. The three ends were then imaged using a f=150 mm plano-convex lens, L5, onto three parallel vertical slits (9), each of width 100 μm and height 2.5 mm with an inter-slit spacing of 4.0 mm.

The slits were manufactured on 370 μm thick brass using the spark--erosion technique. The object and image distances of the intermediate imaging system were 210 mm and 525 mm respectively, giving a magnification of 2.5. Thus each fibre optic was imaged onto one of the slits, and formed an image in the slit plane of a circle of diameter 1 mm. This final section of the optics was aligned as described below, so that each slit bisected the vertical diameter of each magnified fibre end image. The total area of the image was thus 0.785 mm^2 and the slit sampled an area of 0.1 mm^2 (12.74%). The fibre optic output cone was measured experimentally and had a value of f/4. Therefore with a magnification of 2.5, the spectrometer input cone was identical to the f/10 collection cone of the spectrometer. For the centre fibre optic and slit which are coaxial with the spectrometer input axis, this input cone was well matched into the f/10 spectrometer. For the slit on either side, the input cones were displaced in the horizontal direction at the spectrometer collimating mirror by 11.6 mm. This displacement with a collimating mirror diameter of 100 mm results in a light loss of < 15%. Although the overall relay optic losses are greater than those of a conventional arrangement, the reasonably large collection solid angles more than compensated for this loss. The individual losses of each scattering collection system were unimportant as regards calibration, as each was calibrated separately as described in section 6.6.1.

6.4 OPTICAL ALIGNMENT OF THE SYSTEM

An alignment target module (ATM) facilitated the accurate alignment of both the input laser beam and the collection optics. It consisted of a tube section which could be accurately located over the end of the centre electrode of the Plasma Focus and attached to this is an alignment plate which was rotated normal to the axis of which ever optics were being aligned. Mounted on this was an adjustable diaphragm stop, the centre of which coincided with the pinch z-axis 10 mm below the end of the electrode. Either black Polaroid film or a scatter--plate could then be mounted behind the diaphragm stop.

Input Laser Beam

The incident laser beam was aligned by using a HeNe alignment laser located on the ruby laser bench (section 4.3.2). This had first been aligned so that it was coaxial with the ruby laser output. Having checked that the HeNe laser ouput was coaxial with the input tube, the ATM stop and the laser dump, the input focussing lens, L1 was then positioned and adjusted so that the focussed HeNe spot on paper placed behind the ATM stop was central with respect to it. The alignment was checked and finely adjusted by centralising the burn mark on black polaroid film from a focussed ruby laser pulse. The burn marks were taken with the vacuum chamber pumped down to prevent air breakdown infront of the target paper. These burn marks were also used to determine the focussed laser spot diameter, by suitable attenuation of the incident laser beam. With the 1 m focussing lens used, the spot diameter was 5.5 mm.

Collection Optics

The intermediate object plate imaging system was aligned first by removing the imaging lens, L5 and the centre fibre optic from its mouting hole in the intermediate object plate. A HeNe alignment laser was then mounted and adjusted so that its beam passed through this hole and through the centre of the centre slit. The position of the laser spot relative to cross-wires mounted on the spectrometer collimating mirror was then observed. By adjustment of the intermediate object plate and realignment of the HeNe laser it was possible to achieve a situation where the mounting hole, the centre slit and the centre of the spectrometer collimating mirror were all coaxial. Having achieved this situation, the centre fibre optic and the imaging lens, L5 were then carefully replaced.

The alignment module described above, fitted with the scatter-plate and a stop diameter of 4 mm, was positioned on the centre electrode of the Plasma Focus and illuminated with a HeNe laser. Each of the scattering collection lenses, L2 and L3 was then adjusted in turn so that the alignment module was illuminating two of the fibre optics. The intermediate object plate imaging lens, L5 was then adjusted so that each image of the two illuminated fibre optic ends was centralised on their respective side slits in both the horizontal and vertical directions. The alignment module was then turned through 45 degrees to illuminate the 45 degree scattering fibre optic. Further course adjustment of L5 was unnecessary as the image of the end of this fibre optic was found to be centralised on the centre slit. The whole of the alignment of L5 was finely adjusted by attenuating the HeNe illumination beam to a level where the OMA could be used in the real time mode (section 5.3) to observe the HeNe laser line (632.9 nm) due

to each slit. By peaking the signal for each slit simultaneously, accurate alignment of L5 was accomplished. Each of the collection lenses, L2-4 was then similarly finely adjusted by observing the HeNe laser line with the OMA real time mode.

6.5 ADDITIONAL EXPERIMENTAL CONSIDERATIONS

The rapidly changing number of electrons contained within the scattering volume during the Plasma Focus discharge lifetime, results in a range of scattered light signal levels. The limited dynamic range of the OMA detector (section 5.4.4), therefore placed a requirement that a range of attenuation of the scattered light signal level was desirable to prevent saturation of the OMA. This was particularly important for the 10 degree $\underline{k}$ antiparallel to $\underline{z}$ arrangement, as very large enhancements were observed with this $\underline{k}$ orientation at certain times during the plasma discharge. Therefore a preliminary trial of the apparatus was undertaken to assess the optimum attenuation of each scattering arrangement during each phase of the discharge. This was accomplished by testing each of the three scattering arrangements separately, the other two collection systems being physically blocked. This preliminary work enabled the optimum ND filter values to be established for each arrangement and phase of the plasma, with the composite nature of the contribution to the background plasma emission described in section 6.1, being taken into account. It was found that no attenuation of the 45 degree scattering system was required for any phase of the plasma. The ND filters employed were calibrated at 694.3 nm using a spectrophotometer. The same instrument was used to determine the attenuation characteristics of the HN22 sheet polarisers

for incident plane polarised light of the preferred polarisation.

6.6 CALIBRATION OF THE SCATTERING SYSTEM

6.6.1 SENSITIVITY CALIBRATION OF THE SCATTERING SYSTEM

The three scattering systems, consisting of the scattering collection optics and grating spectrometer - OMA detector head combination, were calibrated for sensitivity using a spectral irradiance lamp in conjunction with an opal flat.

The spectral irradiance of the standard lamp was known from a calibration undertaken by the National Physical Laboratory (NPL). Figure 6.6 illustrates the optical layout used for the sensitivity calibration of each scattering arrangement.

The opal flat was positioned below the centre electrode of the Plasma Focus by securing it to the ATM located on the centre electrode. The ATM had been designed so that when it was used with the opal flat, the surface of the flat would be coincident with the plasma z-axis. The flat was normalised relative to the flat-filament axis by observation of the back reflection from the flat viewed through the standard lamp adjusted to low intensity. The opal flat has the property of scattering light from its surface isotropically into 2π str with an efficiency of >95% at 694.3 nm for normal incidence illumination and 45 degree viewing. A separate calibration by NPL tabulated the reflectance efficiency of the opal flat as a function of wavelength, $R_{ef}(\lambda)$. The lamp was operated under identical conditions to that employed by NPL in calibrating the lamp. These consisted of operating the lamp (type KH6) in series with a paraffin filled resistor of

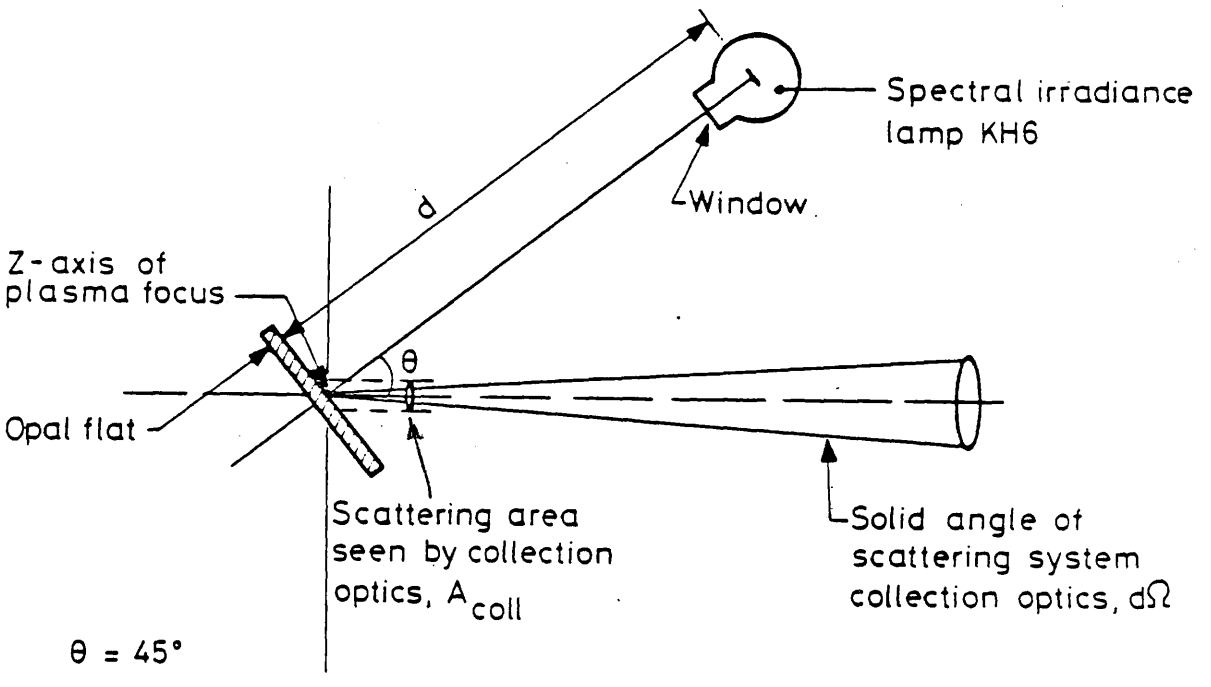

Figure 6.6
Optical layout for sensitivity calibration of the scattering collection and detection systems.

0.05 ohm at a current of 22.1 A. The current was measured and set by observing the voltage drop across the 0.05 ohm resistor and was set at 1.105 V. All electrical connections were made using heavy gauge copper cable. The lamp current was allowed to stabilise by running the lamp for approximately 1½ hours before calibration measurements were made.

If the collection optics view a scattering volume on the z-axis with a cross sectional area, A_{coll} normal to the scattering direction, then the area projected onto the inclined opal flat viewed by the collection optics will be

$$A_{flat} = \frac{A_{coll}}{\cos\vartheta} \qquad (6.2)$$

The light intensity falling on the opal flat is

$$I_{flat} = I_R \times \left(\frac{1}{d^2}\right) \quad (mW.m^{-2}.nm^{-1}) \qquad (6.3)$$

where I_R is the spectral irradiance of the lamp in units of milliwatts/m^2/nm at 1 metre from the lamp (NPL units) and d is the distance in metres between the filament and the flat.

The power, P_{coll} collected by the collection optics which have a solid angle, $d\Omega$ str, is given by

$$P_{coll} = I_{flat} A_{flat} R_{ef}(\lambda) \frac{d\Omega}{2\pi} \quad (mW.nm^{-1}) \qquad (6.4)$$

the light being scattered isotropically into 2π str with an efficiency of $R_{ef}(\lambda)$.

If the inverse linear dispersion of the spectrometer-OMA combination is D_S nm/channel then the number of photons, N_P, collected by the collection optics in each channel wavelength interval per second is given by

$$N_P = \frac{I_R A_{coll} R_{ef}(\lambda)}{2\pi d^2 \cos\theta} d\Omega \times D_S\left(\frac{\lambda}{hc}\right) \times (10^{-3}) \quad (photons.channel^{-1}.s^{-1}) \qquad (6.5)$$

The inverse linear dispersion of the detection system was measured in a separate calibration (section 6.6.2).

The sensitivity calibration was done using the Accumulation Mode of the OMA with the detector head ungated. Eight separate runs were made. In each case 2000 scans were accumulated into memory. After each signal accumulation, the standard lamp source was blocked and 2000 scans were accumulated into the second OMA memory as a background measurement. This is small compared with the signal measurement and is made up of electronic noise and stray light from the room. Subtraction

of the background memory from the signal plus background memory gave an effective measure of the signal due to the standard lamp. By averaging the eight separate calibration runs, an average count per channel per 2000 scans for each of the 500 channels was obtained. Knowing that each scan is equivalent to 32.768 ms enabled the average count per channel per second to be calculated. From the dispersion calibration the wavelength range of each channel was known and hence the spectral irradiance for each channel wavelength increment could be calculated from the NPL calibration. Having calculated an N_p value for each channel (eq 6.5), an overall sensitivity could then be calculated in terms of photons/count. Figure 6.7 shows a plot of channel number against sensitivity for the 45 degree scattering collection optics of the multiple-k scattering experiment. The data from this and similar curves for the two 10 degree collection arrangements was used to convert the units of the scattered data profiles absissa from counts to energy.

6.6.2 DISPERSION CALIBRATION OF THE DETECTION SYSTEM

Two separate dispersion calibrations were carried out for each scattering arrangement. One was with the detector ungated enabling a dispersion factor to be measured for use with the sensitivity calibration. The second was with the detector gated to provide a dispersion factor for the scattered profile fitting. The need for two separate measurements and the small variance between them is due to the fact that it as impossible to achieve a 'perfect' adjustment of the high-voltage gating pulse and a slight magnification or demagnification of the image in the intensifier section results.

The calibration was achieved by using two low pressure spectral

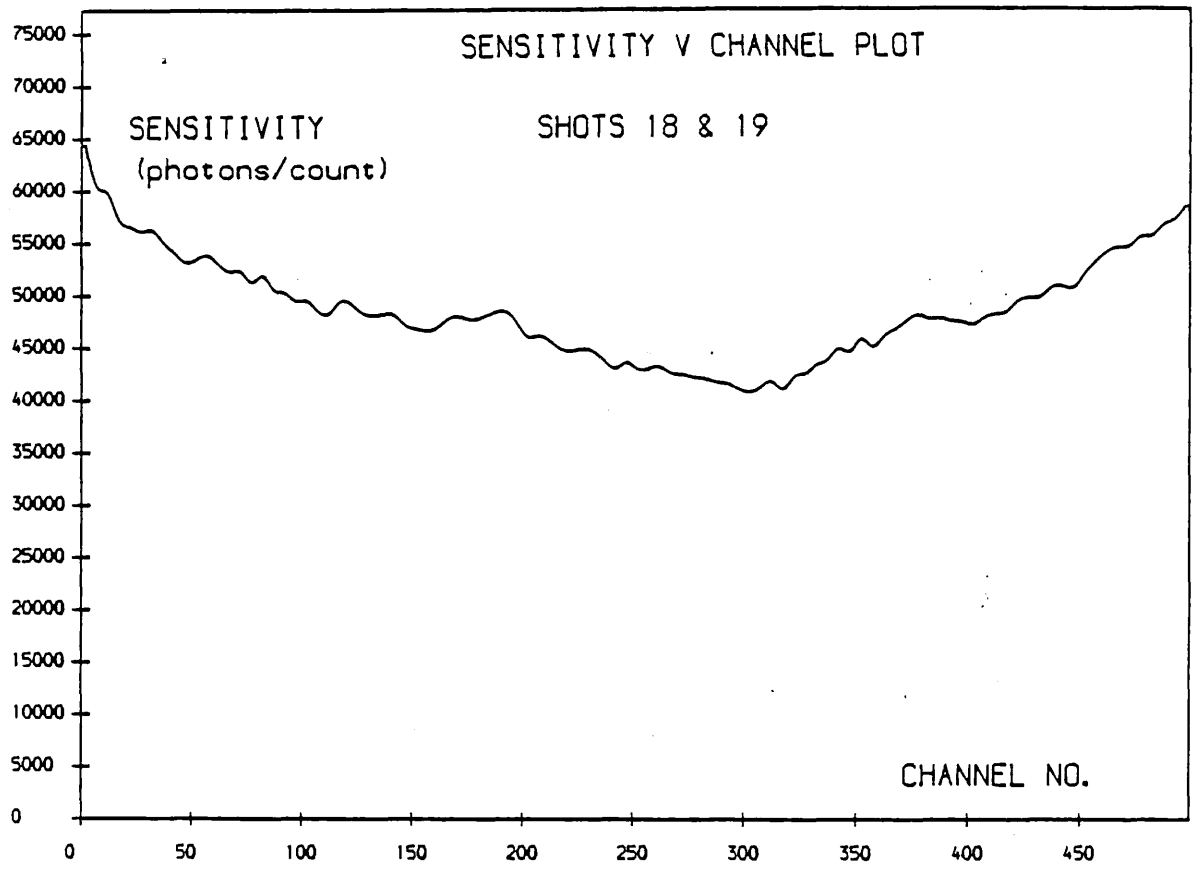

Figure 6.7
Plot of sensitivity in photons/count against channel no.
for 45 degree multiple-k scattering collection system

calibration sources of neon and argon (Ealing Beck type 26-4861 & 4846). These provided spectral lines at: neon; 692.95 nm and argon; 696.54 nm both within the 'wavelength window' of the detection system when the grating was set at 694.3 nm.

For each of the calibrations a 100 scans were accumulated into memory. The gated mode calibration was achieved with a gating repetition rate of 10 kHz. The exact channel location of the peak of each spectral line was determined by fitting a Gaussian profile. This was done using a least-squares grid search computer code which will be described in chapter 7. From the peak positions, the linear dispersions of the two setups could be calculated and in addition the channel/wavelength

equivalents could be calculated using linear interpolation for the sensitivity calibration. In the gated mode which was used for analysing the scattering signals, the inverse linear dispersion was 0.0194 nm/channel for an input slit coaxial with the spectrometer optical axis (45 degree scattering arrangement) and for the two off--axis slits (10 degree scattering arrangements) the value was 0.0181 nm/channel.

6.6.3 DETECTION SYSTEM INSTRUMENT PROFILE

The wavelength power spectrum, $P_M(\lambda)$ measured by any dispersive instrument of a signal wavelength power spectrum, $P_S(\lambda)$ will consist of a convolution of the signal spectrum with the instrument profile, $I(\lambda'-\lambda)$ of the dispersive detection system

$$P_M(\lambda) = \int_{-\infty}^{\infty} P_S(\lambda') I(\lambda'-\lambda) d\lambda' \qquad (6.6)$$

Therefore to establish the signal spectrum, $P_S(\lambda)$ from a measured spectrum we need to know the instrument profile, $I(\lambda'-\lambda)$ for the dispersive detection system employed.

The dispersive detection system used for the scattering experiments consisted of the grating spectrometer and the OMA. As the OMA has an instrument function due to cross-talk between individual channels, the detection system instrument profile will in itself be a convolution of the spectrometer and OMA instrument functions. In addition the ruby laser line profile needs to be taken into account.

The spectrometer instrument function is a result of several factors. Theoretically it is a convolution of the diffraction limited profile and a 'top hat' function due to the finite width of the input slit.

However, the effects of a finite input cone, spherical optics and possible optical misalignment need to be considered.
The quoted OMA cross-talk is as follows [60]: For a 10 micron line centred on channel I, >50% of the signal will be in channel I, and >97% of the signal will be in channels I-1, I,and I+1.

As an alternative to this complex calculation, an approximation to the detection system instrument profile, $I(\lambda'-\lambda)$ can be simply achieved by experimental measurement. The experiment consisted of measuring the spectrum of 'induced' stray light due to the ruby laser. The experimental measurement therefore includes the effect of a finite laser line width ($\sim$0.01 nm). Stray light was induced by placing a diffuser infront of the laser input window to enhance the normally unobservable stray light level. With the vacuum chamber pumped to its base pressure of 5×10^{-6} torr, a ruby laser pulse was recorded with the OMA. The OMA output display consisted of three profiles, one for each collection and input slit arrangement. It was found that a Gaussian could be fitted with acceptable accuracy to each of the recorded profiles using a least-squares grid search fitting routine (chapter 7). From each profile, the central channel number (not necessarily an integer) could be determined and normalised weighting coefficients for this channel and for the eight integer channel shifts on either side of the centre were calculated. Figure 6.8 shows the measured data points and fitted Gaussian profile for the centre slit (45 degree scattering arrangement). The normalised instrument profile weighting coefficients, C_{I+p} (p=-8,-7,....,+7,+8) for the I-8 to I+8 channels, where I is the central channel number, are also tabulated. The utilisation of these coefficients in the analysis of the experimental scattering results will be described in chapter 7. As each of the three slits was calibrated separately, the broadening of the instrument

profile for the two side slits due to their misalignment with the spectrometer optical axis can be determined. The Gaussian instrument profile 1/e full widths for each $\underline{k}$ were:

10 degree $\underline{k}$ antiparallel to $\underline{z}$ - 7.51 channels (0.136 nm)

45 degree $\underline{k}$ orthogonal to $\underline{z}$ - 6.43 channels (0.125 nm)

10 degree $\underline{k}$ orthogonal to $\underline{z}$ - 7.35 channels (0.133 nm)

were the bracketed values in nanometres include the difference in inverse linear dispersion for axial and non-axial slits (section 6.6.2). The increase in 1/e width of the side slits due to their non-axial position is therefore < 9%.

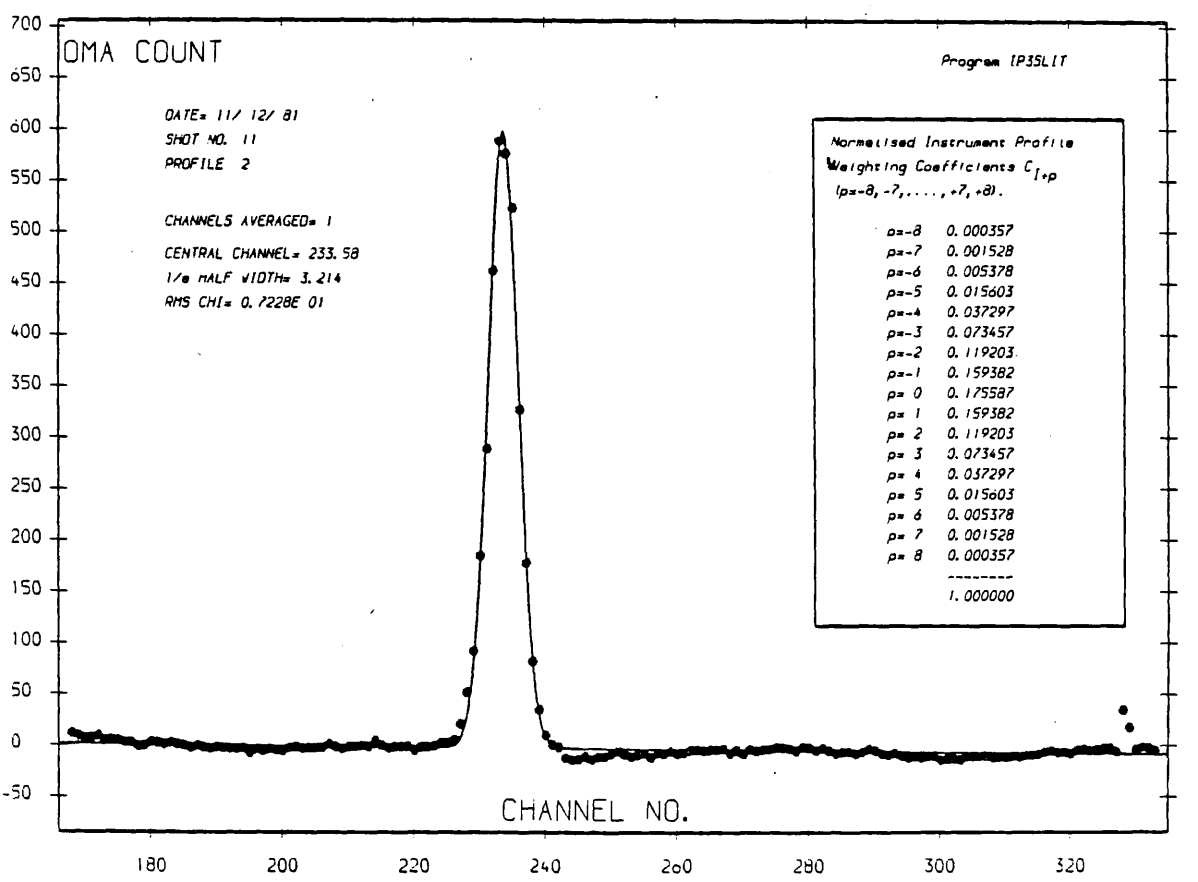

Figure 6.8
Instrument profile for a 100 micron input slit showing grid least squares fitted Gausian to data points and table of normalised instrument profile weighting coefficients, C_{I+p} (p=-8,-7,....,+7,+8).

CHAPTER 7 ANALYSIS AND INTERPRETATION OF THE RESULTS

7.1 INTRODUCTION

The analysis and interpretation of the results of the multiple-$\underline{k}$ laser scattering measurements are presented in this chapter. The analysis of scattering data from the Plasma Focus presents several problems. Firstly, the assumption of homogeneous plasma conditions is not valid in the case of the Plasma Focus for a scattering volume with dimensions which are of the order of the plasma radius. Secondly, the effects of an electron-ion relative drift velocity on the scattered 10 degree $\underline{k}$ antiparallel to $\underline{z}$ spectrum are complicated by the plasma current being confined to the plasma skin during the collapse phase ($t \leq 0$) as observed by Faraday rotation measurements [25]. Thirdly, the effect of scattering from a plasma having rapidly changing conditions with a finite duration laser pulse needs to be considered. The solution to these problems was the development of a time convolved, double radial shell scattering volume model. Each of the spectra from the three $\underline{k}$ arrangements were analysed using an essentially similar profile fitting technique based on this model. The complementary nature of the analysis and interpretation of the spectra measured using the three $\underline{k}$'s will become apparent as the techniques are described.

7.2 EXPERIMENTAL RESULTS

Fifty three triple spectra results were recorded for the time period t=-35 ns to t=+40 ns. At the begining and end of each experimental run, an 'induced stray light' shot was recorded by placing a diffuser in front of the laser input window as detailed in section 6.6.3 to provide calibration data for the laser line centre channel postion for each of the three scattering arrangements. All the data was output from the OMA to a paper tape punch and then reloaded onto a Prime 750 computer for analysis. A Polaroid record, taken from the analogue output of the OMA displayed on an oscilloscope, was kept of each triple spectra, in addition to the laser pulse/plasma dI/dt and laser pulse/OMA H.V. gating pulse monitor oscilloscope traces.

Figure 7.1 shows typical triple spectra recorded on Polaroid film from the OMA analogue display, for plasma times of t=-2.5, +15 and +40 ns. It should be noted that as these represent the 'raw' data, the different neutral density filter values in the respective collection systems must be taken into account when comparing the relative heights of the spectra. These are tabulated for each collection system under the respective spectrum on the t=-2.5 ns shot and were identical for the other two shots displayed. The actual integrated scattered energy of the 10 degree $\underline{k}$ antiparallel to $\underline{z}$ spectrum on the t=-2.5 ns shot is a factor of 0.45 greater than the 10 degree $\underline{k}$ orthogonal to $\underline{z}$ spectrum. This enhancement factor was 2.2 and 30 for the t=+15 ns and t=+40 ns shots respectively. In the final shot (t=+40 ns), it can be seen that with the ordinate axis expansion used, the 45 degree spectrum has decayed to the baseline level, although with the ordinate axis expansion increased, this spectrum was still observable at this time.

7.3 ANALYSIS OF THE RESULTS

The triple spectra data from each shot was divided into three separate data subsets, one for each of the three spectra. The two division channel numbers were based on the considerations detailed in section 6.1 and indicated in figure 6.1. In addition, the number of baseline data points was expanded for each region, by including data points in the data subsets from beyond the cross-over channel numbers. This results in an overlapping baseline cross-over region which facilitated more accurate baseline profile fitting. Unless otherwise stated in the relevant sections, 150 channels were used for the analysis of each of the 10 degree spectra and 250 channels for the 45 degree spectra. The sensitivity calibration (section 6.6.1) and the wavelength calibration (section 6.6.2) for each of the three arrangements, were then used to convert each data subset from units of OMA counts to J/str and from channel number to wavelength respectively. The conversion to J/str included the individual solid angles of each of the scattering arrangements and the transmission factor of the ND filter value used. This permitted direct comparison of the scattered energy level of each of the three spectra to be made.

7.3.1 THE DOUBLE RADIAL SHELL SCATTERING VOLUME MODEL

In section 3.4 it was concluded that the radial electron density profile combined with a probable electron and ion temperature profile that peaks in the sheath region, due to plasma current heating there, could account for the range of temperature values determined by previous experiments. Therefore, for scattering experiments having a plasma volume of dimensions of the order of the plasma radius at

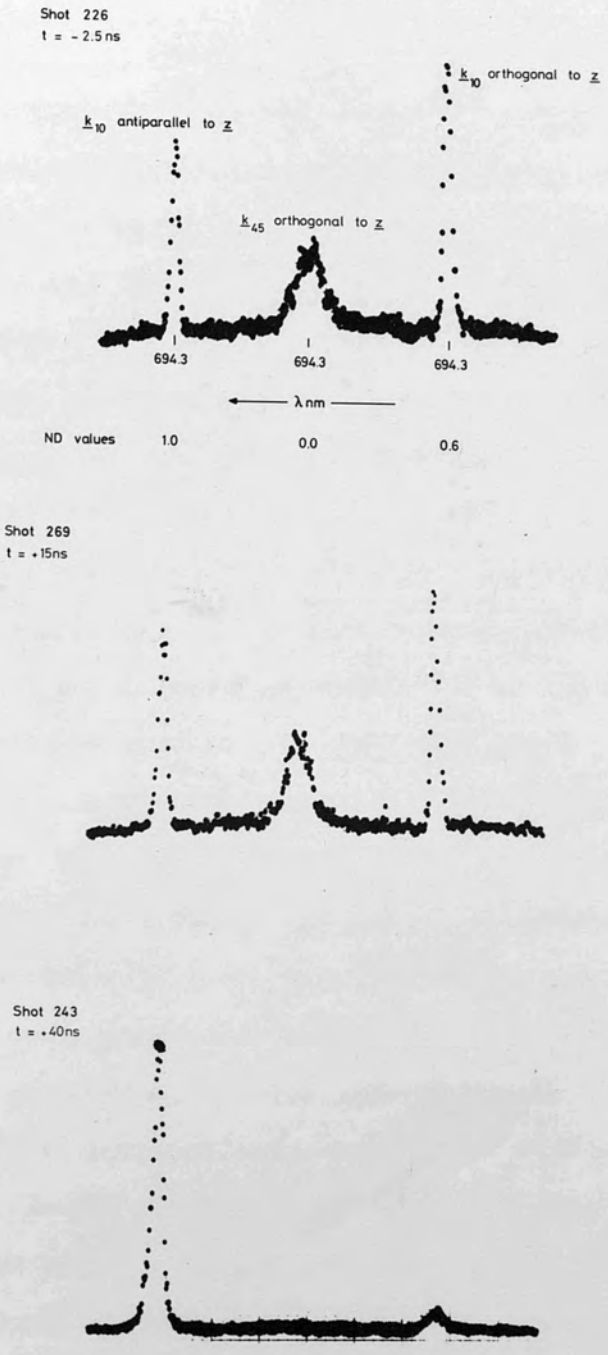

Figure 7.1
Optical Multichannel Analyser analogue display of triple spectra results for shots timed at t = -2.5, +15 and +40 ns.

t=0 ns, the fitting of a single theoretical scattered profile to the data on the assumption of a homogeneous plasma is not appropriate.

The problem of analysing the scattered profile originating from an inhomogeneous plasma can be demonstrated if we make some simple assumptions about the radial variation of the plasma parameters. At peak compression, t=0 ns, the radial electron density profile can be approximated as linear with radius, peaking at r=0. It will be assumed for the example, that T_i and T_e increase linearly with radius and that the ratio T_e/T_i is equal to unity across the radial range. If we take the boundary conditions for the n_e/T_e range specified in section 3.4; $n_e=2x10^{25}$ m^{-3}, $T_e=50$ eV at r=0 and $n_e=2x10^{24}$ m^{-3}, $T_e=2$ keV for the edge of the sheath region, then the plot shown in figure 3.7 (p.66) can be envisaged as being a plot of α and $S_i(\underline{k})$ with plasma radius, where the vertical dotted line A is the plasma axis (r=0) and line B is the plasma edge. For the 10 degree scattering arrangements, assuming a thermal plasma, the $S_i(\underline{k})$ curve (curve-2S) is essentially constant with radius. The measured width of the scattered profile will therefore be approximately proportional to the average plasma ion temperature, though the shape, dependant on the ratio T_e/T_i, will be more difficult to interpret. However, for the larger scattering angle of 45 degrees (curve-3S) the scattered profile will be dominated by the core region of the plasma. To overcome this problem and determine the T_i and T_e radial profiles from the data analysis, one would ideally like to a fit a composite function of the scattered profiles originating from a large number of radial shells. However, because the radial temperature profiles do not have a well defined theoretical analytic form, the number of parameters to be fitted to the data would be prohibitively large. The model developed to analyse the experimental data of each of the three spectra was therefore based on the division of the plasma

into two radial shells volumes consisting of a core region and a radial shell surrounding it as illustrated in figure 7.2.

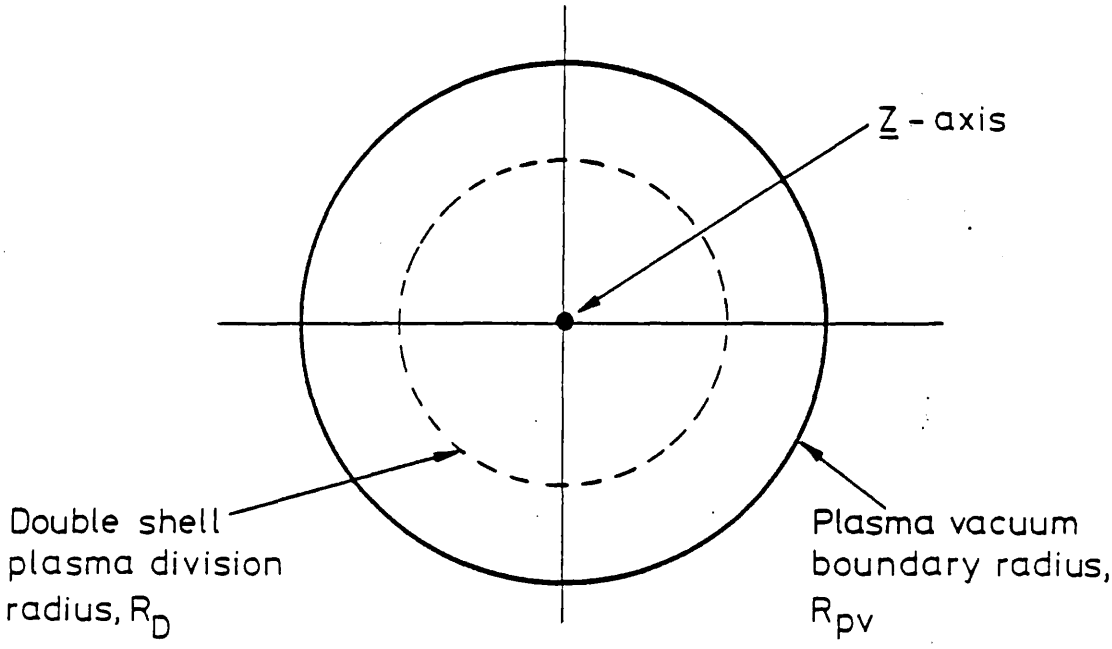

Figure 7.2
Illustration of double radial shell scattering volume division.

In section 3.4.2 it was demonstrated that when the differential scattering vector, $\underline{k}$ has a component orthogonal to the $\underline{z}$-axis, the radial velocity component, resulting from the collapsing sheath, can modify the spectral shape and for larger scattering angles will dominate the spectral width. Therefore the inclusion of the radial velocity component in the model was an important aspect of the analysis.

A profile fitting function was developed for each $\underline{k}$ scattering arrangement based on the double radial shell volume model to permit two different aspects of the Plasma Focus dynamics to be investigated:

(1) To determine the T_i and T_e values for each shell volume from the 10

and 45 degree $\underline{k}$ orthogonal to $\underline{z}$ spectra. This would then provide an indication of the temporal evolution of the radial temperature profiles, particularly around peak compression and thus provide valuable information on the dynamics of the pinch.

(2) Having established the T_i and T_e values of each shell volume for each triple spectra shot, the drift velocity and hence the drift to thermal velocity ratio of the current carrying region during the collapse phase could then be determined by profile fitting to the 10 degree $\underline{k}$ antiparallel to $\underline{z}$ spectrum of each shot. The determination of the localised T_e/T_i ratio for the current carrying region is important, since the enhancenent of the spectrum due to an electron-ion relative drift velocity is paticularly sensitive to this ratio.

7.3.2 THE DOUBLE RADIAL SHELL DIVISION RADIUS

The division of the plasma into two separate radial shells was based on two considerations. Firstly, the division should result in two plasma regions which are of physical significance. Secondly, the difference in the total contribution to the composite scattered profile of the two regions should not be too great, so as to enable profile fitting to be undertaken with reasonable accuracy.

During the collapse phase of the plasma, before t=-10 ns, the plasma can be considered as consisting of a core region surrounded by a collapsing sheath. To illustrate this, consider the radial electron density profile, determined from the holographic interferometry, at time t=-15 ns shown in figure 7.3. The Faraday rotation polarimetry measurements of Muir [25] which are also detailed by Kirk et al [62], indicate that the plasma current is confined to the skin of the plasma with a penetration depth of $\sim$0.7 mm for the time period t=-10 to 0 ns.

It we assume that this dimension is maintained for the earlier time of t=-15 ns, it can be seen in figure 7.3 that this corresponds to the region $r=R_{pn}$ to $r=R_{pv}$, where R_{pn} is the radius of peak density, which is non-axial for $t \leq -10.5$ ns and R_{pv} is the plasma-vacuum boundary radius given by eq 4.8.

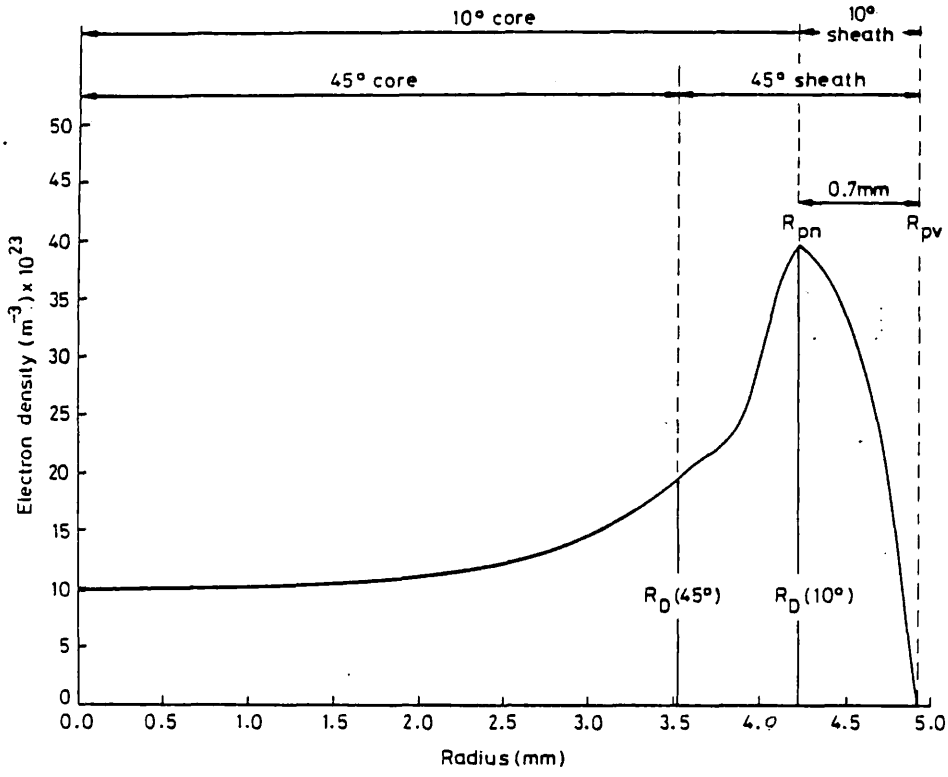

Figure 7.3
Scattering volume radial division positions at time t=-15 ns.

For the analysis of the data from the two 10 degree scattering arrangements, it was therefore logical to base the division of the plasma into two regions, during this phase, by setting the the plasma division radius, $R_D(t)$ equal to the peak density radius, $R_{pn}(t)$. This then enabled the T_i and T_e values for the two regions to be determined from profile fitting to the 10 degree $\underline{k}$ orthogonal to $\underline{z}$ spectrum, from which the temperature values could then be utilised in the profile fitting to the 10 degree $\underline{k}$ antiparallel to $\underline{z}$ spectrum to determine the electron-ion drift velocity in the sheath region and the plasma bulk velocity in the $\underline{z}$ direction for both regions.

Ideally, the same value of $R_D(t)$ would have been adhered to for analysis of the 45 degree $\underline{k}$ orthogonal to $\underline{z}$ spectrum. However, because of the reduced contribution from the sheath region for this scattering angle detailed in the previous section, it was found that insufficient contribution from the defined sheath region was obtained. To overcome this problem the radial division for the 45 degree analysis was redefined so that the radial incremental thickness of the sheath region was double that employed in the 10 degree analysis and therefore approximately equal to the plasma sheath width. This arrangement, shown in figure 7.3, increases the sheath contribution and reduces that of the core and was found to be adequate for times $t \geq -25$ ns.

For times $t > -10.5$ ns, the density profile peaks on axis. Therefore the sheath incremental thickness for the 10 and 45 degree arrangements was defined as constant for later times and equal to their respective values at $t = -10.5$ ns. The division radius of the core and sheath scattering volumes for the three scattering geometries can be summarised as follows:

<u>10 degree scattering arrangements</u>

$$\begin{aligned} R_D(t) &= R_{pn}(t) && t \leq -10.5 \text{ ns} \\ R_D(t) &= R_{pv}(t) - [R_{pv}(-10.5) - R_{pn}(-10.5)] && t > -10.5 \text{ ns} \end{aligned} \qquad (7.1)$$

<u>45 degree scattering arrangement</u>

$$\begin{aligned} R_D(t) &= 2xR_{pn}(t) - R_{pv}(t) && t \leq -10.5 \text{ ns} \\ R_D(t) &= R_{pv}(t) - 2x[R_{pv}(-10.5) - R_{pn}(-10.5)] && t > -10.5 \text{ ns} \end{aligned} \qquad (7.2)$$

The bracketed [ ] section of the above equations has a value of 0.812 mm. Figure 7.4 illustrates the temporal evolution of the plasma--vacuum boundary radius, R_{pv} and scattering volume division radius, R_D for the two scattering angles. As can be seen from this figure the radial thickness of the defined outer sheath regions for each

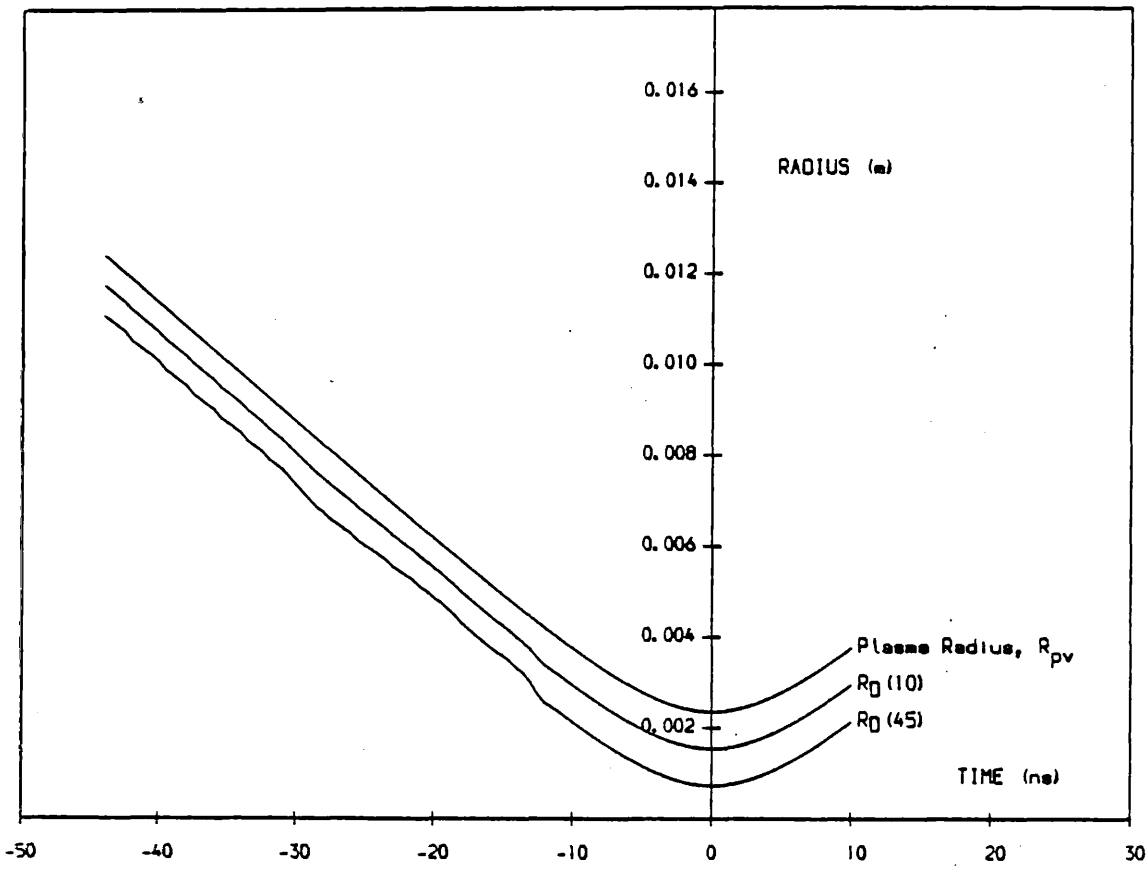

Figure 7.4
Temporal evolution of the plasma-vacuum boundary radius, R_{pv} and defined scattering volume division radii, R_D for the 10 and 45 degree scattering arrangements.

scattering angle remains essentially constant for the whole time region investigated.

7.3.3 THE SCATTERING VOLUME GEOMETRY

The scattered energy spectrum as a function of wavelength shift for each shell volume at a time, t will be given using eq 3.16 by an equation of the form,

$$E_{s_j}(\underline{k},\lambda,t)d\lambda d\Omega = N_j(t)\ C\ S_j(\underline{k},\lambda,t)d\lambda d\Omega \qquad (7.3)$$

where,

$$C = \frac{4E_o}{\pi d^2} \quad r_e^2 \quad \sin^2\gamma \qquad (7.4)$$

and the subscript, j denotes the shell volume region, with j=1 for the core and j=2 for the sheath. The value of γ for each arrangement is: γ =80 degrees for the 10 degree $\underline{k}$ orthogonal to $\underline{z}$ arrangement, γ =90 degrees for the 10 degree $\underline{k}$ antiparallel to $\underline{z}$ arrangement and γ =45 degrees for the 45 degree $\underline{k}$ orthogonal to $\underline{z}$ arrangement.

The choice of dynamic form factor $S_j(\underline{k},\lambda,t)$ will depend on the $\underline{k}$ orientation with respect to the $\underline{z}$-axis. (i.e. for $\underline{k}$ having a component aligned with $\underline{z}$ a relative electron-ion drift velocity needs to be included). Additionally, the dynamic form factor will have to be modified were necessary to include the effects of a radial and bulk velocity component.

The temporal evolution of the radial electron density profile is known from the holographic interferometry, so the electron number, $N_j(t)$ and electron density, $n_{e_j}(t)$ for each shell volume can be calculated, provided the scattering volume geometry is known. As the scattering collection beam waist diameter is of the order of the plasma diameter at peak compression, the effects of having a range of radial velocity components needs to be considered (it was assumed in section 3.4.2 that the beam waist diameter was small compared with the plasma diameter). Therefore the scattering volume geometry needs to be calculated so that these three parameters can be evaluated as a function of time. The calculation for the two $\underline{k}$ orthogonal to $\underline{z}$ arrangements can be generalised to one set of equations and that of the $\underline{k}$ antiparallel to $\underline{z}$ arrangement to another set.

7.3.3.1 VOLUME DEFINED BY k ORTHOGONAL TO z

Figure 7.5a shows the intersection volume formed by the laser beam waist and the collection optics focal beam waist at a scatttering angle, θ , viewed along the z-axis, where d=5.5 mm is the laser beam focussed diameter and w=4.0 mm is the diameter of the collection beam waist. It has been assumed in the figure that with the large f number optics employed, that both beam waists are of constant diameter over the dimensions of the intersection volume.

The cross sectional view of the intersection volume viewed along $\underline{k}_o$ is illustrated in figure 7.5b. To simplify the calculations to be described below, the contributing laser beam cross section can be approximated to a rectangle of dimensions wxA as illustrated in the figure, provided w<d. The dimension A is given by,

$$A = 1/2\ [d+(d^2-w^2)^{\frac{1}{2}}] \qquad (7.5)$$

If we define a position on the scattering plane formed between $\underline{k}_o$ and $\underline{k}_s$ by a radius, r and angle ϕ as indicated in figure 7.5a, then the volume of the radial shell formed between to radial postions r_a and r_b is given by the integral,

$$V_s = F\int_{r_a}^{r_b} dr \int_{\phi_1(r)}^{\phi_2(r)} r.h(r,\phi)\,d\phi \qquad (7.6)$$

where $\phi_1(r)$ and $\phi_2(r)$ are the limits of the angle ϕ set by the intersection volume as a function of r. The factor, F can be set equal to 2, because we can divide the scattering voume into two symmetric parts by the line X-X' and evaluate the integral for one half. The function $h(r,\phi)$ can be derived by trigonometry as illustrated in

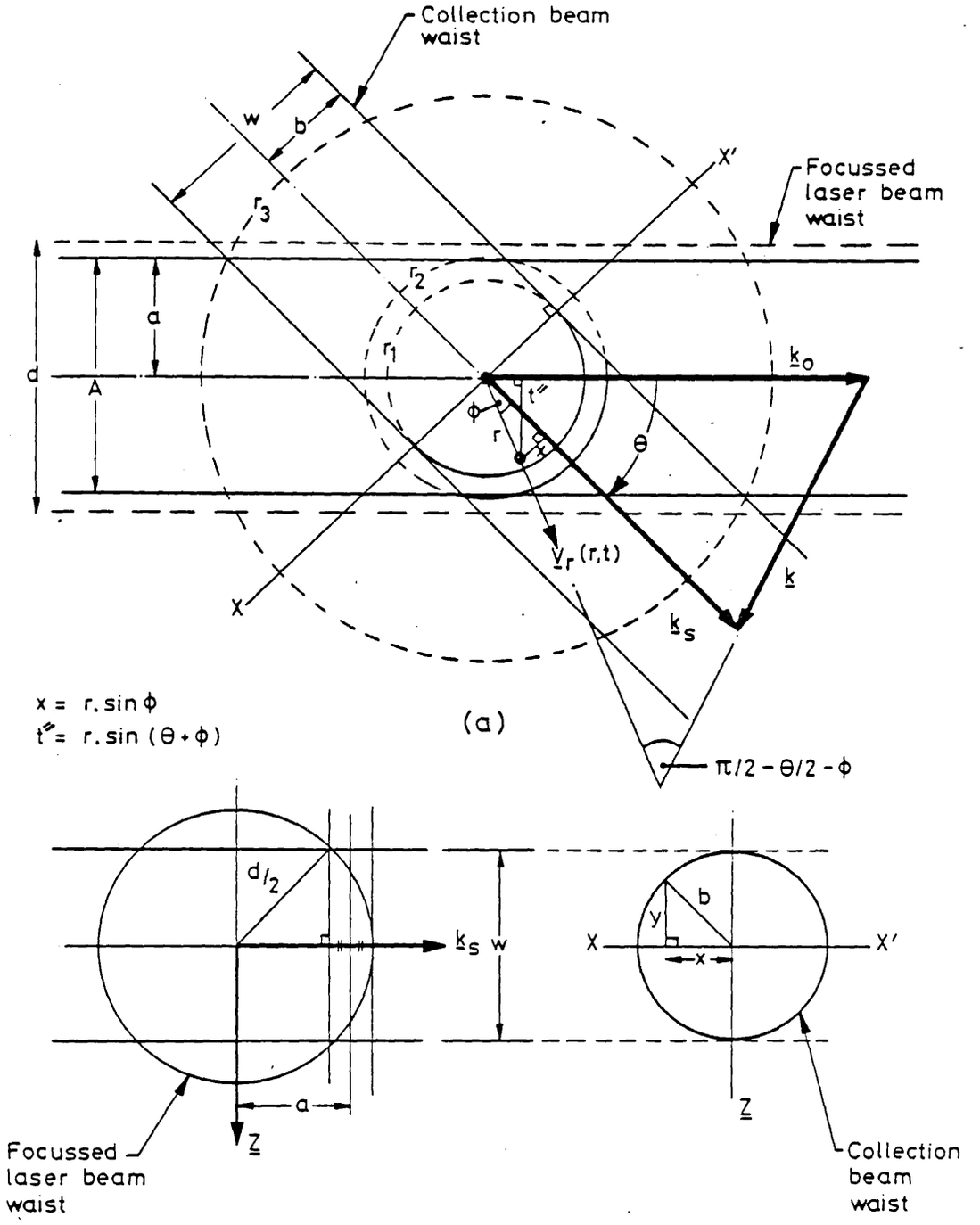

Figure 7.5

Geometry of intersection scattering volume for $\underline{k}$ orthogonal to $\underline{z}$.
(a) Intersection geometry of scattering volume viewed along the $\underline{z}$-axis.
(b) Intersection geometry of the scattering volume viewed along $\underline{k}_o$.
(c) Cross section of collection beam waist viewed along $-\underline{k}_s$.

figure 7.5c and is given by,

$$h(r,\phi) = \begin{cases} 2\left(\frac{w^2}{4} - r^2\sin^2\phi\right)^{\frac{1}{2}} & t''<A/2 \\ 0 & t''>A/2 \end{cases} \qquad (7.7)$$

where t'' given by,

$$t'' = r \sin(\theta+\phi) \qquad (7.8)$$

and indicated in figure 7.5a, limits the integral to within the confines of the approximated diameter, A of the focussed laser beam waist.

The electron number within this volume as a function of time is given by,

$$N_s(t) = F\int_{r_a}^{r_b} n_e(r,t)dr\int_{\phi_1(r)}^{\phi_2(r)} r.h(r,\phi)d\phi \qquad (7.9)$$

where $n_e(r,t)$ is the radial electron density profile as a function of time.

In order to evaluate the integrals, a numerical approximation was used, dividing the intersection volume into three radial ranges which are indicated in figure 7.5a. These are $r=0-r_1$, $r=r_1-r_2$ and $r=r_2-r_3$. Each radial range was then subdivided into 100 radial shells of equal radial thickness to facilitate numerical integration. For each radial shell, the angular range of ϕ was divided into 100 equal angular segements, $h(r,\phi)$ being calculated for the mean value of ϕ for each segment. The values of r_1, r_2 and r_3 and the $\phi_1(r)$ and $\phi_2(r)$ functions for each range were calculated by trigonometry and are summarised here,

$$r_1 = w/2$$

$$r_2 = \left[\left(\frac{A}{2\tan\theta} - \frac{w}{2\sin\theta}\right)^2 + \frac{A^2}{4}\right]^{\frac{1}{2}} \qquad (7.10)$$

$$r_3 = \left[\left(\frac{A}{2\tan\theta} + \frac{w}{2\sin\theta}\right)^2 + \frac{A^2}{4}\right]^{\frac{1}{2}}$$

For range $0 \leq r \leq r_1$,

$$\phi_1(r) = -\frac{\pi}{2} \quad : \quad \phi_2(r) = \frac{\pi}{2} \qquad (7.11)$$

For range $r_1 < r \leq r_2$,

$$\phi_2(r) = -\sin^{-1}\left(\frac{w}{2r}\right) : \phi_2(r) = \sin^{-1}\left(\frac{w}{2r}\right) \qquad (7.12)$$

For range $r_2 < r \leq r_3$,

$$\phi_3(r) = -\sin^{-1}\left(\frac{w}{2r}\right) : \phi_2(r) = \sin^{-1}\left(\frac{A}{2r}\right) - \theta \qquad (7.13)$$

At certain plasma times, the plasma radius will be smaller than the maximum radius of the intersection volume. Therefore, in calculating either integral equation 7.6 of 7.9, the upper limit of the integral, r_b can be set equal to $R_{pv}(t)$ if $r_b > R_{pv}(t)$ and $R_{pv}(t) < r_3$, since $n_e(r,t) = 0$ for $r > R_{pv}(t)$.

7.3.3.2 VOLUME DEFINED BY k ANTIPARALLEL TO z

The scattering volume integral for the 10 degree $\underline{k}$ antiparallel to $\underline{z}$ scattering arrangement is different to the $\underline{k}_o$ orthogonal to $\underline{z}$ arrangements described in the previous section, because the scattering plane is rotated by 90 degrees about the $\underline{k}_o$ axis. Figure 7.6a illustrates the intersection volume defined by the incident laser beam and the scattering collection beam waist viewed orthogonal to both $\underline{k}_o$

and the $\underline{z}$-axis. The intersection volume viewed parallel to the $\underline{z}$-axis is illustrated in figure 7.6b. Provided the plasma-vacuum boundary radius, R_{pv} is greater than the maximum radius, r_3 of the intersection volume, the contributing scattering volume will be identical in size to that of the 10 degree $\underline{k}$ orthogonal to $\underline{z}$ volume. However, for R_{pv} less than r_3, the volume will be different. More importantly the electron number as a function of radius will be marginally different for all R_{pv} values due to the rotation of the scattering plane. The scattering volume and electron number integrals are still given by eqs 7.6 and 7.9 respectively and can be evaluated using the same numerical technique. However, the integration ranges of r and ϕ are now different. The approximation of a rectangular laser beam intersection cross section assumed in the $\underline{k}$ orthogonal to $\underline{z}$ calculation and shown in figure 7.5b, was similarly assumed for the calculation given here, the rectangle again having dimensions of wxA. The collection beam waist of diameter, w, viewed along the $-\underline{k}_o$ direction will have an elliptical cross section as illustrated in figure 7.6c, with minor and major radii of w/2 and w/2cos(θ) respectively. It can be seen from figure 7.6a that the intersection volume when viewed orthogonal to $\underline{k}_o$ is symmetrical about the $\underline{z}$-axis and from figure 7.6b that it is symmetrical about $\underline{k}_o$. Therefore, the integral calculations can be limited to 1/4 of the scattering volume, the value of F in eqs 7.6 and 7.9 being set equal to 4 in this case. Using (r,ϕ) coordinates again to define a position on the x, k_o plane, the volume can be divided into 3 radial ranges, each with an angular ϕ range which were derived by trigonometry. These are summarised as,

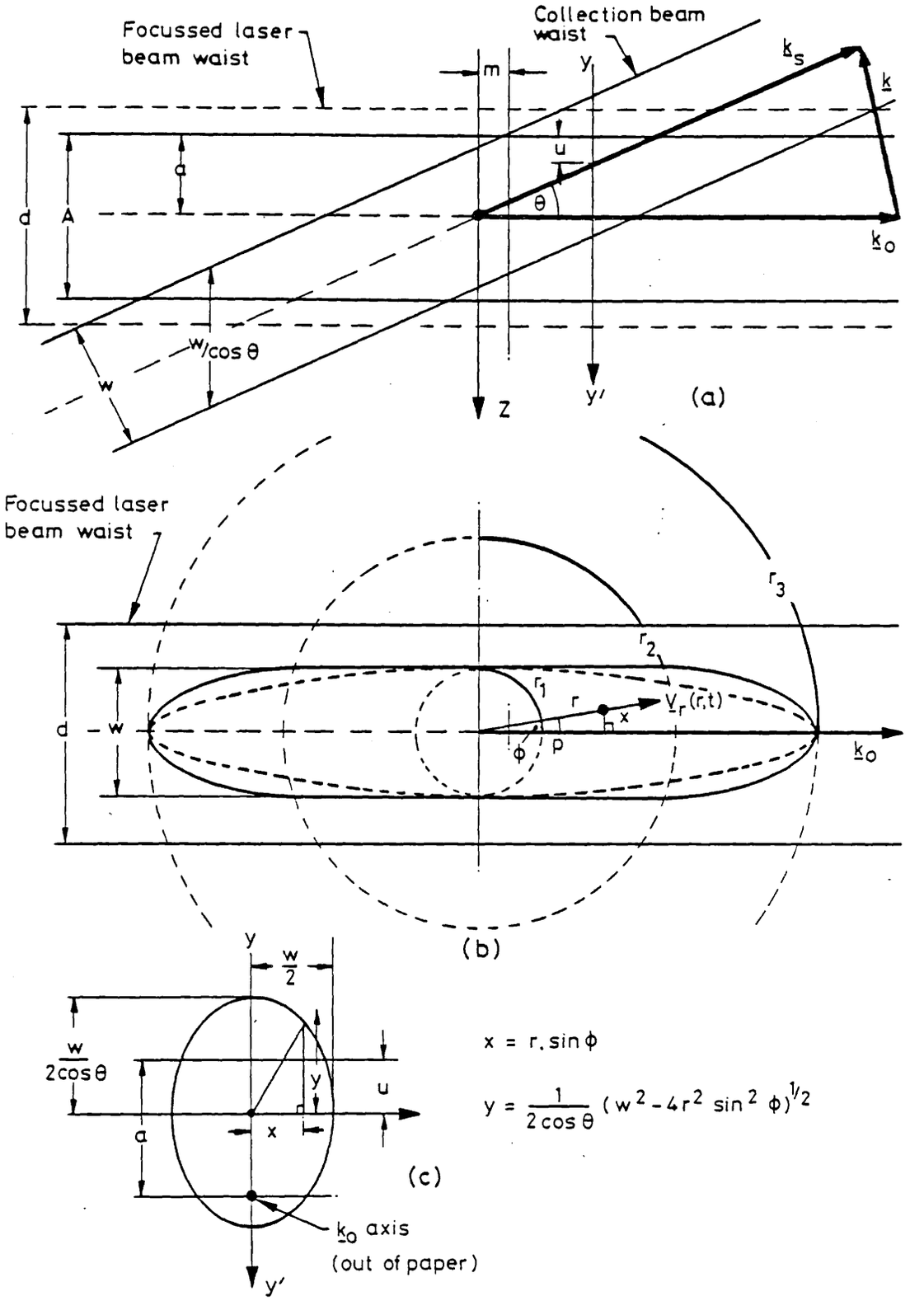

Figure 7.6

Geometry of intersection scattering volume for $\underline{k}$ antiparallel to $\underline{z}$.
(a) Geometry viewed orthogonal to both $\underline{k}_o$ and the $\underline{z}$-axis.
(b) Geometry viewed orthogonal to $\underline{k}_o$ and parallel to $\underline{z}$-axis.
(c) Cross section of collection beam waist viewed along $-\underline{k}_o$.

$$r_1 = \frac{w}{2}$$

$$r_2 = \frac{1}{2}\left(\frac{A^2}{\tan^2\theta} + w^2\right)^{\frac{1}{2}} \qquad (7.14)$$

$$r_3 = \frac{A\cos\theta + w}{2\sin\theta}$$

For range $0 \leq r \leq r_1$,

$$\phi_1(r) = 0 \quad : \quad \phi_2(r) = \pi/2 \qquad (7.15)$$

For range $r_1 < r \leq r_2$,

$$\phi_1(r) = 0 \quad : \quad \phi_2(r) = \frac{\pi}{2} - \cos^{-1}\left(\frac{w}{2r}\right) \qquad (7.16)$$

For range $r_2 < r \leq r_3$,

$$\phi_1(r)=0 \quad : \quad \phi_2(r) = \cos^{-1}\left[\frac{(A^2+4r^2-w^2)^{\frac{1}{2}} - A\sin\theta}{2r\cos\theta}\right] \qquad (7.17)$$

The value of the upper limit of the angular range for $r_2 < r \leq r_3$ is the positive solution of a quadratic. The function $h(r,\phi)$ in eqs 7.6 and 7.9 for this scattering volume orientation has two forms, which are dependent on the relative magnitude of two parameters y and u where

$$y = \frac{1}{2\cos\theta}\left[w^2 - 4r^2\sin^2\phi\right]^{\frac{1}{2}} \qquad (7.18)$$

is indicated in figure 7.6c and u indicated in figure 7.6a&b is given by,

$$u = \frac{w}{2\cos\theta} - [p-m]\tan\theta \qquad (7.19)$$

and can have both positive and negative values. The dimension m indicated in figure 7.6a is given by,

$$m = \frac{A\cos\theta - w}{2\sin\theta} \qquad (7.20)$$

and can have either a positive or negative value depending on the value of θ . The parameter p is the projection of r on the $\underline{k}_o$ axis and is given by $p=r.\cos(\phi)$.

(i) For $y \leq u$,

$$h(r,\phi) = 2y = \frac{1}{\cos\theta}\,[w^2 - 4r^2\sin^2\phi]^{\frac{1}{2}} \qquad (7.21)$$

(ii) For $y>u$,

$$h(r,\phi) = y+u = \frac{1}{2\cos\theta}\,[w^2 - 4r^2\sin^2\phi]^{\frac{1}{2}} + [\frac{w}{2\cos\theta} - (r\cos\phi - m)\tan\theta] \qquad (7.22)$$

The volume and electron number integrals were calculated using an identical technique to the $\underline{k}$ orthogonal to $\underline{z}$ calculation, in that the 3 radial ranges were each divided into 100 radial increments and the angular range at each radius was divided into 100 equal angular segments. The upper radial limit, r_b of either integral equation 7.6 or 7.9, was set equal to $R_{pv}(t)$ for the conditions specified at the end of the previous section.

7.3.4 DOUBLE SHELL SCATTERING VOLUME PARAMETERS

Having evaluated functions to describe the two scattering volume geometries, the calculation of the parameters of each of the shell scattering volumes can now be described, which will then enable the composite scattered profile for both regions to be formulated.

7.3.4.1 ELECTRON NUMBER

The calculation of the electron number within each shell scattering volume as a function of time, $N_j(t)$ was calculated using eq 7.9 for the radial ranges, $r_a=0$ to $r_b=R_D(t)$ for the core region (j=1) and for $r_a=R_D(t)$ to $r_b=R_{pv}(t)$ for the sheath region (j=2), where $R_D(t)$ had a value defined by the appropriate eq 7.1 or 7.2. The integral was calculated using the numerical technique specified in section 7.3.3.1 for the $\underline{k}$ orthogonal to $\underline{z}$ arrangements and section 7.3.3.2 for the $\underline{k}$ antiparallel to $\underline{z}$ arrangement.

7.3.4.2 ELECTRON DENSITY

The electron density of each shell volume could simply be calculated by dividing the electron number of each volume by the scattering volume dimension of the shell calculated using eq 7.6 for the ranges defined in the above section. However, as the electron density varies rapidly with radius, regions of low density and correspondingly low electron number would contribute less to the overall scattered profile of the shell volume than regions of high density. Therefore, the density of each shell scattering volume was calculated by weighting the electron density of each of the 300 radial increments used for the numerical integration by the electron number contained within the increment. The weighted electron density of each shell volume is then given by,

$$n_{e_j} = \frac{\int_{r_a}^{r_b} n_e^2(r,t)dr \int_{\phi_1(r)}^{\phi_2(r)} r.h(r,\phi)d\phi}{\int_{r_a}^{r_b} n_e(r,t)dr \int_{\phi_1(r)}^{\phi_2(r)} r.h(r,\phi)d\phi} \qquad (7.23)$$

where r_a and r_b for each shell are as specified in the previous section.

7.3.4.3 VELOCITY COMPONENTS - k ORTHOGONAL TO z

The calculation of the range of radial velocity component shifts for each shell volume was based on the division of the scattering volume into two halves as is indicated by the line X - X' in figure 7.5a. The wavelength shift of the scattering contribution from a volume located at r, ϕ due to a radial velocity $\underline{V}_r(r,t)$ is given using eq 3.3 by,

$$\Delta\lambda_r(r,\phi,t) = -\frac{n\lambda_o^2}{2\pi c}\,|\underline{k}|\,|\underline{V}_r(r,t)|\cos\left(\frac{\pi}{2} - \frac{\theta}{2} - \phi\right) \qquad (7.24)$$

where n=+1. A shift of the same magnitude, but of opposite sign (n=-1), will be contributed by a volume located diametrically opposite at $r,\phi+\pi$. Although the velocity of the collapsing sheath has been defined as negative, the symmetry of the scattering volume results in identical $\pm$ shifts for either sign of $\underline{V}_r(r,t)$. For a given radius r, the angular range of ϕ can be calculated from the relevant expression for the three radial scattering volume ranges, eqs 7.11-7.13.

The magnitude of the radial velocity of the plasma-vacuum boundary as a function of time, $|\underline{V}_{pv}(t)|$ can be derived from the holographic interferometry analysis (section 4.5.3.5) by calculating the derivative of eq 4.8 with respect to time,

$$|\underline{V}_{pv}(t)| = \left|\frac{R_{pv}(t+\Delta t) - R_{pv}(t-\Delta t)}{2\Delta t}\right| \qquad (7.25)$$

where the coefficients of eq 4.8 for z=10 mm and R_{pv} in metres are

given by $r'_1=1.85\times10^{-3}$, $r'_2=47.64$ and $r'_3=5\times10^{-4}$. The magnitude of the radial velocity of a volume located at a radial position r was then calculated by assuming a linear dependence of the radial velocity with radius. Therefore,

$$|\underline{V}_r(r,t)| = \frac{r}{R_{pv}(t)} |\underline{V}_{pv}(t)| \qquad (7.26)$$

the radial velocity for a volume element located on the $\underline{z}$-axis always being zero. The calculation of the radial velocity component attributable to each shell volume was approximated for the calculation of the dynamic form factor, $S_j(\underline{k},\lambda,t)$ for each volume, by calculating a radius, $R_j(t)$ for each volume which divided the volume radially into two volumes of equal electron number. This radius was calculated numerically by the same technique employed to calculate $N_j(t)$, by evaluating the upper limit of eq 7.9, $R_j(t)$ such that,

$$\int_{r_a}^{R_j(t)} n_e(r,t)dr \int_{\phi_1(r)}^{\phi_2(r)} r.h(r,\phi)d\phi = \frac{N_j(t)}{2} \qquad (7.27)$$

The angular range of ϕ, corresponding to half the scattering volume, was then determined at this radius using the relevant expression, eqs 7.11-7.13, depending on the value $R_j(t)$. This angular range was then divided into five equal angular segments and the ten wavelength shift values for the whole shell volume, $\Delta\lambda_{r_{jkn}}$ (k=1,2,...,5 and $n=\pm1$) were then calculated using eq 7.24 in the form,

$$\Delta\lambda_{r_{jkn}} = n\frac{2\lambda_o}{c}\sin(\theta/2)|\underline{V}_r(R_j,t)|\sin[\phi_k(R_j)+\frac{\theta}{2}] \qquad (7.28)$$

where $|\underline{V}_r(R_j,t)|$ is given by eq 7.26 and,

$$\phi_k(R_j) = \phi_1(R_j) + (k-\tfrac{1}{2})\left[\frac{\phi_2(R_j) - \phi_1(R_j)}{5}\right] \qquad (7.29)$$

7.3.4.4 VELOCITY COMPONENTS - k ANTIPARALLEL TO z

In chapter 3 during the discussion of the previous scattering experiments undertaken by Baconnet et al [16,17] and Bernard - et al [18,19] with a component of $\underline{k}$ aligned with the plasma $\underline{z}$-axis, it was stated that the authors concluded that the modification of the spectrum was due to separate effects. The first is the asymmetry and enhancement of the spectrum due to an electron-ion relative drift velocity, $\underline{D}$, resulting from the plasma current. Secondly, the bulk plasma motion in the direction of the $\underline{z}$-axis will produce a shift of the entire spectrum from the laser wavelength. For the $\underline{k}$ orientation used in the scattering experiment described here, which was dominated by a $\underline{k}$ component antiparallel to $\underline{z}$, this shift will be towards the red. Additionally, because the $\underline{k}$ orientation was inclined at 5 degrees to the $\underline{z}$-axis as illustrated in figure 7.7, the component of $\underline{k}$ orthogonal to the $\underline{z}$-axis, $\underline{k}_r$, will result in a modification of the scattered spectrum due to the radial velocity component. Although $\underline{k}_r$ is a factor of $\sin(\theta/2)=0.087$ of $\underline{k}$, it should be noted that $\underline{k}_r$ is aligned with $\underline{k}_s$ in this case, in contrast to the 10 degree $\underline{k}$ orthogonal to $\underline{z}$ geometry where $\underline{k}$ has its major component orthogonal to $\underline{k}_s$.

(1) Radial velocity component

The wavelength shift of the contribution to the scattered spectrum from a scattering volume located at r,ϕ as indicated in figure 7.6b due to a radial velocity $\underline{V}_r(r,t)$ is given by,

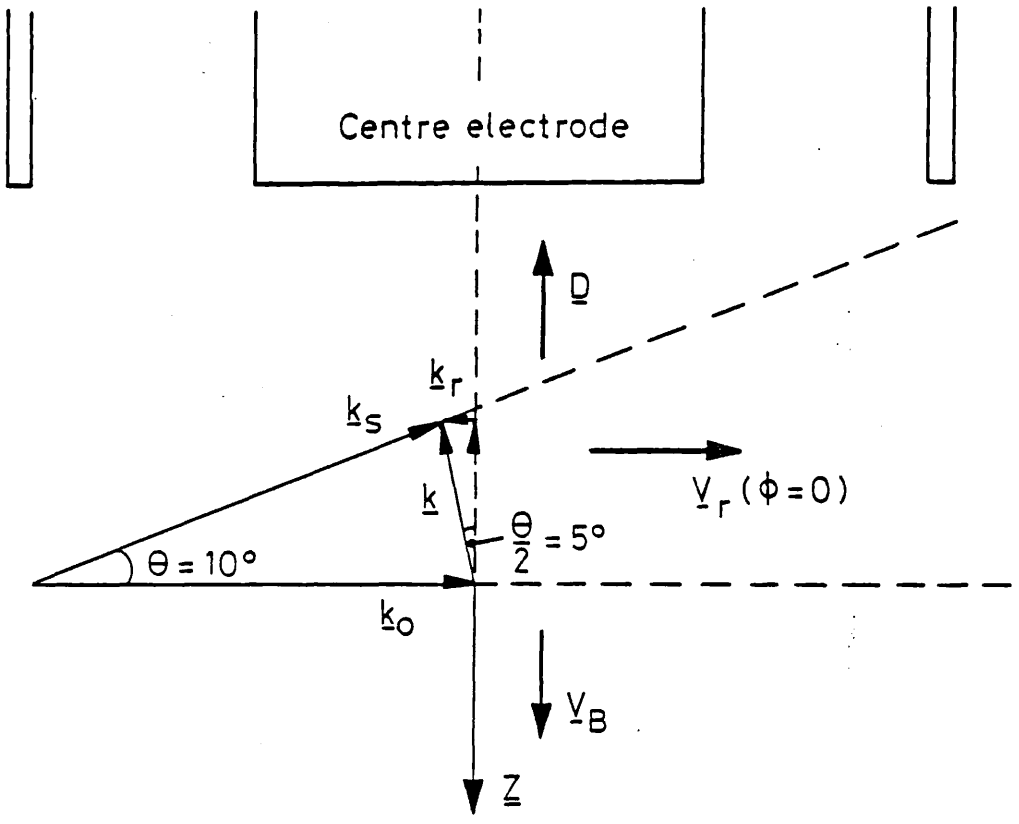

Figure 7.7
Geometry of scattering vector layout for 10 degree $\underline{k}$ antiparallel to $\underline{z}$ arrangement in relation to the radial velocity, bulk velocity and electron-ion relative drift velocity components.

$$\Delta\lambda_r(r,\phi,t) = \frac{n\lambda_o^2}{2\pi c} \; |\underline{k}_r||\underline{V}_r(r,t)|\cos(\phi) \qquad \sim (7.30)$$

where n=+1 and $\underline{k}_r = \underline{k}\sin(\theta/2)$. A shift of the same magnitude, but of opposite sign (n=-1), will be contributed by a volume located at $r,\phi+\pi$. It should be noted that the shift resulting from a volume located at $r,-\phi$ will be identical to that at r,ϕ, so the division of the scattering volume into four equal sections for this $\underline{k}$ orientation is still valid.

The radial velocity components for each shell were evaluated by a similar technique to that used for the $\underline{k}$ orthogonal to $\underline{z}$ arrangements but with eq 7.30 replacing eq 7.24.

The radius dividing each shell volume into two volumes of equal electron number, $R_j(t)$ was calculated using eq 7.27, the integration being done using the method detailed in section 7.3.3.2. The angular range of ϕ was then calculated using the appropriate eq 7.15-7.17 depending on the value of $R_j(t)$. This angular range was again divided into 5 equal angular segments and the ten wavelength shift values for the whole shell volume, $\Delta\lambda_{r_{jkn}}$ (k=1,2,..,5 and n=$\pm$1) were then calculated using eq 3.30 in the form,

$$\Delta\lambda r_{jkn} = \frac{n2\lambda_o}{c} \; |\underline{V}_r(R_j,t)|\sin^2(\theta/2)\cos\,[\phi_k(R_j)] \qquad (7.31)$$

where $|\underline{V}_r(R_j,t)|$ is given by eq 7.26. and ϕ_k is given by,

$$\phi_k(R_j) = (k-\tfrac{1}{2})[\phi_2(R_j)/5] \qquad (7.32)$$

as in this case $\phi_1(R_j)=0$ for all radial ranges.

(2) Bulk Plasma Velocity Component

Defining the bulk plasma velocity, $\underline{V}_B$ to have a direction along the z-axis as indicated in figure 7.7, the frequency shift of the scattered spectrum from the laser frequency, ω_o due to this component will be,

$$\Delta\omega_B = \underline{k}.\underline{V}_B$$

$$= -|\underline{k}||\underline{V}_B|\cos(\theta/2) \qquad (7.33)$$

The wavelength shift of the scattered profile contribution from each shell volume will therefore be given by,

$$\Delta\lambda_{B_j} = \frac{2\lambda_o}{c} \; \sin(\theta/2)\cos(\theta/2)|\underline{V}_{B_j}| \qquad (7.34)$$

i.e. a red-shift for $\underline{V}_{B_j}$ in the $\underline{z}$ direction.

(3) Relative Electron-Ion Drift Velocity

In order to utilize either the dynamic form factors given by eqs 2.47 and 2.48 for the case of a relative electron-ion drift velocity, or eq 2.49 for a drift velocity and stationary magnetic field, $\underline{B}$, we need to calculate for each shell volume the ratio, d_{r_j} of the component of the drift velocity, $\underline{D}_j$ aligned with $\underline{k}$ to the electron thermal speed v_{e_j}.
Using eq 2.46, this is given by,

$$d_{r_j} = \frac{|\underline{D}_j|}{v_{e_j}} \cos(\theta/2) = |\underline{D}_j| \left(\frac{m_e}{2eT_{e_j}}\right)^{\frac{1}{2}} \cos(\theta/2) \qquad (7.35)$$

where the drift velocity is defined as having a direction opposite to the $\underline{z}$ direction and the shell electron temperature, T_{e_j} is in units of eV. The drift to electron thermal speed ratio for each shell volume, D_{t_j} will then be given by,

$$D_{t_j} = \frac{|\underline{D}_j|}{v_{e_j}} = \frac{d_{r_j}}{\cos(\theta/2)} \qquad (7.36)$$

7.3.5 DOUBLE SHELL DYNAMIC FORM FACTOR

In section 2.5.1 it was stated that the Salpeter approximation of the full dynamic form factor was valid provided $T_e/T_i \lesssim 1$. Since the possibility of having radial regions of the Plasma Focus plasma where $T_e/T_i > 1$ existed, it was decided to use of the full dynamic form factor given by eq 2.31, for the analysis of both $\underline{k}$ orthogonal to $\underline{z}$ spectra.

In chapter 2, two dynamic form factors were given for the case of

drift velocity components aligned with the differential scattering vector, $\underline{k}$. The first, given by eq 2.47 excluded magnetic field effects and the second, given by eq 2.49 included the effect of a uniform stationary magnetic field, $\underline{B}$. Since the Plasma Focus has an azimuthal magnetic field, it would seem logical at first to use the second of these two expressions for the analysis of the 10 degree $\underline{k}$ antiparallel to $\underline{z}$ spectra. However, the first expression (eq 2.47) was employed for the following reasons:

(a) The resonance conditions for the electron cyclotron drift instability [36], which can lead to large enhancements of the scattering cross section for small d_r values [35], only occur for ϕ values of eq 2.49 for which $\phi \sim 90$ degrees. This condition is only met over a very limited range of the scattering volume, since the $\underline{k}$ of the antiparallel to $\underline{z}$ geometry is inclined at 5 degrees to the $-\underline{z}$-axis direction.

(2) The magnetic field profile of the sheath region, which has been measured by Muir [25], may be more complex than assumed, due to the possible existence of a filamentary current structure within the sheath region. This will be discussed further in section 7.5.3.

(c) The magnetic field profile of the sheath region, with either a planar or filamentary current structure will be far from uniform. The effect of having a gradient in $\underline{B}$ is to "smear out" the resonances and reduce the growth rate of the instability [36].

The Salpeter approximation of eq 2.47, given by eq 2.48, was not used for the same reasons as specified above for the $\underline{k}$ orthogonal to $\underline{z}$ spectra.

The dynamic form factors for each scattering geometry were modified to include the velocity components specified in the last two sections

as follows:

(1) k orthogonal to z

The dynamic form factor for each shell volume, $S_j(\underline{k}, \lambda, t)$ will now consist of a composite function of the dynamic form factors of the 5 angular segments, for which the radial velocity component shift has positive and negative values. The α value of the form.factor for each shell will be given using eq 3.1 by,

$$\alpha_j = 1.075 \times 10^{-5} \frac{\lambda_o}{\sin(\theta/2)} \left[\frac{n_{e_j}}{T_{e_j}}\right]^{\frac{1}{2}} \qquad (7.37)$$

where T_{e_j} is in units of eV. The dimensionless wavelength parameters x_e and x_i defined by eq 3.17 are redefined for each of the 10 angular radial velocity wavelength shift values by,

$$x_{e_{jkn}} = -\frac{c}{2\lambda_o \sin(\theta/2)} \left(\frac{m_e}{2eT_{e_j}}\right)^{\frac{1}{2}} (\lambda+\Delta\lambda_{r_{jkn}}) \qquad (7.38)$$

$$x_{i_{jkn}} = -\frac{c}{2\lambda_o \sin(\theta/2)} \left(\frac{m_i}{2eT_{i_j}}\right)^{\frac{1}{2}} (\lambda+\Delta\lambda_{r_{jkn}})$$

where T_{i_j} is the shell volume ion temperature in units of eV and $\Delta\lambda_{r_{jkn}}$ is given by eq 7.28.

The modified dynamic form factor for each shell volume is then given by,

$$S_j(\underline{k},\lambda,t)\,d\lambda\,d\Omega = \frac{1}{2\sum_{k=1}^{5} h(R_j,\phi_k)} \sum_{k=1}^{5} h(R_j,\phi_k) \qquad (7.39)$$

$$\times \sum_{n=\pm 1} S(x_{e_{jkn}}, x_{i_{jkn}}, \alpha_j)\, dx_{e,i}\, d\Omega$$

where $S(x_{e_{jkn}}, x_{i_{jkn}}, \alpha_j)$ has the form of eq 2.31 with Z=1 and the weighting factor $h(r,\phi)$ given by eq 7.7 is because of the circular cross section of the collection beam waist. The contribution of each angular segment being weighted by the mean h value of the segment where $\phi_k(R_j)$ is given by eq 7.29. The 1/2 factor is a result of the $n=\pm 1$ summation.

(2) <u>k antiparallel to z</u>

The modified dynamic form factor for each shell volume is similar to the $\underline{k}$ orthogonal to $\underline{z}$ case, but with the dimensionless wavelength shift parameters redefined to include the bulk velocity,

$$x_{e_{jkn}} = -\frac{c}{2\lambda_o \sin(\theta/2)} \left(\frac{m_e}{2e\,T_{e_j}}\right)^{\frac{1}{2}} (\lambda+\Delta\lambda_{r_j}+\Delta\lambda_{B_j})$$

$$x_{i_{jkn}} = -\frac{c}{2\lambda_o \sin(\theta/2)} \left(\frac{m_i}{2eT_{i_j}}\right)^{\frac{1}{2}} (\lambda+\Delta\lambda_{r_j}+\Delta\lambda_{B_j}) \qquad (7.40)$$

The modified form factor including radial, bulk and drift velocity components for each shell volume is then given by,

$$S_j(\underline{k},\lambda,t)\,d\lambda\,d\Omega = \frac{1}{2\sum_{k=1}^{5} h(R_j,\phi_k)} \sum_{k=1}^{5} h(R_j,\phi_k) \times \sum_{n=\mp 1} S(x_{e_{jkn}}, x_{i_{jkn}}, \alpha_j, d_{r_j})\,dx_{e,i}\,d\Omega \qquad (7.41)$$

where $S(x_{e_{jkn}}, x_{i_{jkn}}, \alpha_j, d_{r_j})$ has the form of eq 2.47 with Z=1, α_j is given by eq 7.37 and d_{r_j} by eq 7.35. The weighting factor $h(r,\phi)$ for the elliptical cross section of the collection beam waist is given by eq 7.21 or 7.22 depending on the values of R_j and ϕ_k which are given by

eq 7.27 and eq 7.32 respectively.

7.3.6 LASER PULSE CONVOLUTION

In section 3.4.2 it was stated that the radial velocity component cannot be ignored for shots timed at t=0 ns (zero radial velocity) because of the finite length of the laser pulse. A detailed study of the 20 ns FWHM laser pulse indicated that the pulse shape could be approximated by a triangular waveform which is illustrated in the normalised power plot of figure 7.8. The time of the peak of the pulse is defined as T=0 and it should be noted that the pulse is not symmetrical about this time.

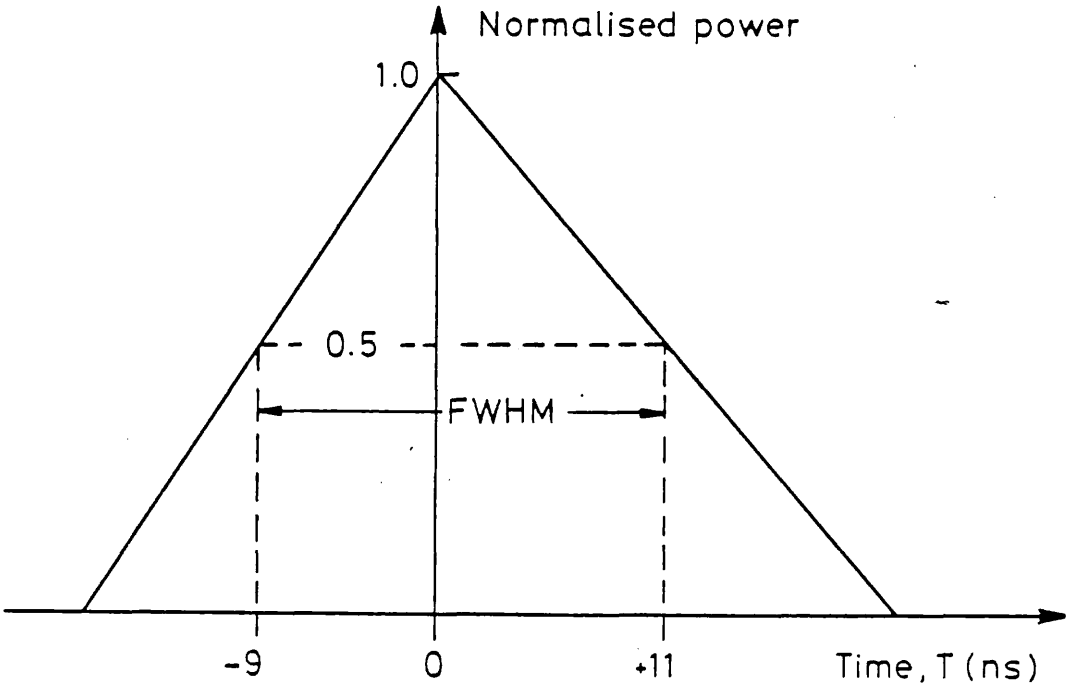

Figure 7.8
Triangular waveform approximation of ruby laser pulse used for the temporal convolution of the scattering dynamic form factor.

In order to include the temporal variation of the radial velocity component and the electron number and density, the full scattered

energy spectrum function for each shell scattering volume at a time t, was defined as the temporal convolution of the weighted profiles at (t+T), where T=-9, 0 and +11 ns. The composite scattered energy profile function for both shell scattering volumes is therefore given by,

$$E_s(\underline{k},\lambda,t)d\lambda d\Omega = R_A C d\lambda d\Omega \sum_{j=1}^{2} \sum_{T=-9,0,+11} W_T\, N_j(t+T) S_j(\underline{k},\lambda,t+T) \qquad (7.42)$$

where the constant C is given by eq 7.4, $S_j(\underline{k},\lambda,t)$ is given by eq 7.39 or 7.41 as appropriate to the scattering geometry $\underline{k}$ orientation, $d\Omega=1$ since the scattering data has been converted to units of J/str and the weighting factor, W_T is given by,

$$W_T = \begin{cases} 1/2 & T=0 \text{ ns} \\ 1/4 & T=-9, +11 \text{ ns} \end{cases}$$

The parameter, R_A which was a relative amplitude factor was incorporated to compensate for three possible errors:

(i) Errors in the assessment of the volume integral resulting in a larger or smaller electron number contribution within the scattering volume.

(ii) A Gaussian laser output would provide a Gaussian focussed laser beam waist. However, the poor spatial quality of ruby laser output beams, makes the focussed profile difficult to assess, so a flat topped profile has been assumed across the diameter of the focussed laser beam waist.

(iii) Shot to shot variation in both the plasma and laser pulse.

The inclusion of the relative amplitude factor within the fitting routine was designed to prevent the shape factor of the fitted profile being greatly modified due to scattering data amplitude variations due

to the above three effects.

It should be noted that in defining the composite scattered energy profile, it has been assumed that the parameters to be determined from the profile fitting procedure, which are T_{i_j} and T_{e_j} for the $\underline{k}$ orthogonal to $\underline{z}$ analysis and V_{B_j} and d_{r_j} for the $\underline{k}$ antiparallel to $\underline{z}$ analysis, are constant during the temporal convolution period. This is the principal disadvantage of using a long probing laser pulse length and an integrating detection system, as the parameters determined from the profile fitting represent the average of the parameters over the pulse length.

7.3.7 SCATTERED PROFILE LEAST SQUARES FITTING TECHNIQUE

An excellent review of data analysis techniques is given by Bevington [63]. Here, we will limit the discussion to the technique used to fit a profile function dependent on M non-linear parameters to the experimental data.

The fitting function for the analysis of each of the data sets will consist of the composite scattered energy profile given by eq 7.42 plus a background baseline function, $E_B(\lambda)$. In addition, we need to include the effect of the detection system instrument profile broadening in the fitting routine. The function to be fitted to the experimental data will therefore consist of the background plus composite scattered energy profiles convolved with the instrument profile. Each value of the fitting function, $E_F(\lambda)$ for the ith OMA channel, having a calibrated wavelength λ_i, is therefore given by,

$$E_F(\lambda_i) = \sum_{p=-8}^{+8} C_{I+p} \left\{ E_B(\lambda_i) + E_S(\underline{k}, \lambda_{i+p}, t) d\lambda d\Omega \right\} \qquad (7.44)$$

where C_{I+p} (p=-8,-7,...,+7,+8) are the 17 normalised instrument profile weighting coefficients for the appropriate scattering arrangement. These were determined from profile fitting to the measured instrument profiles, described in section 6.6.3 and values for the 45 degree scattering arrangement are tabulated in figure 6.8 (p180).

7.3.7.1 METHOD OF NON-LINEAR LEAST SQUARES

We can define a measure of goodness of fit, χ^2 of the fitting function, $E_F(\lambda)$ to a set of experimental data points, E_i as,

$$\chi^2 = \sum_i \left\{ \frac{1}{\sigma_i^2} [E_i - E_F(\lambda_i)]^2 \right\} \qquad (7.45)$$

where σ_i are the uncertainties in the data points E_i. According to the method of least squares, the optimum values of the fitted parameters a_ℓ (l=1,2,..,M) are obtained by minimising χ^2 with respect to each of the parameters simultaneously,

$$\frac{\partial \chi^2}{\partial a_\ell} = \frac{\partial}{\partial a_\ell} \sum_i \left\{ \frac{1}{\sigma_i^2} [E_i - E_F(\lambda_i)]^2 \right\} \qquad (7.46)$$

It is generally not convenient to derive an analytic expression for calculating the parameters of a non-linear function $E_F(\lambda)$. Instead, χ^2 must be considered a continuous function of M parameters, a_ℓ (l=1,2,...,M) describing a hypersurface in M-dimensional space. The space must be searched for the appropriate minimum value of χ^2.

One of the difficulties of this type of search is that for an

arbitrary function, there may be more than one local minimum of χ^2 within a reasonable range of values for the parameters a_ℓ. Unless the range of the parameters can be restricted to a region where it is known that there is only one minimum, it is advantageous to conduct a course grid search of the parameter space to locate the main minima and therefore limit the range of parameters over which to refine the search.

7.3.7.2 GRID SEARCH

If the variation of χ^2 with each parameter a_ℓ is fairly independent of how well optimised the other parameters are, then the optimium values can be determined most simply by minimising χ^2 with respect to each parameter separately. By making successive iterations of locating the local minimum for each parameter in turn, the absolute minimum may be located with any desired precision. This method is known as a grid search. The main disadvantage of this technique, is that if the variations of χ^2 with various parameters are not independent, then the interations will converge on the minima very slowly. Nevertheless, the simplicity of the calculations involved in a grid search often compensate for this inefficiency.

The procedure of the grid search is as follows:

(1) One parameter a_ℓ is incremented by a quantity Δa_ℓ, where the magnitude of this quantity is specified and the sign is chosen such that χ^2 decreases.

(2) The parameter a_ℓ is repeatedly incremented be the same amount Δa_ℓ until χ^2 starts to increase.

(3) Assuming that the variation of χ^2 with a_ℓ near the minimum can be described as a parabolic function, the values of χ^2 for the three final values of a_ℓ can be used to determine a value of a_ℓ corresponding to

the minimum of the parabola, as illustrated in figure 7.9. The value of a_ℓ at the mimima is given by,

$$a_\ell(\min) = a_\ell(3) - \Delta a_\ell \left[\frac{\chi^2(3) - \chi^2(2)}{\chi^3(3) - 2\chi^2(2) + \chi^2(1)} + \frac{1}{2} \right] \qquad (7.47)$$

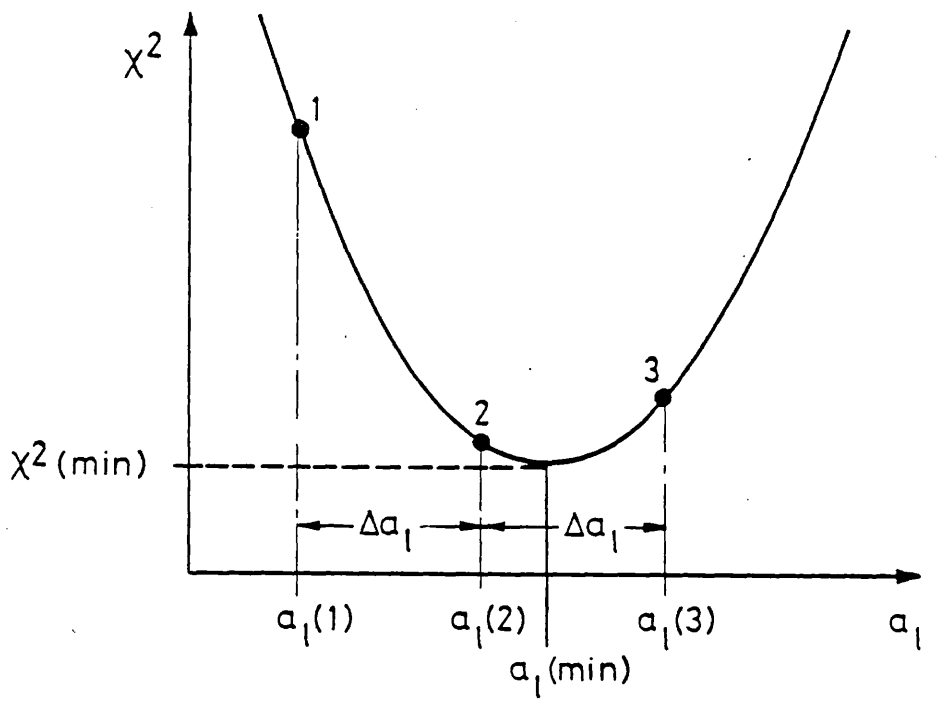

Figure 7.9
Parabolic interpolation to find $a_\ell(\min)$ for minimum χ^2 using the values of χ^2 for $a_\ell(1)$, $a_\ell(2)$ and $a_\ell(3)$.

(4) χ^2 is minimised for each of the other parameters in turn by repeating steps 1 to 3.

(5) The above four steps are repeated until the last iteration yields a negligibly small decrease in χ^2.

In fitting a function $E_F(\lambda)$ of the form given by eq 7.44, consisting of a background function and a peak function (scattered profile function), the general procedure is to fit $E_F(\lambda)$ simultaneously

over the whole range of data points. If however the background function varies slowly under the peak and can be reasonably interpolated under the peak, it is often preferable [63] to fit the background function outside the range of the peak and to fit the peak function only in the region of the peak. The parameters of each contributing function are therefore optimised for the separate regions of the data. The reason for this is that if the composite function is fitted over all the data points simultaneously, the value of χ^2 may be considerably influenced by the region where the peak merges with the background. This problem is particularly aggrevated where the number of counts in the peak is large and Poisson statistics are assumed. In using this separate fitting arrangement for the peak and background functions, the tail of the peak was included in the baseline fit and vice-versa. The cross-over points between the two fitting regions were calculated as those positions corresponding to a fraction of the maximum value of the peak function. The fractional value used for the analysis of all three triple spectra was 0.05.

The background function fitted in all cases was a quadratic with parameters a_l (l=1,2,3),

$$E_B(\lambda) = a_1 + a_2\lambda + a_3\lambda^2 \qquad (7.48)$$

where λ is the wavelength shift from the laser wavelength, λ_o.

7.3.7.3 UNCERTAINTY IN THE DATA POINTS

In section 3.5.5.2 were the signal to noise ratio of the scattered light was considered, it was assumed that the standard deviation, σ_i in the number of photons, y_i counted by a single OMA channel would be given by a Poisson distribution,

$$\sigma_i(\text{counts}) = [y_i(\text{counts})]^{\frac{1}{2}} \tag{7.49}$$

We therefore need to convert the standard deviation, σ_i from units of counts to J/str in a similar way to the data conversion described in section 7.3. If the conversion factor for the ith OMA channel is CF_i ($J.str^{-1}.count^{-1}$), then σ_i in J/str is given by,

$$\sigma_i = CF_i\left[\frac{E_i}{CF_i}\right]^{\frac{1}{2}} = \left[CF_i \times E_i\right]^{\frac{1}{2}} \tag{7.50}$$

7.3.7.4 ERROR DETERMINATION OF FITTED PARAMETERS

If the variation of χ^2 with respect to each parameter is independent of the values of the other parameters (at least near the minimum), the uncertainty, σa_ℓ in determining each parameter is given [63] by,

$$\sigma a_\ell^2 = \frac{2}{\partial^2\chi^2/\partial a_\ell^2} \tag{7.51}$$

In the grid search, the parameters are considered to be independent and the curvature of χ^2 can be determined from the final three values of a_ℓ of the search, which were used to determine the a_ℓ value at the minima of χ^2 by the parabolic interpolation. This yielded a value for σa_ℓ (l=1,2,...,M) from the final minimisation of χ^2 with respect to each

fitted parameter a_ℓ ($l=1,2,....,M$).

7.3.8 IMPLEMENTATION OF FITTING ROUTINES

The three spectra from each triple spectra shot were analysed as follows:

(1) 10 and 45 degree k orthogonal to z

The fitting function given by eq 7.44 was used with the shell dynamic form factor given by eq 7.39. To establish a greater independence of the fitted parameters, resulting in a faster convergence of the χ^2 minimum condition, the temperature parameters fitted were T_i and the ratio T_e/T_i for each shell volume. These were chosen because T_i essentially determines the width of the profiles and the the ratio T_e/T_i the profile shape. Additionally, the relative amplitude factor, R_A and the three baseline parameters were fitted.

Error in T_i and T_e of each shell volume

The error in T_i for each shell volume was determined directly from the fitting routine using eq 7.51. It was assumed that the error in the dispersion calibration was negligible in comparison to the fitting errors.

The fitting error in the ratio T_e/T_i can be similarly determined using eq 7.51. In determining the error in T_e however, the error in the density of the shell volume determined from the holographic interferometry must be taken into account. In section 2.5.1 it was stated that the Salpeter approximation allows eq 2.31 to be reduced to

eq 2.33 provided that the β^2 factor given by eq 2.34 is less than 3.45. Provided that this situation exists, then the β^2 factor essentially determines the shape of the ion spectrum. The effective fitted value of β^2 will be independent of variations in density as these will be compensated by a change in the fitted T_e/T_i ratio. We can therefore assume the Salpeter approximation for the calculation of the error in T_e provided that the fitted parameters result in a calculated $\beta^2 < 3.45$. The fitting error in the value of β^2 will be given by,

$$\delta\beta^2 = \left(\frac{\partial\beta^2}{\partial T_R} \cdot \delta T_R\right) = \frac{\beta^2}{T_R}\left(\frac{\alpha^2}{1+\alpha^2}\right)\delta T_R \qquad (7.52)$$

where $T_R = T_e/T_i$ and δT_R is the fitting error in T_R, determined using eq 7.51.

Writing $\alpha^2 = C' n_e/T_e$ where $C' = [\lambda_o/7400 \times \sin(\theta/2)]^2$, β^2 can be written as,

$$\beta^2 = \left[\frac{C' n_e}{1+C'(n_e/T_e)}\right] \cdot \frac{1}{T_i} \qquad (7.53a)$$

or

$$T_e = \frac{\beta^2 T_i C' n_e}{C' n_e - \beta^2 T_i} \qquad (7.53b)$$

The error in T_e is then given by,

$$\delta T_e = \left\{\left(\frac{\partial T_e}{\partial \beta^2}\ \delta\beta^2\right)^2 + \left(\frac{\partial T_e}{\partial T_i}\ \delta T_i\right)^2 + \left(\frac{\partial T_e}{\partial n_e}\ \delta n_e\right)^2\right\}^{\frac{1}{2}} \qquad (7.54)$$

$\beta^2 < 3.45$

where δT_i is the fitting error in determining T_i and δn_e is the error in n_e.

On evaluation of the derivatives and substituting for $\delta\beta^2$ from eq 7.52, the fractional error in T_e, $f_{T_e} = \delta T_e/T_e$ is given by,

$$f_{T_e} = \left\{ f_{T_R}^2 + \left(\frac{1+\alpha^2}{\alpha^2}\right)^2 f_{T_i}^2 + \left(\frac{1}{\alpha^2}\right)^2 f_{n_e}^2 \right\}^{\frac{1}{2}} \qquad (7.55)$$

$\beta^2 < 3.45$

where f indicates the fractional error in each parameter. It can be seen that for large α values ($\alpha >> 1$), f_{T_e} is dominated by the error in T_R and T_i as expected. From the assessment of errors discussion of section 4.5.3.4, values of f_{n_e} of 0.15 and 0.35 were used for the core and sheath regions respectively in the error calculations. The condition $\beta^2 < 3.45$ was found to be generally satisfied for both the core and sheath regions of all the shots analysed.

(2) 10 degree k antiparallel to z

The fitting function given by eq 7.44, with the shell dynamic form factor given by eq 7.41, was then used to analyse the 10 degree $\underline{k}$ antiparallel to $\underline{z}$ spectrum of each shot, using the shell temperatures and relative amplitude factor, R_A determined from the analysis of the 10 degree $\underline{k}$ orthogonal to $\underline{z}$ spectrum. The fitted parameters in this case were the shell bulk velocities, $\underline{V}_{B_j}$ and the sheath drift velocity, $\underline{D}_{j=2}$, in addition to the baseline parameters. Only shots timed at $t \leq 0$ ns were analysed, as the plasma current distribution is ill defined following peak compression. It can now be seen that the inclusion of the relative amplitude factor, permitted relative calibration to be made between the two 10 degree scattering arrangements on any shot, minimising the error in the determination of the sheath drift velocity ratio due to shot to shot variance in the scattering volume electron number and laser pulse energy.

For shots timed at $t > 0$ ns, only the baseline function, $E_B(\lambda)$ given

by eq 7.48 was fitted to the data points on either side of the peak function, to enable the total scattered energy to be determined as described in the subsequent section (3).

Error in V_B, D and D_t

The error in each shell bulk velocity, was determined directly from the fitting routine using eq 7.51. It was assumed that the error in $\underline{V}_B$ resulting from the dispersion calibration was negligible compared with the fitting error.

The fitting error in $\underline{D}$ can be determined similarly using eq 7.51. However, in determining $\underline{D}$ from the fitting routine, it is the component drift ratio, d_r that is being adjusted in the dynamic form factor. This fitted ratio is independent of the electron temperature of the shell volume, although it is sensitive to the temperature ratio T_e/T_i. Therefore, to a first approximation, the error in d_r, δd_r will be given by eq 7.51. The error in $\underline{D}$ is then given by the compounded error in d_r and σ_e,

$$f_D = \left\{\left(\frac{\delta d_r}{d_r}\right)^2 + \frac{1}{4} f_{T_e}^2\right\}^{\frac{1}{2}} \qquad (7.56)$$

where f_{T_e} is the fractional error in T_e evaluated using eq 7.55 from the analysis of the 10 degree $\underline{k}$ orthogonal to $\underline{z}$ spectrum.
The fractional error in the ratio of the drift to thermal electron speeds will be the same as the fractional error in determining d_r from the fitting procedure.

(3) Total Scattered Energy

Having fitted the appropriate profile function to each spectra, the total integrated scattered energy of each spectra and the individual shell volume contributions were then computed as follows.
The total scattered energy was evaluated by summing the energy of each channel minus the fitted baseline function value for that channel,

$$E_T(\underline{k}) = \sum_i \left\{ E_i - E_B(\lambda_i) \right\} \tag{7.57}$$

The individual shell volume energy contribution to the above total was evaluated in a similar fashion using the appropriate fitted shell dynamic form factor for the $\underline{k}$ orientation given by eq 7.39 or 7.41,

$$E_{s_j}(\underline{k},t)\,d\lambda\,d\Omega = \sum_i \left\{ R_A C\,d\lambda\,d\Omega \sum_{T=-9,0,+11} [W_T\, N_j(t+T) \right.$$

$$\left. \times\, S_j(\underline{k},\lambda_i,t+T)] - E_B(\lambda_i) \right\} \tag{7.58}$$

Error in the total scattered energy

The error in the determination of the total scattered energy of each spectra or the contribution from each shell volume is subject to the errors from two calibrations: the sensitivity calibration of the detection system discussed in section 6.6.1 and the individual calibration of the neutral density filters and polarisers employed in the collection optics. The compounded error resulting from these was estimated as being $\leq 20\%$.

7.3.9 LIMIT OF THE DOUBLE SHELL MODEL

The limit of the double shell model technique for determining a composite profile function was found to be set by the ratio of the contributing shell volume scattered energies, $E_{s_1}(\underline{k},t)/E_{s_2}(\underline{k},t)$, where E_{s_1} and E_{s_2} were determined using eq 7.58. It was found that for $E_{s_1}/E_{s_2}>30$, the fitting errors in T_i and the ratio T_e/T_i for the sheath region became prohibitively large. Therefore a restriction of $E_{s_1}/E_{s_2}\leq 30$ was implemented. The effect of this was to restrict the use of the double shell model to a specific time region. This was t=-35 ns to t=+10 ns for the 10 degree $\underline{k}$ orthogonal to $\underline{z}$ analysis and t=-25 ns to t=0 ns for the 45 degree $\underline{k}$ orthogonal to $\underline{z}$ spectra. The shots outside this time region were analysed using the fitting fucntion given by eq 7.44, but with the scattered energy contribution given by eq 7.42, being limited to the core (j=1) region only. This restriction is not a major problem since the plasma becomes disrupted by instabilities soon after t=0 ns and the use of the double shell technique would no longer be resonable.

7.4 RESULTS OF THE ANALYSIS

The fitted profiles for each spectrum of one triple spectra shot timed at t=0 ns are shown in figures 7.10a-c. Figure 7.10a shows the 10 degree $\underline{k}$ orthogonal to $\underline{z}$ spectrum, figure 7.10b the 45 degree $\underline{k}$ orthogonal to $\underline{z}$ spectrum and figure 7.10c the 10 degree $\underline{k}$ antiparallel to $\underline{z}$ spectrum. This shot was within the temporal period for which a double profile could be fitted for each of the three spectra. In each figure the two dotted lines indicate the fitted profiles for each of

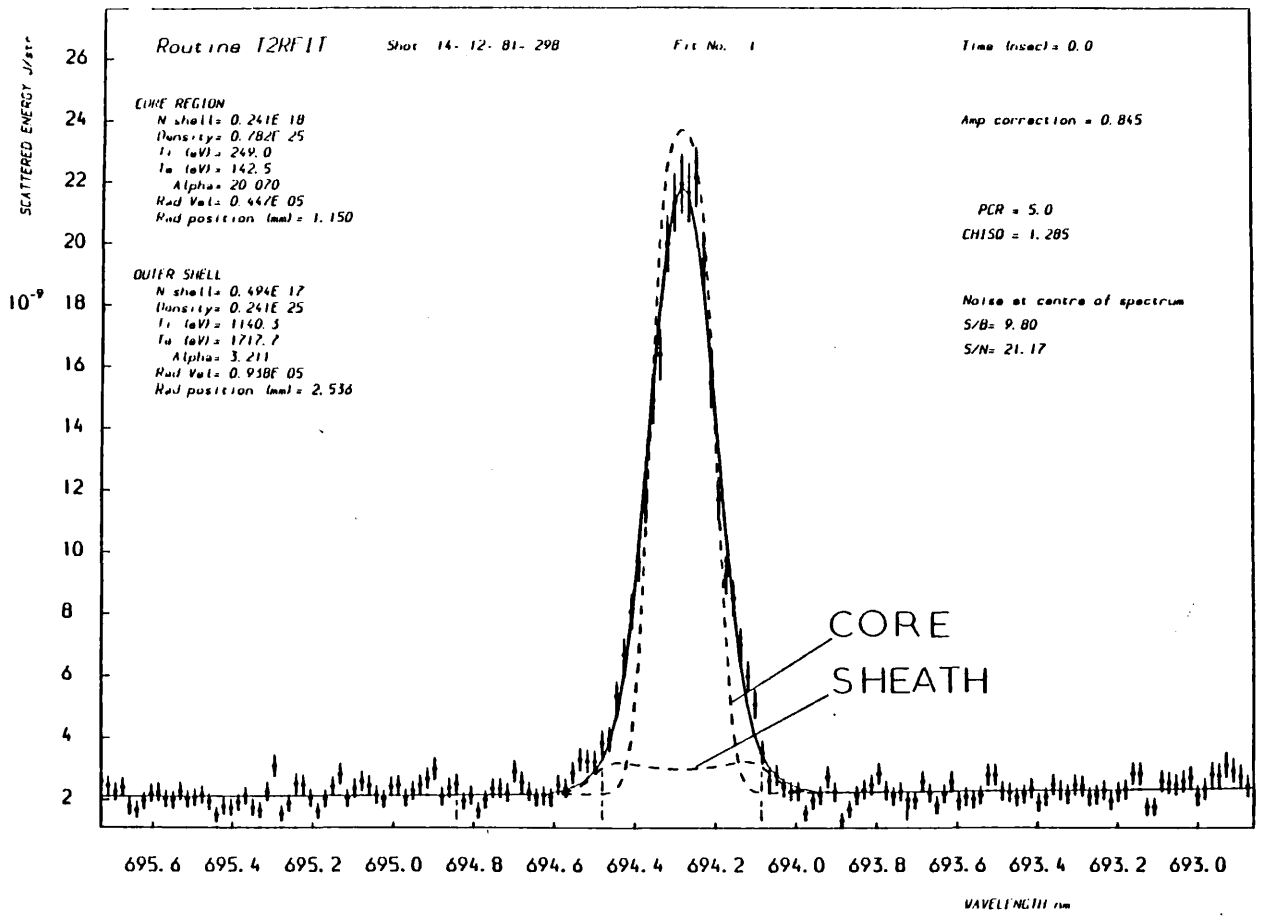

Figure 7.10a

Double shell volume composite profile fit to 10 degree k orthogonal to z spectra at t=0 ns to determine fitted parameters of T_i and T_e for core and sheath regions.

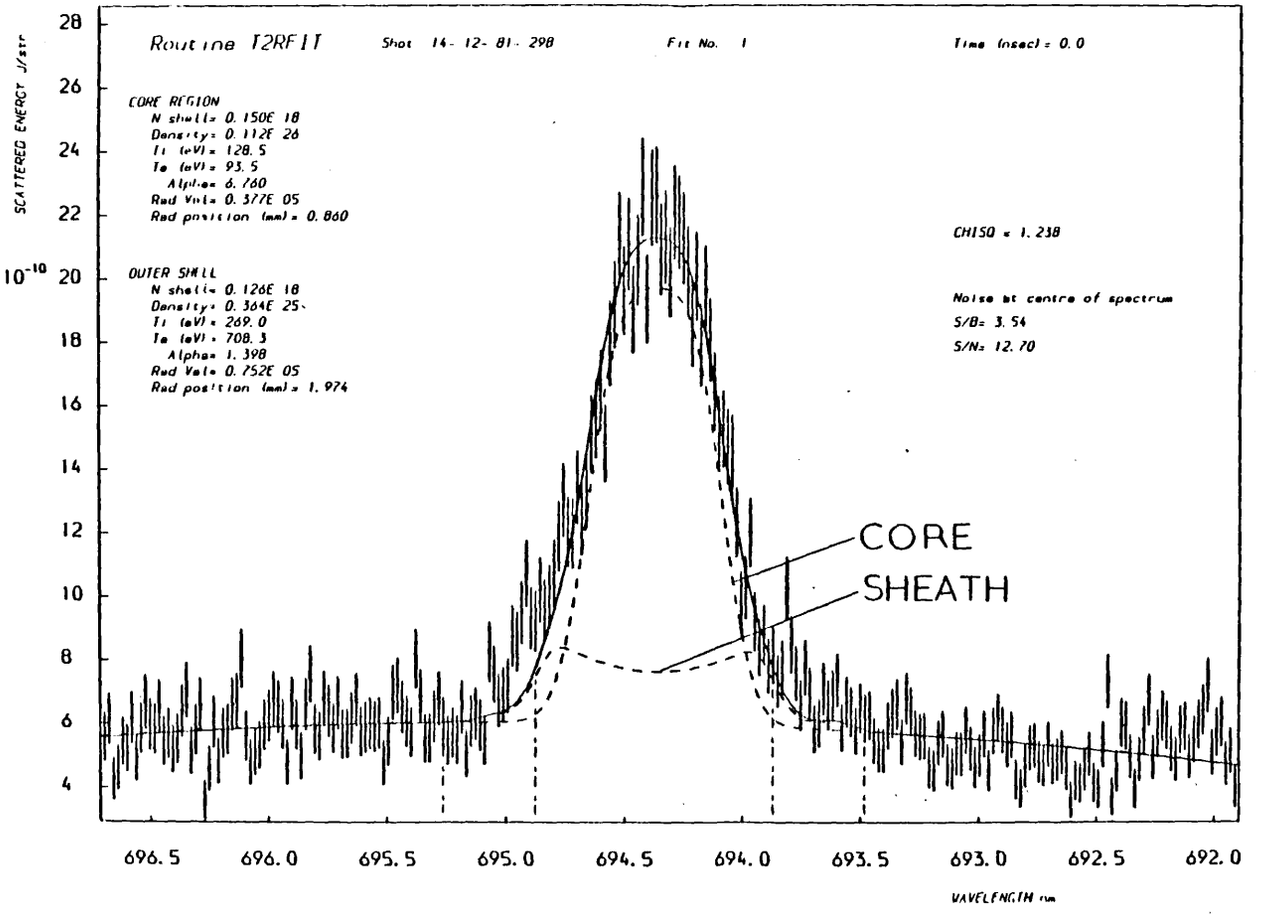

Figure 7.10b

Double shell volume composite profile fit to 45 degree $\underline{k}$ orthogonal to $\underline{z}$ spectra at t=0 ns to determine fitted parameters of T_i and T_e for core and sheath regions.

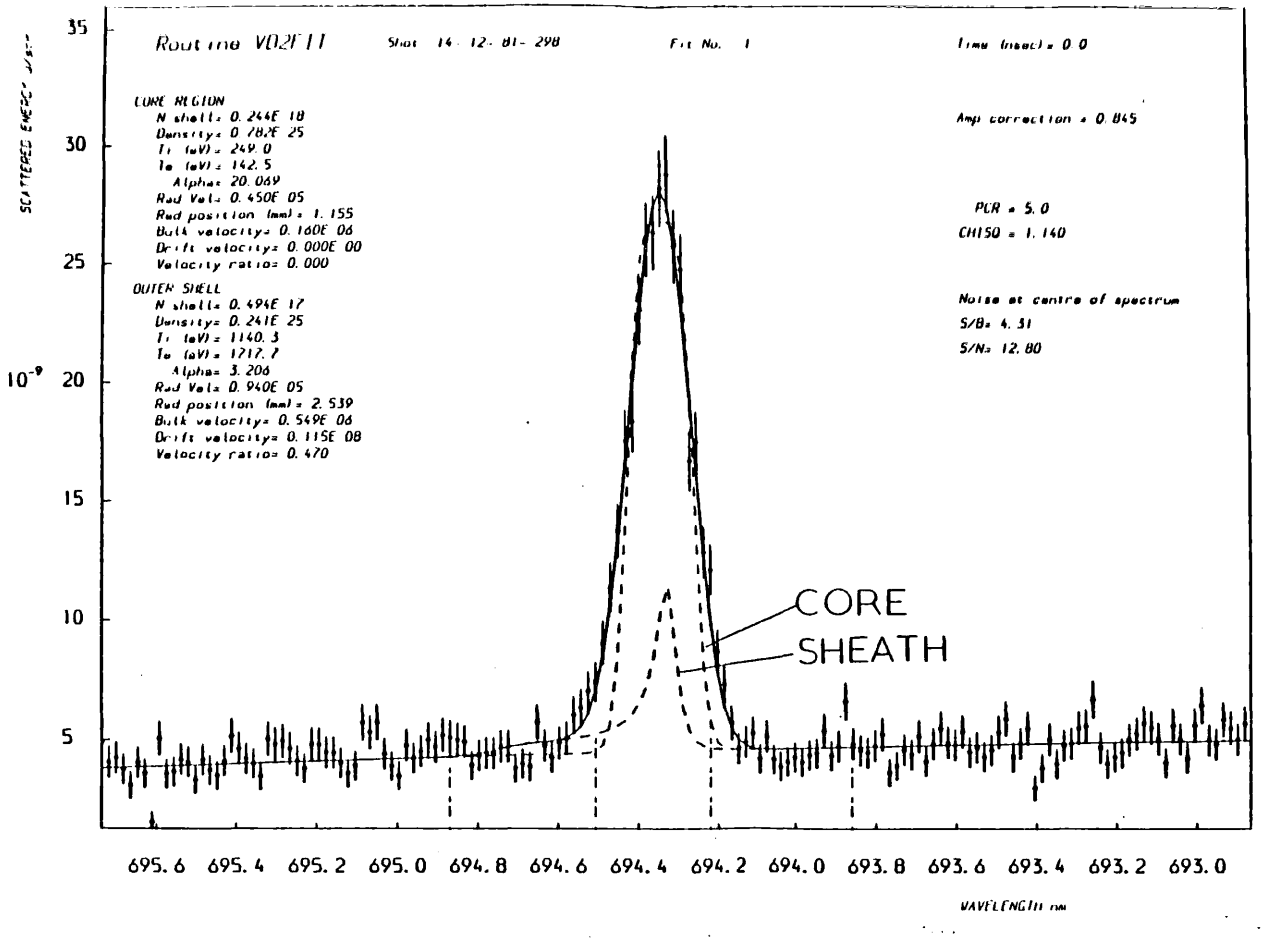

Figure 7.10c

Double shell volume composite profile fit to 10 degree $\underline{k}$ antiparallel to $\underline{z}$ spectra at t=0 ns to determine fitted parameters of $\underline{D}$ for the sheath region and $\underline{V}_B$ for the core and sheath regions.

the shell volumes plus the baseline profile and the continuous line is the fitted function, $E_F(\lambda)$ given by eq 7.44, consisting of the superposition of the two shell and baseline profiles convolved with the instrument profile. The figures also tabulate the measured signal to background (S/B) and signal to noise (S/N) ratios at the centre of each spectrum. The S/B ratio for the 10 degree $\underline{k}$ orthogonal to $\underline{z}$ spectrum is an order of magnitude smaller than that calculated for the core region contribution in section 3.5.5.3, although the S/N ratio is only reduced to 2/3 of the calculated ratio. The 45 degree spectrum has a S/B ratio which is $\sim$25% of the calculated value for the core contribution and a S/N ratio of similar magnitude to the calculated value. The calculations of section 3.5.5.3 were of course based on the classical bremsstrahlung law, so the lower observed S/B ratios are probably as a result of other significant background emission contributions such as recombination.

The temporal evolution of the parameters determined from the analysis of the spectra of each $\underline{k}$ arrangement will now be detailed. In all the results presented, the error in the timing of each shot is $\pm$2.5 ns. This figure was the estimated error in determining the relative timing of the peak of the ruby laser pulse and the dI/dt plasma trace.

7.4.1 10 DEGREE k ORTHOGONAL TO z

Two distinct groups of spectra were revealed from the analysis. One type had a thermal scattering level, the spectra being symmetric about the laser wavelength and the relative amplitude factor R_A derived from the fitting routine was in the range 0.75 - 1.25. The second type, which will be termed anomalous, showed a supra-thermal scattered

energy level and broadening relative to the thermal shots. Some of these shots were strongly asymmetric, with the peaks of the spectrum shifted either to the red or blue of the laser wavelength. These shots were additionally associated with large enhancements of the 10 degree $\underline{k}$ antiparallel to $\underline{z}$ spectrum which will be discussed in section 7.4.3. We will consider the results of the analysis of the thermal level spectra first.

Thermal Level Shots

Figures 7.11-7.14 show the shell temperature parameters determined from the analysis of the 10 degree $\underline{k}$ orthogonal to $\underline{z}$ spectra. The data points for $t \geq +10$ ns, indicated by triangles in figure 7.11 and 7.12, were derived from single shell profile fitting for the core region as detailed in section 7.3.9. In each of the four figures, the data for $t \leq +10$ ns has been divided into two groups indicated by filled and open circular data points. The reason for distinguishing between the two groups will become apparent on studying the sheath ion (fig 7.13) and electron (fig 7.14) temperature plots. It can be seen that the data points appear to fall onto two different profiles as a function of time, which will be termed mode A and B as indicated. Although this division may seem arbitrary at this stage, it will be seen from the sheath ion temperature plot derived from the 45 degree spectra analysis, that a similar division of the data is observed there, but with a different relationship between the temperature profiles. In each plot the assumed temperature profile outside the time period investigated is indicated by a dotted line. In plotting the profiles it was assumed that the sheath ion and electron temperatures at t=-40 ns are equal and have a value of 100 eV. It can be seen from comparing figure 7.13 and 7.14, that the T_e/T_i ratio for one set of

data points is approximately unity at peak compression (T_i=1.4 keV, T_e=1.65 keV), while the other indicates a T_e/T_i ratio of $\sim$2.7 (T_i=850 eV, T_e=2.3 keV).

The core region ion and electron temperatures rise constantly during the peak compression phase to values at t=0 ns of $T_i \sim$ 250 eV, $T_e \sim$ 200 eV and continue to rise to a peak value of $T_i \sim$ 300 eV, $T_e \sim$ 225 eV at t=+10 ns. It should be noted that the spread of data points after peak compression is probably due to the onset of the pinch break-up, the plasma disruptions resulting in shot to shot variation of the plasma within the scattering volume. The steady rise of the core temperature during the compression phase should be contrasted with the initial rapid rise in sheath temperature from t=-40 ns to -20 ns following which the temperature remains approximately constant until t=0 ns.

A plot of the total scattered energy of the 10 degree $\underline{k}$ orthogonal to $\underline{z}$ spectra as a function of time, derived from using eq 7.57 for each shot, is shown in figure 7.15. As would be expected, the scattered energy rises during the collapse phase as the number of scattering electrons within the scattering volume increases. The converse following t=0 ns is also observed.

Anomalous Shots

The temporal evolution of the core ion temperature is again plotted in figure 7.16, but with the anomalous shots now included. These are indicated simply by their error bars. The mass of data points along the bottom of the plot are those of the thermal level shots. One shot prior to peak compression was observed at t=-20 ns. The analysis of

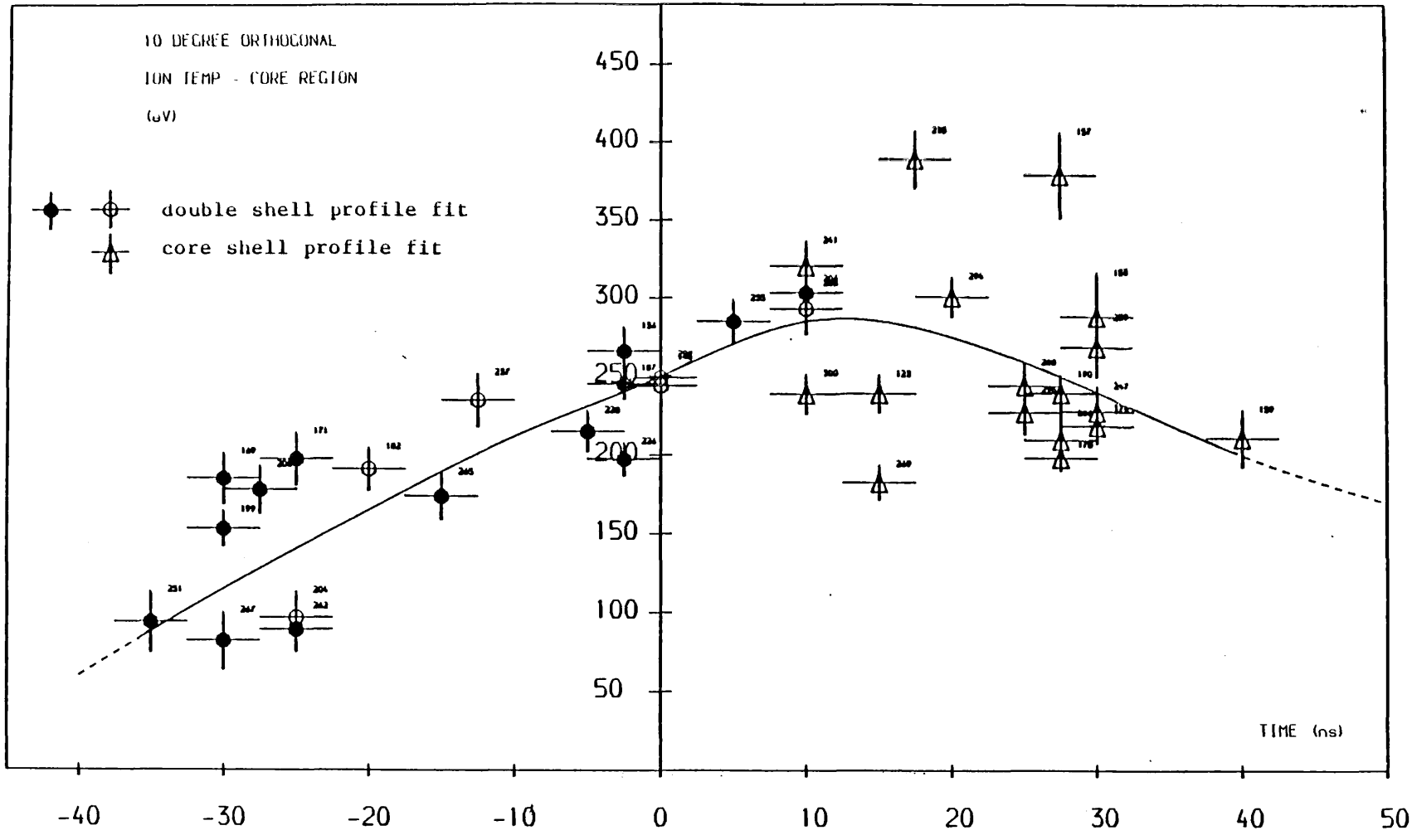

Figure 7.11
Temporal variation of the core ion temperature determined from the 10 degree k orthogonal to z spectra.

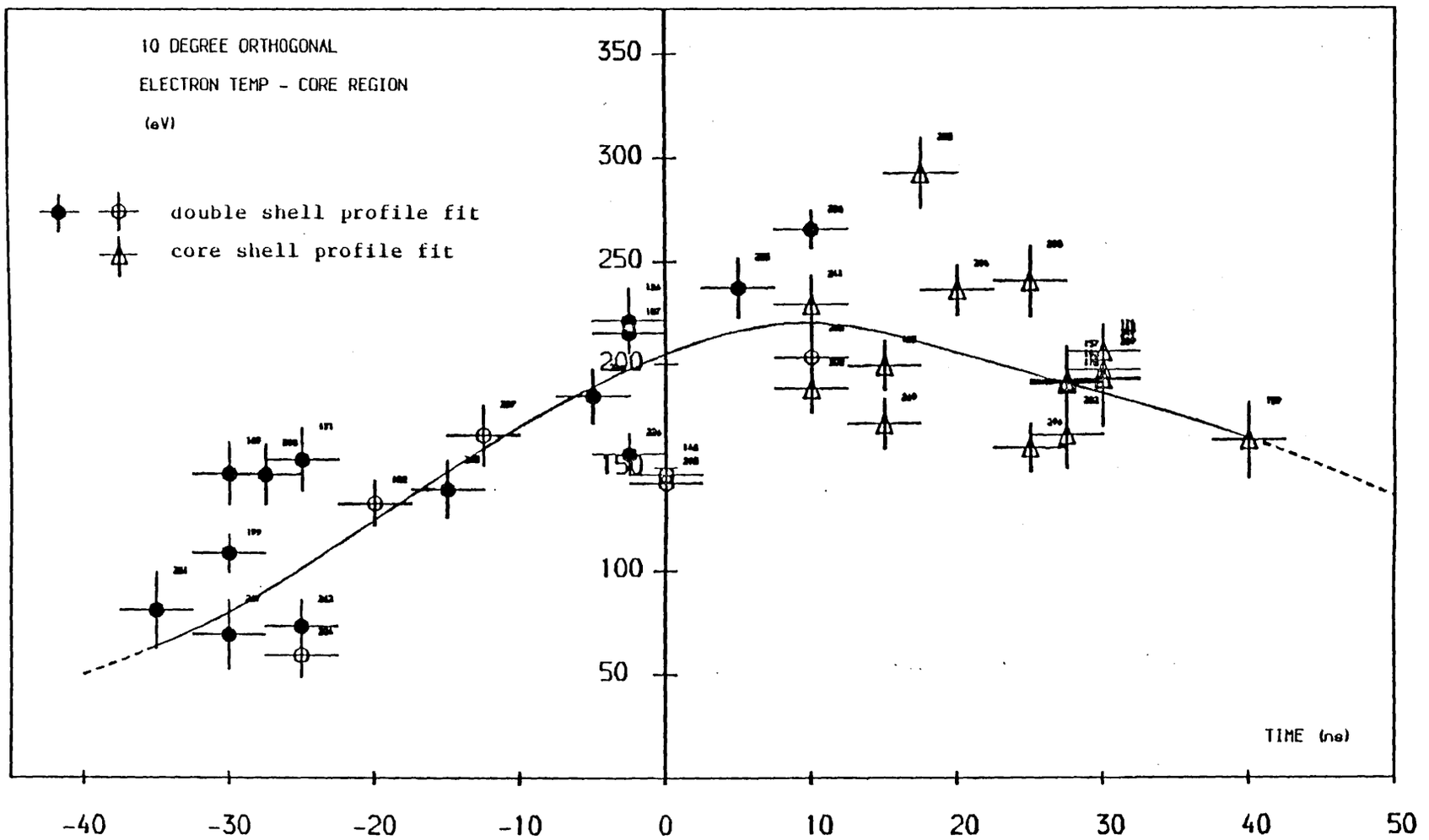

Figure 7.12
Temporal variation of the core electron temperature determined from the 10 degree k orthogonal to z spectra.

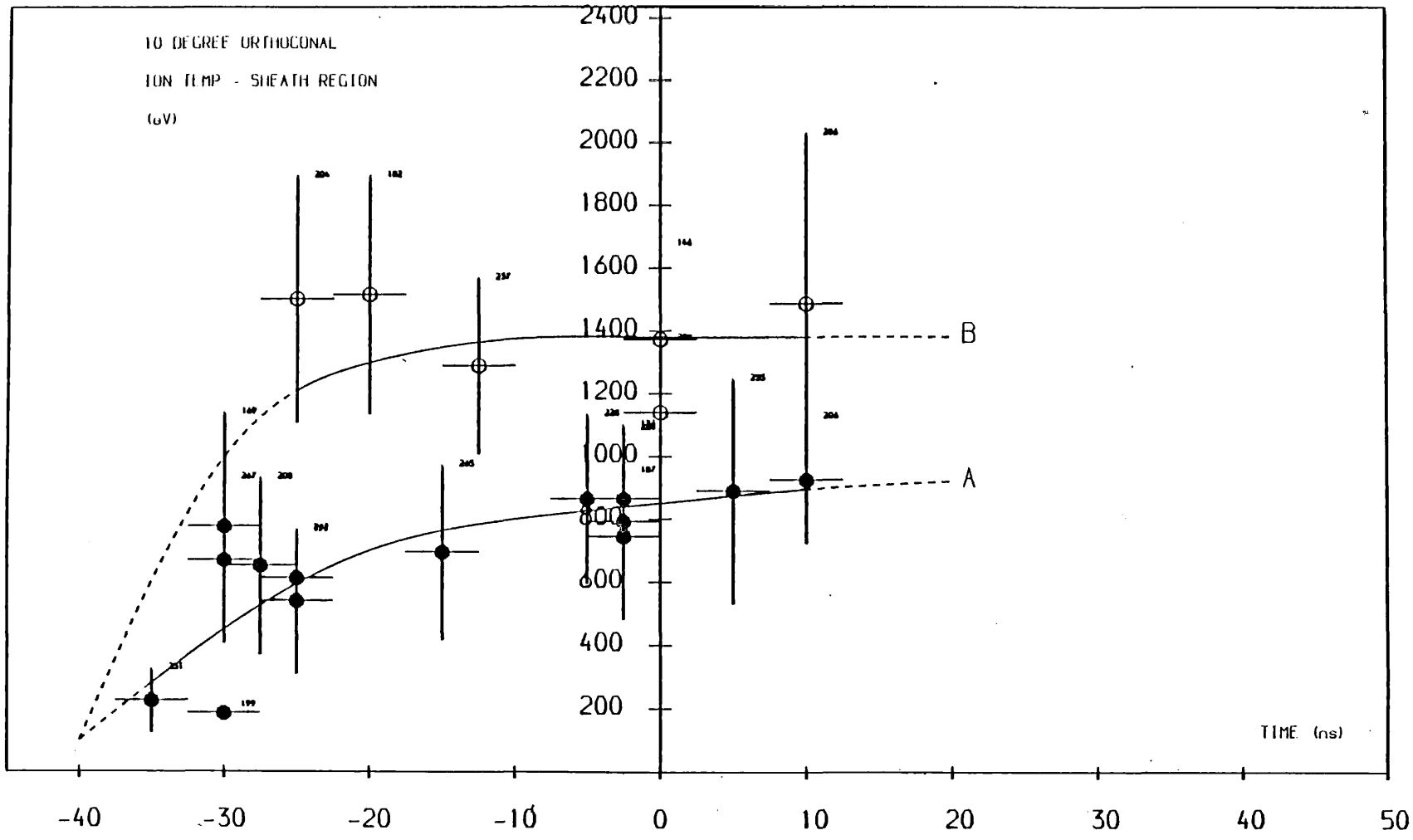

Figure 7.13
Temporal variation of the sheath ion temperature determined from the 10 degree k orthogonal to z spectra.

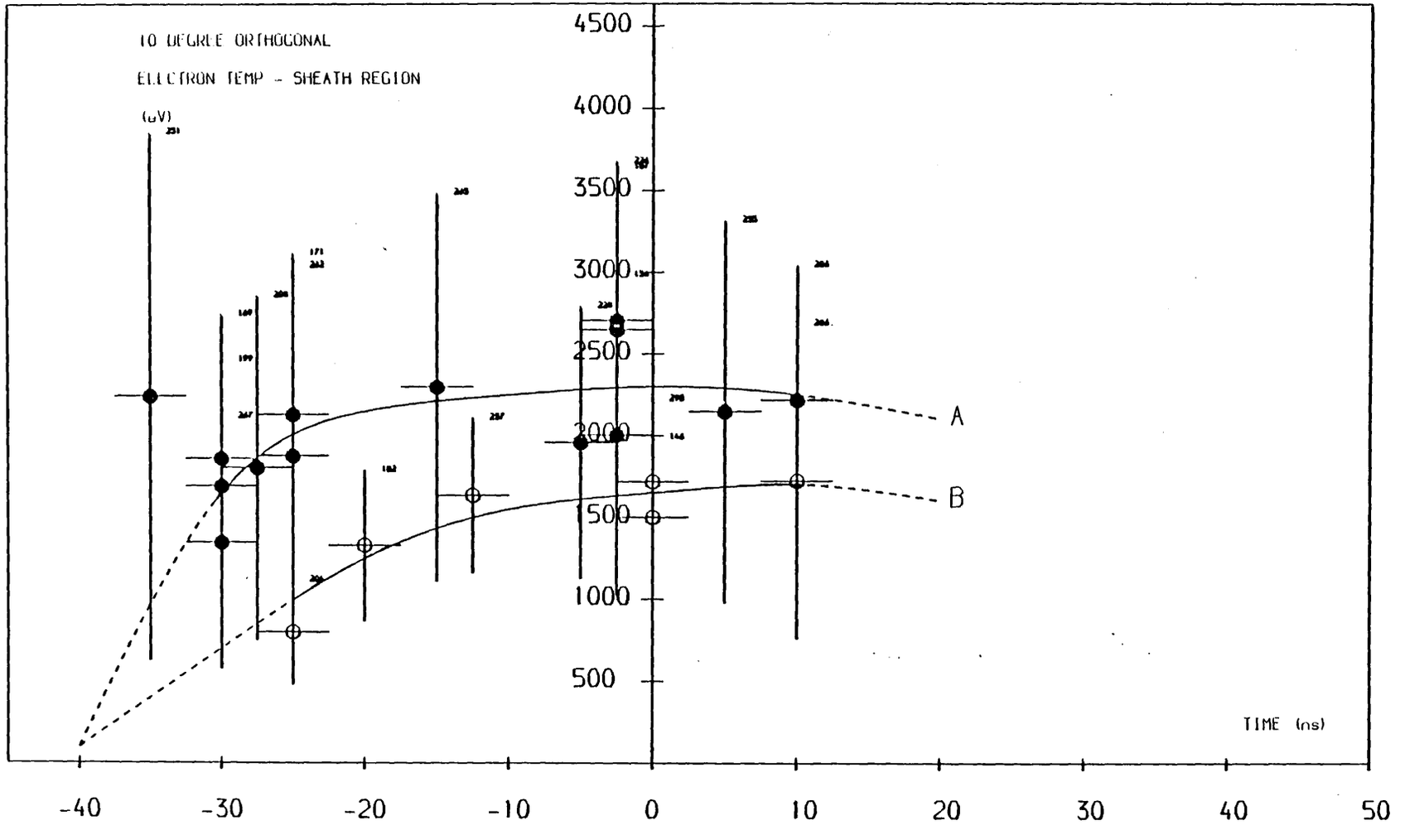

Figure 7.14
Temporal variation of the sheath electron temperature determined from the 10 degree $\underline{k}$ orthogonal to $\underline{z}$ spectra.

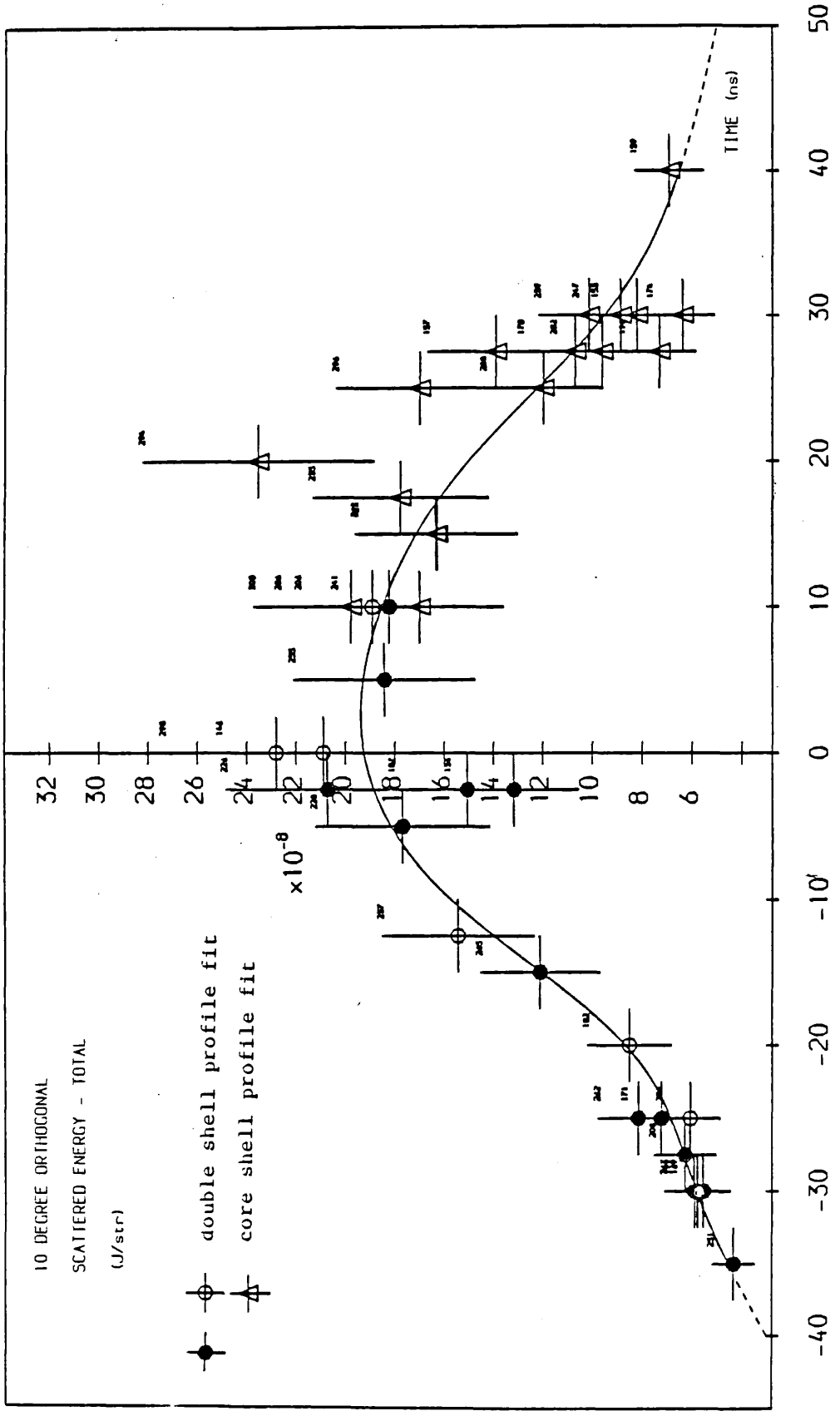

Figure 7.15

Temporal variation of the total scattered energy of the 10 degree $\underline{k}$ orthogonal to $\underline{z}$ spectra for thermal shots only.

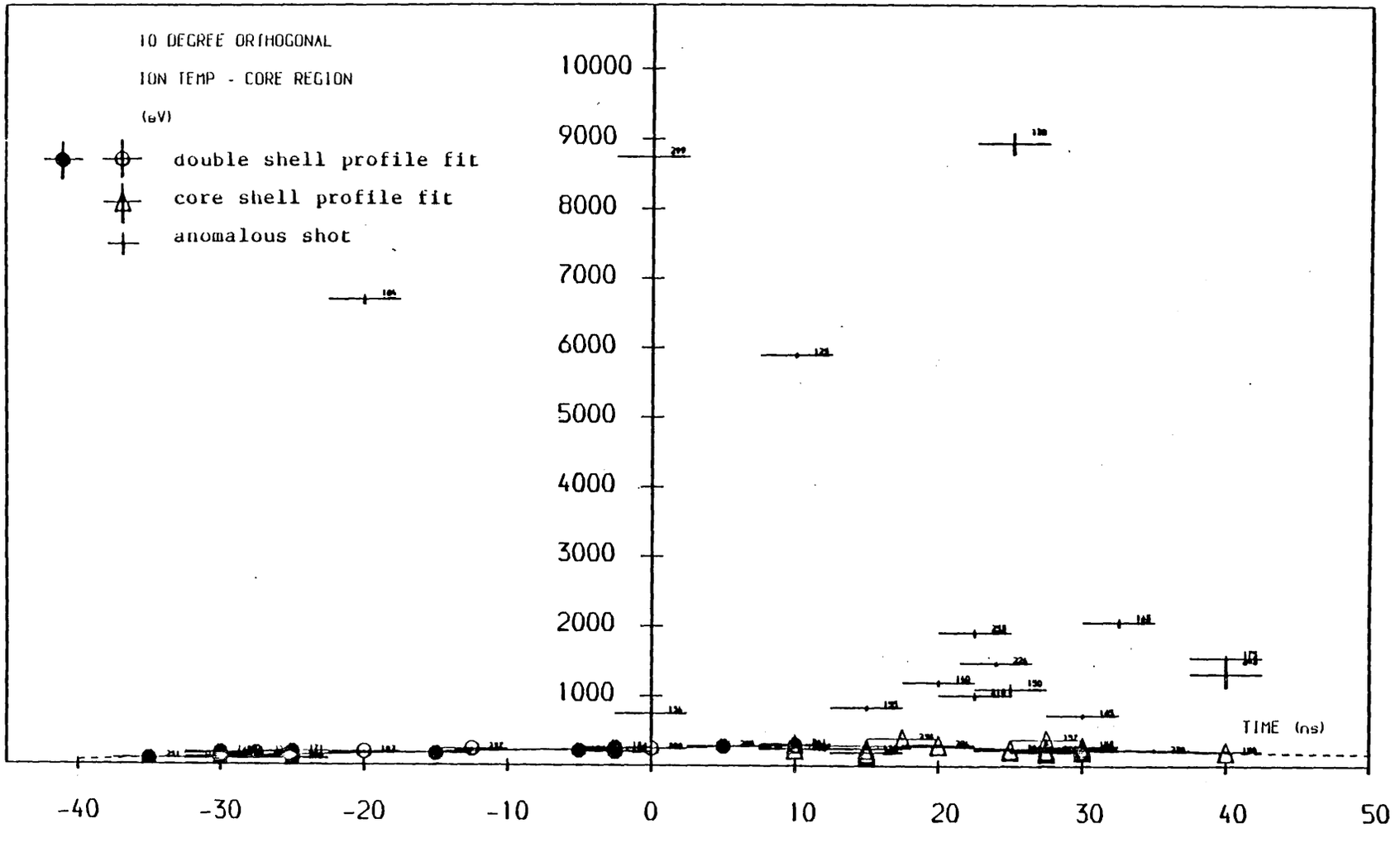

Figure 7.16
Temporal variation of the core ion temperature for thermal and anomalous shots determined from the 10 degree k orthogonal to z spectra.

the anomalous shots was based on a single shell volume fitting function only. As the gross broadening of the spectra is probably as a result of plasma turbulence, the fitting of a dynamic form factor based on eq 2.31 is not valid. However, the use of such a form factor gave an indication of the width of these spectra relative to their thermal counterparts. Figure 7.17 shows a plot of the ratio of the total scattered energy of the anomalous spectra to the thermal scattering level, indicated by the curve in figure 7.15, as a function of time. It can be seen that enhancements of up $\sim$25 above the thermal level were observed.

From the two figures (7.16 and 7.17) two types of anomalous shot were discernable:

(a) The first type showed a moderate enhancement in scattered energy, with a scattered to thermal energy ratio in the range 0.5 - 3. These shots were associated with a broadening of the spectrum, with a 1/e half width equivalent to an ion temperature in the range 500 eV to 2 keV and were symmetric about the laser wavelength.

(b) The second type showed large scale enhancements of the scattered energy, the ratio of the scattered to thermal level being in the range 4 - 25. These shots had 1/é half widths equivalent to ion temperatures in the range 2 - 9 keV, with the exception of one shot with a width equivalent to 230 eV. Some of these shots were symmetric about the laser wavelength, others showed strong asymmetry with either positive or negative peak shifts from the laser wavelength in the range 0.1 - 0.25 nm. In analysing the above shots two modifications were made to the analysis technique. Firstly, to overcome the effects of the gross spectral broadening, the number of data points used was increased from 150 to 250. Secondly, the peak shifts were analysed by including an additional fitted wavelength shift parameter in eq 7.38.

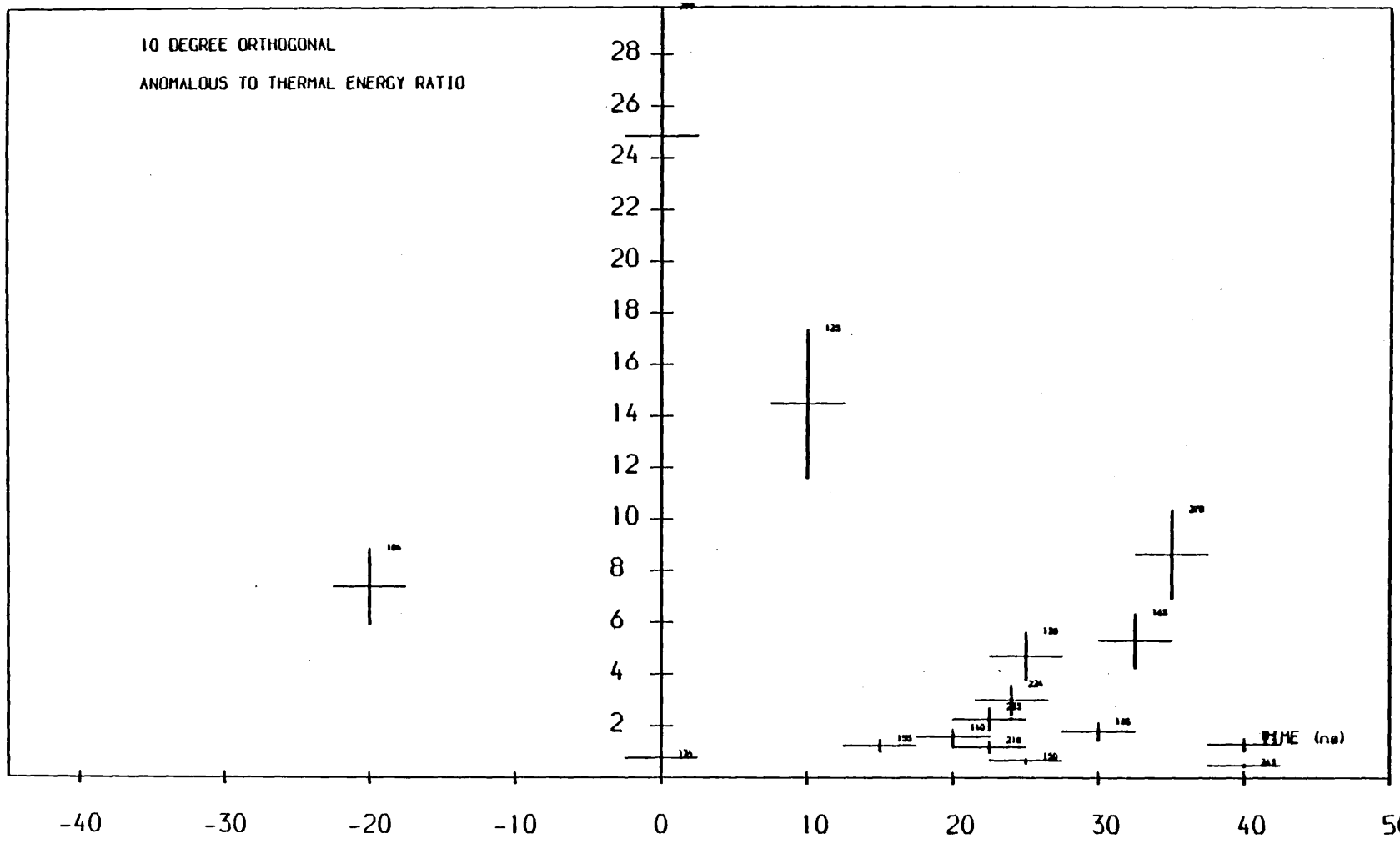

Figure 7.17
Temporal variation of the ratio of the total scattered energy to the thermal energy level of the 10 degree k orthogonal to z anomalous spectra.

The mechanisms responsible for these anomalous shots will be discussed in detail in section 7.5.8.

7.4.2 45 DEGREE k ORTHOGONAL TO z

The equivalent profiles to figures 7.11 to 7.14 for the 45 degree analysis are shown in figures 7.18-7.21 respectively. It should be noted that these plots include both the shots termed thermal and anomalous in the previous section, since for this $\underline{k}$ arrangement there was no discernable difference between the two types. The anomalous shots in the 10 degree $\underline{k}$ orthogonal to $\underline{z}$ analysis having a thermal scattering level for the 45 degree $\underline{k}$ orthogonal to $\underline{z}$ arrangement. The range of the fitted relative amplitude factor was slightly larger than that for the 10 degree $\underline{k}$ orthogonal to $\underline{z}$ analysis and had values of 0.7 - 1.3. The shots for $-25\ \text{ns} \leq t \leq 0\ \text{ns}$ indicated by filled or open circles in the 10 degree $\underline{k}$ orthogonal to $\underline{z}$ analysis are similarly indicated in figures 7.18 to 7.21. The shots outside this time region were fitted for a single shell volume profile as was detailed in section 7.3.9 and are again indicated by triangles in the plots.

With this scattering arrangement, the most obvious difference is in the sheath temperature plots (figs 7.20 and 7.21). The relative position of the two groups of data points (mode A and B) indicated in figure 7.13 for the sheath ion temperature determined from the 10 degree $\underline{k}$ orthogonal to $\underline{z}$ analysis are now reversed in figure 7.20. Additionally, the sheath electron temperature plot of figure 7.21, no longer shows a division as was the case with the 10 degree $\underline{k}$ orthogonal to $\underline{z}$ plot shown in figure 7.14. Both temperature plots for the sheath region show far lower temperatures than were indicated from the

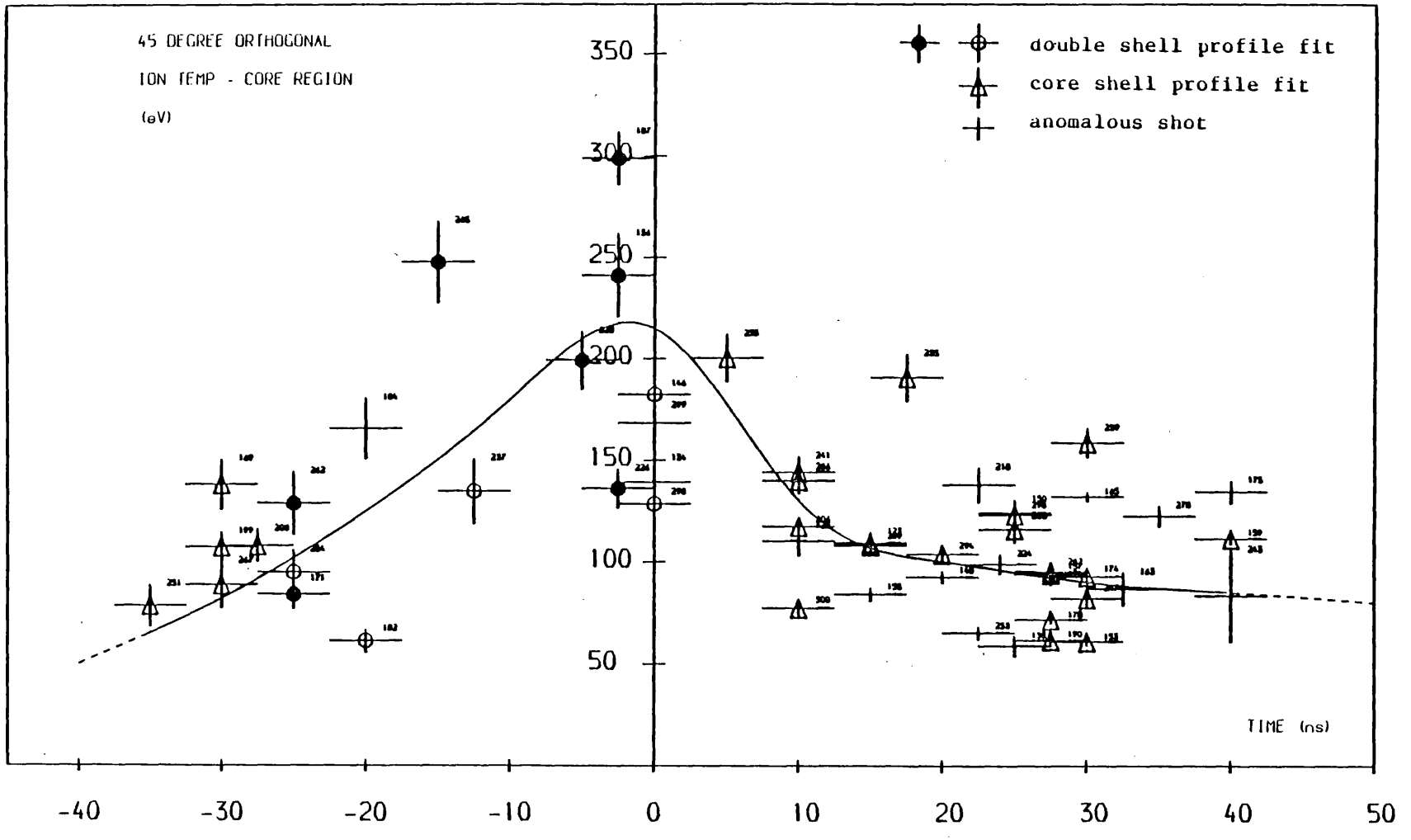

Figure 7.18
Temporal variation of the core ion temperature determined from the 45 degree k orthogonal to z spectra.

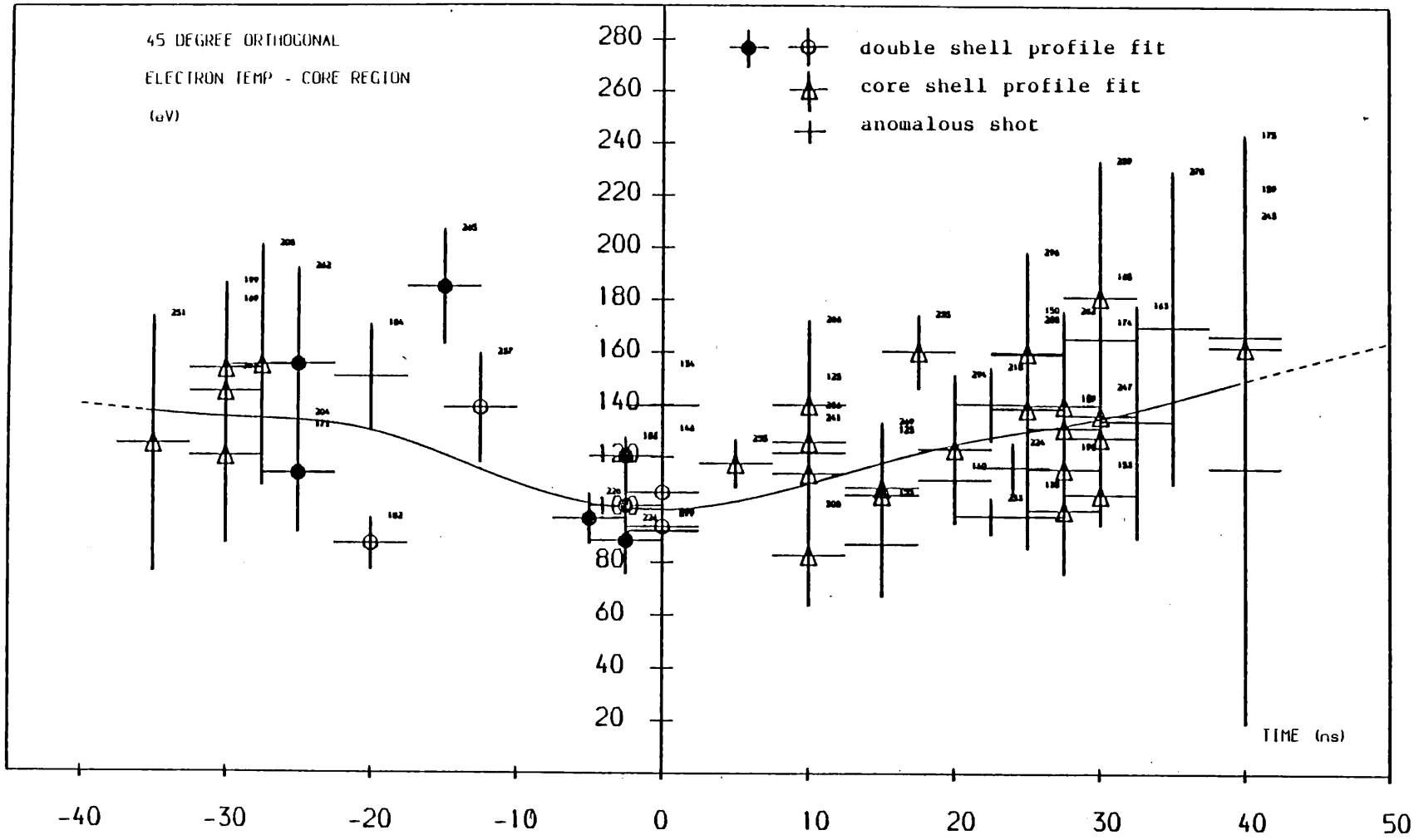

Figure 7.19
Temporal variation of the core electron temperature determined from the 45 degree k orthogonal to z spectra.

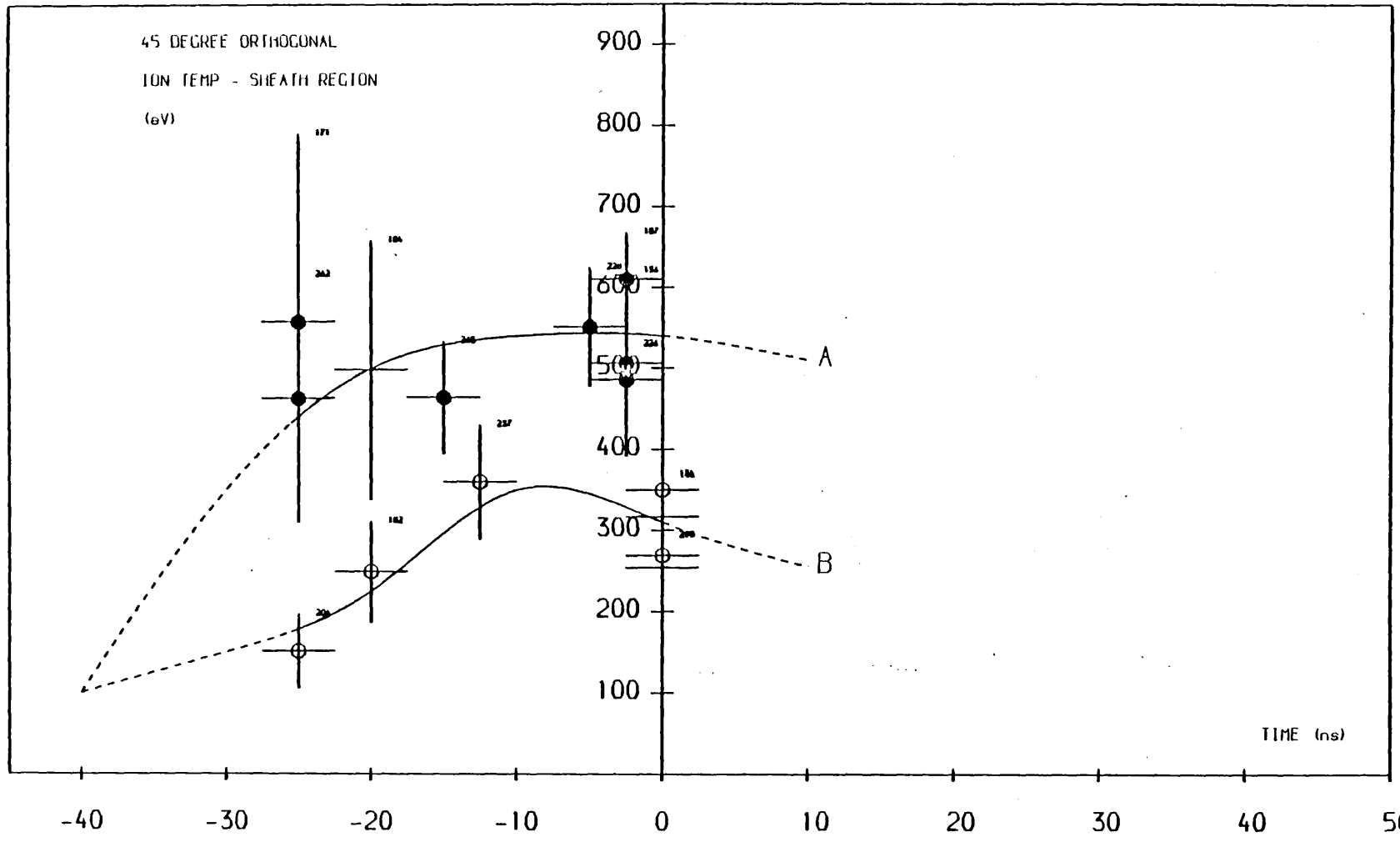

Figure 7.20
Temporal variation of the sheath ion temperature determined from the 45 degree $\underline{k}$ orthogonal to $\underline{z}$ spectra.

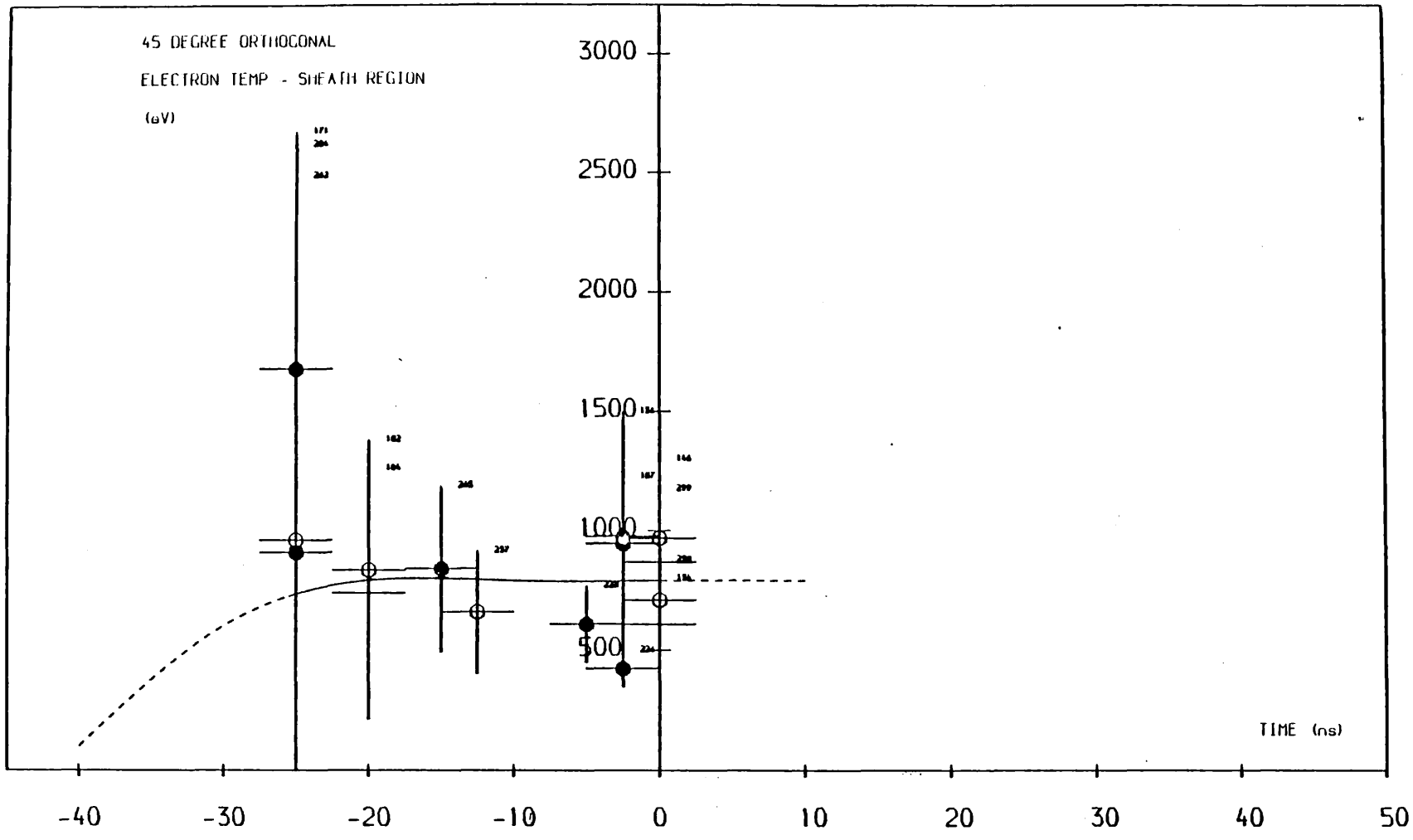

Figure 7.21
Temporal variation of the sheath electron temperature determined from the 45 degree k orthogonal to z spectra.

10 degree analysis, with a peak $T_i \sim 300 - 550$ eV, $T_e \sim 800$ eV. The reason for this discrepancy between the two sets of results will be discussed in section 7.5.1.

In figure 7.18 it can be seen that the core ion temperature rises constantly during the collapse phase to a value of $T_i \sim 215$ eV at t=0 ns, following which it decreases. This should be contrasted with the 10 degree analysis (fig 7.11) where the ion temperature continues to increase until t=+10 ns. The core electron temperature (fig 7.19) shows a steady fall in temperature during the collapse phase to a value at t=0 ns of $T_e \sim 100$ eV, which is very different to the behaviour indicated by the 10 degree analysis (fig 7.12).

The total scattered energy of the 45 degree spectra as a function of time is plotted in figure 7.22, which shows a similar form to that of figure 7.15 for the 10 degree spectra, peaking at t=0 ns as expected, with a large spread of the data following peak compression resulting from the shot to shot variance of the scattering volume electron number during the break-up phase.

7.4.3 10 DEGREE k ANTIPARALLEL TO z

Thermal level shots

The parameters determined from analysing the 10 degree $\underline{k}$ antiparallel shots which had a thermal 10 degree $\underline{k}$ orthogonal to $\underline{z}$ scattering level in the time region t=-35 ns to t=0 ns are shown in figures 7.23-7.26. The filled and open circle nomenclature of the shots from the 10 degree $\underline{k}$ orthogonal to $\underline{z}$ analysis is still adhered to.

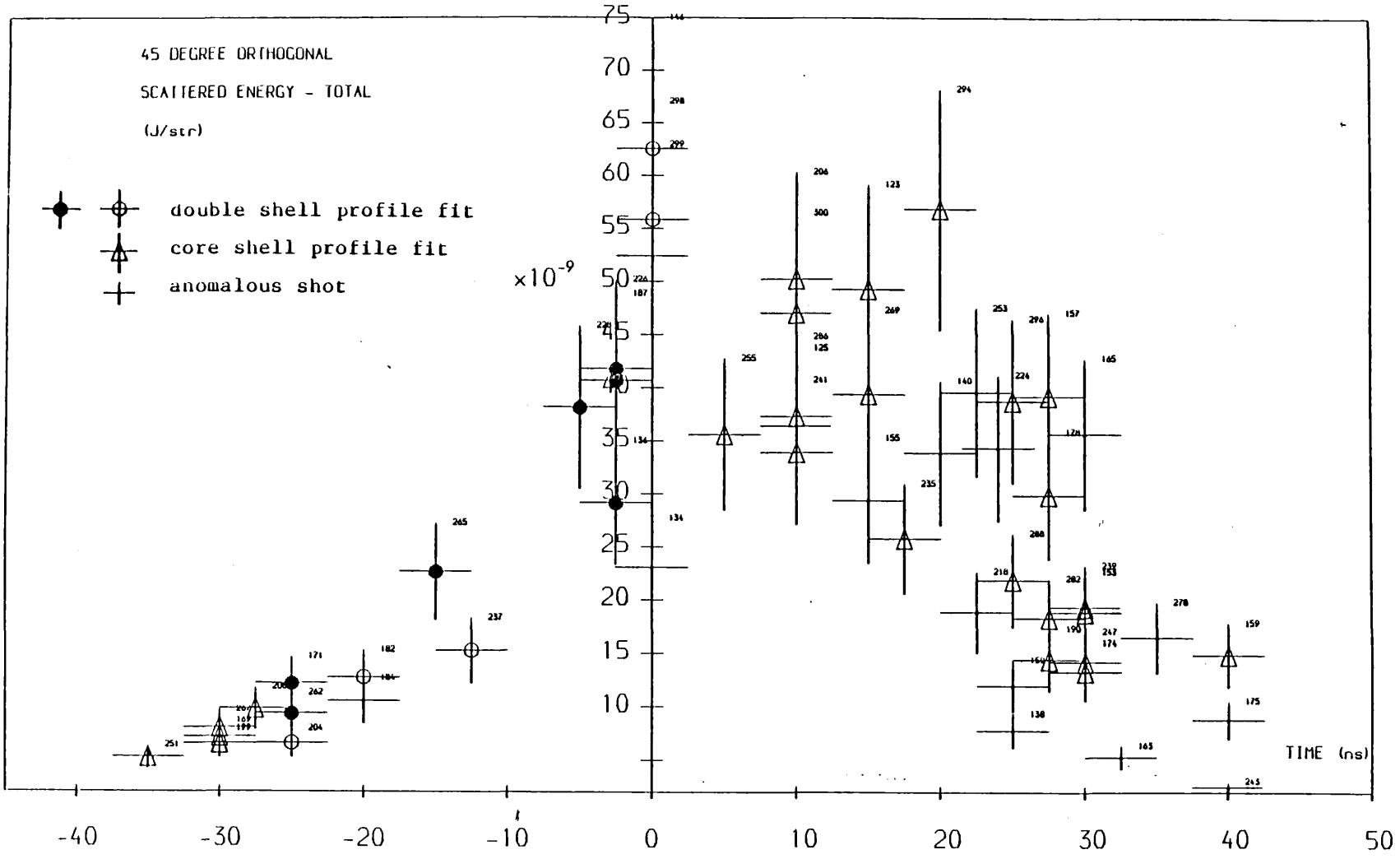

Figure 7.22

Temporal variation of the total scattered energy of the 45 degree k orthogonal to z spectra for thermal and anomalous shots.

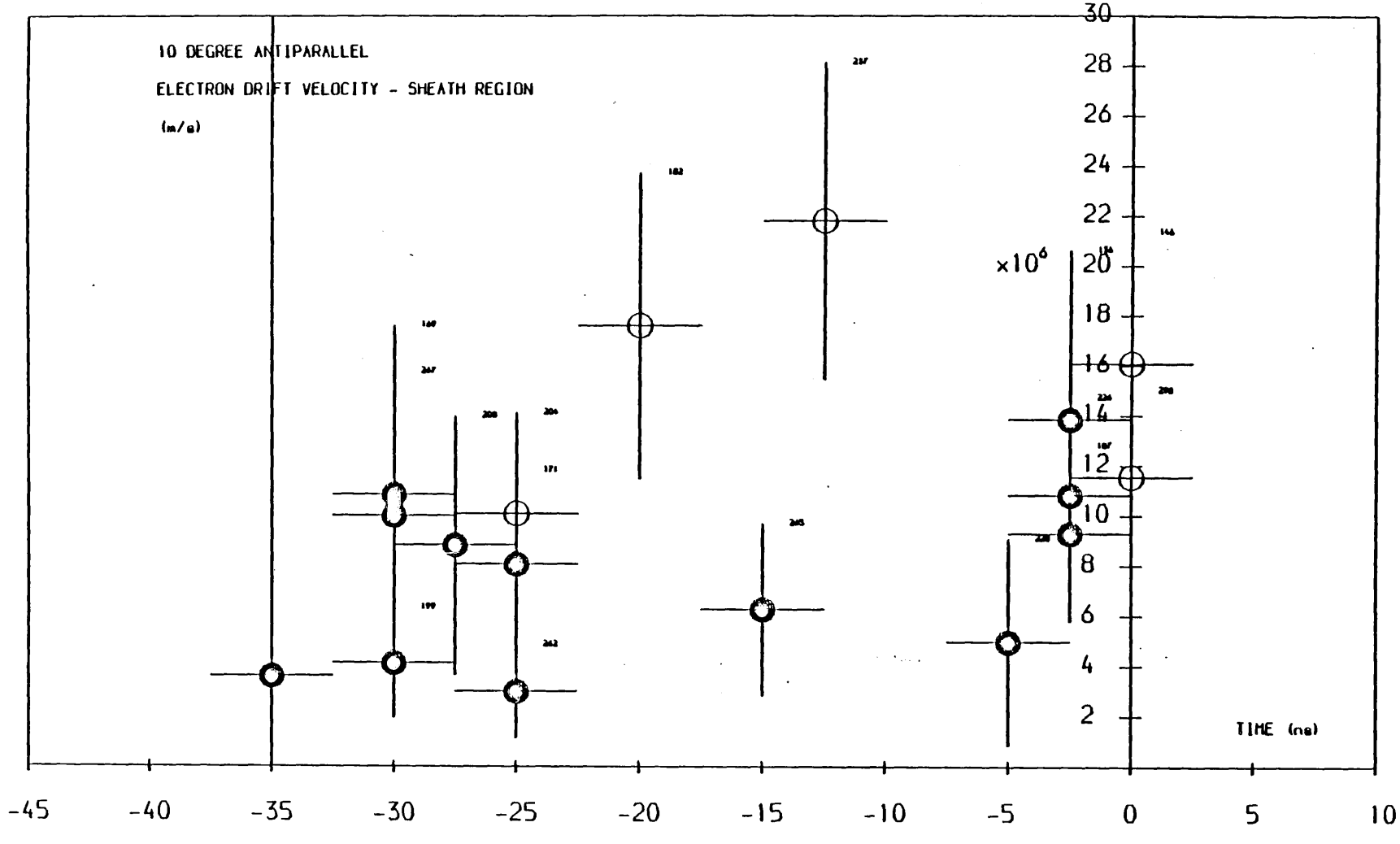

Figure 7.23
Temporal variation of the sheath relative electron-ion drift velocity, D determined from the 10 degree k antiparallel to z spectra.

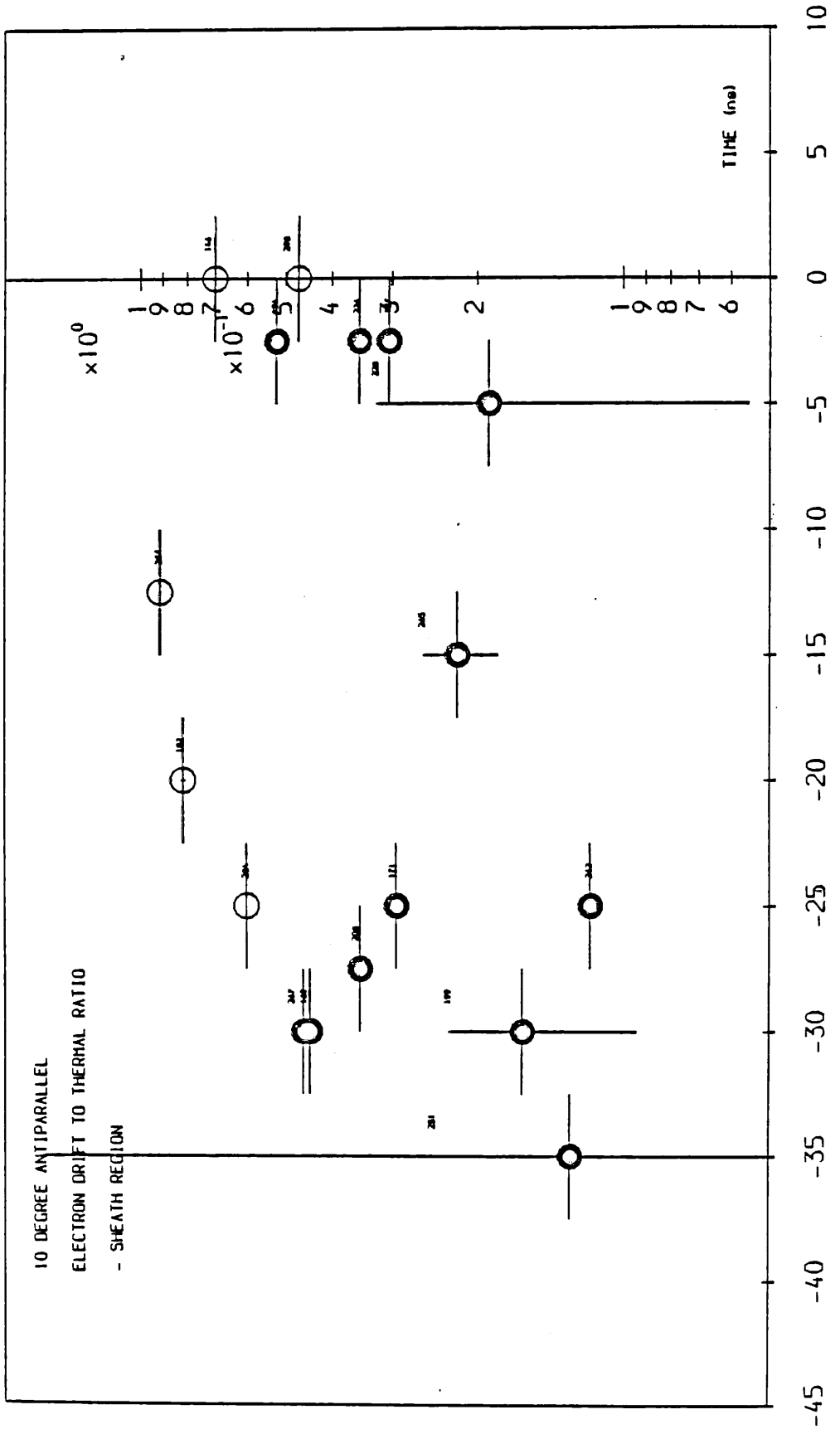

Figure 7.24

Temporal variation of the sheath electron drift to thermal speed ratio, D_l determined from the 10 degree $\underline{k}$ orthogonal and antiparallel to $\underline{z}$ spectra.

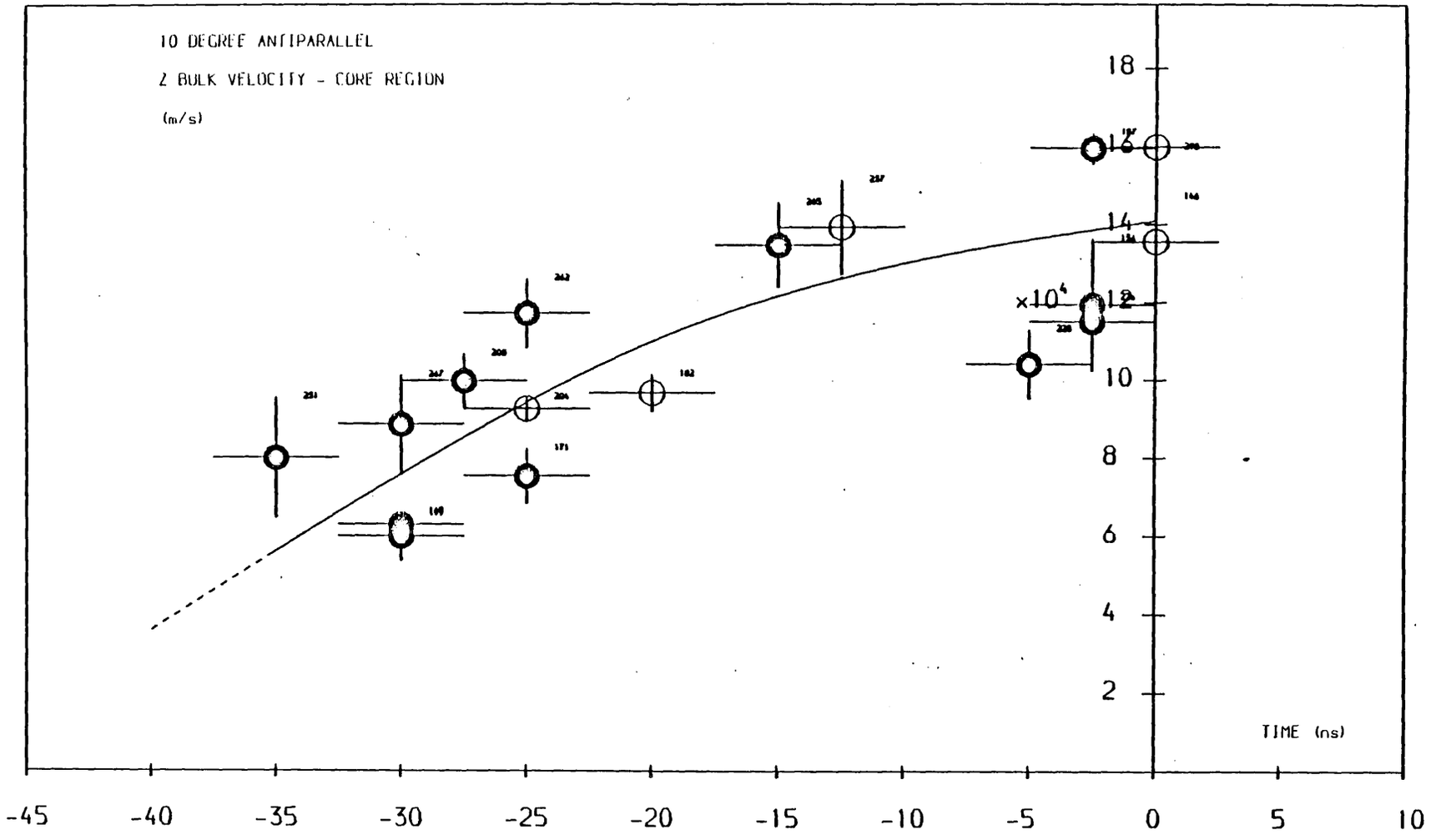

Figure 7.25
Temporal variation of the core plasma bulk velocity, $\underline{V}_{\beta}$ determined from the 10 degree $\underline{k}$ antiparallel to $\underline{z}$ spectra.

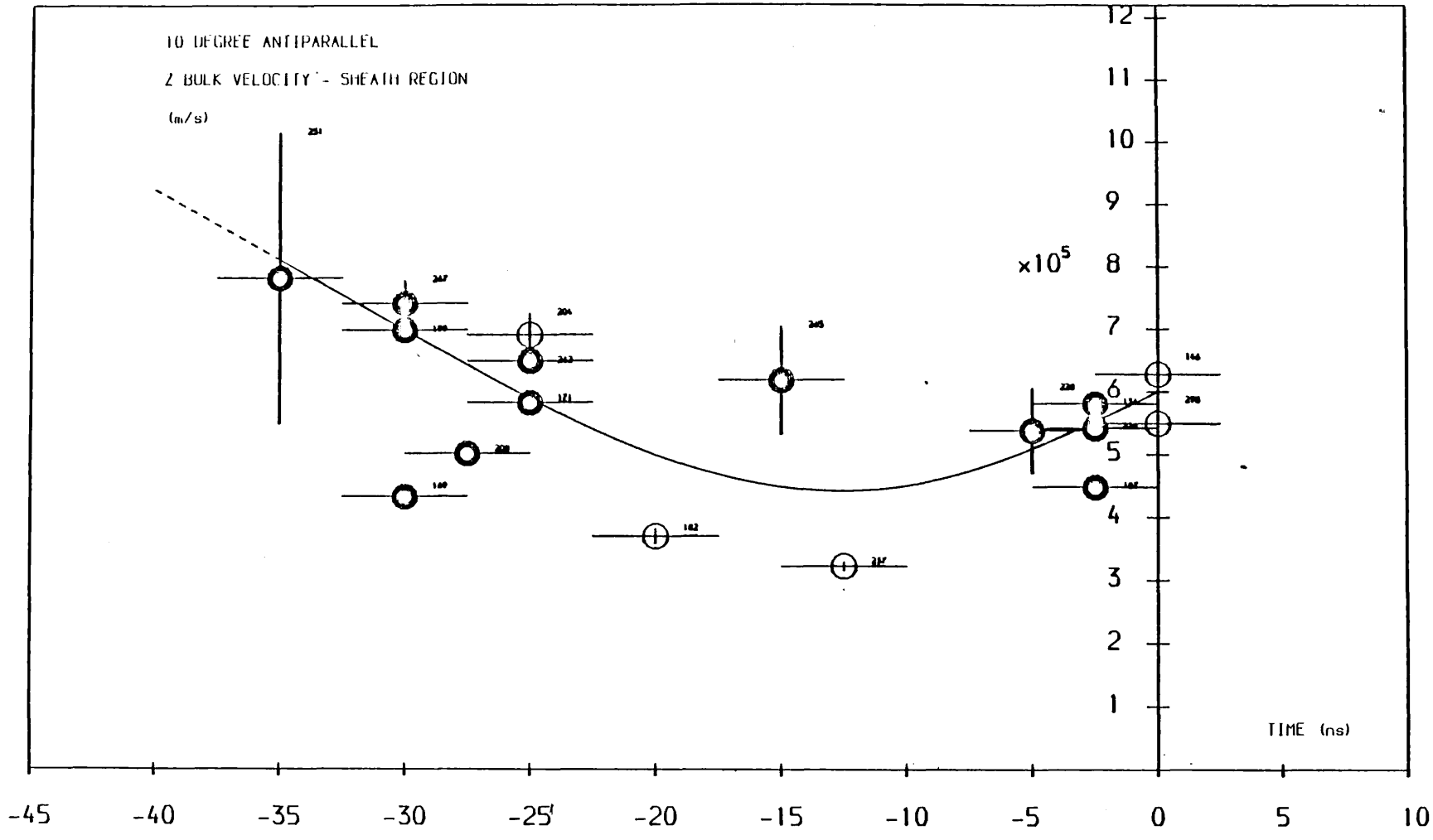

Figure 7.26
Temporal variation of the sheath plasma bulk velocity, $\underline{V}_{\beta}$ determined from the 10 degree $\underline{k}$ antiparallel to $\underline{z}$ spectra.

Figure 7.23 shows the the sheath relative electron-ion drift velocity as a function of time. It can be seen that the open circle shots (mode B) maintain a higher level of drift velocity relative to the filled circle shots (mode A) throughout the time period investigated. Using eq 7.36, the ratio of the sheath electron drift to thermal speed, D_t as a function of time can be plotted as shown in figure 7.24. It can be seen that the shots are still divisible into the two groups of data points. The value of the drift ratio at t=0 ns $\sim$0.5, but for earlier times it approaches unity for the open circle shots.

The core bulk velocity in the $\underline{z}$ direction is plotted in figure 7.25. It shows a steady rise during the collapse phase to a value at peak compression of 1.4×10^5 m.s^{-1}. The sheath bulk velocity shown in figure 7.26 shows a very different behaviour however. It falls from an initial value of $\sim 8 \times 10^5$ m.s^{-1} at t=-35 ns to $\sim 4 \times 10^5$ m.s^{-1} at t=-15 ns, before rising again to a value of 6×10^5 m.s^{-1} at t=0 ns.

The total scattered energy of all the thermal shots in the time period t=-35 ns to t=+40 ns is shown in figure 7.27 and can be compared with the 10 degree $\underline{k}$ orthogonal to $\underline{z}$ spectra energy shown in figure 7.15. It can be seen that the shots following peak compression have a similar total scattered energy level to those for $t \leq 0$ ns, suggesting that the drift velocity on these shots is comparable to that in the sheath during the collapse phase. The scattered energy of the 10 degree $\underline{k}$ antiparallel to $\underline{z}$ spectra at t=0 ns is approximately 25% greater than that of the 10 degree $\underline{k}$ orthogonal to $\underline{z}$ spectra. It should be noted that this enhancement originates from the sheath scattering volume only, the local enhancement of this region at t=0 ns is $\sim$400%, which was calculated using eq 7.58 for the fitted sheath profile of both

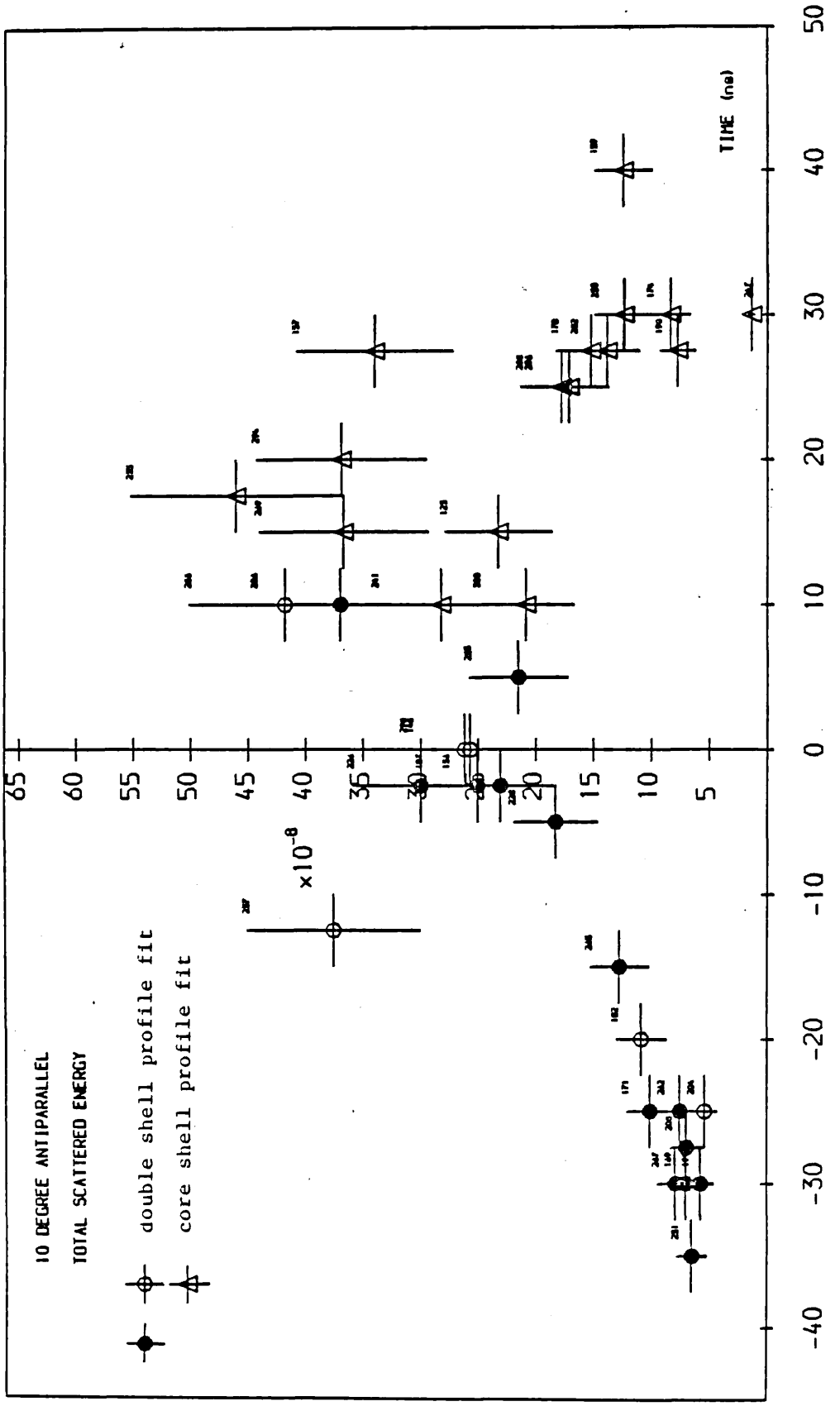

Figure 7.27

Temporal variation of the total scattered energy of the 10 degree $\underline{k}$ antiparallel to $\underline{z}$ spectra for thermal shots only.

10 degree scattered spectra. The core region contribution for both $\underline{k}$ arrangements is of course identical, after allowing for the marginal difference in scattering volume geometries and γ values.

Anomalous shots

Figure 7.28 shows a plot of the ratio of the total scattered energy of the 10 degree $\underline{k}$ antiparallel to $\underline{z}$ spectra shots, termed anomalous in the 10 degree $\underline{k}$ orthogonal to $\underline{z}$ analysis, to the thermal scattering level indicated by the curve in figure 7.15. The peak value of the enhancement factor of these shots above the thermal level is ~ 77. The enhancement levels are similarly divided into two ranges consistent with the two types of anomalous shots observed with the 10 degree $\underline{k}$ orthogonal to $\underline{z}$ arrangement. The first type specified in that section, had enhancements relative to the thermal scattering level in the range 4 - 15. The second type of anomalous shot exhibited enhancements in the range 40 - 77.

7.5 INTERPRETATION OF THE RESULTS

7.5.1 RADIAL TEMPERATURE PROFILES - COLLAPSE PHASE

The first observation of the temporal variations of the core and sheath temperatures as determined from the 10 and 45 degree $\underline{k}$ orthogonal to $\underline{z}$ analysis, is that the core region is significantly cooler than the sheath region for the time period t=-35 ns to t=0 ns. The second notable feature of the analysis for this time period, is the existence of two temperature profile modes. Similar features to this

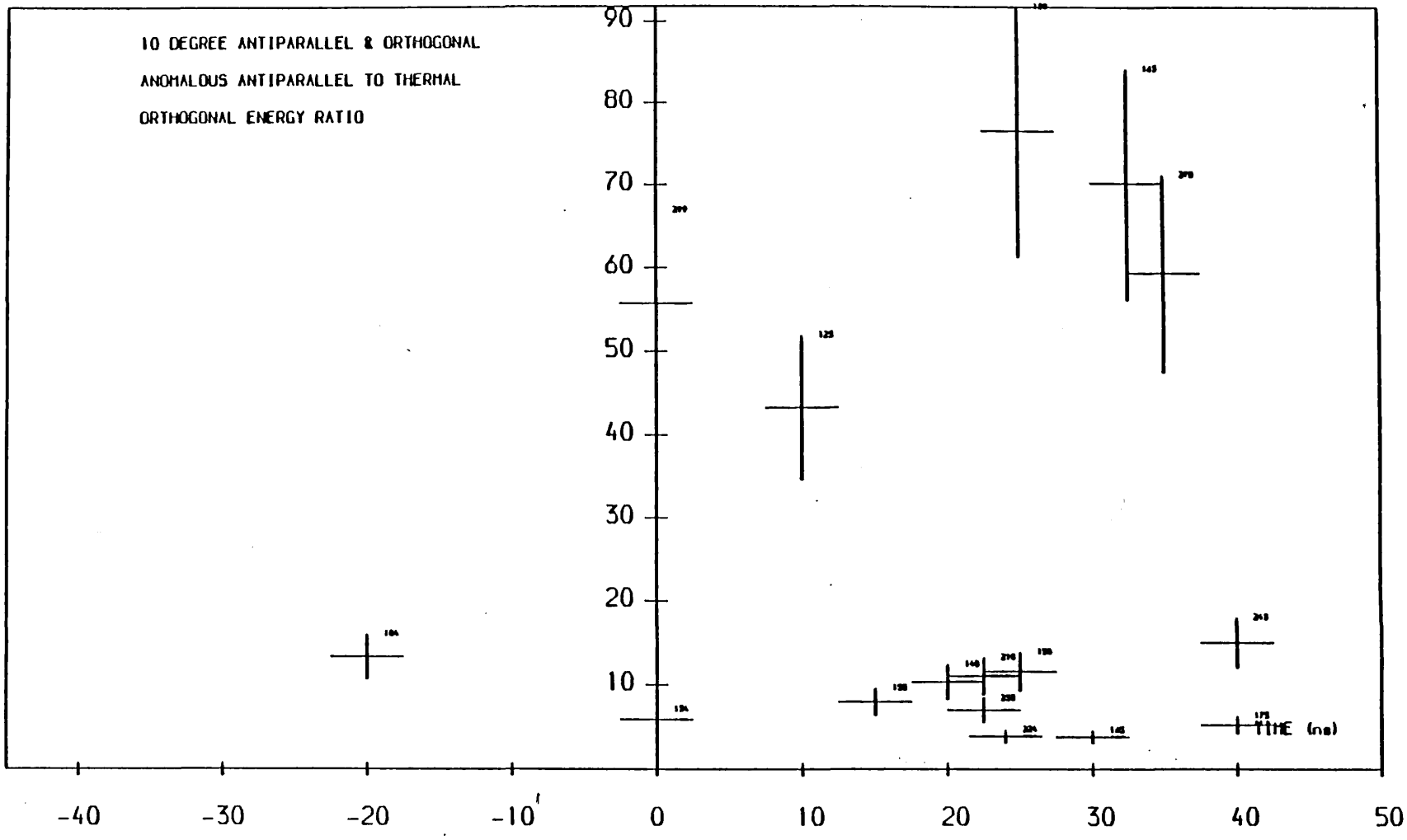

Figure 7.28
Temporal variation of the ratio of the total scattered energy to the thermal energy level for the 10 degree $\underline{k}$ antiparallel to $\underline{z}$ anomalous spectra.

have been reported previously for the T_e values at peak compression by Bertalot et al [45]. Their spatial T_e measurements using X-ray techniques (see section 3.3) indicate T_e maxima of >2.0 keV for approximately 50% of the plasma shots. In the other shots the maximum electron temperature was up to 0.5 keV. Before discussing these observations further, several inconsistencies in the temporal temperature plots (figs 7.11-14 and 7.18-21) are apparent:

(a) The sheath temperatures determined from the 10 degree analysis are far larger than those originating from the 45 degree analysis.

(b) The double ion temperature profiles (modes A & B) observed for the sheath region from the 10 degree analysis are reversed for the 45 degree analysis.

(c) The double electron temperature profiles observed for the sheath region from the 10 degree analysis are not observed in the 45 degree analysis.

(d) From the 10 degree analysis the core electron temperature is indicated as steadily increasing during the collapse phase and peaks at t=+10 ns. The 45 degree analysis suggests that it decreases during the collapse phase to t=0 ns, then increases again.

(e) The core ion temperature determined from the 10 degree analysis peaks at t=+10 ns, whereas from the 45 degree analysis it peaks at t=0 ns.

These inconsistencies can be explained if we consider the relative average radii, $R_j(t)$ for the core and sheath region of the 10 and 45 degree analysis and the variation of the scattering parameter α with radius for each scattering angle. From these considerations it is additionally possible to formulate an idea of the radial temperature profiles during the collapse phase.

Figures 7.29a-c show plots of the temperature values of each shell scattering volume plotted against their respective shell average radius, $R_j(t)$ given by eq 7.27, at plasma times of t=-20, -10 and 0 ns respectively. The radial electron density profile at each time (not convolved with the laser pulse FWHM) is indicated by the thick line in each case. The data points in each figure are from left to right: the T_i and T_e values of the 45 degree core region, the T_i and T_e values of the 10 degree core region, the two T_i and one T_e values of the 45 degree sheath region and finally the two T_i and T_e values for the 10 degree sheath region. The filled (mode A) and open (mode B) circle nomenclature previously defined for the double temperature profiles is adhered to, a dotted circle indicating those points where only single profiles were observed with time. At the top of each plot, the range of the shell volumes for each scattering angle is indicated, the bracketed figures underneath showing the electron number for each radial range at that scattering angle. The 10 degree core region is made up of two parts, consisting of the defined 45 degree core region (I), plus the inner sheath region (II). Similarly the 45 degree sheath region consists of the inner sheath region (II) and the defined 10 degree sheath region (III). The reasoning behind the plotted temperature profiles will become apparent as we proceed with the interpretation. In each plot the continuous lines indicate the T_i and T_e profiles for the mode A data points and the dotted lines those for the mode B data points.

Figures 7.30a&b show plots of the scattering parameter, α for the core and sheath region of the 10 and 45 degree spectra, which were derived from the fitted T_e and n_e values for each shot. The error in α for each shot was calculated as half the compounded error in n_e and T_e. Two additional dotted lines have been plotted on the 10 degree

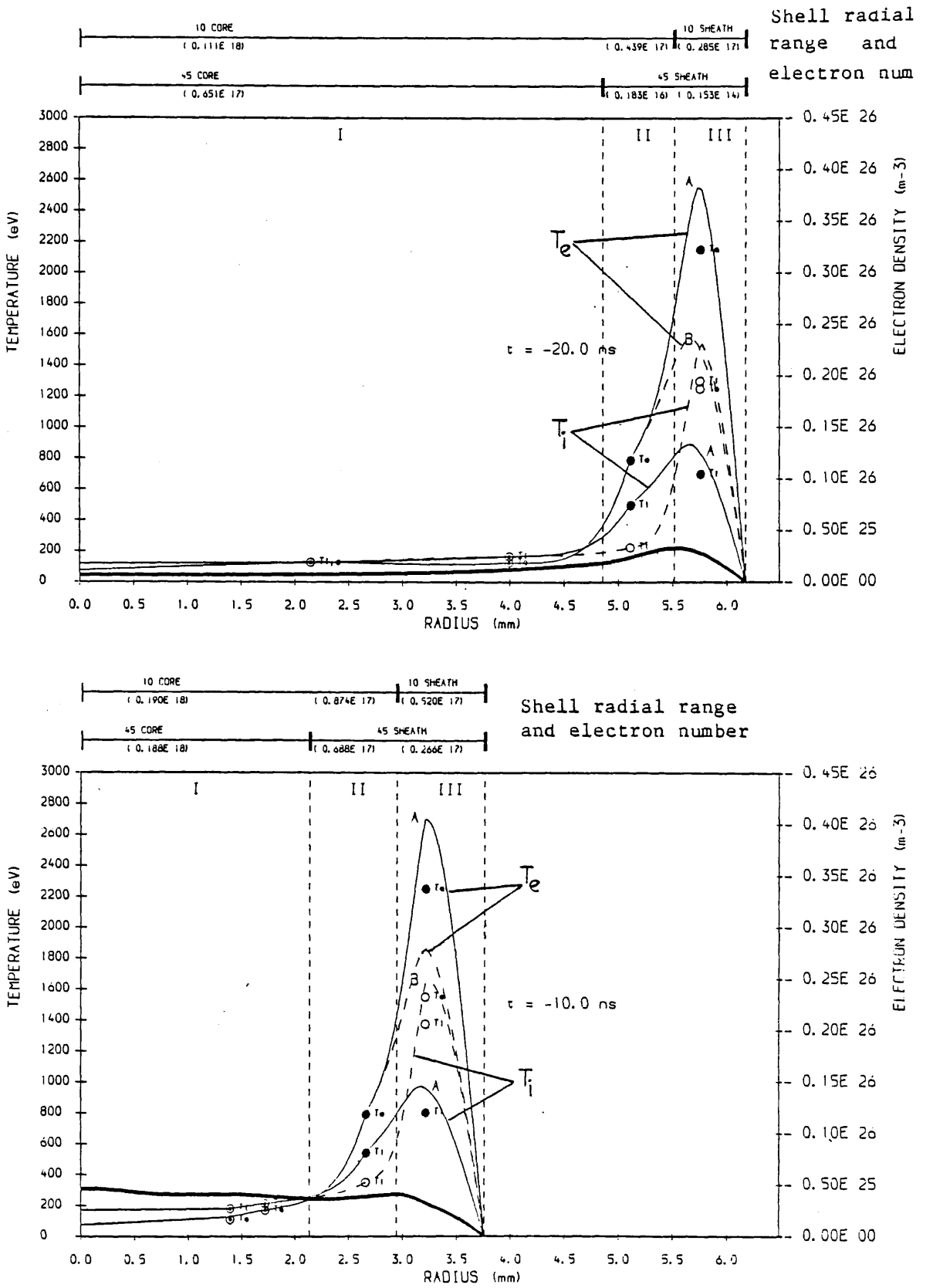

Figure 7.29a&b

10 and 45 degree core and sheath temperatures and assumed temperature profiles for (a) t=-20 ns, (b) t=-10 ns.

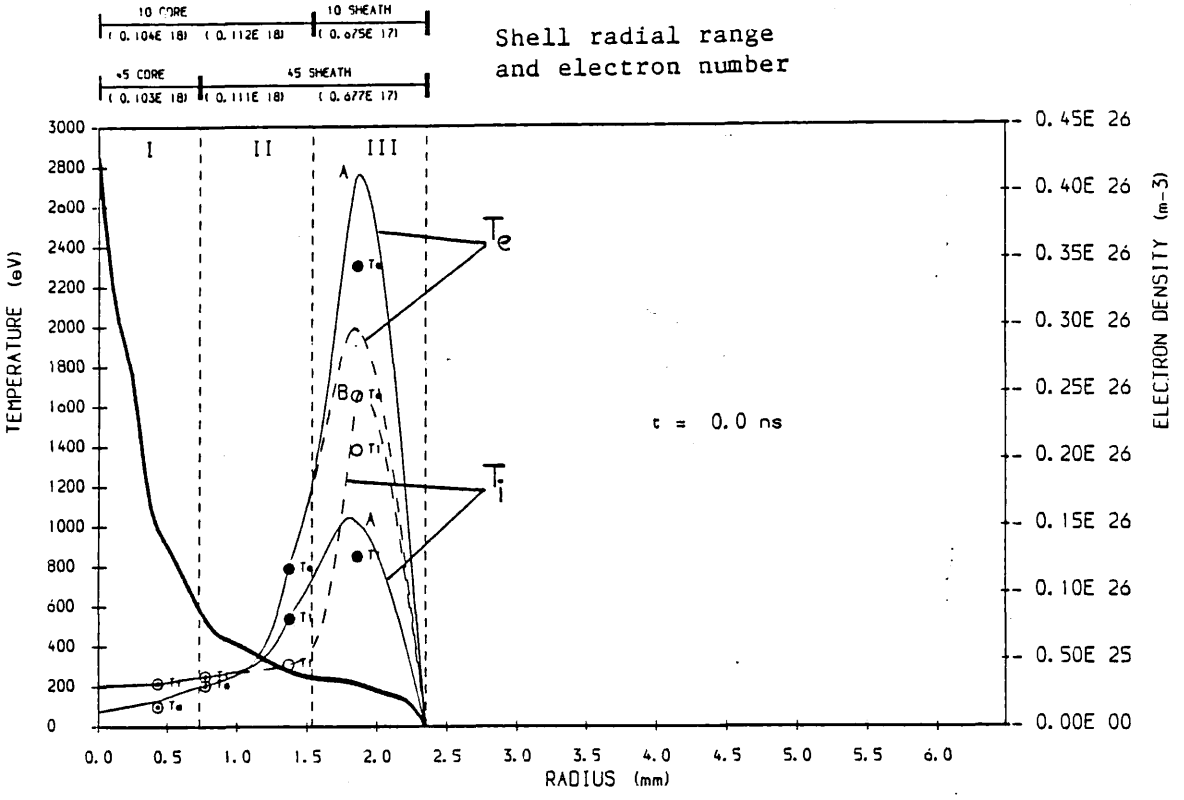

Figure 7.29c
10 and 45 degree core and sheath temperatures and assumed temperature profiles for t=0 ns.

plot (7.30a), one for each temperature mode, which indicate the equivalent α values for the defined 10 degree sheath region (III) and determined T_e and n_e parameters, but with a scattering angle of 45 degrees.

Consider the situation at t=0 ns. The α value of the sheath region for the 10 degree scattering has a value of ~ 3 and the equivalent value for the 45 degree scattering would be ~ 0.65. Taking $T_e/T_i=1$, the ratio of the total scattered energy of the ion feature for the two scattering angles can be calculated using eq 3.6 for each α value. This gives $S_{i_{10}}(\underline{k})/S_{i_{45}}(\underline{k})=6.27$. Additionally, if we observe figures 7.29a-c, we see that the electron number for the outer sheath

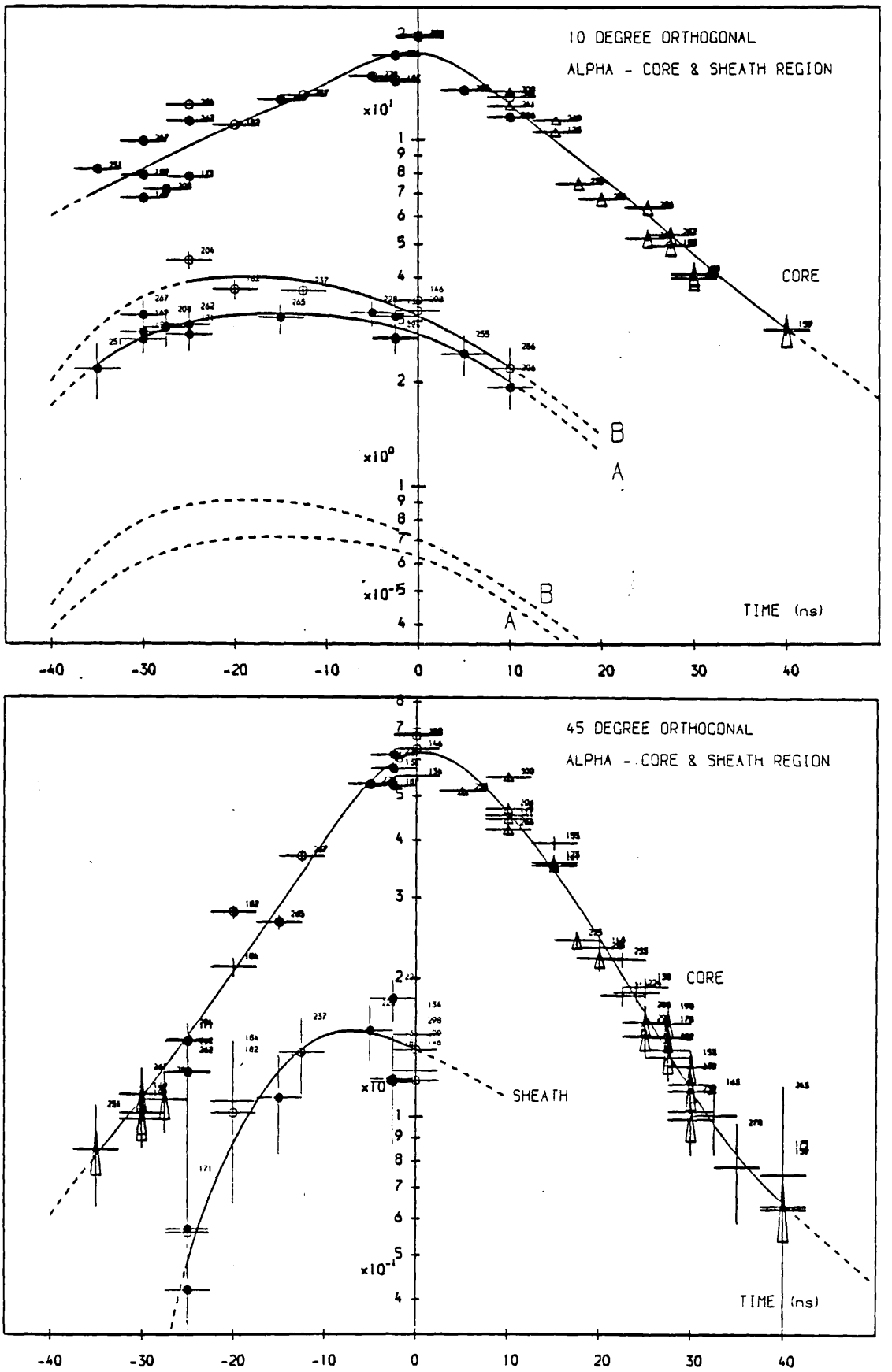

Figure 7.30

Temporal variation of the scattering parameter, α for the core and sheath regions of (a) the 10 degree $\underline{k}$ orthogonal to $\underline{z}$ spectra (b) the 45 degree $\underline{k}$ orthogonal $\underline{z}$ spectra.

region (III) of the defined 45 degree sheath volume is always smaller than the inner sheath region (II), being only $\sim$ 0.8% of the total sheath number at t=-20 ns, rising to a maximum $\sim$38% at t=0 ns. It should be noted that these figures are based on the unconvolved density profile, although a convolution of the electron numbers at times t, t-9 and t+11 ns as described in section 7.3.6 does not change the dominant contribution of the inner sheath region to the 45 degree sheath scattering. The reason for the higher average sheath temperatures obtained from the 10 degree analysis can now be seen in terms of the above two physical effects.

Four temperature profiles based on the data points can be constructed as indicated in figures 7.29a-c, bearing in mind the fact that the determined temperature parameters represent the average value for each shell volume. Any fine structure in the profiles is not discernable from the available data.

The inconsistencies (b) and (c) can now be seen as resulting from the relative slopes of the temperature profiles across the inner sheath region (II). From these it can be seen that the effective penetration region of the high temperature sheath T_i profile for the mode A temperature curves ($T_e >> T_i$) is approximately twice that for the mode B curves ($T_i \sim T_e$).

The core region T_i profile has been drawn flatter than the T_e profile up to r=0 as time progresses. The reason for this is to explain the inconsistency between the 10 and 45 degree core T_e value as a function of time detailed in (d). During the collapse phase the axial electron density increases as the hollow radial electron density profile of earlier times becomes parabolic at t=0 ns. This will result

in the dominant contribution to the 45 degree core region gradually shifting towards the axis, resulting in the average indicated T_e value decreasing. The 10 degree core spectrum will not be subject to this effect, because of its relatively flat $S_i(\underline{k})$ profile across the range of n_e/T_e values as is indicated in figure 3.7 (p.66). Following peak compression (t=0 ns) the opposite effect will result in an increasing 45 degree core T_e value as the axial density decreases and the density profile flattens across the scattering volume. The observed continued rise in the 10 degree core T_i value until t=+10 ns, not observed in the 45 degree analysis, probably results from the same sensitive 45 degree radial contribution. An increase in the outer core T_i and T_e values will increase the average temperature determined by the 10 degree scattering but will not effect the 45 degree core profile which will be axially dominated during this time period. Additionally, the 45 degree core shell volume has a smaller radial range than that of the equivalent 10 degree volume.

7.5.2 PLASMA BULK VELOCITIES - COLLAPSE PHASE

The core bulk velocity as a function of time shows a behaviour very much as expected during the collapse phase of the plasma, increasing as the compression proceeds to a value of 1.4×10^5 m.s^{-1} at t=0 ns. This value is similar to that observed by Bernard et al [19].

The sheath bulk velocity is more difficult to intergret. It probably results from several plasma velocity components. Firstly, the pinch is quasi-cylindrical, the collapsing sheath not being parallel to the $\underline{z}$-axis and the axial length of the plasma, defined by the return current sheath position, increases during the collapse phase (see section 4.5.3.5). This results in a velocity component parallel to the

z-axis. Secondly, one would expect that the mass motion of the plasma in the z-axis direction resulting from the collapsing sheath to maximise at the plasma radius, R_{pv}. The combination of these two components probably accounts for the temporal behaviour of the sheath bulk velocity.

7.5.3 SHEATH DRIFT VELOCITY

During the collapse phase of the plasma the electron drift velocity, $\underline{D}$ was determined as being in the range 2.5×10^6 m.s^{-1} to 2.2×10^7 m.s^{-1} for t=-35 ns to t=0 ns. By direct comparison, the Faraday rotation polarimetry measurements of Muir [25] on the same Plasma Focus device, operated under identical conditions, determined the peak drift velocity as increasing from 1.2×10^5 m.s^{-1} at t=-10 ns to 4.7×10^5 m.s^{-1} at t=0 ns. There is therefore greater than an order of magnitude discrepancy between the values determined by the two techniques. At peak compression, with $\underline{D} \sim 1.5 \times 10^7$ m.s^{-1}, the discrepancy is a factor of 32. In order to draw a conclusion from this discrepancy, several factors must be considered:

(1) The Faraday rotation polarimetry technique was used to measure the Faraday rotation angle of a polarised probe beam as a function of impact parameter and time. From these measurements the radial magnetic field profile as a function of time was determined by Abel inversion of the Faraday rotation data in conjunction with the radial electron density profile. The radial current distribution was then derived using Ampere's law, based on the assumption that the current had a planar distribution azimuthally about the sheath penetration region. It is not possible to distinguish using this technique between the assumed current distribution and evenly distributed filamentary current

channels. The latter would result in a greatly enhanced localised current density, $\underline{J}_z$ and hence drift velocity, $\underline{D}$. The two being related by the expression,

$$\underline{J}_z = -n_e \, e \, \underline{D} \qquad (7.59)$$

This increase in current density will result in a larger drift velocity ratio, D_t for the region, provided that the electron temperature and hence electron thermal speed are not also increased due to electron heating by turbulence within the filamentary current channels.

(2) If the assumptions of the above scenario are correct and the plasma current is distributed amongst filamentary channels, then the cross sectional area of all the filaments at t=0 ns must be to a first order approximation 1/30th of that of the current penetration region. This implies that the observed enhancement of the 10 degree $\underline{k}$ antiparallel to $\underline{z}$ spectrum for $t \leq 0$ ns (collapse phase), results from a volume which is 1/30th of that assumed in the analysis. The implication of this is that the drift ratio, D_t must be larger than the values determined, to account for the decreased electron number contribution. The alternative to this is that the filamentary channels result in localised electron heating, increasing the localised T_e/T_i ratio which could also account for the necessary increase in enhancement from a smaller volume.

The observation of filamentary current structures within the current sheath region has been noted previously by Bostick et al [43a]. They observed such structures simultaneously using image converter and Schlieren or shadowgraph photographic techniques. When using the image converter and shadowgraph techniques simultaneously, it was found that under certain conditions, the filamentary structure was too fine to be

resolved by the image converter, but were still nevertheless observable in the shadowgraph. Their image converter photographs indicate that the sheath region is corrugated in the azimuthal direction and that the filamentary structures lie in the grooves of the corrugations. They concluded therefore, that any planar one-dimensional model of the current sheath is very far from its true structure.

In assessing the effects of the high drift velocity on the plasma, resulting from current filamentation, it should be noted that it is difficult to estimate exactly when the drift velocity ratio starts to rise to high values, due to the temporal convolution resulting from using a scattering laser pulse length with a FWHM=20 ns. For instance, a shot timed at t=-20 ns may recieve little contribution to the enhancement of the scattered spectrum from times $\sim$-30 ns, but very large enhancement contributions from times $\sim$-10 ns. The exact temporal evolution of the drift velocity is important for two reasons. Firstly, current driven turbulent heating may contribute significantly to the rapid rise in sheath temperature that is observed from t=-40 ns to t=-20 ns. Secondly, the resulting enhanced turbulence level may well offer an explanation for the anomalous resistivity required to produce a rapid magnetic field diffusion observed by Muir [25] following peak compression. Consideration of these observations is given below in the subsequent sections.

7.5.4 PLASMA RESISTIVITY AND MAGNETIC FIELD DIFFUSION

The electrical resistivity of a plasma can be written in terms of the effective electron collision frequency, ν as [64],

$$\eta = \frac{m_e \nu}{n_e e^2} \tag{7.60}$$

A relatively simple solution for the collision frequency is given by Spitzer [64] for the case of a Lorentz gas, a hypothetical fully ionised plasma where the electron-electron collisions are ignored and the positive ions are at rest. The effective collision frequency is then obtained by averaging the velocity dependent collision frequency over the velocity distribution of the electrons, which for the case of a Maxwellian distribution yields a value for the resistivity on evaluation of the constants of,

$$\eta_L = 3.04 \times 10^{-5} \frac{Z \ell n\Lambda}{T_e^{3/2}} \text{ ohm-m} \tag{7.61}$$

where T_e is in units of eV, Z is the ionic charge and Λ is the Coulomb parameter defined by Spitzer [64] as the ratio of the Debye length to the mean impact parameter for a 90 degree deflection of an electron by an ion due to classical Rutherford scattering. This ratio is given by Spitzer as,

$$\Lambda = \frac{3[4\pi\varepsilon_o \kappa T_e (^oK)]^{3/2}}{2\sqrt{\pi}\, e^3 Z n_e^{\frac{1}{2}}} = 1.55 \times 10^{13} n_e^{-\frac{1}{2}} [T_e(eV)]^{3/2} \tag{7.62}$$

For the case of an ionised gas, electron-electron encounters must be taken into account. The classical plasma resistivity parallel to a

magnetic field is then given by,

$$\eta_{\parallel} = \frac{1}{\gamma_E} \times 3.04 \times 10^{-5} \quad \frac{Z \ \ell n\Lambda}{T_e^{3/2}} \tag{7.63}$$

where the correction factor γ_E is dependent on the ionic charge and is tabulated by Spitzer [64]. For the case Z=1, γ_E =0.582.

For a current transverse to a strong magnetic field, the resistivity of an ionised gas is given by that for a Lorentz gas divided by a correction factor γ_{EB} [64], where $\gamma_{EB} = 3\pi/32 = 0.295$. This yields an expression for the transverse resistivity of,

$$\eta_{\perp} = 1.03 \times 10^{-4} \quad \frac{Z \ \ell n\Lambda}{T_e^{3/2}} \quad \text{ohm-m} \tag{7.64}$$

As the electrical current in the Plasma Focus is perpendicular to the magnetic field, we need only consider the transverse resistivity. At peak compression, t=0 ns, the electron density within the current carrying region is $\sim 2.6 \times 10^{24}$ m^{-3}. With T_e in the range 1.65 to 2.3 keV, $\ln\Lambda \sim 14$. Therefore the classical transverse resistivity of the sheath region at t=0 ns is in the range 2.1×10^{-8} ohm-m to 1.3×10^{-8} ohm-m.

A magnetic field will diffuse into a conductor within a time period τ_B given approximately by Boyd & Sanderson [65] as,

$$\tau_B = \frac{\mu_o L^2}{\eta} \tag{7.65}$$

where η is the electrical resistivity and L is a characteristic length. In the case of the Plasma Focus, both the resistivity and a characteristic length given by the plasma radius are known, so a

magnetic field diffusion time can be estimated.

At t=0 ns, the plasma radius R_{pv}=2.35 mm and with a resistivity in the range 2.1×10^{-8} to 1.3×10^{-8} ohm-m, τ_B is in the range 330 μs to 534 μs. However, the results of the Faraday rotation polarimetry measurements of Muir [25], indicate that following peak compression (t=0 ns), the magnetic field diffuses rapidly to the plasma axis within a time period of $\sim$10 ns. This suggests that the plasma resistivity during this period is anomalous and is larger than the Spitzer value by a factor of $3\text{-}5\times10^4$. Similar anomalous resistivity factors of 10^3 to 10^4 have been measured by Bernard et al [66] using magnetic probes. This anomalous resistivity was thought to be as a result of high levels of plasma turbulence. As large drift currents are present within the sheath region during the collapse phase, the anomalous resistivity probably results from current driven electrostatic wave turbulence. In this situation the drifting electrons scatter from the enhanced plasma wave turbulence, resulting in a shorter effective collision time than that for binary electron-ion collisions. The possible electrostatic waves which may be responsible for this anomalous resistivity will be discussed further in the section on current driven turbulence (section 7.5.6).

7.5.5 HEATING MECHANISMS

(i) Adiabatic Compression

During the latter stages of the collapse phase, the plasma is compressed in a manner which may be assumed to be adiabatic. During the period t=-10 ns to 0 ns, the plasma velocities are less than the sound speed, therefore shock waves with their associated non-reversible

change of state do not exist. However, one non-reversible process does exist during this phase of the plasma. This is the reduction of electron line density due to the bulk plasma velocity in the $\underline{z}$ direction, resulting in an out flow of heat from the system. Neglecting this process for the time being, the rise in temperature of the plasma due to an adiabatic compression can be calculated.

Using the adiabatic compression relation, PV^{γ}=constant and noting that the volume is proportional to the plasma radius squared, we obtain,

$$\overline{T}\ r^{2(\gamma-1)} = \text{constant} \qquad (7.66)$$

where $\overline{T}$ is the average plasma temperature. Assuming γ=5/3, the increase in average plasma temperature between t=-30 ns and t=0 ns when the radius contracts from 8.75 mm to 2.35 mm is approximately 5.8. In the sections below it will be demonstrated that the rise in sheath temperature is largely as a result of other heating mechanisms, so we will only consider the rise in core temperature for comparison with the above value for adiabatic compression. From the analysis of the 10 degree $\underline{k}$ orthogonal to $\underline{z}$ spectra, the average temperature of the core region, $\overline{T}=(T_e+T_i)/2$ increases from $\sim$100 eV at t=-30 ns to $\sim$225 eV at t=0 ns, an increase of 2.25. It should be noted however, that approximately 50% of the particles are lost from the system during the time period t=-20 ns to t=0 ns [25], as the electron line density decreases. Following peak compression when the plasma expands, adiabatic cooling will occur. Such behaviour is observed for the core ion temperature from the analysis of the 45 degree $\underline{k}$ orthogonal to $\underline{z}$ spectra, the core electron temperature in this case being subject to radial density profile effects as detailed in section 7.5.1. In the case of the 10 degree $\underline{k}$ orthogonal to $\underline{z}$ spectra the core temperature

continues to rise until t=+10 ns and then decreases. This is probably as a result of heating of the outer 10 degree core region as has already been discussed in section 7.5.1.

(ii) Shock Heating

During the time period t=-10 ns, to t=0 ns the plasma-vacuum radial velocity at z=10 mm decreases from 2.68×10^5 m.s^{-1} to zero. The kinetic energy of the sheath region is largely carried by the plasma ions. Taking the full width of the sheath region (inner and outer sheath), the number of ions within this area per unit length is 9×10^{19} m^{-1}, which will have a mass of 3×10^{-7} kg.m^{-1}. Calculating eq 7.27 numerically for the whole plasma, the average radius of this region at t=-10 ns is 2.7 mm, which will have a radial velocity using eq 7.26 of 1.93×10^5 m.s^{-1}, giving a kinetic energy per unit length of 5.59 kJ.m^{-1}. Assuming that this energy is dissipated into the thermal energy of all the plasma ions (ion viscosity scales as $T_i^{5/2}$), the heat gained by each ion would be 237 eV. If this energy is dissipated into only the sheath ions, the heat gain would be 388 eV per ion.

(iii) Magnetic Compression

Muir [25] estimates that the work done by the magnetic field per unit length during the time period t=-10 ns to t=0 ns is $\sim$ 5.5 kJ.m^{-1}. On taking an average line density of 2.2×10^{20} m^{-1} during this period, the energy gain per particle is 156 eV.

(iv) Sheath Region - Ohmic Heating

Since the plasma current is restricted to the outer sheath region during the collapse phase, only this region will obtain energy directly from Ohmic heating. The power dissipated per unit volume is given by $\eta_\perp J_z^2$ and the Joule heating per unit length by $\eta_\perp J_z^2 A_c$, where A_c is the cross sectional area of the current carrying region. Assuming that the energy from Ohmic heating is thermalised throughout the outer sheath region of cross sectional area A_s containing $n_{e\ell}$ electrons per unit length, then the eV heating rate per electron, H_R within the outer sheath region is given by,

$$H_R = 6.24 \times 10^9 \frac{\eta_\perp J_z^2 A_c}{n_{e\ell}} \text{ eV/electron/ns} \qquad (7.67)$$

Substituting for $\eta_\perp$ from eq 7.64 and J_z from eq 7.59 we get,

$$H_R = 1.65 \times 10^{-32} \frac{(n_e D)^2 A_c \ell n\Lambda}{n_{e\ell} T_e^{3/2}} \text{ eV/electron/ns} \qquad (7.68)$$

At t=-40 ns, $n_{e\ell}$ for the outer sheath region is 4×10^{19} m^{-1}, $\bar{n}_e=8.9\times10^{23}$ m^{-3} and the cross sectional area $A_s=4.5\times10^{-5}$ m^3. Taking the electron temperature at this time to be $\sim$100 eV, $\ln\Lambda\sim10$. The drift veleocity at this time is $\sim2\times10^6$ $m.s^{-1}$, so assuming that the cross sectional area of the filaments $A_c=A_s/10$, we get H_R=59 eV-/electron/ns.

The outer sheath T_e reaches an average value (of the two modes) $\sim$1 keV by t=-30 ns. At this time, $n_{e\ell}=5\times10^{19}$ m^{-1}, $\bar{n}_e=1.35\times10^{24}$ m^{-3}, giving $\ln\Lambda\sim13$ and the sheath region cross sectional area $A_s=3.7\times10^{-5}$ m^3. Taking $\underline{D}=5\times10^6$ $m.s^{-1}$ with $A_c=A_s/10$ we get H_R=23 eV/electron/ns.

If the resistivity is anomalous during this period by only $\sim$100,

then the electron heating rate will be increased by two orders of magnitude, while the magnetic field diffusion time will still be $\sim 4\,\mu s$, which is long compared with the collapse phase time scale. It is interesting to compare these figures with those estimated by Bertalot et al [45], who concluded that Ohmic heating was insufficient to account for the observed electron heating rate. It should be noted however, that the authors assumed a value of $\underline{D}=6\times10^{4}$ m.s^{-1}, which is approaching two orders of magnitude smaller than the values utilised here. The effect of filamentary current structures within the sheath region therefore has a significant effect on the Ohmic heating rate which is proportional to D^2.

7.5.6 CURRENT DRIVEN TURBULENCE AND TURBULENT HEATING

We have seen in the preceding sections, that very large drift velocities occur within the sheath region during the collapse phase, in addition to an anomalous resistivity at $t \geq 0$ ns, which is significantly larger than the classical Spitzer value. The electron-ion drift velocity will result in the excitation of high frequency electrostatic waves. Therefore, it is appropriate at this point to consider whether such turbulence can account for the rapid rise in sheath temperature and perhaps offer an explanation for the estimated resistivity level which will account for the rapid magnetic field diffusion.

There are five principle electrostatic waves with sufficiently high growth rates to be of consequence to the Plasma Focus. These are the Buneman two-stream instability [67,68], the ion-acoustic instability [69], the electron-cyclotron drift instability [36,70,71,-73], the lower-hybrid drift instability [73,74,75] and the modified two stream instability [75,76]. The principle characteristics of these

five instabilities are listed below:

(a) Buneman two-stream

For $D>v_e$ ($D_t>1$) the two stream instability is likely to dominate. It has a characteristic frequency of the order ω_{pe}, given by eq 2.7 and a growth rate, $\gamma_{TS}\sim(m_e/m_i)^{1/3}\,\omega_{pe}$. The drifting electrons are scattered by the wave giving an effective collision time, $\tau_{TS}\sim\gamma_{TS}^{-1}$, which is shorter than that for binary electron-ion collisions, resulting in an anomalously high plasma resistivity.

(b) Ion-acoustic

For $v_e>D>C_s$ ($D_t<1$), $T_e/T_i>1$, where C_s is the ion sound speed given by $C_s=(ZeT_e/m_i)^{\frac{1}{2}}$, the ion-acoustic instability is most likely to dominate. The instability has a characteristic frequency of the order of ω_{pi}, where ω_{pi} is the ion plasma frequency given by, $\omega_{pi}=(n_ie^2/m\varepsilon_o)^{\frac{1}{2}}$. The growth rate, $\gamma_{IA}\sim(m_e/m_i)^{\frac{1}{2}}\,(D/C_s)\omega_{pi}$. The waves propagate in a cone away from the perpendicular magnetic field direction. Energy is transfered from those drifting electrons that are resonant with the sound wave to the wave, which then interacts with those ions having velocities close to its phase velocity. The plasma resistivity is enhanced due to electrons scattering off the wave. The effective collision frequency is given by Sagdeev & Galeev [69] as, $\nu_{IA}\sim(D/C_s)(T_e/T_i)\omega_{pi}$. As in Ohmic heating, the turbulent heating from this process increases mainly the electron temperature. Even in the situation of the total wave energy being absorbed by the ions, the heating rates for the electrons and ions are limited by the inequality [69], $T_i/T_e\ll C_s/D$.

When the temperature ratio $T_e/T_i\leq1$ and $D<v_e$ ($D_t<1$), the other three listed instabilities may possibly exist:

(c) Electron-cyclotron drift

For $\omega_{pe} >> \omega_{ce}$, where ω_{ce} is the electron-cyclotron frequency given by eq 2.50, the electron cyclotron drift instability may occur and has a characteristic frequency $\sim\omega_{ce}$ and a growth rate $\gamma_{EC}\sim(m_e/m_i)^{\frac{1}{4}}\omega_{ce}$. The instability arises from the resonant coupling of a Doppler-shifted ion mode with the electron-cyclotron mode, feeding energy into the electrons. The effective electron collision frequency is given by Forslund et al [71] as, $\nu_{EC}\sim\omega_{ce}$. The nonlinear development of the instability depends on the product kr_{ec}, where r_{ec} is the electron--cyclotron radius given by $r_{ec}=(2m_e T_e/e)^{\frac{1}{2}}\ (1/B)$. The dominant modes of the instability satisfy the condition $kr_{ec}>2\pi$ [71].

(d) Lower-hybrid drift

The instability has a characteristic frequency $\omega_{LH}=(\omega_{ce}\omega_{ci})^{\frac{1}{2}}$ where ω_{ci} is the ion cyclotron frequency given by $\omega_{ci}=eB/m_i$. The growth rate $\gamma_{LH}\sim\omega_{LH}$ is maximised for wavevectors k such that $kr_{ec}\sim 1$. The effective collision frequency is given by $\nu_{LH}\sim 0.1(\omega_{pe}/\omega_{ce})^2\omega_{LH}$ [73].

(e) Modified two-stream

This instability also has a characteristic frequency $\sim\omega_{LH}$ and a growth rate $\gamma_{MTS}\sim\omega_{LH}$. The growth rate is maximised for wavevectors k such that $kr_{ec}<1$. The waves propagate away from the perpendicular magnetic field direction, but in a much narrower cone than the ion-acoustic instability. This instability is also unstable for $T_e >> T_i$.

Electron heating for the Buneman instability is so rapid that the condition for its existence, $D>v_e$ is unlikely to be met during the collapse phase of the plasma. Assuming at t=-40 ns $T_e \sim 100$ eV would require $\underline{D}>6\times10^6$ m.s^{-1}. Gladd [75] concluded from comparison of the

lower-hybrid drift and modified two-stream instability, that under most conditions the lower-hybrid drift instability will dominate. Deutsch- & Kaeppeler [73] in comparing the lower-hybrid and electron-cyclotron drift instabilities, calculate that for plasma conditions of $n_e=1x10^{25}$ m^{-3}, $T_e=T_i=50$ eV and $\underline{B}=20$ T, the relative growth rates of the two instabilities, $\gamma_{LH}/\gamma_{EC}=0.2$. Therefore for high density regions, the electron-cyclotron drift instability cannot be neglected, but for lower densities the lower-hybrid drift instability need only be considered since γ_{LH}/γ_{EC} increases as n_e^{-2}. For high density plasma regions, assuming $T_e=1$ keV and $\underline{B}=20$ T, for the antiparallel scattering geometry with $\underline{k}_{10}=1.58x10^6$ m^{-1}, $kr_{ec}=8.4$, satisfying the condition $kr_{ec}>2\pi$ for the dominant modes of the electron-cyclotron drift instability. However, the effects of a gradient in $\underline{B}$, which result in a "smearing out" of the resonances and a suppression of the growth rate [36] need to be assessed.

We are therefore left with three possible instabilities which are of relevance to the collapse phase of the plasma. These are the ion--acoustic, electron-cyclotron drift and lower-hybrid drift instabilities. In considering which of these instabilities may be driven by the high drift currents, we need to assess several observations of the results of the experiments. These are the temporal characteristics of the double temperature modes of the sheath region during the collapse phase and the required anomalous resistivity level at t=0 ns to account for the rapid magnetic field diffusion time $\sim$ 10 ns following peak compression. Because of the rapidly changing conditions during the collapse phase, it would be naive to suggest that either of the two temperature modes and the rapid field diffusion time may be accounted for by just one instability mechanism.

Figure 7.31 shows the temporal evolution of the temperature ratio T_e/T_i during the collapse phase, where (a) illustrates the ratio for the outer (current carrying) sheath region derived from the analysis of the 10 degree $\underline{k}$ orthogonal to $\underline{z}$ sheath temperatures and (b) the ratio for the inner sheath region derived from the analysis of the 45 degree $\underline{k}$ orthogonal to $\underline{z}$ temperatures. The marked difference between mode A and mode B temperature profiles is very apparent from these plots. In order to assess the requirements for rapid magnetic field diffusion, the principle plasma parameters for the sheath and core regions as defined for the 10 degree scattering geometries at t=0 ns, when the magnetic field is still confined to the skin region, are tabulated in table 7.1. The table includes the effective anomalous collision frequency required to account for the magnetic field diffusion time of 10 ns, which was calculated using eq 7.60 and 7.65. In addition the effective collision frequencies of the three instabilities under consideration are listed.

If we consider first the mode A outer sheath temperature structure (fig 7.31a), it can be seen that the sheath T_e value increases rapidly from t=-40 ns resulting in a T_e/T_i ratio equal to 3.7 by t=-30 ns. This is paralleled by a slower increase in T_i throughout the collapse phase, resulting in a steady decrease in the T_e/T_i ratio following t=-30 ns to a value of 2.7 at t=0ns. The inner sheath T_e/T_i ratio for mode A, indicated in figure 7.31b, has a similar shape, but lower T_e/T_i ratios are reached. For the assumed initial conditions of the sheath at t=-40 ns, $T_e \sim T_i$, either the lower-hybrid or electron--cyclotron drift instabilities are the most likely ones to dominate, leading to the rapid rise in T_e in conjunction with Ohmic heating. As has already been noted, Bertalot et al [45] have observed similar rapid increases in T_e to >2.0 keV in $\sim$ 10 ns, but for times closer to t=0 ns.

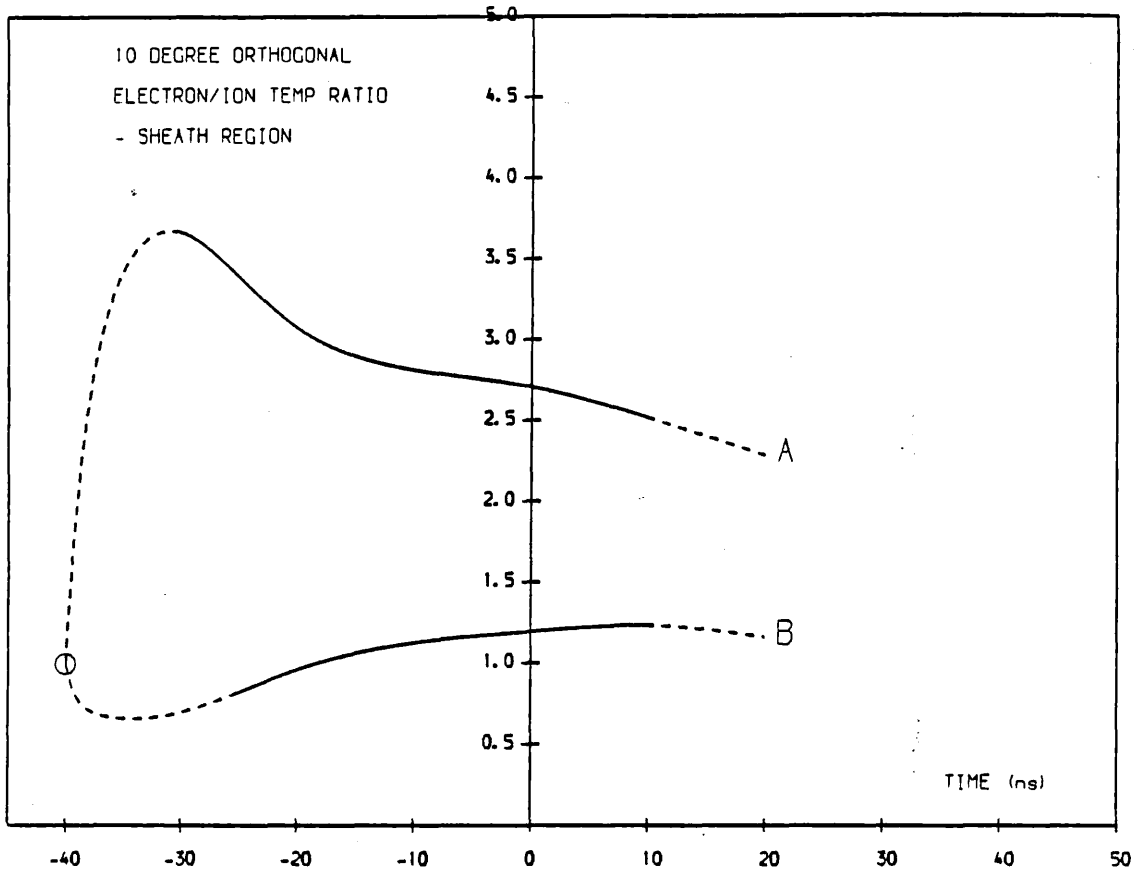

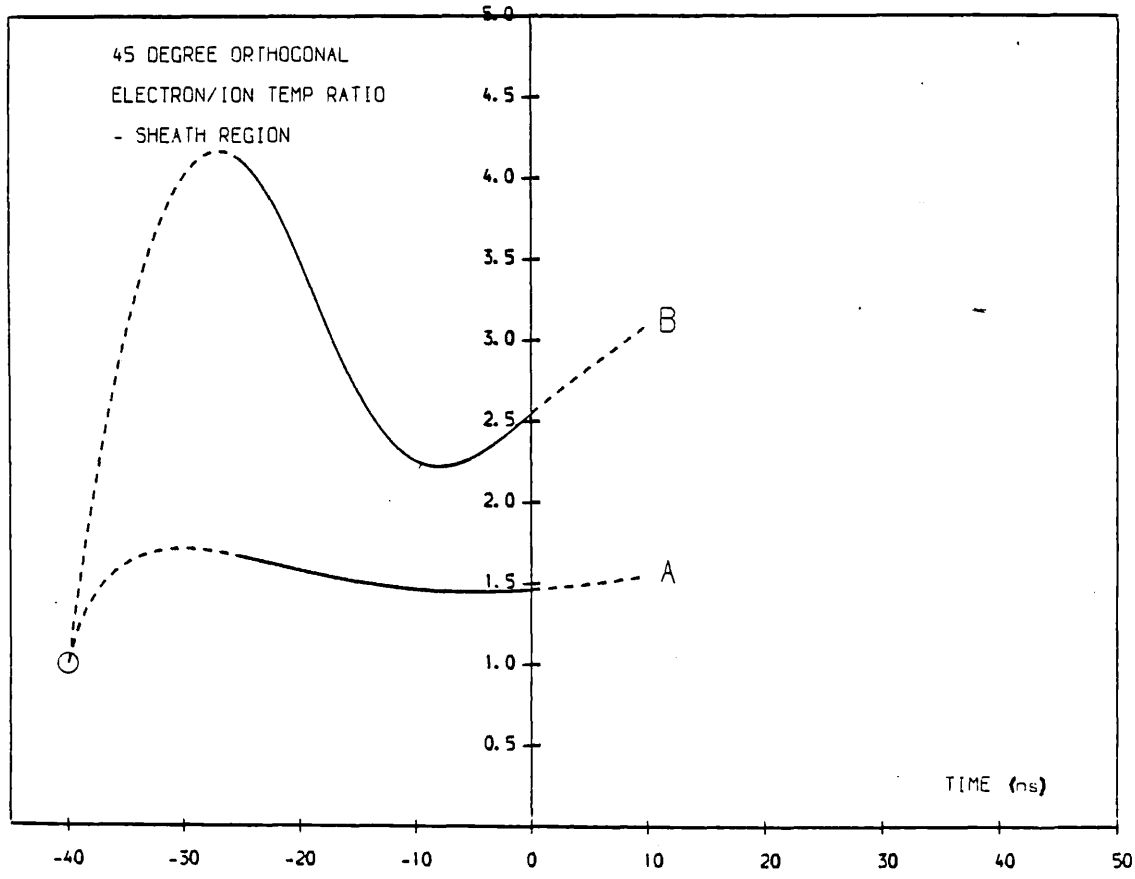

Figure 7.31

Temporal evolution of T_e/T_i ratio for double temperature mode structure during the collapse phase of the plasma for (a) the outer sheath region (b) the inner sheath region.

Parameter	Sheath region		Core Region
	Mode A	Mode B	
n_e (average)	2.6×10^{24} m^{-3}		7.5×10^{24} m^{-3}
T_e	2.3 keV	1.65 keV	250 eV
T_i	850 eV	1.4 keV	200 eV
$\underline{D}$	1.5×10^{7} m.s^{-1}		------
$\underline{B}$ (average)	20 T		------
$\omega_{pe} = \left(\frac{n_e e}{m_e \varepsilon_o}\right)^{\frac{1}{2}}$	9.0×10^{13} rad.s^{-1}		1.5×10^{14} rad.s^{-1}
$\omega_{pi} = \left(\frac{n_i e^2}{m_i \varepsilon_o}\right)^{\frac{1}{2}}$	1.5×10^{12} rad.s^{-1}		2.6×10^{12} rad.s^{-1}
$\omega_{ce} = \frac{eB}{m_e}$	3.5×10^{12} rad.s^{-1}		------
$\omega_{ci} = \frac{eB}{m_i}$	9.6×10^{8} rad.s^{-1}		------
$\omega_{LH} = (\omega_{ce}\omega_{ci})^{\frac{1}{2}}$	5.8×10^{10} rad.s^{-1}		------
$C_s = \left(\frac{ZeT_e}{m_i}\right)^{\frac{1}{2}}$	3.3×10^{5} m.s^{-1}	2.8×10^{5} m.s^{-1}	9.8×10^{4} m.s^{-1}
$\nu_{ei} = 2.9\times10^{-12} \frac{n_e Z \ln\Lambda}{T_e^{3/2}}$	9.6×10^{8} s^{-1}	1.6×10^{9} s^{-1}	7.7×10^{10} s^{-1}
ν_{ei} (anomalous) $= 1.96\times10^{-11} n_e$	5.1×10^{13} s^{-1}		1.5×10^{14} s^{-1}
$\nu_{IA} = \frac{D}{C_s}\frac{T_e}{T_i}\omega_{pi}$	1.8×10^{14} s^{-1}	9.5×10^{13} s^{-1}	------
$\nu_{EC} \sim \omega_{ce}$	3.5×10^{12} s^{-1}		------
$\nu_{LH} \sim 0.1 \left(\frac{\omega_{pe}}{\omega_{pi}}\right)^2 \omega_{LH}$	3.8×10^{12} s^{-1}		------

Table 7.1
Principle plasma parameters at peak compression, t=0 ns.

They concluded that only the lower-hybrid instability had sufficient a high growth rate to account for the high electron heating rates, although as was noted earlier in section 7.5.5, their assumed lower Ohmic heating rates were based on a planar current distribution resulting in lower drift velocities. However, from the calculations detailed above of Deutsch & Kaeppeler [73] of the relative growth rates of the lower-hybrid and electron cyclotron drift instabilities, it would seem that for the initial low density sheath at t=-40 ns with $\bar{n}_e = 8.9 \times 10^{23}$ m^{-3}, the lower-hybrid drift instability is the most likely one to dominate. From the list of effective collision frequencies at t=0 ns (table 7.1), it can be seen that only the ion-acoustic instability would seem to have an enhanced collision frequency of sufficient magnitude to explain the observed field diffusion time. Certainly the temperature ratio of mode A at t=0 ns of ~ 2.7 and the the drift velocity $D \sim 45 \times C_s$ would provide ideal conditions for the existence of ion-acoustic turbulence. It is highly likely therefore, that following the rapid rise in T_e, the resultant high T_e/T_i ratio leads to the onset of the ion-acoustic instability. The reason why the rapid field diffusion is not observed until after t=0 ns is probably as a result of the temporal convolution of the 10 degree $\underline{k}$ antiparallel to $\underline{z}$ spectra indicating higher drift velocities for the early collapse phase than exist in reality. This effect was detailed in section 7.5.3.

The second mode B temperature structure which indicates initial ion heating rates greater than that of the electrons for the outer sheath region (fig 7.31a), but a rapid increase in T_e/T_i for the inner sheath region (fig7.31b), is more difficult to break down into possible instabilities mechanisms. It should be noted that the above statement does not mean that the inner sheath electron temperature increases more

rapidly than that of the outer, as can be seen from figures 7.14 and 7.21. The effect on the T_e/T_i ratios is simply as a result of the outer sheath ion temperature rise. With the initial conditions of $T_e \leq T_i$, it would seem that either the electron-cyclotron or lower-hybrid instability would provide the heating mechanism in conjunction with Ohmic heating. The rapid ion heating, with the initial conditions assumed, is more difficult to explain. Possibly very localised regions (i.e. within the confines of the current filaments) are subject to rapid electron heating, which then provides a localised $T_e/T_i >> 1$ for the onset of ion-acoustic turbulence which heats the ions.

The reason for the double temperature structure is probably due to the plasma conditions at the onset of the collapse phase. Slightly different electron density and temperature gradients and variations in the filamentary current structures at this stage being responsible for the instability route followed during the collapse phase. Bertalot- et al [45] noted that the double T_e modes they observed were probably due to the growth rate of the lower-hybrid instability being sensitive to the density gradient [73]. The initial conditions of the collapse phase are probably strongly dependent on the initial formation of the plasma across the insulator. Therefore the physics of this stage probably has a strong bearing on the later plasma parameters and structure.

Note on Rapid Magnetic Field Diffusion

It should be stressed at this point, that the observations of rapid magnetic field diffusion and partial current constriction on axis by Muir [25], were based on the averaging of data over a large number of plasma shots. The observation of filamenatary current structures on

axis following this phase were only observed on $\sim$ 25% shots, so the exsistence of rapid field diffusion on every shot may not be true. This irreproducibility is similary observed from the scattering results for $t \geq 0$ ns, when only approximately 40% of the 10 degree spectra showed anomalous behaviour. The difference in these two observed figures probably results from the different plasma dimensions observed by the two diagnostics. There exists a strong possibility therefore, that the rapid magnetic field diffusion may be related to only one of the two temperature profile modes. From the conclusions of the above discussions, mode A with the higher T_e/T_i ratio and therefore higher probability of ion-acoustic turbulence, with its associated high effective collision frequency, is the most likely candidate.

7.5.7 PLASMA TEMPERATURE - POST COMPRESSION PHASES

From the results of the 10 and 45 degree $\underline{k}$ orthogonal to $\underline{z}$ analysis of the thermal level shots, it can be seen that no significant bulk plasma heating occurs folllowing peak compression. The reason for the further rise in the 10 degree core temperature until t=+10 ns, has already been discussed in section 7.5.1. Adiabatic expansion, particle loss in the $\underline{z}$-direction and radiation losses result in a bulk plasma cooling which is approximately temporally symmetric with the collapse phase. Therefore any substantial plasma temperatures ($\geq$ keV) must be restricted to very small plasma volumes, otherwise they would have been discernable from the analysis of the 10 degree $\underline{k}$ orthogonal to $\underline{z}$ thermal level spectra, which as has already been demonstrated is not significantly effected by low n_e/T_e ratios as is the case for the 45 degree $\underline{k}$ orthogonal to $\underline{z}$ spectra.

7.5.8 ANOMALOUS SHOTS

The anomalous shots observed for $t \geq 0$ ns (with the exception of one shot at t=-20 ns), were associated with an above average enhancement of the 10 degree $\underline{k}$ antiparallel to $\underline{z}$ spectrum. The 10 degree $\underline{k}$ orthogonal to $\underline{z}$ spectrum of these shots exhibited broadening and enhancement relative to the thermal level shots of the same time period. Some of these spectra were asymmetric, with the peak of the spectrum being either blue or red shifted with respect to the laser wavelength. No discernable modification to the 45 degree $\underline{k}$ orthogonal to $\underline{z}$ spectrum was observed on these shots compared with the thermal level shots.

On comparing the level of enhancement of the 10 degree $\underline{k}$ antiparallel to $\underline{z}$ spectra of these shots with that observed for the sheath region for $t \leq 0$ ns, it is highly probable that the drift to electron thermal ratio is greater than unity. Whether this situation prevails for long, allowing for a possible rapid increase in the localised T_e value due to the Buneman two-stream instability, is debateable. In assessing the mechanisms that are likely to be responsible for the observed anomalous behaviour, two other factors need to be considered. Firstly, the anomalous shots appear to be divided into two types, which were characterised in sections 7.4.1 and 7.4.3. Secondly, the observation of localised, high density, intense X-ray emission spots reported previously [39,42,43], cannot be explained from adiabatic compression. They are therefore possibly related to these anomalous scattering observations.

The various mechanisms which may account for the anomalous scattering behaviour will now be discussed:

(A) If we consider first, those anomalous shots that show only small

scale enhancements for both the $\underline{k}$ orthogonal and antiparallel to $\underline{z}$ 10 degree spectra, then possibly ion-acoustic turbulence alone may account for the observations. With current driven ion-acoustic turbulence, energy oscillations occur within the Cherenkov cone about the $-\underline{z}$-axis direction having a cone angle $\theta = \cos^{-1}(C_s/D)$ [69]. With $D >> C_s$, their will be wave turbulence with the wavevectors having significant components aligned with the differential scattering vectors of the 10 and 45 degree $\underline{k}$ orthogonal to $\underline{z}$ scattering geometries. The lack of modification to the 45 degree spectra is probably due to the significant Landau damping of the smaller scale length ($2\pi k^{-1}$) ion turbulence. From this observation a lower limit for the scale length of the turbulence can be calculated. This will be greater or equal to the scale length for scattering of the 45 degree geometry, which has a value of 9.1×10^{-7} m.

(B) The second type of anomalous shots show very large enhancents of both 10 degree spectra. Additionally the 10 degree $\underline{k}$ orthogonal to $\underline{z}$ spectra are broadened with 1/e half widths equivalent to ion temperatures of up to 9 keV and shifts of the peak of the spectrum from the laser wavelength of up to 0.25 nm. Using eq 3.3, this shift is equivalent to a radial velocity component of 6.2×10^5 m.s^{-1}. Since no modification of the 45 degree spectrum is observed, the most probable explanation of this behaviour is a small, localised, high density, high T_e volume within the scattering volume. Two possible sources of such a volume exist:

(i) During the break-up phase of the plasma, necking of the plasma due to m=0 "sausage" instabilities is observable in the holographic interferograms. It is possible that the plasma current passing through the necking leads to a very high localised T_e value. Depending on the density within the necking region, the n_e/T_e ratio may be small enough

such that no significant contribution to the 45 degree spectrum originates from the necking volume. From figure 3.7 (p66), this suggests that the localised n_e/T_e ratio is $\leq 1\times10^{21}$ $m^{-3}.eV^{-1}$. If we assume that the density is $\sim 1\times10^{25}$ m^{-3} within the necking region, then the T_e value is $\geq$10 keV. This figure is in approximate agreement with the maximum observed widths of the 10 degree $\underline{k}$ orthogonal to $\underline{z}$ spectra. However, the total electron number density within such a small volume will not account for the observed level of scattered energy of such shots assuming thermal level scattering. One is therefore lead to the conclusion that the enhancement and broadening observed is again due to high levels of turbulence, but in this case from a very localised region. Using the discussions in (A) above, the lower limit for the scale length of turbulence must again be $\geq 9.1\times10^{-7}$ m. The observed positive or negative shifts of the peaks of the 10 degree $\underline{k}$ orthogonal to $\underline{z}$ spectra may be due to m=1 "kink" instabilities which are also observed in the holographic interferograms during the time period of the anomalous shots. It is possible that localised regions of the plasma may acquire large radial velocity components during this disruptive period of the plasma.

(ii) The second explanation of the observed behaviour of this class of anomalous shot is that they are associated with the previously reported observations [39,42,43] of localised intense X-ray emission spots. The arguments presented above for the necking region of an m=0 "sausage" instability similarly apply in this case. That is, that high levels of turbulence with a lower scale length limit of $\geq 9.1\times10^{-7}$ m, exist within the hot spot region. Due to the disruptive nature of the plasma at this time, these hots spots may gain sufficient radial velocity to explain the observed shifts of the 10 degree $\underline{k}$ orthogonal to $\underline{z}$ spectra. The formation mechanism of such regions of plasma is difficult to explain, but it may well be associated with the rapid contraction of

the current distribution on axis as observed in the Faraday rotation measurements of Muir [25].

Both the necking theory and the suggestion above of localised turbulent volume formation, due to the rapid current contraction, are consistent with the observations of axial current filaments inferred from the measurements of Muir [25]. These filaments had durations of $\leq$2.5 ns, the limit being set by the bandwidth of the detection system. From these measurements magnetic field strengths of 44 and 57 Tesla for times of t=+10 and +15 ns were determined respectively due to filaments of 42 and 72 kA respectively. These currents are approximately 12 - 21% of the plasma current at this time. An upper limit on the radius of the filaments of 190 - 250 microns was set by the spatial resolution of the Faraday rotation diagnostic. The calculated [25] current density of the filaments gives a drift to thermal ratio, D_t of only 0.05, assuming an electron temperature of 1 keV. The scattering results however, suggest that a much higher drift ratio ocuurs. Muir [25] estimates that for D_t=1, the axial filaments would have to have diameters of 30 and 57 microns respectively, giving current densities of 1.5×10^{13} A.m^{-2} and 7.0×10^{12} A.m^{-2}. Filaments of these radii and currents would have self magnetic fields of 280 and 253 Tesla respectively. It is possible that either turbulent heating or if the resistivity within the filaments is sufficiently anomalous, that Joule heating will result in an increase in kinetic pressure within the filament which is larger than the filament magnetic pressure, resulting in break-up of the filament. Such a mechanism may account for the short observed lifetime of the filaments. Similar observations of axial current filamentation have been reported by other researchers. Neff et al [24] observed subnanosecond electron beams >0.5 MeV using a Cherenkov detector. The time duration of these beams was less than

0.4 ns with an estimated beam current of 40 kA. Ion beams have been observed by Filippov et al [21] and Nardi et al [22].

It has been previously demonstrated for times $t \leq 0$ ns, that the enhancement of the 10 degree $\underline{k}$ antiparallel to $\underline{z}$ spectrum, relative to the 10 degree $\underline{k}$ orthogonal to $\underline{z}$ spectrum, results from a localised volume (the current carrying sheath region). In a similar way, the enhancement of the anomalous shots is probably very much larger than the maximum of $\sim$ 77 observed, due to the localised nature of the source. Consider the scattering volume illustrated in figure 7.32.

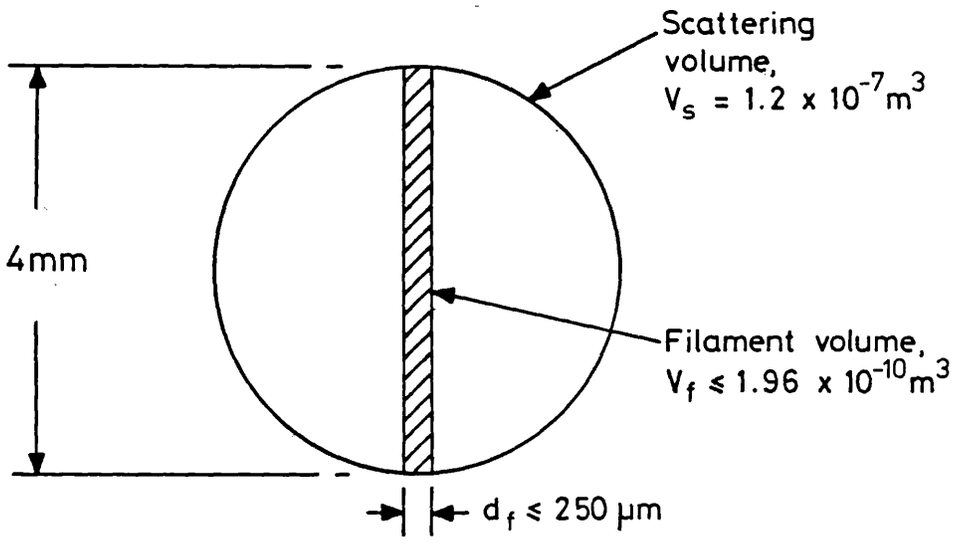

Figure 7.32
Illustration of the scattering volume containing a current filament.

The scattering volume at t=+25 ns is $\sim 1.2 \times 10^{-7}$ m^3 . Assuming that the current filament diameter, $d_f \leq 250\ \mu m$, the volume of the filament within the scattering volume, $V_f \leq (\pi d_f^2/4) \times 4.0 \times 10^{-3}$ m^3 $= 1.96 \times 10^{-10}$ m^2 . Therefore the localised enhancemnt for the filament volume will be

increased by a factor $\geq$ 612. This increases the maximum observed enhancement above the thermal level to $\geq$ 77 x 612 = 4.7×10^4. This figure may in fact be even larger as a result of the short duration of the filaments.

7.5.9 COMMENTS ON THE NEUTRON PRODUCTION MECHANISM

The intense nuclear fusion reaction rate in the Plasma Focus has been the subject of intensive study [9,19,66] and controversy over the last two decades. Typically 10^9 to 10^{10} neutrons per discharge are produced from a device of the size described in this thesis. The neutron emission is anisotropic, with a factor of up to 3 times more neutrons emitted in the z-axis direction than in a direction perpendicular to the axis [13]. The neutron energy spectrum exhibits a large axial energy shift of between 200 and 700 keV from the 2.45 MeV DD neutron line [13]. A correlation between this shift and the anisotropy factor has also been observed.

Two simple models have been invoked to account for the neutron emission from the Plasma Focus. These are the beam-target and moving boiler models, both of which are discussed by Gentilini et al [77]. In the beam-target model, neutrons are assumed to be produced from the interation of a beam of deuterons, accelerated to energies of $\leq$0.25 MeV, with plasma ions and the cold background filling gas. In the moving boiler model, the neutron emission is assumed to originate from a thermonuclear plasma region with a temperature ~ 10 keV and with a centre of mass velocity of approximately $10^6 m.s.^{-1}$ in the z-direction. Neither of these models by themselves however, is totally in agreement with experimental observations.

One immediate conclusion from the measurement of the ion temperature derived from the thermal shots in this study, is that the average particle temperature is insufficient to account for the observed neutron production based on a thermonuclear model. Additionally, the observed maximum axial bulk velocity of the core region of 1.4×10^5 $m.s^{-1}$ is insufficient to support the moving boiler model, though the sheath bulk velocity approaches the required magnitude. The large scale enhancements of the 10 degree $\underline{k}$ antiparallel to $\underline{z}$ spectra, which have been interpreted as consistent with axial current filaments, suggest that some form of beam-target model may be appropriate. However, the broadening and enhancement of the 10 degree $\underline{k}$ orthogonal to $\underline{z}$ spectra observed on similar shots, was interpreted as originating from highly turbulent localised regions. It is possible that such regions may be responsible for those experimental results which suggest a moving boiler model for the neutron production, assuming the regions obtain a sufficiently high axial velocity.

The scattering results of this study would therefore support both models and it is probable that both processes, not excluding other possibilities, may be involved in producing the observed neutron emission characteristics of the Plasma Focus.

CHAPTER 8 CONCLUSIONS AND SUGGESTIONS FOR FUTURE WORK

The application of a multiple-$\underline{k}$ laser scattering technique to the Plasma Focus device has led to significant improvements in determining the ion and electron temperatures of the plasma. Additionally, the diagnostic has provided a further insight into the dynamics of this complex plasma. In particular, it has indicated the presence of filamentary current structures both during the collapse phase, within the sheath region and in the phases following peak compression.

The use of a multiple-$\underline{k}$ scattering arrangement has largely overcome the problem of interpreting the scattered data from an irreproducible, inhomogeneous plasma, a problem which had hindered the conclusions of previous workers using single-$\underline{k}$ arrangements. The provision of a detection system having a large number of channels, has enabled a more detailed analysis of the results to be undertaken than had been previously possible. Direct comparison of the results of the analysis of the two scattering geometries with scattering vectors, $\underline{k}$ orthogonal to the pinch $\underline{z}$-axis, in conjunction with a clearer view of the effects resulting from rapidly changing radial electron density and temperature profiles, has permitted a comprehensive picture of the temperature profiles as a function of time to be constructed. From this analysis, it has been possible to understand the results of previous scattering experiments undertaken with a range of single-$\underline{k}$ systems. The range of temperatures that were determined from these measurements [15,16,17,-18,19,20] are generally correct once the plasma radial velocity and the effect of a rapidly changing n_e/T_e radial profile are taken into consideration. The effect of the latter is particularly important for large scattering angles (θ=45-90 degrees) with λ_o=694.3 nm, since the

major radial contribution to the cooperatively scattered light becomes increasingly shifted towards the plasma axis as the scattering angle is increased.

During the collapse phase of the plasma, the plasma current is restricted to the plasma skin with a penetration depth $\sim$ 0.7--0.8 mm [25]. On comparison of this dimension with a minimum plasma radius of 2.35 mm at z=10 mm, it can be seen that this region of the plasma contains only a minor fraction of the total electron number within the scattering volume. Therefore, with a scattering volume having dimensions of the order of the plasma diameter, the sheath region will make only a minor contribution to the total scattered light, irrespective of the scattering angle and laser wavelength selected. This small contribution leads to two problems. The 1/e half width of the scattered light profile will be dominated by the temperature of the core region. Secondly, the localised T_e/T_i ratio of the current carrying sheath region needs to be determined, since the enhancement of the 10 degree $\underline{k}$ antiparallel to $\underline{z}$ spectrum is very sensitive to this ratio. The development of a double radial shell scattering volume model was therefore the most important aspect of the analysis work. Employing this technique permitted a more accurate picture of the radial temperature profile of the Plasma Focus to be determined than had been previously achieved, in addition to determining an estimate of the temporal development of the drift velocity during the collapse phase. The values of the latter are significantly larger than had been previously assumed [25,45].

Interpretation of the data following peak compression (t=0 to +40 ns) is made more difficult due to the random break-up behaviour of the pinch. However, the large scale enhancements of the 10 degree $\underline{k}$

antiparallel to $\underline{z}$ spectra of up to 77 times the thermal level during this phase, strongly support the existence of ion/electron beams in agreement with the results of previous researchers [21,22,23,24,25]. The large scale enhancements and broadening of the 10 degree $\underline{k}$ orthogonal to $\underline{z}$ spectra that were observed when no similar modification of the 45 degree spectrum was apparent, may be interpreted as consistent with the observations of localised high density, turbulent, hot spots [39,42,43]. The multiple-$\underline{k}$ technique has again been useful in this instance for two reasons. The simultaneous observation of the large scale enhancement of the spectra of the two 10 degree scattering arrangements, strongly suggests that the high density hot spot formation is associated with the existence of ion/electron beams. Secondly, as no modification of the 45 degree $\underline{k}$ orthogonal to $\underline{z}$ spectrum is observed on these anomalous shots, a lower limit for the scale length of the turbulence associated with such events can be calculated.

A summary of the results of the investigation of each phase of the Plasma Focus is detailed below, followed by suggestions for future work on the Plasma Focus using laser scattering techniques. The chapter is concluded with possible alternative applications of the techniques utilised to provide a multiple-$\underline{k}$ scattering arrangement.

8.1 SUMMARY OF RESULTS AND THEIR INTERPRETATION

Collapse Phase

During the collapse phase of the plasma, prior to t=0 ns, the plasma radial geometry was successfully approximated for analysis

purposes as a double radial shell model, consisting of a sheath region collapsing on a core region. At a $\underline{z}$-axis position of 10 mm the sheath plasma-vacuum boundary contracts radially with a velocity of 2.68×10^5 m.s^{-1} to a minimum radius of 2.35 mm at t=0 ns. For the 10 degree $\underline{k}$ orthogonal to $\underline{z}$ spectra analysis the sheath region was assumed to have a radial incremental thickness in the range 0.7-0.8 mm, corresponding to the current penetration depth measured by Faraday rotation polarimetry [25]. A value of double this incremental thickness was used for the analysis of the 45 degree $\underline{k}$ orthogonal to $\underline{z}$ spectra. During the period t=-40 ns to t=0 ns, the major plasma heating was found to occur in the sheath region.

From comparison of the results of the two $\underline{k}$ orthogonal to $\underline{z}$ scattering arrangements, the existence of a double temperature structure mode within the sheath region has been established. There is evidence [45] to suggest that this behaviour is not peculiar to the Plasma Focus employed in this investigation. Both sheath temperature modes exhibit rapid electron and ion heating relative to the core region.

One temperature profile mode (mode A) shows an initial rapid rise in the electron temperature for the current carrying sheath region from an assumed value of 100 eV at t=-40 ns to $\sim$ 1.65 keV at t=-30 ns resulting in a T_e/T_i ratio of 3.7. This is paralleled by a slower rise in the ion temperature throughout the phase. The final temperatures at t=0 ns are $T_i \sim 850$ eV, $T_e \sim 2.3$ keV. During the period after t=-30 ns the T_e/T_i ratio decreases to a value of 2.7 at t=0 ns. The inner sheath region shows a similar temporal temperature development but with smaller T_e/T_i ratios. This temperature profile mode was interpreted as resulting from initial Ohmic and current driven lower-hybrid drift

turbulent heating of the electrons between t=-40 ns and t=-30 ns. Following this, the increase in the T_e/T_i ratio will then permit the ion-acoustic instability to grow and dominate, resulting in a rise in sheath ion temeperature as the collapse phase proceeds. The effective collision frequency of the current driven ion-acoustic turbulence is sufficient to account for the observed rapid magnetic field diffusion time $\sim$ 10 ns [25] following peak compression.

The second temperature profile mode (mode B), indicates a rapid rise in the ion temperature for the current carrying outer sheath region, in conjunction with a rise in electron temperature in both the outer and inner sheath regions. The T_e/T_i ratio of the outer sheath region initially becomes less than unity, the temperatures rising to final values at t=0 ns of $T_i \sim 1.4$ keV, $T_e \sim 1.65$ keV. The T_e/T_i ratio of the inner sheath region rapidly rises to a value of ~ 4.2 at t=-30 ns and then decreases to $\sim$ 2.5 by t=0 ns. The different T_e/T_i ratio behaviour of the two sheath regions is the result of the ion heating being restricted to the outer sheath region in comparison with mode A described above, where ion heating of the inner sheath region was also apparent. The approximately equal ion and electron heating rates of the outer sheath region are more difficult to interpret. It is possible that localised electron heating within the filamentary sheath current structure provides localised conditions of $T_e/T_i >> 1$ leading to the onset of ion-acoustic turbulent heating.

The double temperature mode structure was interpreted as being as a result of different initial conditions of the plasma at the commencement of the collapse phase. Variations in the temperature and density gradients and perhaps the filamentary current structure being responsible for the instability route followed to peak compression. It

is important to note that the conditions at the onset of the collapse phase are likely to be strongly dependent on the plasma formation across the insulator, so the physics of this period probably has a strong bearing on the dynamics of the pinch in later phases.

The core region will not benefit from Ohmic or turbulent heating resulting from an electron-ion drift velocity, due to the absence of current in this region. The temperature rise to $T_i \sim 250$ eV, $T_e \sim 200$ eV at t=0 ns, principally results from the adiabatic compression of the plasma.

The analysis of the 10 degree $\underline{k}$ antiparallel to $\underline{z}$ spectra were undertaken using the temperatures determined from the 10 degree $\underline{k}$ orthogonal to $\underline{z}$ spectra, where the sheath region was assumed to correspond to the current penetration depth determined by Faraday rotation polarimetry [25]. The results indicate that the electron-ion relative drift velocity in the sheath region is in the range $2.5 \times 10^6 - 2.2 \times 10^7$ m.s^{-1}, which corresponds to an electron drift to thermal speed ratio of 0.1 - 0.9. These measurements suggest that the plasma current is restricted to filamentary channels within the sheath region as opposed to the planar current shell model that was assumed by Muir [25]. The results of the latter limit the electron drift to thermal ratio to a maximum of 0.025 at t=0 ns, assuming an electron temperature of 1 keV. The conclusions of a filamentary current structure within the sheath region are in agreement with the optical observations of Bostick et al [43a].

Post Compression Phase

From the analysis of the thermal level 10 and 45 degree $\underline{k}$

orthogonal to $\underline{z}$ spectra, no bulk plasma heating was observed for the time period t=0 ns to t=+40 ns. Approximately 40% of the shots in this time period exhibited anomalous behaviour, which was observed in the two 10 degree scattering arrangements, but produced no discernable modification of the 45 degree spectrum relative to the thermal shots. These anomalous shots were divisible into two groups based on the observed modifications of the 10 degree spectra.

The first group showed a scattered to thermal energy ratio for the 10 degree $\underline{k}$ orthogonal to $\underline{z}$ spectra of 0.5 - 3, with broadening of the spectra to 1/e half widths equivalent to ion temperatures in the range 500 eV - 2 keV. All the spectra were symmetric about the laser wavelength. The 10 degree $\underline{k}$ antiparallel spectra of these shots had enhancements in the range 4 - 15 above the thermal level. These observations were interpreted as being consistent with current driven ion-acoustic turbulence over a large cone angle about the $-\underline{z}$-axis direction. From the lack of modification to the 45 degree spectrum, a lower limit for the scale length of the turbulence of $\geq 9.1 \times 10^{-7}$ m was calculated.

The second group of anomalous shots had enhancements of the 10 degree $\underline{k}$ orthogonal to $\underline{z}$ spectra in the range 4 - 25. The spectra exhibited gross broadening relative to their thermal counterparts, with 1/e half widths equivalent to ion temperatures in the range 2 - 9 keV. Some of these spectra were strongly asymmetric, with peaks shifted both to the blue and red of the laser wavelength by 0.1 - 0.25 nm. The 10 degree $\underline{k}$ antiparallel to $\underline{z}$ spectra of these shots exhibited enhancements above the thermal level in the range 40 - 77. This simultaneous anomalous behaviour of both 10 degree spectra was interpreted as being consistent with electron/ion beams leading to the

formation of localised high density, highly turbulent hot spots. If the source of the enhancement of the 10 degree $\underline{k}$ antiparallel to $\underline{z}$ spectrum is assumed to be a current filament of diameter $\leq$ 250 microns, then the localised enhancement of the scattered light is $\geq 4.7 \times 10^{7}$ above the thermal level. The asymmetry and shifts observed in some of the 10 degree $\underline{k}$ orthogonal to $\underline{z}$ spectra were considered to result from these localised regions gaining radial velocity components of up to 6.2×10^{5} m.s^{-1}, due to the onset of the disruptive phase of the plasma. The lack of modification of the 45 degree spectrum, again permitted a lower limit to be set on the scale length of the turbulence associated with these shots of $\geq 9.1 \times 10^{-7}$ m.

8.2 FUTURE RESEARCH

The results of this investigation of the Plasma Focus device using cooperative laser scattering techniques were subject to a variety of limitations resulting from both the experimental apparatus and method. These limitations are outlined below and suggestions for future improvements and other experimental developments are discussed.

(A) The investigation of the temporal variation of the scattered spectra was subject to the convolution of profiles resulting from the evolution of the plasma over the ruby laser pulse length. The available laser energy and a minimum OMA gating time of 40 ns, limited the minimum laser pulse FWHM to 20 ns. Recent developments in OMA's, which were briefly discussed in the introduction to chapter 5, include diode array devices with microchannel intensifiers which can be gated to a minimum of 5 ns. The use of such devices in conjunction with a

frequency doubled Neodymium laser (530 nm) of suitable energy would greatly improve the temporal resolution of the scattering system.

(B) The vacuum chamber on the Culham Plasma Focus, precluded scattering angles and $\underline{k}$ vector orientations other than those listed in section 3.5.2. For the further study of the post peak compression turbulence with $\underline{k}$ vectors aligned to the plasma z-axis, it would be desirable to increase the range of scattering angles available with this geometry so that the level of enhancement as a function of $\underline{k}$ could be determined. Additionally, a detail investigation of the source of the turbulence would provide valuable information of the post compression dynamics of the pinch. Three possible experimental schemes for further investigation of this feature of the pinch are considered below:

(i) The multiple-$\underline{k}$ scattering technique could be easily utilised in its present form to measure the spectrum from three scattering geometries having $\underline{k}$ vectors aligned with the plasma z-axis. Scattering angles of 10, 20 and 30 degrees with a ruby laser, would provide a suitable range of $\underline{k}$ values to study the relative enhancement of the spectra.

(ii) The time resolved $\underline{k}$ spectrum technique employed by Baldis - et al [78], using a large diameter collection lens imaged onto a streak camera slit to study CO_2 laser-plasma interactions, could be adapted to study the turbulence $\underline{k}$ spectrum in the post compression phase of the Plasma Focus.

(iii) A detailed investigation of the spatial origin of the turbulence in the post compression phase would be of great significance to the dynamics of the pinch. In particular, it may well give a clear indication of the neutron production mechanism. It would be of fundamental interest to be able to distinguish between a filamentary source or a localised hot spot and to study the source as a function of

time. A possible experimental arrangement to study this could be undertaken with a streak camera employed in the spatial mode. It is envisaged that a reasonable length of the plasma $\underline{z}$-axis could be illuminated with a long probe laser pulse (20-50 ns) using a cylindrical focussing lens. The scattering collection system with a forward scattering angle of $\sim$10 degrees with $\underline{k}$ aligned to the $\underline{z}$-axis would image the axial plasma volume onto the streak camera slit, background plasma emission being limited using a narrow band interference filter centred on the laser wavelength. By streaking over a time period from say t=0 ns to +50 ns, it would be possible to distinguish between point and filamentary sources. The enhancement as a function of time and the duration of the source could be additionally investigated using this arrangement. In the case of a filamentary source, the diameter of this could be measured using the same technique, but with the line illumination and streak camera object volume rotated orthogonal to the plasma $\underline{z}$-axis. A more complete picture of the physical processes involved could be obtained, if a time resolved neutron diagnostic and an x-ray pin-hole camera were employed in conjunction with the obove suggested experiments.

(C) The major limit on the sensitivity of the collection-dispersion--detection system used for the experiments was the coupling efficiency of the circular cross section fibre optic output ends to the vertical input slits on the grating spectrometer. The losses that occur here could be easily overcome in future applications of this technique by using fibre optic bundles with a circular input cross section and a rectangular output cross section having an aspect ratio optimised for the slit dimensions. With these improvements, the technique of using multiple input slits could be used for applications other than multiple-$\underline{k}$ scattering measurements. Spatial measurements of either

scattered laser light or plasma line emission could be readily determined provided that sufficient photons are available per detection channel. With the recent developments in diode arrays, which can now provide up to ~730 intensified channels, there is the possibility of increasing the number of input slits and collection geometries, the number depending on the width of the dispersed spectra to be analysed.

REFERENCES

[1] Peacock N.J., Robinson D.C., Forrest M.J., Wilcock P.D. & Sannikov V.V., Nature, London, (1968), 224, 488.

[2] Bretz N., Dimock D., Foote V., Johnson D., Long D. & Tolnas E., Applied Optics, (1978), 17, 2, 192-202.

[3] Evans D.E. & Carolan P.G., Phys. Rev. Lett., (1970), 25, 1605.

[4] Forrest M.J., Carolan P.G. & Peacock N.J., Nature, London, (1978), 271, 718.

[5] Baldis H.A., Samson J.C. & Corkum P.B., Phys. Rev. Lett., (1978), 41, 25, 1719-1722.

[6] Baldis H.A. & Walsh C.J., Phys. Rev. Lett., (1981), 47, 23, 1658-1661.

[7] Mather J.W., Phys. Fluids Supp., (1964), S28.

[8] Mather J.W., Phys. Fluids, (1965), 8, 366.

[9] Mather J.W., Methods of Exp. Phys., (1971), 9B, 178.

[10] Filippov N.V., Filippova T.I. & Vinogradov V.P., Nuc. Fusion, (1962), Suppl. part 2, 577.

[11] Morgan P.D., PhD Thesis, University of London, 1974.

[12] Decker G. & Wienecke R., Physica, (1976), 82C, 155-164.

[13] Schmidt H., Proc. 2nd Int. Conf. on Emerging Nuc. Energy Systems, Lausanne, (1980).

[14] Maisonnier Ch., Pecorella F., Rager J.P., Samuelli M., Strangio C. & Messina A., Proc. 5th Int. Conf. on Plasma Phys. and Controlled Nuc. Fusion Research, Tokyo, (1974), paper IAEA-CN-33/E 6-2.

[15] Forrest M.J. & Peacock N.J., Plasma Phys., (1974), 16, 489.

[16] Baconnet J.P., Cesari G., Coudeville A. & Watteau J.P., Phys. Lett., (1969), 29A, 1, 19.

[17] Baconnet J.P., Cesari G., Coudeville A. & Watteau J.P., Proc. 9th Int. Conf. on Phenomena in Ionised Gases, Bucharest, (1969), paper 5.3.6.

[18] Bernard A., Coudeville A., Garconnet J.P., Jolas A., De Mascureau J. & Watteau J.P., Phys. Lett., (1971), 35A, 1, 7.

[19] Bernard A., Coudeville A., Jolas A., Launspach J. & De Mascureau J., Phys. Fluids, (1975), 18, 2, 180. (and references therein)

[20] Downing J.N. & Eisner M., Phys. Fluids, (1975), 18, 8, 991.

[21] Filippov N.V. & Fillippova T.I., JETP Lett., (1979), 29, 12, 689-693.

[22] Nardi V., Bostick W.H., Feugeas J., Prior W. & Cortese C., Proc. 7th Int. Conf. on Plasma Physics and Controlled Nuc. Fusion Research, Innsbruck, (1978), paper IAEA-CN-37/U-3-3.

[23] Harries W.L., Lee J.H. & McFarland D.R., Plasma Phys., (1978), 20, 95-106.

[24] Neff W., Krompholz H., Ruhl F., Schonbach K. & Herziger G., Phys. Lett., (1980), 79A, 165-166.

[25] Muir D.G., PhD thesis, University of London, 1983.

[26] Salpeter E.E., Phys. Rev., (1960), 120, 1528.

[27] Rosenbluth M.N. & Rostoker N., Phys. Fluids, (1962), 5, 776.

[28] Bernstein I.B., Trehan S.K. & Weenink M.P.H., Nuc. Fusion, (1964), 4, 61.

[29] Evans D.E. & Katzenstein J., Rep. Prog. Phys., (1969), 32, 207-271.

[30] Sheffield J., "Plasma Scattering of Electromagnetic Radiation", Academic Press, Inc. (London) Ltd, (1975).

[31] Kunze H.J., "Plasma Diagnostics", (ed- Lochte-Holtgreven W.) North Holland Publ., Amsterdam, (1968), chapter 9.

[32] Fried B.D. & Conte S.D., "The Plasma Dispersion Function", Academic Press, Inc. (New York), (1961).

[33] Bohm D. & Gross E.P., Phys. Rev., (1949), 75, 1851.

[34] Carolan P.G., PhD Thesis, The Queen's University of Belfast, 1973.

[35] Boyd T.J.M., Evans D.E. & Gardner G.A., 10th Int. Conf. on Ionised Gases, Oxford, (1971), paper 5.3.2.

[36] Gary S.P. & Sanderson J.J., J. Plasma Phys., (1970), 4, 739-751.
Gary S.P., J. Plasma Phys., (1970), 4, 753-760.

[37] (a) Forrest M.J., Morgan P.D., Peacock N.J., Kuriki K., Goldman M.V. & Rudolph T., Phys. Rev. Lett., (1976), 37, 25, 1681.
(b) Peacock N.J., Forrest M.J., Goldman M.V., Rudolph T., Morgan P.D., Kuriki K. & Offenberger A.A., Proc. 6th Int. Conf. on Plasma Phys. and Controlled Nuc. Fusion Research, Berchtesgaden, (1976), paper IAEA-CN-35/G4-4.

[38] Tanimoto M., Koyama K., Matsumoto Y. & Sugiura M., 6th Int. Conf. on Plasma Phys. & Controlled Nuc. Fusion Research, Berchtesgaden, 1976, paper IAEA-CN-35/G4-1.

[39] Neil G.R. & Post R.S., Plasma Phys., (1981), 23, 5, 425.

[40] Evans D.E., Plasma Phys., (1970), 22, 573.

[41] Hirschberg J. & Platz P., Appl. Opt., (1965), 4, 1375.

[42] Peacock N.J., Hobby M.G. & Morgan P.D., Proc. 4th Int. Conf. on Plasma Phys. and Controlled Nuc. Fusion Research, Madison, (1971), paper IAEA-CN-28/D-3.

[43] (a) Bostick W.H., Nardi V. & Prior W., Annals New York Acad. Science, (1975), 251, 2-29.
(b) Bostick W.H., Nardi V. & Prior W., Proc. 5th Int. Conf. on Plasma Phys. and Controlled Nuc. Fusion Research, Tokyo, (1974), paper IAEA-CN-33/E 6-3.
(c) Bostick W.H., Nardi V. & Prior W., Proc. 6th Int. Conf. on Plasma Phys. and Controlled Nuc. Fusion Research, Berchtesgaden, (1976), paper IAEA-CN-35/PD2.

[44] Peacock N.J., "X-ray and Neutron Production Optimization in the Dense Plasma Focus", Air Force Weapons Laboratory Report, (1973), Report No. AFWL-TR-73-147.

[45] Bertalot L., Deutsch R., Herold H., Jager U., Kaeppeler H.J., Mozer A., Oppenlander T., Ruckle B., Sadowski M., Schilling P. & Schmidt H., Proc. 8th Int. Conf. on Plasma Phys. and Controlled Nuc. Fusion Research, Brussels, (1980), paper IAEA-CN-38/G-1-2.

[46] Forrest M.J., Jones P.A., Peacock N.J., Prentice R., Seldon A.C., Walker C.I. & Ward S., JET Design Study 8.2, "Spatial Scan Thomson Scattering", Part 2, Jan 1980.

[47] Peacock N.J., Speer R.J. & Hobby M.J., J. Phys. B, (1969), 2, 798.

[48] Mather J.W. & Bottoms P.J., Phys. Fluids, (1968), 11, 611.

[49] Mather J.W. & Bottoms P.J., Phys. Fluids, (1968), 11, 3, 611.

[50] Jahoda F.C. & Siemon R.E., Los Alamos Report LA-5058-MS, (1972).

[51] Faw R.E. & Dulforce T.A., Culham Report CLM-RR/S2/19, (1977).

[52] Veron D., Report EUR-CEA-FC-980, (1978).

[53] Bockasten K., J. Opt. Soc. Am., (1961), 51, 943.

[54] Falconer I.S. & Ramsden S.A., J. Appl. Phys., (1968), 39, 3449.

[55] Evans D.E., Forrest M.J. & Katzenstein J., Nature, London, (1966), 212, 21-3.

[56] Prentice R., "The DITE Tokamak Multi-pulse Thomson Scattering System", UKAEA Culham Laboratory Report No. CLM-R 179.

[57] Kronast B. & Pytrzyk Z.A., Phys. Rev. Lett., (1971), 26, 67.

[58] Offenberger A.A., Burnett N.H., Strilchuk A.R. & Way-Nee D.F., Rev. Scientific Instr., (1974), 45, 11, 1400.

[59] Godfrey L.A., Nodwell R.A. & Curzon F.L., Phys. Rev. A, (1979), 20, 2, 567.

[60] "Model 1205A Operating & Service Manual", Princeton Applied Research Corp., NJ USA.

[61] "Model 1211 Operating & Service Manual", Princeton Applied Research Corp., NJ USA.

[62] Kirk R.E., Muir D.G., Forrest M.J. & Peacock N.J., Proc. Int. Conf. on Plasma Phys., Goteborg, (1982), paper 14P-I-03. (bound in thesis)

[63] Bevington P.R., "Data Reduction and Error Analysis for the Physical Sciences", McGraw-Hill Book Co., London, (1969).

[64] Spitzer L., "Physics of Fully Ionised Gases", Interscience Publishers, Inc., New York, (1956).

[65] Boyd T.J.M. & Sanderson J.J., "Plasma Dynamics", Thomas Nelson and Sons Ltd., London, (1969).

[66] Bernard A., Coudeville A., Garconnet J.P., Jolas A., De Mascureau J. & Nazet C., Proc. 8th European Conf. on Controlled Fusion and Plasma Phys., Prague, (1977), I, 64.

[67] Buneman O., Phys. Rev., (1959), 115, 503.

[68] Hirose A., Plasma Phys., (1978), 20, 481-485.

[69] Sagdeev R.Z. & Galeev A.A., "Nonlinear Plasma Theory", Edited by O'Neil T.M. & Book D.L., W.A. Benjamin, Inc., New York, (1969).

[70] Forslund D.W., Morse R.L. & Nielson C.W., Phys. Rev. Lett., (1970), 25, 1266-1270.

[71] Forslund D.W., Morse R.L. & Nielson C.W., Proc. 4th Int. Conf. on Plasma Phys. and Controlled Nuc. Fusion Research, Madison, (1971), paper IAEA-CN-28/E-18.

[72] Lashmore-Davies C.N., J. Phys. A, (1970), 3, L40.

[73] Deutsch R. & Kaeppeler H.J., "Microinstabilities in a Radially Contracting Inhomogeneous Plasma Slab II. Lower-Hybrid and Electron-Cyclotron Drift Instabilities in the Plasma Focus", Report No. IPF-80-13, (1980), Institut fur Plasmaforschung der Universitat Stuttgart, Stuttgart.

[74] Krall N.A. & Liewer P.C., Phys. Rev. A, (1971), 4, 2094.

[75] Gladd N.T., Plasma Phys., (1976), 18, 27-40.

[76] Gary S.P., Plasma Phys., (1973), 15, 399-410.

[77] Gentilini A., Maisonnier Ch., & Rager J.P., Report CNEN 79.7/p, (1979).

[78] (a) Baldis H.A. & Walsh C.J., Proc. Int. Conf. on Plasma Phys, Goteborg, (1982), paper 11P-I-10.
(b) Baldis H.A., Walsh C.J. & Benesch R., IEEE Int. Conf. on Plasma Phys., Ottawa, (1982).

SYMBOLS

a_ℓ - least squares fitting parameter
A - approximated focussed laser beam waist width
A_c - cross-sectional area of current carrying region
A_o - cross-sectional area of focussed laser beam waist
A_s - cross-sectional area of plasma sheath region
$\underline{B}$ - magnetic field
c - velocity of light
C, C' - constants
C_{I+p} - normalised instrument profile weighting coefficients
CF_i - OMA counts to energy. str^{-1} conversion factor for ith OMA channel
d - diameter of focussed laser beam waist
d_f - diameter of plasma current filament
d_r - ratio of the product of the magnitude of the electron-ion drift velocity and cosine of the angle between it and the differential scattering vector to the electron thermal speed
D_t - ratio of the magnitude of the electron-ion drift velocity to the electron thermal speed
$\underline{D}$ - electron-ion drift velocity
e - elementary charge
E_B - background (bremsstrahlung) energy
E_i - scattered energy detected by ith OMA channel normalised to steradians
$E_F(\lambda)$ - scattered energy fitting function (convolved with the instrument profile)
E_o - incident laser energy
E_s - scattered energy
E_T - total integrated scattered energy
$\underline{E}_o$ - incident laser electric field
$\underline{E}_s$ - scattered wave electric field
f - optical transmission factor of collection system
- fractional error in a parameter
F - fringe shift
- scattering volume division factor
$F_{e,i}$ - velocity distributions of electrons and ions
g - Gaunt factor
$G_{e,i}$ - electron and ion dielectric susceptibilities
h - Planck constant
- impact parameter (interferometry)
H_R - electron heating rate
I - plasma current

I_o - incident laser intensity
j - shell volume subscript: j=1, core: j=2, sheath
$\underline{J}_z$ - plasma current density
$\underline{k}$ - differential scattering vector
$\underline{k}_o$ - incident laser wave vector
$\underline{k}_s$ - scattered wave vector

$\hat{\underline{k}}$ - unit vector parallel to $\underline{k}$
L - characteristic length of plasma (radius)
L_n - density scale length
m - scattering volume parameter
$m_{e,i}$ - electron and ion masses
n_c - critical electron density (cut-off density)
$n_{e,i}$ - electron and ion densities

$n_{e\ell}$ - electron line density

n_p - plasma peak density
N - electron number
N_{Bc} - number of detected bremsstrahlung photons
N_{BP} - number of bremsstrahlung photons reaching detector
N_{SC} - number of detected scattered photons
N_{SP} - number of scattered photons reaching detector
N_{TC} - total number of detected photons
p - gas filling pressure
$P_B(\lambda)$- power spectrum of bremsstrahlung emission
P_o - incident laser power
P_s - scattered wave power
$P(\underline{k},\omega)$-scattered power frequency spectrum

Q - quantum efficiency of detector
r - radial position
r_e - classical electron radius
r_{ec} - electron cyclotron radius

r_1', r_2', r_3' - plasma vacuum boundary hyperbolic equation coefficients

R_A - relative amplitude factor
R_D - radial shell model division radius
R_j - shell volume equipartition radius
R_{pn} - peak density radius

R_{pv} - plasma vacuum boundary radius
$\underline{R}$ - vector from detector to electron
$\underline{R}_e$ - position of an electron
$\underline{R}_d$ - position of detector
$S(\underline{k})$ - total integrated scattered energy
$S(\underline{k},\omega)$ - dynamic form factor
t - time
t' - retarded time
t'' - scattering volume parameter
t_g - detector gating time
T - laser pulse time relative to peak
$T_{e,i}$ - electron and ion tmeperatures
$\overline{T}$ - average plasma temperature
T_R - ratio of electron and ion tmeperatures
u - scattering volume parameter
$v_{e,i}$ - electron and ion thermal velocities
V - capacitor bank voltage
V_f - current filament volume (within scattering volume)
V_s - scattering volume
V_p - plasma volume
$\underline{V}_B$ - plasma bulk velocity parallel to $\underline{z}$-axis
$\underline{V}_{pv}$ - plasma-vacuum boundary radial velocity
$\underline{V}_r$ - plasma radial velcity
w - diameter of scattering collection beam waist
W_T - laser pulse temporal weighting factor
$W(x)$ - plasma dispersion function
$x_{e,i}$ - dimensionless frequency/wavelength variables
y - scattering volume parameter
y_i - ith OMA channel count
z - plasma z-axis position
Z - ion charge
α - scattering parameter
α_{jk} - Bockasten Abel inversion coefficients
β^2 - scattered profile shape factor
γ - angle between scattered wave vector and incident electric field vector
- ratio of specific heats
- growth rate of plasma instabilities (i.e γ_{LH} - growth rate of lower-hybrid drift instability)
γ_E, γ_{EB} - resistivity correction factors

ε - plasma dielectric coefficient
ε_0 - permittivity of free space
η - resistivity
θ - scattering angle
- Cherenkov cone angle (ion-acoustic instability)
κ - Boltzmann constant
λ - wavelength shift
λ_D - Debye length
λ_0 - incident laser wavelength
Λ - Coulomb parameter
$d\lambda$ - detection system wavelength bandwidth
$\Delta\lambda_{B,r}$ - wavelength shift due to bulk and radial plasma velocity components
$\Delta\lambda_w$ - 1/e wavlength half width of spectrum
μ_0 - permeability of free space
ν - frequency
- collision frequency due to a plasma instability (i.e. ν_{LH} - collision frequency of lower-hybrid drift instability)
ν_{ei} - electron-ion collision frequency
σ_{a_ℓ} - uncertainty in determining curve fitting parameters
σ_i - uncertainty in experimental data point i
$\sigma(\underline{k},\omega)$ - differential cross-section
σ_T - Thomson cross-section
τ_B - magnetic field diffusion time
ϕ - angular position co-ordinate
- angle between $\underline{k}$ and $\underline{B}$
Φ - angle between radial velocity component and $\underline{k}$
χ^2 - measure of goodness of fit of theoretical curve to experimental data
ω - angular frequency shift
ω_{ac} - ion acoustic frequency
ω_{ce} - electron-cyclotron frequency
ω_{ci} - ion-cyclotron frequency
ω_{LH} - lower-hybrid frequency
ω_o - incident laser angular frequency
ω_p - frequency shift of peak of spectrum from laser frequency
ω_{pe} - electron plasma frequency
ω_{pi} - ion plasma frequency
ω_s - angular frequency of Doppler shifted scattered wave
$d\omega$ - detection system frequency bandwidth
$\Delta\omega_{B,r}$ - frequency shift due to bulk and radial plasma velocity components
$d\Omega$ - solid angle of collection optics

PUBLICATIONS

Proc. Int. Conf. on Plasma Physics, Goteborg (1982), paper 14P-I-03.

NEW EVIDENCE FOR NON-THERMAL FLUCTUATIONS IN THE PLASMA FOCUS USING IMPROVED LIGHT SCATTERING TECHNIQUES

R E Kirk*, D G Muir*, M J Forrest, N J Peacock

Culham Laboratory, Abingdon, Oxon, OX14 3DB
(Euratom/UKAEA Fusion Association)

*On attachment from Royal Holloway College, University of London

ABSTRACT

Refined optical laser scattering techniques have been used to investigate the dynamics of the plasma focus device. Holographic interferometry, Faraday rotation and co-operative laser light scattering have provided detailed temporal evolution of the plasma parameters. Of these, three are believed to be unique measurements in this device, namely, the radial magnetic and current density profiles and three simultaneous scattered ion spectra.

The physical understanding of the plasma focus device [1] has been hitherto restricted by the difficulties in diagnosing such complex transient plasmas. Here, we report the application of three complementary optical diagnostics techniques to investigate the collapse and dense-pinch phases of a focus described previously [2,3] with a stored energy of 25 kJ at 23 kV and with a filling pressure of 1.8 torr of deuterium. Holographic interferometry, Faraday rotation and co-operative laser light scattering from a multiple beam output Q-switched ruby laser producing pulses of 15-300 MW and 1.5-30 ns FWHM provide comprehensive temporal information on the plasma parameters. These include the radial electron density profile $n_e(r)$, the azimuthal magnetic field $B_\theta(r)$, the current density distribution $J_z(r)$ and three ion fluctuation spectra $S_i(\underline{k},\omega)$.

The Faraday rotation (FR) technique [4] is based on the differential half-shade method [5] with a viewed plasma chord diameter of 250 μm and has a temporal resolution of 2.5 ns and an angular rotation resolution of 0.4 mrad. The detailed temporal evolution of the FR observed at a given chord impact parameter is built-up over several plasma shots, using a 30 ns 20 MW laser pulse, while the spatial variation is obtained by repeating the measurement over several impact parameters. By combining the FR measurements with electron density distributions obtained using 1.5 ns exposure holographic interferometry, the magnetic field structure is obtained by Abel inversion [6]. The current density is then obtained with Ampere's law.

The ion feature of the Thomson scattered light spectrum has been measured synchronously for three differential scattering vectors $\underline{k}$ and two values of the scattering parameter $\alpha = (k\lambda_D)^{-1}$. Three sets of collection optics [7] view essentially identical scattering volumes situated at a position on the pinch $\underline{z}$-axis 10 mm below the centre electrode, with the laser incident, $\underline{k}_{inc}$ normal to this axis. Two scattering angles of 10 and 45 degrees (and thus two different α values) having differential scattering vectors $\underline{k}$ with no component parallel to the $\underline{z}$-axis (i.e. no current driven effects) yield thermal levels of the scattered light. This has enabled the effects of the radial velocity component [8] and plasma impurities [9] on the ion spectrum to be measured by cross correlating the effects for both α values for a single shot. A second 10 degree scattering direction is in the plane defined by $\underline{z}$ & $\underline{k}_{inc}$ and permits the additional effects on the scattered light spectrum due to a relative electron-ion drift velocity [10] parallel to the $\underline{z}$-axis to be measured. The temporal evolution of the ion features for these three $\underline{k}$ vectors has been built up over a large number of shots from t = -50 ns to +80 ns relative to the peak compression of the pinch.

The FR measurements obtained at a z position = 5 mm indicate that the maximum rotation, observed at peak compression of the pinch (t = 0 ns), was 0.475 degrees. Abel inverted magnetic field profiles are shown in Fig. 1. At times t = -8 ns and t = 0 ns, the field and hence current is confined to the plasma skin with penetration depths 0.5 and 0.7 mm respectively. During these times, the plasma current is 340 kA $\pm$ 30%, which is 70% of the load current. Figure 2 shows the scattered data obtained from a shot at t = -5 ns. For times before peak compression it is observed that the 10 degree $\underline{k}$ parallel to $\underline{z}$ spectrum is enhanced with respect to the thermal spectrum by 20% at t = -40 ns rising to 100% at t = 0 ns. The enhanced spectrum is characterised by being asymmetric with its peak blue shifted with respect to the ruby wavelength. This is interpreted as being due to an electron-ion drift

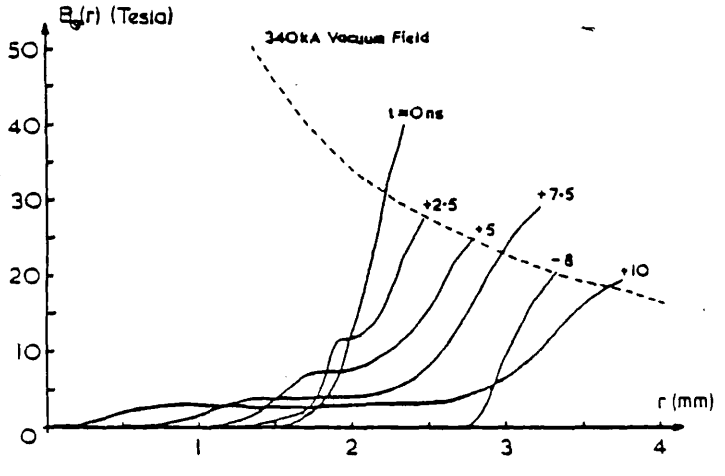

Fig. 1

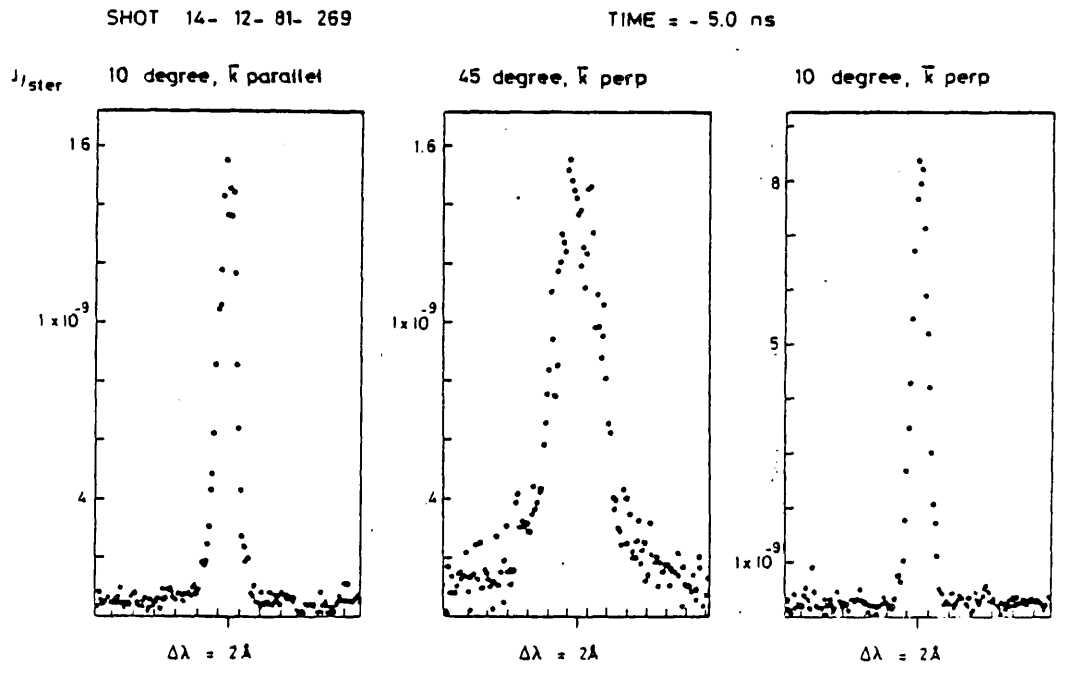

Fig. 2. Scattered data from optical multichannel analyser

velocity, v_d, with a $v_d/v_{th} \sim$ 0.1-0.8 which is in agreement with the plasma current being carried in the skin. During this period profile fitting of the two thermal level spectra indicates that allowing for radial velocity effects the average parameters across the plasma diameter are Ti $\sim$ 400 eV, Te $\sim$ 800 eV and a radial velocity of $\sim$ 2.0 x 10^5m/s which is in agreement with the radial velocities observed from the holographic interferometry. Pressure balance calculations from the magnetic field profiles indicate that with a Te/Ti $\sim$ 2 the plasma edge temperatures are Ti $\sim$ 600 eV and Te $\sim$ 1200 eV from which the $\underline{B}$ penetration depth is $\sim$ 2-3 ion Larmour radii and $\omega_{ce}\tau_{ei} \sim 10^2$.

The important feature of the FR results is the observation of a rapid diffusion of the magnetic field after peak compression towards the axis (penetration time $\sim$ 10 ns). The current density profiles shown in Fig. 3 clearly illustrates this diffusion. At t = +2.5 ns, the current structure has divided into two annular rings. At times t = +5 ns and t = +7.5 ns it is seen that one ring is radially contracting, while the other is expanding. At t = +10 ns, the current has all but reached the axis. This rapid field diffusion could be explained as being due to an enhancement of the resistivity to $\sim 10^4$ Spitzer due to the Hall term $[1 + (\omega_{ce}\tau_{ei})^2]$. The rapid collapse of the current density distribution as observed, has been proposed as a possible ion acceleration mechanism for neutron production in the plasma focus [11].

During some plasma shots, relatively large rotations $\sim$ 1 degree were observed at times between +10 ns and +15 ns with duration of $\lesssim$ 2.5 ns. At a slightly later time interval of +15 to +20 ns (due to the difference in z-axis observation positions) very large enhancements are observed in the k parallel to z scattered spectrum which are typically five to ten times the thermal level.

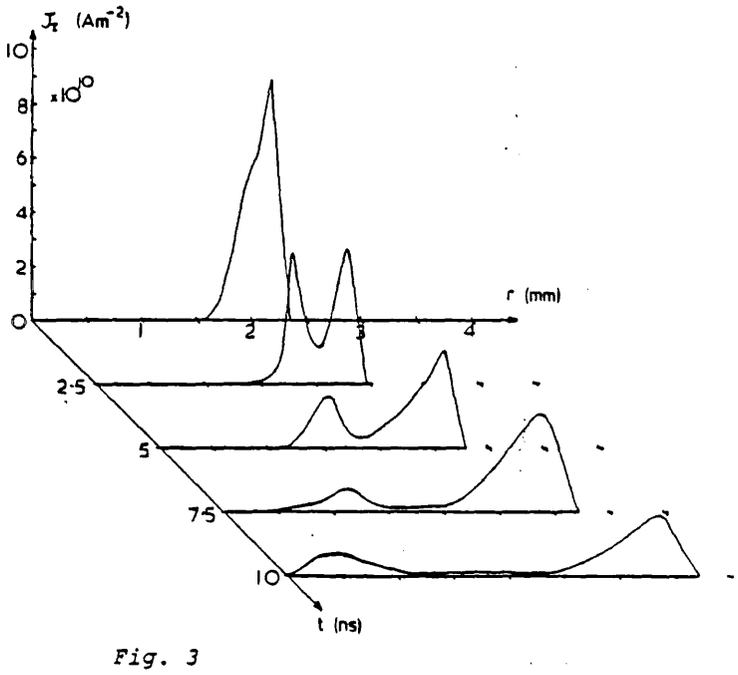

Fig. 3

Enhancements of up to 30 times have been observed. The indication is that during this period v_d/v_{th} becomes greater than unity. Abel inversion of the FR profiles has revealed the existence at these times of beam currents on the axis carrying $\gtrsim$ 60 kA, i.e. $\gtrsim$ 20% of the plasma current. In conclusion we report the first detailed FR and scattering observations of the plasma focus giving firm evidence for the existence of current redistribution and the resultant production of axial beam currents during the dense pinch phase.

REFERENCES

[1] Mather, J.W., Phys. Fluids, 8 336, (1965).

[2] Peacock, N.J., Speer, R.J. & Hobby, M.J., J. Phys. B. 2, 798 (1969).

[3] Peacock, N.J., Hobby, M.G. & Morgan, P.D., Plasma Physics and Controlled Fusion Research, IAEA, Vienna, 1, 537 (1971).

[4] Muir, D.G. et al, to be published.

[5] Falconer, I.S. & Ramsden, S.A., J. Appl. Phys., 39, 7, 3449 (1966).

[6] Bockasten, K., J. Opt. Soc. Am., 51, 9, 943, (1961).

[7] Kirk, R.E. et al, to be published.

[8] Downing, J.N. & Eisner, M., Phys. Fluids (USA), 18, 8, 991, (1975).

[9] Evans, D.E., Plasma Physics, 12, 573, (1970).

[10] Evans, D.E. & Katzenstein, J., Rep. Prog. Phys., 32, 207, (1969).

[11] Bernstein, M.J., Phys. Fluids, 13, 11 2858, (1970).

Proc. 11th Euro Conf. Controlled Fusion and Plasma Physics, Aachen, W Germany (1983) Vol.7D, Part 1, E12, p571.

THE SIGNIFICANCE OF NEW MEASUREMENTS OF DENSITY FLUCTUATIONS AND THE CURRENT DISTRIBUTION IN THE CULHAM PLASMA FOCUS

M J Forrest, R E Kirk*, D G Muir*, N J Peacock

Culham Laboratory, Abingdon, Oxon, OX14 3DB, UK
Euratom/UKAEA Fusion Association

The use of refined optical diagnostic techniques in the Culham Laboratory Plasma Focus indicates hitherto unresolved features in the temporal and spatial evolution of the current, the plasma dynamics and its microstructure. Experiments were carried out on a Mather type Plasma Focus with a standard operating condition of 27.25 kJ stored energy at 24 kV and a deuterium gas filling pressure of 1.8 torr.

Holographic interferometry, Faraday rotation and multiple k vector cooperative laser light scattering from a two beam output Q-switched ruby laser provides temporal information on the radial electron density profile $n_e(r)$, the azimuthal magnetic field $B_\theta(r)$, the current density distribution $J_z(r)$ and three different resolved k ion fluctuation spectra $S_f(k.\omega)$.

The Faraday rotation technique [1] is based on the differential half shade method with a viewed cord diameter of 250 μm and has a temporal resolution of 2.5 ns and an angular rotation resolution of 0.4 mrad. Figure 1 shows the evolution of the current density profile derived from the magnetic field measurements and the holographic electron density profiles.

Fig 1 Temporal evolution of the axial current density distribution

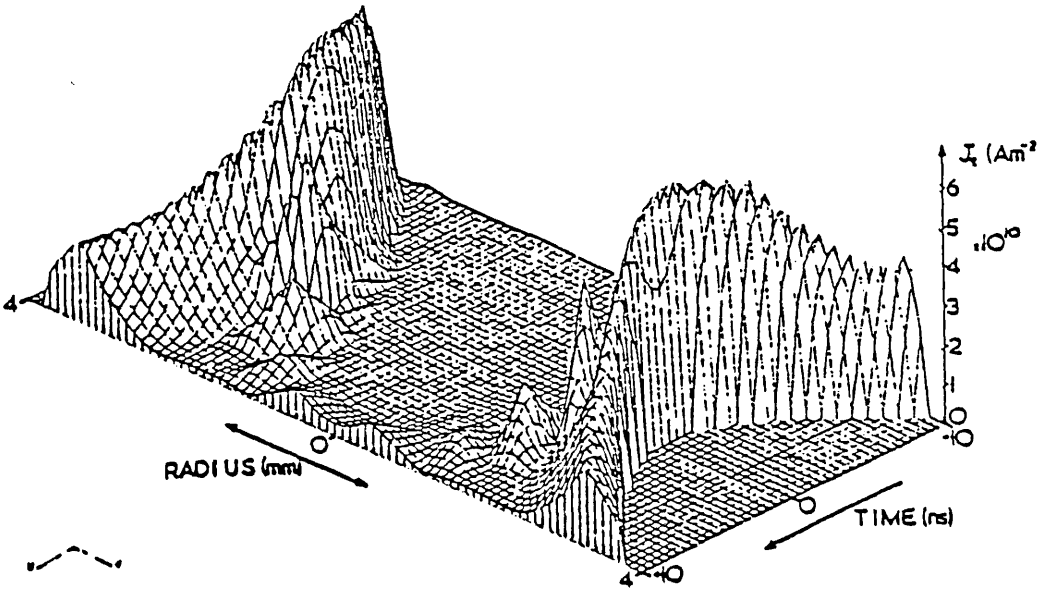

In the compression phase - 10ns to 0ns most of the circuit current is carried in a thin skin of near classical penetration depth. This thickness is equivalent to an ion Larmor radius and is half the plasma sheath. At peak compression there is complete redistribution of the current flow, manifested by a bifurcation of a fraction of the current into a turbulent core with 70% of the current remaining in the outersheath.

We consider magnetic field diffusion time as that for a field diffusing into a conductor, then $\tau_B = r L^2/\eta$. At the time t = -10ns, the plasma radius is 3.76mm, and the resistivity is $5.5 \times 10^{-7}\Omega$-m. Therefore, the field would diffuse to the axis in a time 32 μs. At peak compression, the diffusion time would be = 63 μs. These times are very much larger than the nanosecond timescales of the plasma, and explain why the magnetic field is present only within the shocked layer or skin of the plasma. The field cannot diffuse ahead more rapidly than it is convected.

During the dense pinch phase, the magnetic field is observed to diffuse rapidly to the plasma axis in a 10ns period commencing from peak compression. From the expression for the magnetic field penetration time, a perpendicular resistivity of $6.9 \times 10^{-4}\Omega$-m would be required to achieve this. This resistivity is consistent with an electron temperature of only 1.3 eV. Therefore, the plasma resistivity during this period is anomalous, and is larger by a factor approximately 6000 to that at peak compression. Thus, the electron-ion collision frequency is also anomalously high by this factor.

At later times, +10 - +15 ns, spikes are observed on the Faraday rotation data and are what would be observed for a single large axial current filament, or with many close packed axial filaments. The estimated value of beam current density is 3.7×10^{11} AM^{-2}. This is larger than the maximum current density at peak compression of the pinch and the maximum current density of the radially contracted current ring at time t = +10ns by factors 4 and 47 respectively.

From the magnetic field profiles for the current filaments the maximum field strengths are between 44 and 57 Tesla at radii 0.19 and 0.25 mm for times t = +10 and +15 ns respectively. We estimate that the half maximum radii of the filaments is between 167 and 217 μm. It should be noted that the derivation of the field strengths depend on a band width detector limited to 5 GHz: thus the values of the filament radius should be considered as the upper limits.

Observations using cooperative laser scattering [2] during the time period, when Faraday rotation 'spikes' were observed, demonstrated that scattering with a differential scattering vector parallel to the current was highly enhanced (up to a factor of 30) over thermal levels of scattering. Comparison of the data with calculated $S_f(\omega,k)$ form factor assuming a variable v_d/v_{th} parameter leads us to the conclusion that the

ratio of electron drift velocity to thermal velocity must be the unity again indicating that the current is carried by particle beams during this phase of the discharge.

Our results are supportive for the models for ion acceleration proposed by Bernstein [3] and of Gary and Hohl [4]. These models make two basic assumptions; firstly anomalous resistivity is required to produce a rapid diffusion of the current channel on to the axis of symmetry; secondly the ions have to be collisionless during the ion acceleration period with a Hall term $\omega_{ci}\,\tau_{ii} > 1$. There is clear experimental evidence for both these plasma conditions being fulfilled. Classical collisionality would predict $\omega_{ei}\tau_{ii}$ at peak compression. However the observations that beam generation is suppressed during the period 0 - 10 ns is almost certainly due to the additional collisionality factor imposed by ion accoustic turbulence during this time. For later times > +10ns as the core plasma expands the onset of axial beam currents and the concomitant rise in fusion reaction rate are inferred to be a consequence of the ions once again becoming collisionless with $\omega_{ci}\tau_{ii} > 1$. The local acceleration region probably moves with the axial velocity of the expansion zone.

The ion feature of the Thomson scattered light spectrum has been measured synchronously for three differential scattering vectors k and two values of the scattering parameter $\alpha = (k\lambda_D)^{-1}$. Three sets of collection optics view essentially identical scattering volumes situated at a position on the pinch $\underline{z}$ axis 10 mm below the centre electrode, with the laser incident, $\underline{k}_{inc}$ normal to this axis. Two scattering angles of 10 and 45 degrees (and thus two different α values) having differential scattering vectors $\underline{k}$ with no component parallel to the $\underline{z}$ axis (ie no current driven effects) yield thermal levels of the scattered light. This has enabled the effects of the radial velocity component on the ion spectrum to be measured by cross correlating the effects for both α values for a single shot. A second 10 degree scattering direction is in the plane defined by $\underline{z}$ and $\underline{k}_{inc}$ and permits the additional effects on the scattered light spectrum due to a relative electron-ion drift velocity parallel to the $\underline{z}$ axis to be measured. The temporal evolution of the ion features for these three k vectors has been built up over a large number of shots from t = -35ns to +40ns relative to the peak compression of the pinch.

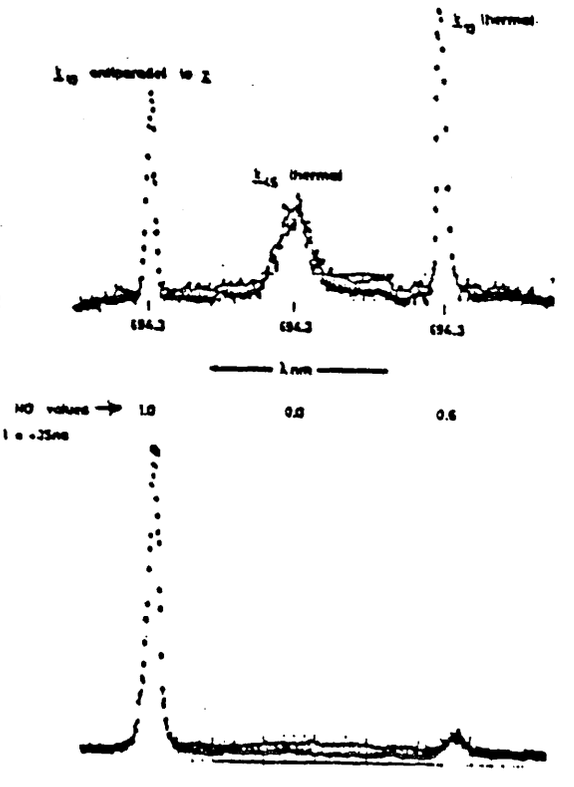

Fig 2 Triple spectra OMA analogue results obtained from multiple-k experiment at times t = -5ns and t = +3 5ns. N.D. values relate to attenuation of individual collection systems.

The fact that the plasma is characterised by annular division into a skin and a core has lead the $S_i(\omega,k)$ data to be treated as originating from such zones. For example at t = 0 the inner zone has T_i = 200 and T_e = 180 eV while the outer current carrying zone has T_i = 1200 eV and T_e = 2250 eV.

For times before peak compression the 10 degree k spectrum is enhanced with respect to the thermal spectrum by 20% at -40 ns rising to 100% at t = 0ns. This is accompanied by a blue shift and profile fitting indicates an electron-ion drift velocity v_d such that $v_d/v_{th} \sim 0.1 - 0.8$. The values are an order of magnitude greater than those indicated by the Faraday polarimetry which assumed a distributed current shell within the plasma sheath region (outer zone). This therefore provides strong evidence for the existence of filamentary current structure within the sheath region, even during the collapse phase.

As indicated earlier, enhancement of up to 30 times thermal has been observed at later times in the plasma which confirms plasma turbulence. Inspection of the scattering from the three vector scattering arrangement showed that for some shots with a higher degree of enhancement on the 10°k there was virtually no scattering at 45°. This implies that the factor of 4.53 in k between 10° and 45° was sufficient to make the 45° scattering non cooperative. We can therefore set an upper limit to the turbulence scale length in the range 1.5 10^{-5}cm to 6.6^{-5}cm.

REFERENCES

[1] D G Muir, PhD Thesis, University of London, 1983
[2] R E Kirk, PhD Thesis, University of London, 1983
[3] M J Bernstein, Phys Fluids 13 (1970) 2858
[4] S P Gary, F Hohl, Phys Fluids 16 (1973) 997

*On attachment from Royal Holloway College, University of London, UK

Proc. 3rd Int. Workshop on Plasma Focus Research, Stuttgart, (Sept 84.) p119

LASER LIGHT SCATTERING FROM DENSITY FLUCTUATIONS IN THE CULHAM FOCUS

R E Kirk*, M J Forrest, D G Muir*, M J Peacock

Culham Laboratory, Abingdon, Oxon, OX14 3DB, UK
(Euratom/UKAEA Fusion Association)

The ion feature $S_i(k,\omega)$ in the spectrum of laser light scattered from a dense plasma focus Peacock et al (1971) is recorded synchronously for three different scattering vectors $\underline{k}$ and two values of the scattering parameter $\alpha = (k\lambda_D)^{-1}$.

The scattering geometry is shown in Fig 1. where the $\underline{k}$ vectors, $\underline{k} = (\underline{k}_{scat} - \underline{k}_{inc})$ are chosen so that density fluctuations in the ion current direction $\underline{k}_{10°}$ (anti-parallel) can be compared with those in the orthogonal plane, $\underline{k}_{10°}$ (orthogonal). The scattering geometry allows a range of $\underline{k}$'s from $1.6 \times 10^4 cm^{-1}$ to $7 \times 10^4 cm^{-1}$ by comparing $\underline{k}_{10°}$ (orthogonal) with $\underline{k}_{45°}$ (orthogonal). The irradiated and viewed volume of the plasma is 4mm long axially with a mean orthogonal diameter of 5mm centred on the axis of symmetry. Light scattered over a 20ns interval from all the electrons within this scattered volume contributed to the cooperative ion feature $S_i(k,\omega)$. In order to interpret the spectrum, the density structure and the magnetic field structure have been evaluated as a function of time using holographic - interferometry and Faraday rotation polarimetry, Muir (1983), Forrest et al (1983). The polarimetry results, Muir (1983), indicates a thin outer skin, $\delta = 2r_{ci}$, which carries most of the current during the collapse phase. However, complete redistribution of the current flow occurs during the 10ns or so following peak compression and allows 30% of the current to diffuse into the core. It seems plausible, therefore, to base the analyses of the $S_i(k,\omega)$ spectra during the compression phase on contributions from two spatially separate regions viz, a thin, outer current-carrying shell and an inner core, each region having quite distinct plasma parameters.

Using this two component plasma model, with the interferometrically measured density and mass motion parameters for each component then analyses of $S_i(k,\omega)$ for $\underline{k}$ (orthogonal) predicts temperatures ~ 1 keV for the current sheath and much lower values ~ 200 eV in the core. Two apparently distinct sets of T_e/T_i parameters can be found in the sheath region viz $T_e = T_i \sim 1.5$ keV and $T_e = 2.2$ keV, $T_i \sim 850$ eV. The value of $n_e S_i(k,\omega)$ integrated over the scattering volume is close to the level expected for thermal fluctuations. Transposing these values of temperature to the $S_i(k,\omega)$ ($k_{10°}$ anti-parallel) spectrum one then derives on a best-fit basis the spectral shift due to current drift as well as the bulk, axial v_z and compressional (v_r) velocities for the different plasma regions. The results of such an analysis is shown in Fig 2.

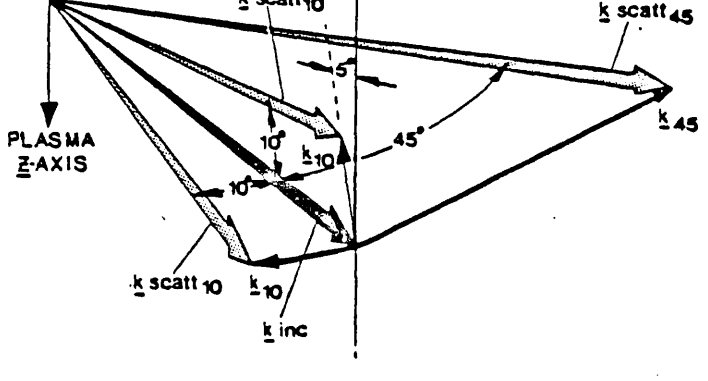

Figure 1 Schematic diagram of scattering vectors relative to focus axis of symmetry (Z-axis). $\underline{k}_{10°}$ (anti-parallel), $\underline{k}_{10°}$ (orthogonal), $\underline{k}_{45°}$ (orthogonal) are measured synchronously.

Figure 2 Example of scattered light spectrum, ———, at t=0ns for $\underset{\sim}{k}_{10}$. (anti-parallel). Analysis is based on two spatially separate fluids viz a relatively high temperature current sheath — · — · (r_s = 2.5mm, n_e = 2.4 x $10^{18}cm^{-3}$, T_e = 967 eV T_i = 350 eV, $(k\lambda_D)^{-1}$ = 4.3, v_r = 9 x 10^6cm s^{-1}, v_z = 3.5 x 10^7cm s^{-1}) and a core region ------ (r_c = 1.1mm, n_e = 7 x $10^{18}cm^{-3}$, T_e = 107 eV, T_i = 182 eV, $(k\lambda_D)^{-1}$ = 23, v_r = 4 x 10^6cm s^{-1}, v_z = 2 x 10^7cm s^{-1}). The contribution from the sheath region is blue-shifted with respect to the core region.

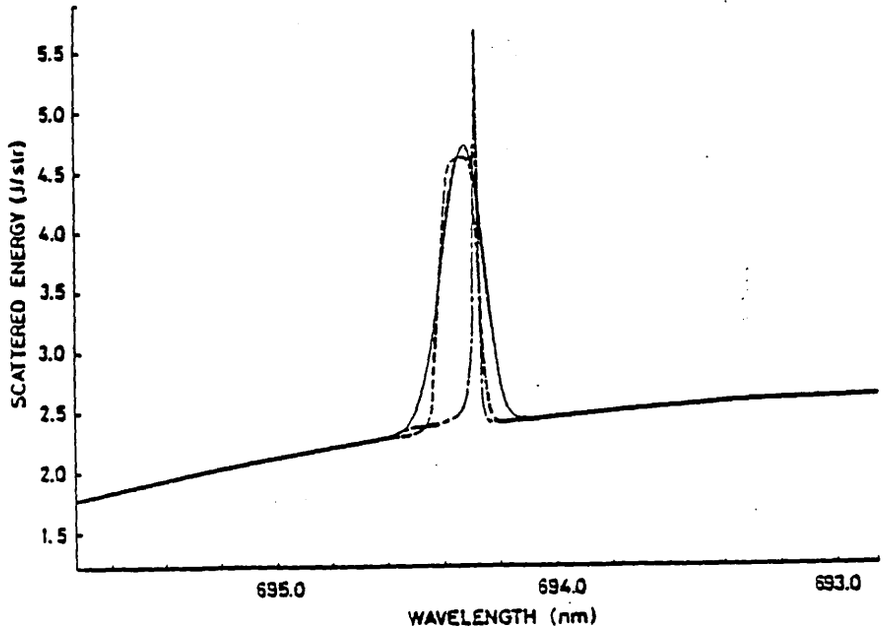

The electron drift parameter derived from the relative blue-shift of the spectrum from the sheath region is significant and can approach the electron thermal velocity as indicated in Fig 3. Polarimetry however indicates $\bar{v}_d/v_{th} \ll 1$ during the collapse phase, Muir (1983). These two contradicting conclusions can most readily be reconciled by postulating filamentation of the current in the sheath region. Turbulence driven by the filamentary current then explains the high T_e and supra-thermal level of the blue-shifted optic in the scattered spectrum for the sheath region, Fig 2. It remains somewhat puzzling however why the average skin depth measured by polarimetry is governed by classical diffusion until peak compression, Muir (1983).

During the period t = 0 $\pm$ + 15ns, Fig 4, there is rapid, anomalous diffusion of the poloidal magnetic field into the core region. The electrical conductivity is ~ 10^{-4} x Classical, Muir (1983). It is of some interest to speculate on which mechanism could account for this onset of anomalous behaviour. Current-driven, ion-acoustic turbulence, electron-cyclotron drift instabilities, Forsland et al (1971), Lower Hybrid drift instability (Bertalot et al (1980), have all been suggested. At t = 0ns mixing of the high temperature outer skin with the lower temperature core plasma may create an appropriate density gradient to trigger one or more of the above non-linear processes.

The plasma conductivity at t = 0ns is

$$\sigma_{AN} = 10^{-4}\,\sigma_{class} = 10^{-4}\,\frac{\omega_{pe}^2}{2\nu_{ei}} = 10^{13}s^{-1} \text{ (shell region)} \rightarrow 2.5 \times 10^{12}s^{-1} \text{ (core region)}.$$

This is of the same order of magnitude as reported by Bernard et al (1975, 1978) for the region outside the pinch.

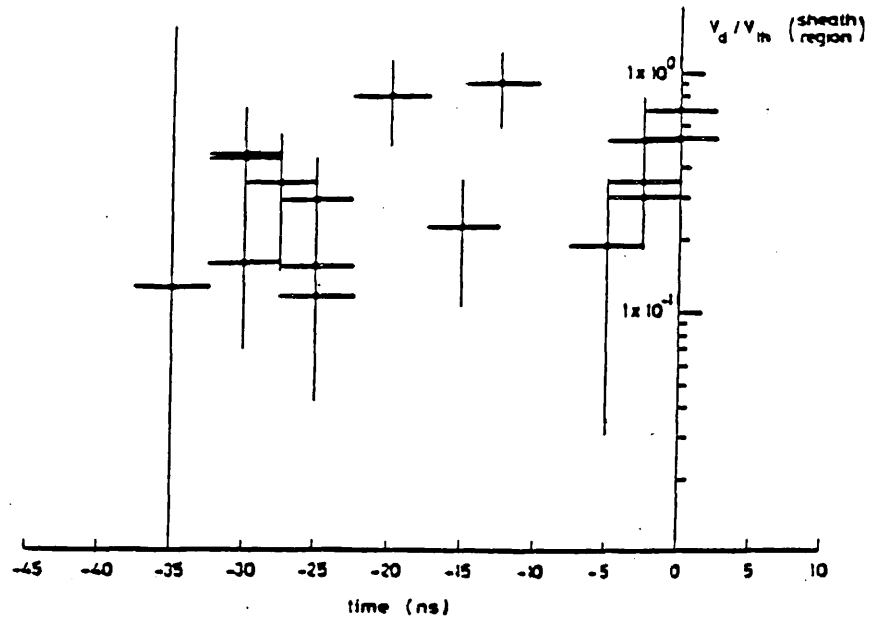

Figure 3 Ratio of electron drift to thermal velocity in the sheath region derived from analysis of scattered light spectra along $\underline{k}_{10°}$ (anti-parallel); see eg Fig 2.

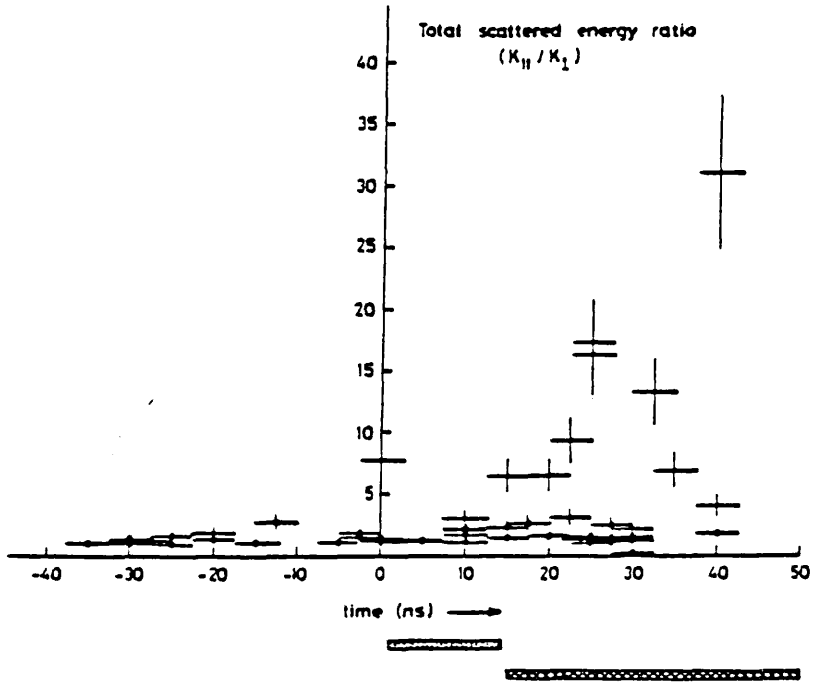

Figure 4 - Ratio of total scattered light (energy), from whole of laser irradiated volume, for $\underline{k}_{10°}$ (anti-parallel)/$\underline{k}_{10°}$ (orthogonal).
:::::::::: indicates period of anomalous current penetration into core
xxxxxxx indicates period of beam current propagation and particle acceleration.

The 'effective' collision rate, Ω_{AN}, due to induced turbulence should be able to account for these values of σ_{AN}. A consideration of the effective collision rates for several instability mechanisms indicate that turbulence with $\Omega_{AN} = \omega_{ce}$ or ω_{pi} comes closest to accounting for the anomalous factor, suggesting electron cyclotron drift and current-driven ion acoustic waves. In the former case, Forslund (1971), the dominant $|k|$ for linear growth is $\underline{k}v_e/\omega_{pe} = 0.5$, ie $\underline{k} = 2 \times 10^4 cm^{-1}$ which is close to our experimental $\underline{k}_{10°}$. Our experiments, Forrest et al (1983), indicate, moreover, that the shorter scale lengths ie $(\underline{k}_{45°})^{-1}$ are damped out during the later (> +15ns) beam propagation phase of the discharge, while the $\underline{k}_{10°}$ spectra became extremely non-thermal, Fig 4.

During the period (t > +15ns) following the anomalous field diffusion the polarimetry shows very clear evidence for short-lived (< 2ns) beam currents flowing within a diameter < 250 μm, Muir (1983). These beams are correlated with the very strong enhancement of $n_e S_i(k,\omega)$ shown for some discharges in Fig 4. The maximum enhancement is x 30 above thermal in Fig 4 but since this value is derived by integration over the total scattering volume while the beams occupy only ~ 10^{-3} of the volume then the <u>local</u> enhancement $n_e S_i(k,\omega) = 3 \times 10^4\ n_e$. Other authors eg Neil and Post (1981) report X-ray filamentation, dense local plasma regions, and > 100 keV ion and electron acceleration during this phase of the discharge. The acceleration mechanism for the class of particles orbiting the axis of symmetry has been discussed by Gary and Hohl (1970), Gary (1974), Bernstein (1970), Potter and Haines (1971). The basic conditions necessary for these models to hold ie, anomalous diffusion followed by collisionless, $\omega_{ci}\ \tau_{ii} > 1$, conditions, are observed in this study.

References

Bernard A, Garconnet J P, Jolas A, Le Breton J P, De Mascureau J, Proc Plasma Physics and Controlled Fusion Research, 1978 (7th Conf Proc Innsbruck, 1978). Publ IAEA Vienna Vol II, pp 159-172.

Bernard A, Coudeville A, Jolas A, Launspack J and de Mascureau J, Phys Fluids <u>18</u>, 180-194 (1975).

Bernstein M J, Phys Fluids <u>13</u>, 2858 (1970).

Bernstein M J, Phys Rev Lett <u>24</u>, 724 (1970).

Bertalot L, Deutsch R, Herold H, Jager U, Kaeppeler H J, Mozer A, Oppenlander T, Ruckle B, Sadowski M, Schilling P, Schmidt H, Proc 8th Int Conf on Plasma Physics and Controlled Fusion Research, Brussels, (1980). paper-CN-38/9-1-2, pp 177-185.

Forrest M J, Kirk R E, Muir D G and Peacock N J, Proc 11th Europ Conf on Controlled Fusion and Plasma Physics (Aachen, Sept 1983).

Forslund D, Morse R, Nielson C, Proc 4th Conf on Plasma Physics and Controlled Nuclear Fusion Research (1971) Publ IAEA Vienna Vol II, pp 277-290 (1971).

Gary S P, Hohl F, Phys Fluids <u>16</u>, 997-1002 (1970).

Gary S P, Phys Fluids <u>17</u>, 2135-2137 (1974).

Muir D G, PhD Thesis, University of London (1983).

Neil G R and Post R S, Plasma Physics <u>23</u>, 425-434 (1981).

Peacock N J, Hobby M G and Morgan P D, Plasma Physics and Controlled Fusion Research (IAEA Vienna (1971) Vol I, pp 511).

Potter D E and Haines M G, Plasma Physics and Controlled Fusion Research (IAEA, Vienna (1971) Vol I,pp 611).

*Royal Holloway College, University of London

1984 IEEE Int. Conf. on Plasma Science, Book of Abstracts, May 1984, St Louis, Missouri, USA

5A3 - INVITED PAPER

TIME AND SPACE HISTORY OF TURBULENCE IN THE PLASMA FOCUS USING LASER SCATTERING TECHNIQUES

R E Kirk*, M J Forrest, D G Muir*, N J Peacock

Culham Laboratory, Abingdon, Oxon, OX14 3DB, UK
(Euratom/UKAEA Fusion Association)
*Royal Holloway College, University of London

The ion feature $S_i(k,\omega)$ in the spectrum of laser light scattered from a dense plasma focus, Peacock et al (1971) is recorded synchronously for three different scattering vectors $\underline{k}$ and two values of the scattering parameter $\alpha=(K\lambda_D)^{-1}$.

Using a two plasma component model, Kirk et al (1983), $S_i(k,\omega)$ is interpreted in terms of scattering from the outer current sheath and an inner plasma core. The electron and ion temperatures, the bulk plasma motion, the electron density n_e, and drift velocity, v_d, are evaluated for each separate plasma region. The electron drift parameter (v_d/v_{th}) derived from the relative blue-shift of the spectrum is significant in the sheath region and can approach unity. These parameters, as well as the density fluctuation level, $n_eS_i(k,\omega)$, give some insight into the level of turbulence in the sheath region during the implosion phase.

Several electron heating mechanisms have been considered. Lower hybrid and electron cyclotron drift instabilities are indicated as possible mechanisms for increasing the sheath temperature early in the implosion. A period of highly resistive field diffusion is observed to follow peak compression and this can most readily be ascribed to the onset of ion acoustic instabilities. Following the anomalous field diffusion period there is clear evidence from short-lived, <2ns, beam currents on the magnetic axis. These electron beams evidently give rise to intense, local turbulence levels with $n_eS_i(k,\omega)=3\times10^4\ n_e$.

During this late phase of the discharge, which is synchronous with the neutron emission, the basic conditions necessary for the acceleration of those ions which orbit the axis of symmetry, Gary (1974), are observed in this study.

References

1. Peacock N J, Hobby M G, Morgan P D, Plasma Physics and Controlled Fusion Research. IAEA, Vienna. (1971) Vol 1 pp511.

2. Kirk R E, Forrest M J, Muir D G, Peacock N J, Proc 3rd Int Workshop on Plasma Focus Reseach (1983). Stuttgart. IPF - 83-6 119-122.

3. Gary S P, Phys Fluids 17 (1974) 2135-2137